Development of a high-performance artificial neural network model integrated with finite element analysis for residual stress simulation of the direct metal deposition process

Farshid Hajializadehkouchak

A Thesis
In
The Department
of
Department of Mechanical, Industrial, and Aerospace Engineering

Presented in Partial Fulfillment of the Requirements
For the Degree of
Doctor of Philosophy (Mechanical Engineering)
At
Concordia University
Montreal, Quebec, Canada

November 2022

CONCORDIA UNIVERSITY

SCHOOL OF GRADUATE STUDIES

This is to certify that the thesis prepared

By: Farshid Hajializadehkouchak

Entitled: Development of a high-performance artificial neural network model integrated with finite element analysis for residual stress simulation of direct metal deposition proces

and submitted in partial fulfillment of the requirements for the degree of

Doctor Of Philosophy (Mechanical Engineering)

complies with the regulations of the University and meets the accepted standards with respect to originality and quality.

Signed by the final examining committee:

______________________________ Chair
Dr. Anjali Awasthi

______________________________ External Examiner
Dr. Yaoyao Fiona Zhao

______________________________ Examiner
Dr. Ramin Sedaghati

______________________________ Examiner
Dr. Farjad Shadmehri

______________________________ Examiner
Dr. Biao Li

______________________________ Thesis Supervisor
Dr. Ayhan Ince

Approved by ______________________________
Dr. Muthu Packirisamy, Graduate Program Director

11/8/2022 ______________________________
Dr. Mourad Debbabi, Dean
Gina Cody School of Engineering and Computer Science

Abstract:

Development of a high-performance artificial neural network model integrated with finite element analysis for residual stress simulation of direct metal deposition process

Farshid Hajializadehkouchak, Ph.D.

Concordia University, 2022

Additive manufacturing (AM) processes are among the manufacturing methods implemented in various industries. Direct metal deposition (DMD) is part of AM processes that uses the laser heat source to deposit the metallic material in the form of powder or wire onto a substrate and build a component in a layer-by-layer scheme. The DMD process is known to be cost-effective and easily adaptable for building complex structures. During a DMD process, material experiences several heating and cooling cycles which lead to the formation of residual stresses and distortions of the fabricated part.

There are several experimental-based methods and techniques for measuring the residual stresses of metallic components. However, the application of these methods can damage the fabricated parts or may require considerable time and tooling expenses for the experiment. Alternative solutions such as finite element (FE) analysis were developed to predict the residual stresses without damaging the part. The application of the FE in assessing the residual stress distribution is time-efficient and cost-effective. The FE analysis of DMD process includes thermal and mechanical analyses; the temperature history of the elements is obtained by performing a pure heat transfer analysis, then it is applied to the mechanical model to calculate the structural response of the part. One of the shortcomings of the FE analysis of DMD process corresponds to the high computational time of the mechanical analysis. Therefore, several techniques and approaches were developed in the literature to address this issue and improve the computational efficiency of the FE method.

Throughout this thesis, a novel approach of integrating the FE analysis with artificial neural networks (ANNs) is presented as an efficient method for improving the computational time of predicting the residual stresses in DMD fabricated parts. ANNs are part of machine learning (ML) algorithms that tries to determine the logical relationship between the given inputs and the associated output(s). A feed-forward ANN with gradient descent backpropagation developed in Keras was implemented. The ANN is trained by feeding the dataset into the network and minimizing the error function.

In the present study, several structures made from AISI 304L with 12-layers and 18-layers deposition were considered. and a detailed thermomechanical FE analysis was performed on them.

Temperature history of the elements along with their dimensional features of 12-layers structures were extracted as the inputs and the corresponding residual stress components were recorded as the outputs to train the ANN. On the other hand, the temperature history of the elements and their geometrical features extracted from 18-layers structures were fed into the trained ANN for making predictions. The results of the integrated ANN-FE are compared with the results of the residual stresses of 18-layers obtained from the detailed thermomechanical analysis. The prediction errors were calculated and shown in the form of 3D contours and scattered errors. Moreover, the histogram analysis was performed for each 18-layers structures to better present the fraction of the elements with the associated error ranges. Finally, the computational times are recorded and compared with the results of the detailed FE analysis to evaluate the efficiency and performance of the proposed novel ANN-FE method.

The results showed that for almost all of the structures and all the stress components, the predicted pattern and magnitude of the residual stress were consistent with the detailed FE analysis. For some of the structures, very high errors were observed which were associated with the low-stress state zones in which the actual stress magnitude was low and the high errors pose no critical condition. Although there are some predictions showing higher errors in some regions, the majority of the elements in the structures showed prediction errors of less than 15% supported by the histogram analysis. Significant improvement in the computational time of the 18-layers structures was also achieved (6 times as an average). The computational time of predicting the residual stresses in the DMD parts was improved substantially with low loss in the accuracy of the predicted results. Therefore, the proposed method can be implemented for investigating the effects of the hyperparameters on the residual stresses in DMD process.

Acknowledgements

I would like to thank my supervisor, Prof. Ayhan Ince, for his invaluable support, insight, patience, and guidance throughout all these years. He always encouraged me and challenged me to extend my knowledge and get the best of myself in every stage of this study. His knowledge taught me how to become a good researcher and also his high ethics showed me how a good man should be like. I am truly grateful to be under his supervision for my Ph.D. studies. I appreciate all the efforts he has put to take me to this stage.

Also, I truly acknowledge the funding and financial support I received from the department of Mechanical Engineering and my supervisor, Prof. Ayhan Ince.

Finally, I would like to thank my lovely wife, Mrs. Parisa Fataei, for her unconditional love and support during all these years. I am deeply indebted to her for being by my side at all difficult times and for her patience during the completion of this thesis. I would like to thank my mother and brother for their consistent love and kind support during my whole life that motivated me toward continuing my education to Ph.D. level. I hope I made my father proud of me by reaching the highest educational level he wished for.

Table of Contents

List of Figures

List of Tables

Abbreviations

AM	Additive Manufacturing
CNC	Computer Numerical Control
CAD	computer-aided design
DMD	Direct Metal Deposition
FE	Finite elements
ANN	Artificial Neural Networks
ML	Machine Learning
CFD	Computational Fluid Dynamics
$\bar{\mathbf{X}}$	spatial coordinates vector
$\mathbf{B}$	derivative or kinematic matrix of **N**
$\mathbf{A}$	element surface area
t	time
Q	body heat source
q^p	total temperature-dependent heat flux flows out of the surface A
ρ	material density
P	heat source power
C_p	specific heat of material
η	efficiency of the heat source
k	conductivity
x, y, z	coordinates of elements
T	temperature
a_b, b_b, c_b	length of the ellipsoid in longitudinal, depth, and transverse directions
T^n	Temperature at t^n

v	transverse speed of the heat source
R	Residual value
h	convection coefficient pf surrounding atmosphere
T_∞	ambient temperatures
ϑ	emissivity
Φ	Stefan-Boltzmann constant
q^f	surface traction
ϵ	total strain
ϵ^p	plastic strain
C	4th order temperature-dependent elastic stiffness tensor
ϵ^{th}	thermal strain
λ	plastic multiplier
κ	current yield stress
σ_s	deviatoric stress
σ_m	hydrostatic stress
μ	Lame's coefficient
f	yield function
α	back stress
$\hat{n}$	flow direction
H	hardening value
z_N	net input of the neuron
$\vec{x}$	input vector in ANN
Yb	scaled distance from the substrate

MSE	Mean Square Error
$S11$, $S22$, $S33$	stress components in the X, Y and Z directions
$S12$, $S13$, $S23$	shear components of stress

Chapter 1:

Introduction to the direct metal deposition process

In this chapter, the basics of the DMD process and implementing this process to fabricate a metallic component are discussed briefly and the advantages and disadvantages of the process are compared with the conventional production methods. Furthermore, the main challenges as well as new trends in the field of modeling of the process are provided. The motivation and the novelty of the research are also presented at the end of this chapter.

1.1. Fundamentals in the direct metal deposition processes

DMD processes are known as the incremental addition or deposition of metal alloys to build the final geometry of a part [1, 2] based on a given three-dimensional (3D) computer-aided design (CAD) file. DMD processes benefit from the easily adaptable and adjustable features based on the part's geometry and process parameters. This distinguishes the DMD processes from the old and conventional production methods of metallic components that are not easily adjustable based on the requirements of the given part [3-5]. These features of the DMD process make it very efficient and favorable for rapid prototyping and design purposes where many primary designs have to be fabricated and tested prior to achieving the final configuration of the part [6, 7].

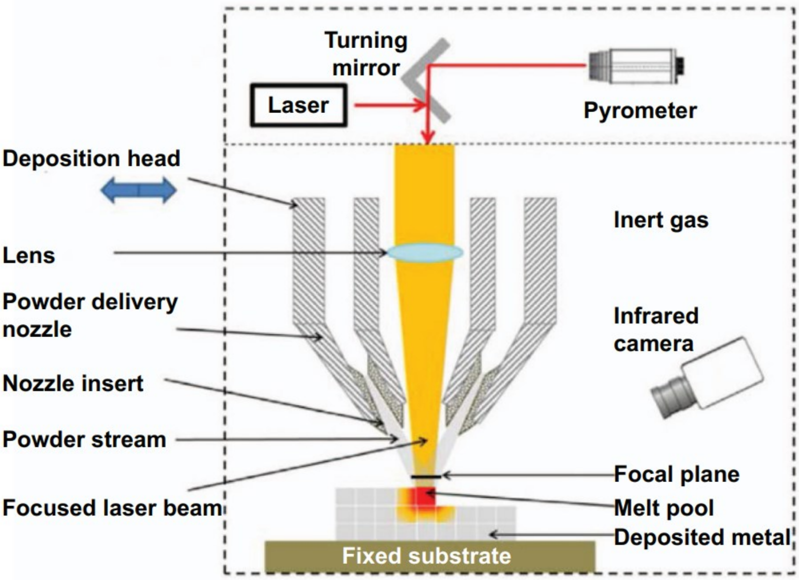

Figure 1 Schematic representation of direct metal deposition process [8]

1.1.1. Advantages of direct metal deposition processes

The unique methodology of the DMD processes for fabricating parts attracts many industries and academic research groups. Employing the DMD process as a producing method will benefit computer-aided-design (CAD), computer-aided-engineering (CAE), computer-aided-manufacturing (CAM), and design-for-manufacturing-and-assembly (DFMA) in different aspects [9, 10]:

- Geometrical complexity

DMD enables the potential of constructing optimized designs which reduces the weight of the final products. This is very critical especially in the automotive and aeronautics industries that fuel consumption is an important factor. Therefore, designers will have more flexibility to design and manufacture products to meet greener and environment-friendly criteria by reduction of emitting greenhouse gasses [10].

- Decreasing joints in an assembly/design

DMD provides the possibility of combining parts necessary for an assembly into one piece to a fewer number of parts. This will remove the need for joints such as welds, bolts, and rivets. Some of the lateral induced deviations including geometrical and dimensional errors come from the joining and assembling of different parts of a system. The capability of the DMD method to combine several parts into one part may lower the weight of the final product and also enhance the geometrical and dimensional tolerances of the final assembly [9].

- Fewer material wastes

Compared to the conventional production processes such as turning and milling which involve the removal of the material to shape the raw material into the final product, the DMD can reduce material waste significantly due to the nature of the process [11].

- Easily adjustable to the modifications

The DMD process is capable of producing parts with very high complexity on the basis of using CAD files. Therefore, it is more affordable and accessible for engineers to fabricate a customized component for a specific application. Furthermore, as there is no need for designing and preparing new dies and modulus for a specific part, it is desirable for the engineers to employ this production method especially at the early stages of product development [11].

1.1.2. Limitations

As a production method, DMD has its own unique and distinct advantages and disadvantages. Up to now, DMD has certain limitations when it is used as the main production method for a specific part. Therefore, the designers and engineers should investigate the possibility of implementing DMD as the fabrication method in the product development process and analyze the trade-off between employing DMD vs. other conventional production methods. Some of the shortcomings of applying DMD process are listed in the following [11]:

- Undesired distortions

The nature of the incremental deposition of the material requires certain conditions which involve the application of a heat source especially for metal alloys. Therefore, the thermomechanical nature of the process makes it very susceptible to deviations of the part from the desired dimensions [7, 10].

- Optimization of the process parameters

In order to achieve a good quality for the manufactured part in an DMD process, the process parameters such as the traveling speed and power of the heat source, number of paths, the thickness of the deposited layer, …. are needed to be optimized which may not seem to be beneficial in the design and developing of a product [7, 10].

- Poor mechanical properties

Application of a heat source for melting the material and solidifying it onto a substrate may result in some defects such as a cavity, porosity, and lack of fusion which results in inhomogeneous properties of the part [11].

- Restriction in size of the component and the production rate

The size of the component that can be built by the DMD machines is normally governed by the size and the working space of the CNC head which is the most used mechanism for controlling and generating the scan paths in DMD processes. Additionally, the deposition rate is usually slow for the fabricating process of the metal alloys to lower the defects and possible lateral deviations of the manufactured part via DMD. Therefore, the production time may increase for large and complex shapes [4, 7, 10].

- Expensive equipment for large-scale productions

Fabricating large-scale parts using the DMD process often comes with higher expenses which are related to the bigger size of CNC machines with very high transitional accuracy in all directions and rotational movements which controls the scanning paths DMD processes [7, 9, 10, 12].

- Environmental effect of the process

DMD processes often uses melting the material in the form of powder or wire which may emit harmful and hazardous gasses and compounds into the environment [4, 10, 11, 13].

Despite all advantages of the DMD processes described so far, applying the method as a production method requires vital considerations to achieve a good quality product [3, 6, 7, 10]. One of the major challenges of additive manufacturing processes of metal alloys is related to the design of thermal and mechanical supports for the parts with significant complexities [11, 14]. Thermal supports are designed and attached to the main part to help with the dissipation of the thermal energy and control the cooling rate of critical points of the part. Mechanical supports are also vital for holding the workpiece throughout the fabrication process to meet the design tolerances and prevent undesired deflections and deviations [15-17]. Designing the thermal and mechanical supports for a complex part and also determining the locations of the supports are crucial to reach a flawless product. This requires experience and knowledge in depositing metal alloys which are dealing with high thermal gradients leading to high residual stresses [15-17]. Furthermore, the stacking or deposition direction of a complex part to reach an acceptable quality of the fabricated part is another key factor that can be time-consuming and may need to be tested several times. The stacking direction of the part has a major impact on the surface finish and also on the residual stresses induced between the layers which may cause delamination [18-20]. Additionally,, the process parameters setup for the DMD processes such as laser power, laser feed rate, the thickness of each layer, ... etc., requires considerable knowledge and experience as well. Inaccurate parameter setup may result in a lack of fusion or overheating of the printed part which in general causes unfavorable consequences such as porosities inside the medium, swelling, and delamination. As the DMD processes are commonly used for the early stages of fabrication and design processes, developing a comprehensive strategy for the early design stage is demanding [10, 17, 21].

After completion of the fabrication process, the part should be cut or removed from the substrate/supports. Normally, the substrate/supports are made of the same material as the part itself to prevent inconsistent thermal expansions of the workpiece and the substrate. After cutting or removing the part from the substrate/supports, lateral deflections may happen that apply residual stresses to the part. This is detrimental where the part has a complex geometry and needs several cuts from the supports [11, 15, 18-21]. Typically, the substrate is preheated to reduce the lateral deflections or deviations of the part after the cut or removal step. All the factors and parameters mentioned have a significant impact on the quality and geometrical accuracy of the fabricated part. However, the cutting process and reliving the residual stresses is the final step in the production chain and it should be performed discreetly [3, 10, 16, 21].

1.2. Residual stress formation in direct metal deposition parts

DMD process is involved with the application of a heat source that melts the material and creates very high thermal gradients that leads to the formation of the residual stresses [3, 7, 10, 11, 15, 18, 21]. As the heat source moves during a typical deposition of a metal alloy, a material point of interest (shown in Figure 2A) experiences steep and inhomogeneous thermal gradients which results in sudden expansion and contraction of the material. As the heat source moves away, the material inside the melt pool starts to solidify and a significant shrinkage occurs in a small fraction of time. Since the yield strength of metal alloys at high temperatures is declined drastically, no considerable compressive stresses were applied to the already deposited volume right behind the heat source because of the sudden thermal expansion. However, the highest compressive strains are imposed on the newly solidified material from the previously deposited volume (Figure 2B). On the other hand, the newly solidified material is cooled down immediately and shrinks which imposes tensile stresses on the previously deposited material. Strains in the longitudinal direction (parallel to the heat source moving direction) are gradually changing from compressive to tensile as the heat source moves further away and the deposit is cooled down to room temperature (Figure 2C). These sequences are repeated for every point of interest in the built component. However, the magnitude of the tensile residual stresses are declined as upper layers are deposited [22].

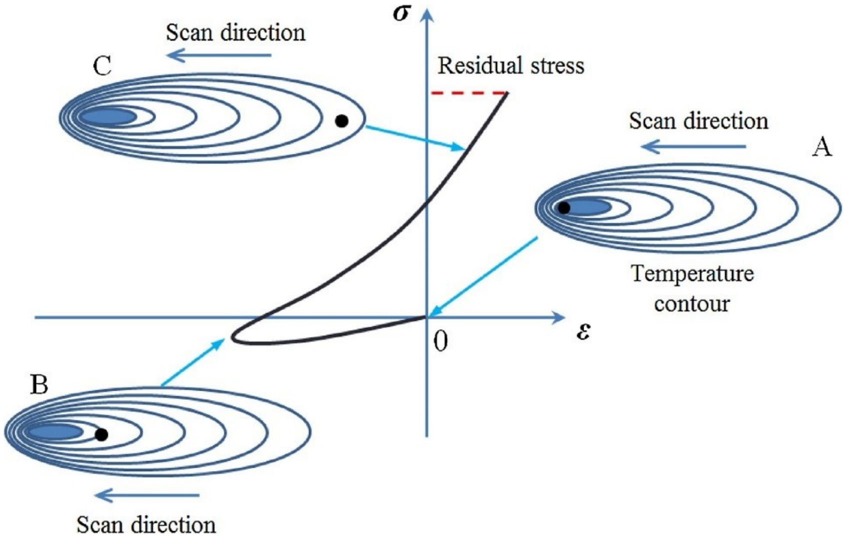

Figure 2 Schematic representation of formation of strains for a point of interest in direct metal deposition process of metal alloys [22]

The presence of residual tensile stresses inside a medium is not beneficial for the sake of corrosion resistance and fatigue strength [23]. In the stacking direction, tensile residual stresses are formed between the newly deposited layer and the substrate or lower layer. Moreover, the residual stresses magnitude is declined and gradually changed into compressive residual stresses as the deposition of upper layers continued. The thermal expansion of layers beneath the heat source applies compressive stresses on the lower layers and compressive plastic strains are formed [24]. The main concern is related to the tensile residual stresses between the newly deposited layer and its substrate as it acts as the driving force for the delamination of the built component. The sequence of formation of residual stresses in longitudinal and stacking directions for the 2nd and 6th layers are shown in Figure 3.

1.3. Evaluation of the residual stresses in direct metal deposition parts

Applying the DMD process as the main manufacturing method for a part requires a comprehensive knowledge and experience to achieve a high-quality component that complies with the original dimensions and tolerances [3, 5, 6, 9, 14, 16, 17, 21]. Commonly, the residual stresses are created after the production process of the part which is not suitable for the application of the part. Therefore, certain techniques are developed to estimate and evaluate the magnitude and distribution of the residual stresses. Due to the complex phenomena of generation of residual stresses, geometrical factors, and many multi-disciplinary factors, it is quite demanding to calculate the residual stresses inside a medium. Consequently, several methods and techniques were developed and utilized to evaluate the residual stresses of AM parts, including destructive tests, non-destructive tests, and numerical methods. In the following, these techniques and techniques are presented and discussed.

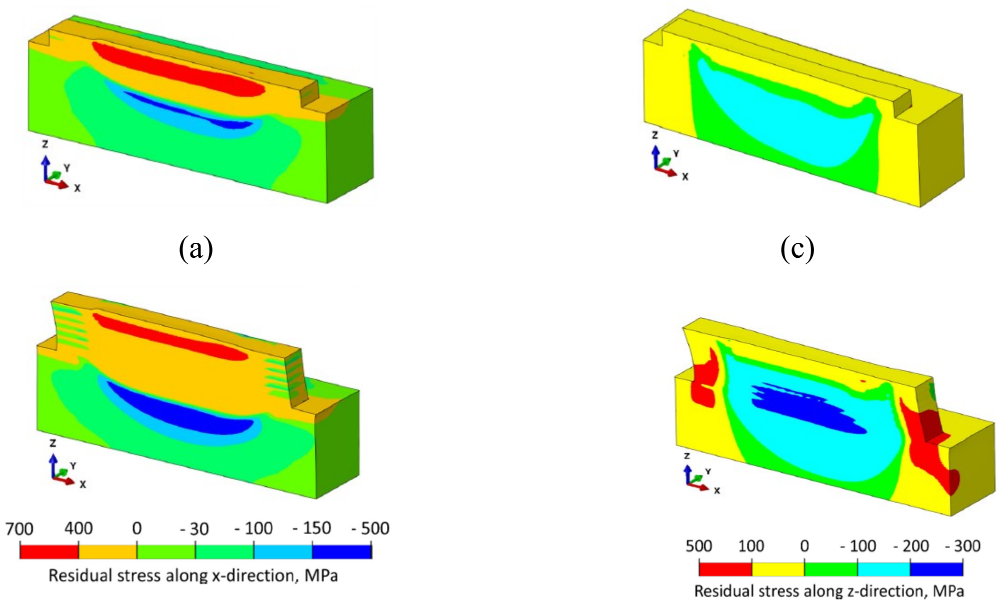

(a) (c)

(b) (d)

Figure 3 Formation of residual stresses in the longitudinal direction (a) 2nd layer, (b) 6th layer, and stacking direction (c) 2nd layer, (d) 6th layer [24]

1.3.1. Destructive tests

Destructive tests to measure the residual stresses refer to the procedures that a specific product is tested using certain equipment, however, the specimen is damaged completely or partially compared to the initial defect-free state. These methods often involve partial removal of material from the location where the residual stresses are supposed to be determined. By removing the material, the residual stresses are relaxed and as a result, the part is deformed freely. Measuring the resultant deformation yields the residual stress in the material-removed area. The most common and well-known methods are as follow:

- Hole drilling: In this method, a very small hole (approximately 1.8 mm in diameter with 2 mm depth) is drilled in the area where the residual stresses are to be evaluated. Before the drilling, several strain gauges are placed in the vicinity of the hole according to certain standards. Relaxation of the residual stresses leads to the small deformation of the part in the vicinity of the hole that is being monitored by strain gauges. The measured strains are then used to calculate the residual stresses. This method is considered one of the fastest and commonly used methods for determining residual stresses especially for evaluating the residual stresses [25].
- Ring core: In the ring core technique, a part of the surface of the specimen is removed in the area where the residual stresses are to be determined. Instead of creating a hole in the hole drilling method, the area to be removed is a washer-type or ring-type surface and the strain gauges are placed at the center of the unremoved surface to measure the deformations after relaxation of the residual stresses. This technique offers higher accuracy compared to the hole drilling as it is associated with a higher area. However, the part is usually more damaged compared to the hole drilling technique. If the residual stresses are not uniform inside the medium and mutate through the thickness, different hole or ring depths can be used to determine the residual stresses associated with the thickness of the part. Incremental drilling is used to generate different depths and measure the strains accordingly to obtain an incremental-based profile for the residual stress through the thickness [26].
- Deep hole drilling: This is a combined method of hole drilling and ring core. The location of the interest is drilled thoroughly and then the diameter of the hole is measured accurately. Then, the core drilling is applied to remove a part of the material around the drilled hole. Afterward, the diameter of the hole is measured again. By calculation of the dimeter variation, the residual stresses that are relieved by removing is found at the location of the interest. This method is accurate but it is more destructive than the other techniques [26].
- Sectioning method: In this method, sections of material of the part are removed and the deformations are recorded via strain gauges and used for determination of the residual stresses. This method is considered as highly destructive compared to the others. The cutting process is very important in the process and needs to be performed discreetly in order to avoid applying further residual stresses on the specimen [27].
- Contour method: During this method, the workpiece is cut using a high precision cutting method such as wire cut or electro-discharge machine to make a clean cut. Then, the contour of the cross-section is measured right after the cut and after passing some time using a coordinate measuring machine (CMM). The distance between corresponding points is

recorded and entered in a finite element-based code to find the resultant residual stresses relaxations that generated the deformations [26].

1.3.2. Non-destructive tests

The workpiece that undergoes destructive tests is partially or completely damaged and may not be used in the service anymore. However, the non-destructive test to measure the residual stresses inside a medium offers more favorable outcomes by not damaging the specimen. The non-destructive methods often use high technology-based procedures to evaluate the residual stresses. Nevertheless, the cost of the equipment and the setup for the test is generally expensive. The non-destructive methods include X-ray diffraction (XRD), neutron diffraction, and magnetic/ultrasonic methods.

- X-ray diffraction: In this method, the X-ray is projected on the specimen at different angles and then detected on the other side of the specimen. The presence of the residual stresses inside a medium alters the distances of the lattice structure. Therefore, comparing the detected beams from both a stress-free medium and a specimen with residual stresses determines the residual stress inside the body. The only requirement of this method is that the material needs to be polycrystalline and the X-ray can produce diffracted beams after the incident. XRD is suitable for residual stress determination under the outer surface of the part and is typically not used for the purpose of residual stress determination for very thick specimens [26, 28].
- Neutron diffraction: Very similar to XRD method, the neutron diffraction method uses different wave-lengths of beams generated from a neutron source. The process is similar but the penetration depth of the beam from a neutron source is greater than that of XRD [26, 28].
- Ultrasonic methods: This method relies on that the sonic waves travel with different speeds inside a stress-free medium and when there are considerable residual stresses inside a part. The transducer transmits the ultrasonic wave inside the medium and then the wave propagates through the body and is detected on the other side. The method is calibrated with a part that is stress-free and then the results are interpreted. This method is prevalent as it is quick, more affordable, portable, and easy to implement without too much cost [26, 28].

Besides these methods, there are several other non-destructive methods that can be used to determine the residual stress scatter experimentally. These methods include the Barkhauser Noise Method which is suitable for ferrous metals, and thermoelastic methods that make use of the different heat transfer characteristics of a stress-free material and one with residual stresses [26, 28].

Among the experimental-based methods, non-destructive techniques are preferred in the approximation and evaluation of the residual stresses in DMD products made from metal alloys. Even though the hole drilling method is the most reliable and applicable method for the determination of the residual stresses in the industry and research studies, the destructive nature of the process is not favorable for DMD products as the materials used in the DMD are often expensive. Hoye et al. [29] used the neutron diffraction method to measure the residual stresses in the wire arc additive manufacturing (WAAM) process of Ti-6Al-4V and reported that the tensile residual stresses along the longitudinal direction are critical. Ding et al. [30] conducted a similar study on a thin-walled mild streel structure made with WAAM and measured the residual stresses by combining the sectioning method with the non-destructive neutron diffraction method. Residual stresses in the longitudinal direction were found to be dominant in the structure. A similar study was performed by Colegrove et al. [31] to assess the residual stresses in mild steel. Wu et al. [32] investigated the residual stress formation in 316 stainless steel during the additive manufacturing process via the neutron diffraction method and also studied the effects of the process parameters on the type and magnitude of the formed residual stresses. The results showed that the compressive residual stresses were found at the central parts of the part and high tensile stresses were reported at the outer and near the surface of the parts.

An et al. [33] used the neutron diffraction method to study the formation of the hoop stresses and biaxial stresses in the curved thin-walled shape fabricated by LPBF from IN625. The residual stresses were also modeled with FE analysis and the results were in good agreement. High hoop stresses were reported in the area close to the base plate and also at the top layer. Cao et al. [34] measured the longitudinal residual stresses of a titanium alloy, Ti-6Al-3V, by using the neutron diffraction that was manufactured with Electron Beam additive manufacturing. Furthermore, the hole-drilling method was also implemented to measure the residual stress and it was shown that the hole-drilling method was capable of catching the longitudinal residual stresses accurately. Simon et al. [35] investigated the residual stresses using the XRD method for 316L stainless steel fabricated by selective laser melting (SLM). Residual stresses were found on the surface of the specimens. Electropolishing was used to remove a thin layer of material so that the XRD method could evaluate the residual stresses in depth. The highest residual stresses were found on the top layer and in the longitudinal direction. Also, large compressive residual stresses were observed in the stacking direction at the mid-part of the specimen up to several layers from the base plate. Ahmed et al. [36] investigated the residual stress distribution of the parts fabricated with SLM method with two materials, Ti-6Al-4V and Inconel 718, using the contour method. High residual stresses were found at the corners and the final layer of the produced parts in the longitudinal direction and compressive residual stresses at the central parts of the specimens for both of the materials. Knowless et al. [37] analyzed the residual stresses on Ti-6Al-4V fabricated with SLM method using the incremental hole drilling technique to measure the residual stresses on the surface and also inside the inner layers. Similar to [36], the highest residual stresses were found on the surface of the last deposited layer and also compressive residual stresses were observed inside the medium and at the central parts of the workpiece. The tensile residual stresses were found to be even higher than the yield strength of the material.

1.3.3. Finite element analysis

Finite element analysis is a well-known numerical method for solving a differential equation of a system and obtaining answers and solutions based on the certain boundary conditions. The DMD processes are associated with the thermomechanical effects of the material during the deposition process. So, in order to obtain the thermal and mechanical responses, the thermal equilibrium and mechanical equilibrium differential equations are needed to be solved simultaneously considering the specific boundary conditions using the FE analysis [38-47].

The FE simulation of the DMD process is quite similar to the simulation of the welding process which has been performed by numerous researchers to obtain the residual stress distribution and also the distortions after the welding. The main difference between the welding process and DMD processes is related to the effect of the element addition in the simulation of AM process which is not considered in the simulation of the welding processes. Commonly, the simulation is performed in commercial FE packages such as ABAQUS, ANSYS, LS-DYNA, …, and all of these packages need to be adopted with a certain technique or add-ins to apply the element addition. A brief introduction to the techniques that used FE analysis and enhanced the performance of the method are discussed in the following [3, 13, 21, 40, 41, 48-50].

- Adaptive mesh technique

The FE analysis is referred to the process of discretizing a continuous medium and applying the equilibrium state for each of the elements and finally, calculating the responses. Therefore, the outcome of the FE method depends on the number of discrete elements. Normally, the higher the number of elements, the more accurate and closer responses to the actual or theoretical response. However, the computational efficiency is dropped if the number of elements exceed certain amount without any improvement in the accuracy of the responses. The computational time of an FE analysis is governed by the number of degrees of freedom (DOF) of the system and a higher number of elements implies higher degrees of freedom and solving more equilibrium equations to obtain the final solution [51-54].

As it was mentioned before, the DMD process of metal alloys are associated with very high and steep thermal gradients near the heat source that may cause excessive and non-realistic distortions of the elements in the FE analysis when the element sizes are too large (coarse mesh) and it could terminate the FE solution. Therefore, the area and the region that undergoes the high thermal gradients are meshed with small-size elements and regions far from the heat source that are not experiencing high thermal gradients can be meshed with a coarser mesh size. This technique is called the adaptive mesh technique for the simulation of the DMD process. Applying this technique to commercial FE packages is a bit challenging and needs certain arrangements which will be discussed in section 5.1. By employing this method properly, the computational time of simulating the DMD process can be reduced significantly specially when a very large and complex component is being studied [30, 38, 48, 55-65].

- Inherent strain method

This method was originally developed for estimating the distortions of welded joints by Udea [66]. The main idea of this method relies on the fact that the inconsistent and inhomogeneous plastic strain that is applied in the body is responsible for the lateral distortions and residual stresses in the weld joints. As every point in the vicinity of the weld line experiences approximately the same thermal condition, therefore, the plastic strain around the weld line is almost the same for all sections perpendicular to the welding direction. In order to employ the inherent strain method in modeling of DMD process, thermomechanical FE analysis should be performed first so that the inherent strains are measured. As the inherent strain components are obtained, they are applied as orthotropic thermal expansion coefficients in commercial FE packages. Afterward, the temperature of the model is enhanced by unity so that the inherent strains are applied on the component [22].

- Discrete element method

In this numerical model, the interaction and contact of particles with other particles and the boundaries simulates the behavior of the material under loading condition. This method is commonly used for micro-scale simulations where the melt-pool and solid/liquid interaction are important. The bond forces between the particles determine the index of severity of the material to the changes and then, the stresses can be calculated. This method was also used for the macro-scale modeling of the DMD processes and especially the powder-bed fusion that the particles are considered as spheres. Certain criteria need to be defined to break the inter-particle bonds during the melting and also to form new inter-particle bonds during the solidification. Furthermore, the boundary condition contact rules are to be established so that the model could be capable of incoming external heat load and also the mechanical constraints. Some of the recent adoptions of this method will be discussed in the literature review but the details and the theory behind it are out of the scope of this study [9, 11, 15, 16, 19-21].

1.4. Objectives and novelty of this work

As previously discussed, one of the main drawbacks of FE-based models to predict residual stress distribution of DMD parts is related to the high computational efforts of the FE analysis. The preceding demonstrates proposed approaches and techniques considered in the present dissertation for improving the computational efficiency of residual stress prediction in DMD parts. A novel modeling approach of integrating the machine learning (ML) concept and FE-based model is proposed to develop a computationally efficient and accurate prediction tool for stress and distortion assessment of DMD parts. A comprehensive review of the recent findings in the field of developing new methods and techniques for the prediction of stress distribution in the DMD parts are presented in Chapter 2. Moreover, state of the art for utilizing ML in the field of solid mechanics and other related fields such as medicine and biomechanics are also provided.

After improving the basic knowledge of DMD processes and learning the approach to simulate them in ABAQUS, several techniques were used to enhance the efficiency of the simulation process. Therefore, the present study was conducted based on the following steps:

1.4.1. Developing a comprehensive finite element-based model

In order to have a better understanding of simulating the DMD process, the first step was to go through the literature and perform a simple DMD-based FE simulation using the commercial FE packages. To perform a reliable and practical FE analysis, one should have a solid understanding of the process in detail and detect any errors and failures in the FE analysis. Furthermore, selecting the FE package to continue working with is quite important. A detailed and clear path of the simulation process should be laid out to approach the commercial FE packages. For this study, ABAQUS was used for its well-known capabilities for developing customized subroutines that provide a lot of freedom for controlling different parameters in the process. Several basic and simple models were made and analyzed and a feasible algorithm was developed for performing FE analysis for a given geometry. The detailed FE solution of the DMD process is discussed in Chapter 3.

1.4.2. Developing an adaptive-mesh-based finite element model

As mentioned before, one of the factors that govern the computational time of the FE analysis is regarded as the total number of degrees of freedom (DOF) of a system. Therefore, reducing the

DOF is beneficial in terms of less computational time. This technique was utilized in the present thesis and applied to simple structures to evaluate its feasibility and efficiency of a given simple structure. The methodology and the algorithm of applying the adaptive-mesh technique are presented in section 5.1.

1.4.3. Integrating machine learning with finite element analysis

A novel approach of integrating machine learning (ML) and FE analysis is proposed in the present study to take advantage of ML to improve the computational time of performing FE analysis of DMD parts. The primary goal is to develop a reliable and pertinent algorithm to integrate the power of ML and FE simultaneously and to obtain the residual stress distributions of DMD fabricated parts. ML has been used in solid mechanics but it was never applied to the evaluation of stress distribution in the DMD fabricated parts. In the present study, artificial neural networks (ANNs) as one of the powerful and well-known ML methods are used. Therefore, the basics and operating mechanism of an ML method and specifically ANNs, are outlined first to make the reader more accustomed to the terminologies and parameters of ANNs. The integration of the FE and ANNs is also presented in detail in Chapter 5.3.

Chapter 2:

Literature review

Finding the response of a system under given circumstance has always been desirable before performing real time and practical experiments and tests [67-71]. Solid mechanics deal with a vast number of fields the reaction and response of the mechanical system for a given condition is favorable and may have a significant impact on the decisions to be made based on the response. In particular, prediction or estimation of the residual stresses in thermomechanical processes is of greatest interest to academia and industry. Thermomechanical processes are commonly referred to as the production processes that the material undergoes thermal strains generated from the expansion/contraction of the material [72-74]. Many of the production methods of metal alloys normally involve the utilization of a heat source during the fabrication process such as welding or the heat is generated as a result of plastic deformations during the forming processes. The area that is affected by the heat is usually called the heat affected zone (HAZ) which is inevitable in the thermomechanical processes. HAZ is the area that should be analyzed and studied discreetly in the thermomechanical processes as it affects the whole properties of the product in terms of thermal and mechanical properties and also alters the geometrical tolerances [75-79].

As mentioned in the introduction, the DMD process is involved with the application of a laser beam as the heat source that melts the powder/wire. The cyclic nature of the melting and solidification during the deposition of material in DMD process categorizes it as a complicated thermomechanical phenomenon. However, the very basic and fundamental theories of heat transfer and equilibrium conditions are applied to the simulation of DMD process analogous to welding [53, 63, 80]. There are numerous research and scientific papers that use various models and techniques to simulate the welding process [81-97]. The major difference between the common modeling approach for DMD processes, which distinguishes the whole simulation, is regarded as the incremental addition of the material. Therefore, the state-of-the-art of mechanisms and approaches that were used for investigating/improving the DMD process of metal alloys are mainly introduced and discussed in the present study.

2.1. Basic applications of numerical-based methods in the simulation of the direct metal deposition process

Many researchers have conducted FE-based simulations considering the DMD process as the sequential process of applying the heat source, obtaining the temperature history of the elements, and finally, applying the thermal history of the elements on the structural analysis to evaluate the mechanical response of the part [62, 98-103]. This approach is called the weakly-coupled thermomechanical approach in which the mechanical response has no impact on the material properties or on the thermal gradients. In this approach, the melt pool and the solid/fluid interactions are not considered and the specimen remains solid in the FE analysis space. The material properties are adjusted to account for the changes in the elevated temperatures of the process. The uncoupled solid-state modeling of DMD processes is time-efficient and relatively easy to apply in commercial FE packages. Matsumoto et al. [104] proposed a FE-based computational model to assess the temperature and the residual stresses of a single-layer deposition of powder onto a substrate using LPBF process. The authors employed the FE to solve the two-dimensional heat conduction analysis and find the temperature distributions of the elements. Therefore, the authors utilized the FE method to solve the force equilibrium equations for the 2D problem and imported the temperature history at each increment to obtain the strains and displacements as well as the residual stresses of a single layer deposit. The temperature history of the elements was mutated to account for the phase change effects happening in the transition temperatures of the material. The authors reported that the deflection of the deposited solid layer was increased as the length of the deposition increased. Furthermore, the authors reported that the solidifying material induces residual tensile stresses between the tracks right after passing the laser. This was also mentioned later in the study by Mukherjee [24]. Nickel et al. [105] used a sequential deposition model similar to [104] and examined the effects of the deposition patterns on the final stresses and distortions of 1117 steel. The results were verified with the experimental tests and they were in good agreement. Klingbeil et al. [106] developed an FE-based analysis with 1-D and 2-D plane strain models of depositing 1018 Carbon Steel via DED process. The authors studied the residual stress effect on the warping of the plates and also investigated the effect of process parameters on the deflection of the material. The results were examined and verified with the experiments. Kruth et al. [107] investigated the formation of the residual stresses in the multilayer selective laser melting (SLM) process and identified the differences between the laser melting and laser sintering process of metal alloys powders. Chine et al. [108] developed thermomechanical models in 1D and 2D to investigate the temporal evolutions and stresses at the solid free form (SFF) process of 304 stainless steel. The authors studied the effects of part constraints and also localized preheating of the deposition area to minimize the residual stress magnitudes. Roberts [109] developed a fully integrated finite element model in ANSYS for evaluating the thermal history and the residual stresses of Ti-6Al-4V in the laser melting process. The experimental tests were also performed to act as the measure for the accuracy of the predicted results using FE analysis. The author reported that the material strain hardening model played a major role in the predicted results for displacements of the fabricated part. Roberts also investigated the effects of the process parameters on the magnitude of the formed residual stresses. The author concluded that the residual stress magnitude increased when the number of laser passes was increased. The author also emphasized on the effect of the deposition length; the residual stress was decreased significantly by 51 MPa when the deposition length was reduced, as was mentioned in [104]. The author also reported that the transverse speed of the laser beam has contradictory effects on the residual stress; the longitudinal and the transverse stresses were increased and decreased, respectively, by decreasing the laser's transverse speed. Arni and Gupta [110] studied the effect of the build direction on the geometrical distortions of metallic parts in the solid freeform fabrication process and presented an approach for the designers to help them select the optimum build direction to minimize the part distortions. Zaeh et al. [111] investigated the effect of the modeling approach on the evaluation of the residual stresses on 1.2709 steel material. The authors presented two modeling approaches, a detailed layer-based model and global-based model of the complete part. The analyses were performed based on the fully coupled approach that considered the thermomechanical features have an impact on one another. In the detailed layer-based model, the effect of the thermal source, scanning speed, and also the trajectory of the laser beam was investigated. However, in the second approach, a uniform heat source was applied to the whole layer at once to demonstrate the layer-by-layer deposition of the whole part. The results were compared with the experimental results. The global model predicted the stresses in the longitudinal (top layer) and stacking (bottom) directions to be 86 MPa and 628 MPa, respectively. However, the results from the neutron diffraction method were reported as 305 MPa and 184 MPa in the longitudinal (top layer) and stacking (bottom) directions, respectively. The most probable reason for the considerable error in the prediction of the residual stresses using the global-based model reflects the inadequate assumptions and simplifications of the model which causes significant errors in the predictions. A similar study was conducted by Krol et al. [54] that applied a uniform heat source on the entire layer at once and completed the whole geometry in a layer-by-layer manner. The experimental tests were also performed to verify the predicted results. The predicted results were reported to be far from the experiments showing that too much simplification may have a negative impact on the results. Gu and He [65] implemented the fully thermomechanical approach to model the SLM process of titanium and nickel powders by applying a Gaussian thermal source distribution. The residual stresses of 86 MP and 23.2 MPa were evaluated in the longitudinal and stacking directions, respectively. The experimental studies also confirmed that the insufficient data in the modeling approach of layer-wise deposition lack the opportunity of studying the effects of the process parameters on the formation and magnitude of the residual stresses as reported in [54]. Lundback et al. [112] reported that the results from the FE analysis is an overestimation of the experimental results in the laser metal deposition process of Ti6Al4V.

2.2. Application of various thermal heat source models in the finite element analysis of direct metal deposition process

Some other researchers studied the effects of the thermal heat source model on the heat transfer phenomena and the final distortions and residual stress formations. Denlinger et al. [113] proposed the double ellipsoid Goldak's heat source model and implemented it in ABAQUS and performed the weakly-coupled thermomechanical analysis to assess the residual stresses and distortions of the Ti6Al4V. The distortions were measured experimentally to compare with the predicted distortions from FE analysis and maximum error of 29% was reported for the FE results. However, the estimated profile and pattern of the predicted distortions were in good agreement with the experimental measurements. Denlinger et al. [114] presented a FE modeling approach for the electron beam additive manufacturing of Ti6Al4V sing Goldak's double ellipsoid heat source model. The relaxation of stresses is proposed in this work to mitigate the high distortion magnitudes reported in the normal FE analysis of the process. The stresses are set to zero when the temperature reaches to a certain point based on the methodology presented. Various relaxation temperatures were analyzed and the temperature of 690°C was found to be the optimum values for Ti6Al4V. Ding et al. [30] performed the coupled FE analysis of WAAM process of mild steel alloy and applied the double ellipsoid Goldak's model as the heat source model into the calculations. The transient and steady state thermal analysis were conducted and their results were employed in the mechanical model to assess the residual stresses. The predicted results from both analyses agreed well with the experimental measurements and the steady stated model represented 80% improvement in the computational time. Parry et al. [115] investigated the scan trajectory effects of the laser beam in SLM of Ti6Al4V on the residual stresses by employing the double ellipsoid Goldak's model and performing the coupled thermomechanical analysis. Time-independent plasticity model with the yield function of Von Mises stress were utilized to account for the cyclic non-linear work hardening. Li et al. [114] developed a multi-scale thermomechanical model for assessing the residual stresses and distortions of AlSi10Mg powder in the SLM process. The micro model was used to generate the temperature history of a single deposition considering the Gaussian distribution heat source model. The temperature history was applied on the meso-model to simulate the deposition of a single layer. Afterwards, the results of the meso-model were applied on the entire body part to determine the residual stresses in the macro-model. Several studies [116, 117] considered simpler models based on Rosenthal [47] melting pool estimation.

2.3. Multi-scale and multi-physics modeling of the direct metal deposition process

Some other research studies focused on a more detailed and complex analysis of the depositing process that involves studying phase changes happening in the melt pool, fluid-solid interactions (FSI) of molten material and solidified deposit, and molten material surface tension forces. This approach is based on solving the Navier-Stokes equations and it is considered as the computational fluid dynamics (CFD) solution to the problem. During the solution, all the factors related to the gravitational body forces, surface tension, and hydrodynamic pressure are considered in the momentum equations and solved alongside with the energy equations accounting for heat transfer (conduction, convection, latent heat, phase changes) phenomena, simultaneously. Megahed et el. [118] implemented CFD analysis and studied the modeling of PBF process to predict the overall characteristics of the fabricated parts such as the geometrical distortions and residual stresses. The authors investigated the effect of the thermal cycles in the melt pool in the formation of porous and defects inside the medium for several metal alloys including SS316L, IN718, and Ti-6Al-4V. The authors concluded that the thermal effects inside the melt pool and the FSI play a major role in the quality of the products fabricated with the PBF process. Srivastava et al. [119] studied the multi-physics continuum modeling of the wire-arc additive manufacturing (WAAM) process and analyzed the effects of heat source models, material models, meshing strategy and boundary conditions on the residual stress and distortion of parts produced with WAAM. The authors reported the high computational time of the FE-based modeling of the WAAM process. Denlinger et al. [61] showed that without considering the solid-state phase transformations of Ti6Al4V, the predicted results from the FE analysis have more than 500% error. However, for the Inconel 625, ignoring the solid-state phase transformation has little effect on the predicted results from FE analysis. This effect was studied by Chen et al. [60] and they also confirmed that for Ti6Al4V, the solid-state phase transformation which partially relieves the induced residual stresses should be considered while simulating the SLM process. They compared the results of the FE analysis with the experimental measurements and reported an error of about 80% in the results of the FE analysis when the solid-state was ignored.

2.4. Improving the computational efficiency of the thermomechanical process modeling

As it was mentioned, the main shortcoming of the numerical-based approaches is associated with the high computational time of the simulation process. Therefore, there are numerous researchers that attempted to solve the issue by developing certain techniques and methods to improve the computational time of the simulations. Some of the techniques introduced here benefit from the innovative application of the FE method and generating user-defined codes to reduce the computational time.

2.4.1. Adaptive mesh technique

As mentioned in section 1.3.3, the adaptive mesh technique was developed based on the fact that the area far from the HAZ experiences lower thermal gradients. Therefore, the size of the elements far from the heat source can be increased or the elements can be coarsened. Hence, the elements of the FE model are decreased. Consequently, the model has a fewer number of degrees of freedom that lead to smaller size of the stiffness and mass matrices and the total number of the equations needed to be solved to determine the thermal and structural response is declined. Baiges et al. [44] implemented an adaptive mesh-based FE analysis to simulate the SLM process. The authors introduced more fined mesh size on the thermo-mechanical affected zone (TMAZ) and kept the area far from the heat source. The applied method of layer-by-layer coarsening is called octree method that was also implemented in [42, 43, 120, 121]. However, two correctional factors were imposed to keeping the results of the adaptive mesh-based approach as accurate as the original FE analysis with very fine mesh. Denlinger et al. [113] utilized a coarsening scheme to improve the computational time. The top two layers are discretized with fine meshes and the other layers are coarsened to lower the computational time. Olleak and Xi [41] used the adaptive mesh-based FE model for simulation of laser powder bed fusion process. The authors implemented the coarsening of the elements for the inactive layers as well as for the lower layers far from the heat source and HAZ. Kollmannsberger et al. [122] have implemented a dynamic mesh-changing algorithm that alters the state variables in the analysis so that the number of nodes in the FE model remains approximately the same and leads to improvement in the computational time of the analysis. Gouge et al. [123] conducted the validation of the results obtained from an adaptive mesh-based FE model of LPBF by comparing them with the results of the experimental data. The authors reported that the inaccuracies in the FE results are issued from the mesh coarsening and refinement processes. Hajializadeh and Ince [124] proposed an adaptive mesh-based technique to enhance the computational efficiency of simulating the DMD process of AISI 304L. Similar to octree adaptive scheme implemented in [44], the top 2-3 layers meshed with fine mesh and the layers below the tip layers start coarsening in 4-5 steps to achieve the coarse mesh at the bottom layer. In the other study, Francois et al. [125] proposed an equivalent model by lumping the laser effect on the powders' interactions in the thermal analysis of the LPBF process and used the adaptive mesh scheme to lower the computational time. Zeng et al. [40] applied the dynamic adaptive mesh technique to reduce the total number of degrees of freedom for the FE analysis. A coarse mesh is used to discretize the whole geometry, then, it is refined as the heat source was applied on a point of interest. Similar to work done in [24, 43], an adaptive mesh is utilized in the modeling of WAAM of H13 steel to ensure that the HAZ is meshed with refined mesh and the thermal gradients are accurately simulated [126]. Similar approach was taken in [49] to save computational time for the thermomechanical analysis of laser-aided additive manufacturing.

2.4.2. Inherent strain method

As it was mentioned in section 1.3.3, the inherent strain method can be used to calculate the final distortion of the workpiece fabricated by welding processes and by adjusting the method of calculating the inherent strains, the method can be applied in the prediction of the stresses and distortions of DMD fabricated parts. It is highly demanding to simulate more complex and large structures using FE analysis because of the lack of substantially powerful computers. The inherent stain proposed by Udea [66] was originally developed for fast prediction of distortions of welded structures. Setien et al. [39] applied the inherent strain method on the twin-cantilever beam manufactured by LPBF method and assessed the distortions of the beam after removing supports. Cheng et al. [58] conducted FE analyses based on the inherent strain technique to determine the residual stresses and strains for preventing the failure of the DMD built components. The inherent strain method is based only on the incompatible plastic strains that are normally obtained from the last increment of the analysis. However, the additive manufacturing processes of metal alloys such as DMD include many deposition cycles and the inherent strains calculated after the completion of the last layer are not accurate measurements of the true or actual inherent strains in DMD processes. This is the main shortcoming of the inherent strain that requires certain adjustments and modifications to be made to calibrate the inherent strains accordingly [127]. Liang et al. [128] modified the calculation of inherent strains of components made with LPBF and estimated the residual stresses and distortion of the cantilever beams with the experimental data. The authors extracted the inherent strains from a small-scale model at the end of each layer deposition (intermediate state) and applied them to the macro model to assess the residual stresses and distortions. The results showed good matching with the experimental data and approved the inherent extraction method implemented in this study. Bugatti and Semeraro [129] attempted to utilize the concept of the inherent strain on the LPBF process of 18Ni300 and compare the results of the inherent strain method with the experimental data. The authors concluded that the difference between the FE and experimental results initiated from the macro-scale effects of the geometry and the inherent strains obtained from the micro model are not suitable in order to be applied in the quasi-static analysis to calculate the distortions and residual stresses of the macro models. Wang et al. [38] developed a modified inherent strain approach to measuring the residual stresses and distortions in the metal additive manufacturing process. Analogous to [128], the inherent strains were extracted at the end of each layer's completion and then applied in the quasi-static analysis. The results were compared with the experimental results and they were found to be in good agreement. Zhang et al. [57] developed an inherent strain-based FE framework for parallel computing of topology optimization for support structures in the LPBF. The authors reported about 6% error in evaluating distortions from the inherent strain-based FE model. Chen et al. [56] developed a method for the multi-scale modeling process of direct metal laser sintering of In718 and proposed a modified technique for extraction for the inherent strains of the micro-scale model. Then, the incompatible inherent strains were applied to the macro-scale model to assess the distortions of the real-scale part. In another study by Liang et al. [130], the effect of the different scanning strategies of the laser beam in the LPBF of In 718 was incorporated into the inherent strain method. The distortion of parts obtained from the experimental tests was validated with the result of the modified novel inherent strain method.

2.4.3. Surrogate modeling

The simulation and analysis of a complex problem such as multi-scale problems require considerable computations and vast knowledge to perform the assessment to achieve the solution. FE-based models that can be used to simulate complex and intricate physical phenomena are expensive in terms of computational time. Furthermore, performing the FE-based calculations requires a solid knowledge of the problem itself and the skills to conduct the FE analysis using commercial FE packages. However, surrogate modeling approaches were developed to skip those complexities and reach the final solution in the shortest time without significant effort to provide the initial data [131-136].

A problem can have several features including the level of non-linearity, required accuracy, the data size of the problem, information to be prepared for the computations, speed of the computations, and the availability of the software or the tool to gather the information [137]. The first step in every surrogate modeling approach is to establish a method to identify important features of a problem and generate the samples or data points. The sampling is often referred to as the design of the experiment as well [138]. If the sampling is conducted via FE simulations of complex multi-physics phenomena, it might be the main fraction of the computational cost.

The type of surrogate modeling approach is selected based on the given problem and its characteristics. Some of the most well-known surrogate models are presented in the following:

- Linear regression and response surfaces

The original and most used surrogate model is the classic polynomial response surface model [139]. In the response surrogate model, the surrogate is established as a linear combination of polynomial functions of the input variables [140]. By substituting the obtained samples (inputs and corresponding outputs) and solving the surrogate equation using the least square method, the unknown coefficients are obtained and the response surface method is ready to be used for the prediction. Polynomial surrogates are not suitable for a problem with a high level of complexity, non-linearities, and multi-dimensional landscapes [141]. Similar to the response surface model, the Kriging model is based on a Gaussian regression that correlates the existing inputs to their associated outputs [142-147].

- Radial basis function

Radial basis functions are broadly considered to be an interpolation technique that generates the weights associated with each input of the dataset and it approximates the corresponding output [136] by employing a certain radial function such as exponential, gaussian, spherical, or spline. Once the inputs and outputs of a problem are substituted in the function, the unknown weights are found by solving the equation using the least square method. The radial basis functions are accurate at the sampling points unlike the regression type of surrogate models such as response surface models. [148-153]. The advanced version of the radial basis functions is now available through its application in conjunction with artificial neural networks.

- Artificial neural networks

The artificial neural networks are operated in a similar format to neurons in the brain [154-159]. Similar to radial basis functions, each input of the data is associated with an arbitrary weight which is multiplied by it and generates the net input of that neuron. Unlike the radial basis functions, the neurons are assigned an activation function that decides to activate or silence the neuron. The output is predicted based on the given inputs and it is compared with the actual output of the system. Afterward, the weights are determined by minimizing the prediction error so that the network can predict reliable results [154, 160-171]. The artificial neural networks are explained in detail in the following section and a comprehensive review is given.

2.5. Application of machine learning algorithms in structural mechanics and direct metal deposition process

During recent years, some researchers and industrial parties have started using the concept of ML in the field of solid mechanics and more specifically, additive manufacturing processes. Koeppe et al. [172] implemented ANNs to develop a framework based on the data obtained from the FE and experiment to evaluate stresses in parts fabricated by polylactic acid. The training and also testing datasets were generated based on the linear elastic-plastic FE models of 85 different configurations. The input data of the network included the loading conditions and the output was stress magnitudes. The predictions made by the ANNs were consistent with the FE results and also the computational time of the prediction reduced significantly. Liang et al. [173] attempted to determine the wall stress distribution of the human Aorta for different patients with different health conditions by integrating computational fluid dynamics (CFD) and ML algorithms. Principal component analysis (PCA) method was implemented as the method for generating the geometry and extracting the shape and characteristics of Aorta of about 730 patients. Then, they ran the CFD analysis to evaluate the stress distribution of the Aorta wall. The training and testing dataset were extracted from the analysis and used for constructing the comprehensive dataset. The authors reported significant improvement in the computational time of determining the wall stress of the human Aorta and the prediction error was estimated to be about 0.49%. Gulikers [46] proposed an approach of integrating FE analysis with ANNs to present a feasible reliable solution for the homogenization of complex and inhomogeneous substructures; i.e. airplane fuselage. For generating the comprehensive dataset for training and testing the neural networks, a sub-modeling approach of FE analysis has been employed and various loading conditions and increments were considered. The feed-forward neural networks were used and trained with the generated dataset. Then, the trained network was utilized in the UMAT subroutine of ABAQUS to replace the elasticity equations for determining strain/stress and substitute the inhomogeneous substructure with an equivalent homogenized element. The authors reported that the computational time of the FE analysis of the fuselage structure was drastically improved by applying the proposed method. Mortazavi and Ince [174] developed an ANN-based framework to predict the crack propagation behavior in long and short cracks. The fatigue crack growth rates were obtained from FE analysis and generated the training and testing dataset for the ANN. The trained network was used for the prediction of the crack growth rates of different alloys such as Ti-6Al-4 V, 2024-T3, and 7075-T6. The authors reported that the proposed model was capable of evaluating of the crack growth rates of long and short cracks. Zhang et al. [175] implemented a neural network based framework to predict the fatigue life of St 316L fabricated by LPBF. The dataset was generated based on the two data sources; by varying the process parameters and testing the fatigue life of the fabricated parts and also from other research papers. The authors reported that the insufficient data for generating a comprehensive data set and variations in the reported data by other researchers made the prediction of some cases not as accurate as it was supposed to be. Singh et al. [176] studied the porosity of the SLM fabricated parts by developing a multi-layer perceptron model. The dataset was generated by varying the process parameters such as laser power, scan speed, and hatch distance and recording the porosity features as the training data. Then, the trained network was utilized to investigate the porosity features of the parts. There are several studies that utilized the concept of ML to create a reliable ML-oriented framework to improve the computational time of analyzing the effect of process parameters on the quality and performance of the DMD fabricated parts [12, 13, 48, 177-186].

Caiazzo and Caggiano [12] implemented the multi-layer perceptron-based model to analyze the geometry and characteristics of the melt pool in LPBF of 2024 Al alloys. The effect of the process parameters on the formation of the melt pool, its shape, and temperature gradients were investigated through the concept of ML. Similar study was conducted by Li et al. [13] to investigate the effects of the process parameters on the shape and characteristics of the melt pool in wire arc additive manufacturing using neural networks.

Artificial neural networks were also used to compensate for the geometrical errors during the production process. Chowdhury and Anand [187] implemented a feed-forward ANN-based model and developed a new framework to compensate for the geometrical distortions of DMD parts during the production steps. The training and testing dataset were generated by varying the process parameters and measuring the distortion/deviations from the originally designed dimensions of the parts under the given conditions. The trained network is then used to predict the distortions and compensate for it in the original CAD file in order to achieve the desired dimensions.

Li et al. [188] implemented the ANNs to present a framework to assess the surface roughness of the DMD parts under experimental conditions and different setups for process parameters. The dataset was generated based on the temperature and vibration of certain points of the part during deposition. Then, the trained network was used to determine the surface roughness and reach a better setup for the process parameters and experiment conditions.

Some researchers utilized ML to facilitate topology optimization under certain constraints. Sosnovik and Oseledets [189] implemented convolutional neural networks or CNN (the type of the neural network that uses images instead of numbers and it is very powerful in the field of image segmentation and clustering) as an intermediate level of the topology optimization process. The authors reported that the computational time to achieve an optimized topology scheme is significantly lowered (approximately 20 times faster).

Some researchers have implemented the ML algorithms such as ANNs to evaluate the behavior of the materials such as metamaterials. Determination of the properties of the metamaterials is a challenging and time-consuming task. Therefore, the machine learning approaches can be implemented to evaluate the properties of these materials in a time-efficient way. Pilania et al. [190] implemented machine learning to predict the chemical behavior of the metamaterials in an efficient way. Liu et al. [55] introduced a systematic framework of microstructure optimization using the concept of machine learning to design a material structure to meet certain mechanical properties of Fe-Ga alloys. Gu et al. [191] implemented the machine learning concept to design a composite with specific properties in different directions. The authors reported significant improvement in the computational time to find the optimum characteristics of the composite to yield certain desired properties while using the ML.

2.6. Summary and conclusion

A considerable number of studies have focused on investigating the residual stress formations and how to develop a robust and accurate model using FE analysis to evaluate the residual stress in DMD processes. Adaptive-mesh-based techniques rely on the fact that by coarsening of the mesh of the part during the FE analysis, total degrees of freedom are reduced. Therefore, the simulation time is reduced accordingly. The procedure to perform the adaptive-mesh-based techniques is often performed in a sequential order; results are mapped to the coarsened mesh for the subsequent layer deposition. Therefore, it is not feasible to perform the adaptive-mesh technique on very large or complex geometries. Hence, this method can only be applied to simple and small structures. The techniques developed based on the concept of inherent strain are also limited to accurate extraction of the inelastic strains. Several studies represented innovative procedures for the evaluation of the inelastic strain. However, there is no comprehensive and general approach for measuring inelastic strains. Furthermore, the application of the inherent strain on a given model and establishing a procedure to obtain the inelastic strains are not unique and it is changed from geometry to geometry.

Therefore, it is favorable to develop a general framework that can be applied to any geometry and also on large-scale components and can improve the computational time of predicting the residual stresses without jeopardizing the accuracy of the results significantly. The integrated ANN-FE framework was introduced to address these shortcomings of other techniques and to present a more general concept of applying ML algorithms to solid mechanics and especially in the field of DMD simulations.

Chapter 3:

Finite element analysis of the direct metal deposition process

The main objective of the present study is to propose a novel and innovative approach to enhance the computational efficiency of simulating the additive manufacturing process of metal alloys such as the direct metal deposition process. The literature review showed that the experimental techniques and methods to assess the magnitude and type of the residual stresses are time-consuming and costly and also may damage the produced part. Therefore, numerical-based methods such as finite element analysis seems to have the potential to be used instead. In this chapter, the finite element analysis of a thermomechanical process such as DMD is presented alongside certain techniques that need to be adopted to account for the addition of the material. The modeling is conducted in ABAQUS commercial software which has been extensively used in the literature for different thermomechanical simulations. ABAQUS provides a huge benefit of accessible libraries for writing used-defined subroutines for material properties, elements, boundary conditions, loading, etc. …, that are coupled with the main analysis. Implementing the user-defined subroutines makes it possible to impose any arbitrary condition in the FE model. However, the implementation of the user-defined subroutines in the thermomechanical analysis is quite demanding and requires comprehensive knowledge in the field such as elasticity and plasticity and how to impose new requirements and solutions into the analysis.

The thermomechanical analysis of AM processes, as the expression implies, consists of thermal and mechanical analyses. The thermal analysis deals with determination of the nodal temperature history during the deposition and cool-down steps. On the other hand, the mechanical analysis assesses the distortions and residual stress distribution of the part under thermal and mechanical boundary conditions. Naturally, the thermal and mechanical analyses are dependent on one another, which means that for any incoming thermal load, thermal strains will be imposed on the part that will result in the formation of residual stresses and distortions. The resultant distortions and residual stresses may have an impact on the geometry of the part which makes it distorted from the initial geometry and could cause some alterations in the thermal and mechanical boundary conditions. Therefore, for every single time increment in the thermal analysis that gives the nodal temperature distribution of that specific increment, the mechanical analysis is performed and the residual stresses and distortions are determined. Afterward, the geometry of the specimen is updated based on the resultant strains. Thereafter, the next thermal analysis increment is performed and mechanical analysis is conducted based on the nodal temperature distribution obtained in the second increment. These cycles of analysis are performed up to the end of the analysis. This solution is often called fully-coupled thermomechanical analysis. The results of the fully-coupled analysis are quite accurate and reliable. However, it is very time consuming and requires very high computational power [192-195]. Alternatively, there is another approach developed and used extensively in the literature to assess the residual stress and distortions of thermomechanical processes called weakly-coupled thermomechanical analysis. During this approach, the thermal analysis is performed prior to the mechanical analysis to get the thermal history of the elements and nodes. Afterward, the thermal history of the elements and nodes is applied in the mechanical analysis to get the mechanical response of the part under the applied loads; which are residual stresses and distortions. As it sounds, the thermal analysis is independent of the mechanical response of the material and the resultant alterations in the geometry and boundary conditions have no impact on the thermal analysis [30, 59, 196, 197]. Hence, the weakly-coupled thermomechanical analysis is faster than the fully-coupled and it requires lower computational power. Moreover, the accuracy of the results from the weakly-coupled FE analysis agrees well with the results of the fully-coupled FE analysis [52]. However, the agility of the process is beneficial in the FE analysis of complex shapes and geometries. Figure 4 demonstrates the steps and procedures implemented in the present study to simulate the DMD process in ABAQUS/STANDARD. Initially, the heat transfer FE model was developed using Python scripts and the process parameters alongside the material properties are passed to the model via corresponding subroutines. Afterward, the nonlinear transient analysis is performed to obtain the 3D temperature history of the elements. The structural FE model is developed using Python scripts and the material properties are passed to the model using corresponding subroutines. Finally, the temperature field is imposed on the structural FE model and the nonlinear elastoplastic analysis is performed to calculate the residual stresses distribution in the structure. In the following, the characteristics of the FE analysis are explained in detail.

3.1. Thermal analysis

The nodal temperature history of the built part needs to be computed in the thermomechanical FE analysis. Pure heat transfer analysis is performed for the given model geometry considering all the material parameters and thermal boundary conditions. It should be noted that the heat transfer analysis strongly depends on appropriate definition of material properties that should be considered temperature-dependent. Moreover, the applied boundary conditions have to be considered temperature-dependent as well to mimic the features of the metal alloys in the elevated temperatures; i.e. the convection factor (h) is dependent on the surface temperature. Considering all the parameters as temperature-dependent leads to severe complexity in the differential equation of the heat transfer analysis. The aforementioned relationship is obtained from the concept of energy conservation of the body and is expressed as [198-203]:

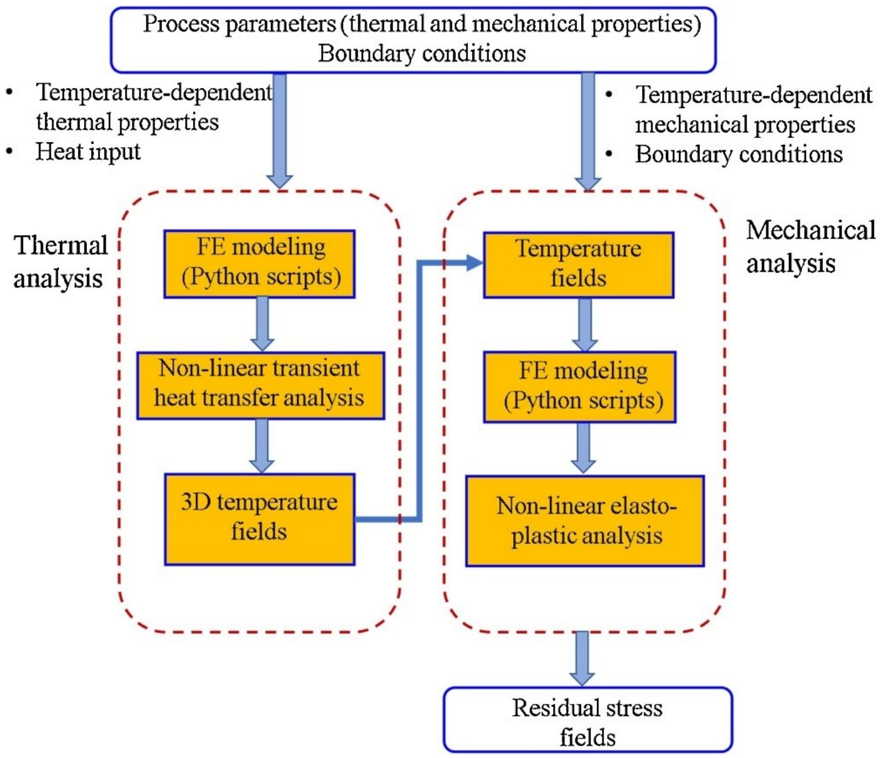

Figure 4 Schematic configuration of a thermomechanical analysis used in the present study for direct metal deposition process modeling

$$Q(\mathbf{X}, t) - \rho C_p(T)\frac{dT}{dt} + \nabla[k(T)\nabla T] = 0 \qquad (1)$$

in which $\mathbf{X}$ is spatial coordinates, t is time, Q is the body heat source, ρ is the material density, C_p is the specific heat of the material, k is conductivity and T is temperature. In order to present the solution for this equation using the FE method, an implicit formulation for temporal derivatives is utilized at any time (t^n) using backward finite difference as [198, 203]:

$$\frac{dT^n}{dt^n} = \frac{T^n - T^{n-1}}{t^n - t^{n-1}} \qquad (2)$$

As the $T^n$and $T^{n-1}$are the temperature values at times $t^n$and t^{n-1}, respectively. The backward difference algorithm is unconditionally stable over the time increment. However, small time steps are required to obtain accurate results [204].

Residual value (R) is obtained from Eq. (1) and its weak formulation is used with the Galerkin FE discretization method to calculate linear shape functions for elements and, finally, calculate the element residual as [198, 203, 204]:

$$R = \int_V \left[B^T k B T^n - N^T Q + N^T N \rho C_p \frac{T^n - T^{n-1}}{t^n - t^{n-1}}\right] dV + \int_A N^T q^p dA \qquad (3)$$

Then, the element stiffness matrix can be obtained as [198, 203, 204]:

$$\frac{dR}{dT^n} = \int_V \left[B^T kB + B^T \frac{\partial k}{\partial T} BTN - N^T \frac{\partial Q}{\partial T} N + N^T N\rho C_p \frac{1}{t^n - t^{n-1}}\right] dV + \tag{4}$$

$$\int_V \left[N^T N\rho \frac{\partial C_p}{\partial T} N \frac{T^n - T^{n-1}}{t^n - t^{n-1}}\right] dV + \int_A N^T \frac{\partial q^p}{\partial T} NdA$$

Where **N** is the linear shape function matrix, **B** is the derivative or kinematic matrix of **N**, V is the arbitrary element volume and A is the element surface area that the convection and radiation are applied. Q is the body heat source and it can be considered as the thermal source in 3D using Goldak's double ellipsoid model shown in Figure 5. q^p is the total temperature-dependent heat flux that flows out of surface A. Q and $q^p$are given in Eqs. (5-6) [51, 203, 205]:

Front-half ellipsoid:

$$Q(x, y, z) = \frac{6\sqrt{3} f_f \eta P}{a_f bc\pi\sqrt{\pi}} e^{-3\left(\frac{x^2}{a_f{}^2} + \frac{y^2}{b^2} + \frac{z^2}{c^2}\right)}$$

Rear-half ellipsoid:

$$Q(x, y, z) = \frac{6\sqrt{3} f_r \eta P}{a_r bc\pi\sqrt{\pi}} e^{-3\left(\frac{x^2}{a_r{}^2} + \frac{y^2}{b^2} + \frac{z^2}{c^2}\right)} \tag{5}$$

$$q^p = h(T - T_\infty) + \vartheta\Phi(T^4 - T_\infty^4) \tag{6}$$

In which, P is power, η is the beam (laser or electron beam) efficiency, $x, y,$ and z are the coordinates, $a, b,$ and c are the length of the ellipsoid in longitudinal, depth, and transverse directions, respectively, v is the transverse speed of the heat source and t is time. a_f and a_r are the semi-axes distances in the front and back of the moving laser beam in the double ellipsoid scheme. h is convection coefficient, T and T_∞ are the nodal (surface) and ambient temperatures, respectively, ϑ is emissivity and Φ is the Stefan-Boltzmann constant. The rear length of the laser beam is considered 4 times of the front length to improve the computational time of the heat transfer assessment. f_f and f_r are the fractions of the heat flux at the front and back of the laser beam, respectively, and can be expressed as following based on the continuity of the volumetric heat [205]:

$$f_r = \frac{2a_r}{a_r + a_f}$$

$$f_f = \frac{2a_f}{a_r + a_f}$$

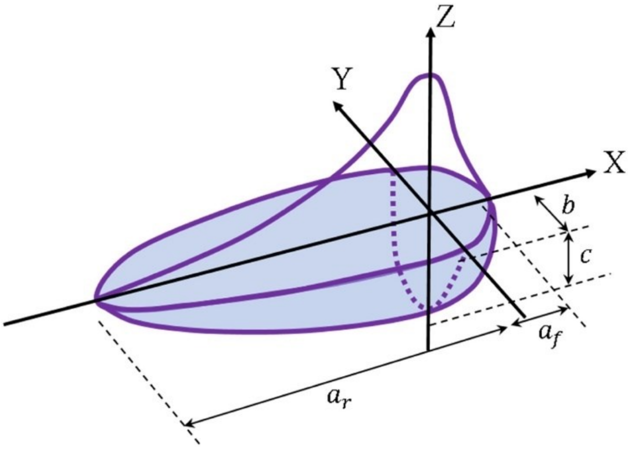

Figure 5 Schematic representation of Goldak's 3D heat source model [51]

It is noted that the material density has not been considered temperature-dependent as its dependency is negligible with respect to temperature. Furthermore, for simplicity, the phase change effects are ignored in the thermal analysis. Eq. (4) is implemented for every element in the discretized body. Then, the nodal temperatures can be obtained by assembling the element stiffness matrices in the global coordinate system. Iterative Newton-Raphson solution scheme can also be used to find nodal temperatures numerically.

Although the main part of the heat transfer phenomenon is carried out by the material conductivity even inside the melt pool, a number of studies emphasize on the effect of convection heat transfer inside the melt pool [24, 206, 207]. The research studies [24, 206, 207] demonstrated over-estimation of the cooling rate in DMD processes because of neglecting the convective heat transfer inside the melt pool. Very steep thermal gradient exists inside the melt pool which results in the formation of turbulent molten material flow. The material flow inside the melt pool has a significant impact on heat transfer analysis and the shape of the melt pool. Considering all the important factors responsible for heat transfer phenomena inside of the melt pool, Mukherjee et al. [24] proposed a novel heat source model in the direct energy deposition (DED) of Ti-6Al-4V and IN 718 powder. The authors reported a very good agreement between experimental and numerical results. Manvatkar et al. [206] proposed a thermal source model taking into account the convective heat transfer inside the melt pool during DED of powder SS316 alloy.

3.2. Mechanical analysis

After performing the heat transfer analysis and acquiring the nodal temperature history, the structural/mechanical model is constructed to obtain the mechanical response of the built component on the basis of the quasi-static analysis. It implies the elements used for the model do not possess a temperature degree of freedom that results in computational efficiency. The mechanical modeling is based on the equilibrium mechanics of a continuum body expressed as [61, 200-202]:

$$\nabla \sigma + b = 0 \tag{7}$$

in which σ is a 2nd order Cauchy stress tensor and b is the body force vector. By imposing the weight functions and implementing the Galerkin method on the weak formulation of the residual, the linear shape functions (same as thermal analysis) are evaluated. The residual for an element is represented as [61, 200-202]:

$$R = \int_V [B^T \sigma^n - N^T b] \, dV - \int_A N^T q^f dA \tag{8}$$

In which q^f is the surface the traction imposed on surface A. Analogous to thermal analysis, the residual is the function of the element degrees of freedom which is nodal displacements in structural analysis. Thus, taking the derivatives of the residual with respect to nodal displacements will result in a material Jacobian or element stiffness matrix as [61, 200-202]:

$$\frac{dR}{dU^n} R = \int_V \left[B^T \frac{d\sigma^n}{d\epsilon^n} B - N^T \frac{db}{dU^n} \right] dV - \int_A N^T \frac{dq^f}{dU^n} dA \tag{9}$$

As small deformation was assumed for the FE-based modeling for the DMD process, the total strain can be decomposed into three different components [198]:

$$\epsilon = \epsilon^e + \epsilon^p + \epsilon^{th} \tag{10}$$

Where $\epsilon, \epsilon^e, \epsilon^p$, and ϵ^{th} are total, elastic, plastic and thermal strains, respectively, $\epsilon^{th} = \alpha \Delta T$, and α is the linear thermal expansion coefficient. Using Hook's law and Eq. (10) [198]:

$$\sigma = C\epsilon^e = C(\epsilon - \epsilon^p - \epsilon^{th}) \tag{11}$$

In which C is a 4th order temperature-dependent elastic stiffness tensor. By applying the boundary conditions on the mechanical FE model, the nodal displacements and stresses are computed using Newton-Raphson iterative scheme, then, the equivalent stress known as von Misses stress is evaluated to check either the element has reached the elastic limit or not. If not, the solution continues in time. As the calculated von Misses stress trespassed the current yield limit, the analysis enters into the plastic region. It was mentioned before that the yield stress of metal alloys are reduced as the temperature increases. Therefore, a proper temperature-dependent yield criterion and flow rule need to be employed. The flow rule (based on Prandtl and Reuss), yield function for isotropic and kinematic hardening rules and flow direction are defined respectively as [208]:

$$\dot{\epsilon}^p = \dot{\lambda}\frac{\partial f}{\partial \sigma} \tag{12}$$

$$f(\sigma, \kappa) = \sqrt{2J_2} - \kappa = 0; \text{ Isotropic hardening}$$

$$f(\sigma, \alpha, \kappa) = \|\xi\| - \kappa = 0, \xi = S - \alpha; \text{ Kinematic hardening} \tag{13}$$

$$\hat{n} = \frac{S}{\|S\|}; S = \sigma - \frac{1}{3}\sigma_m$$

Where λ is plastic multiplier, f is the J_2 plasticity yield function, and κ is current yield stress, α is back stress, S is deviatoric stress, $\hat{n}$ is the flow direction, and σ_m is hydrostatic stress. It should be noted that the J_2 refers to the second invariant of stress for a given element/integration point. By implementing the combined isotropic-kinematic hardening rule, the consistency condition yields the plastic multiplier rate as [208]:

$$\dot{f} = \frac{\partial f}{\partial \sigma} : \dot{\sigma} - H\dot{\lambda} = 0 \tag{14}$$

$$\dot{\lambda} = \frac{\hat{n} : \dot{\epsilon}}{1 + H/2\mu} \tag{15}$$

where H is the hardening value obtained from plastic stress-strain curve and μ is Lame's coefficient. And, the current yield stress and back stress are defined as [208]:

$$\begin{aligned} \dot{\kappa} &= \frac{\beta H}{1 + \frac{H}{\mu}} \hat{n} : \dot{\epsilon} \\ \dot{\alpha} &= \frac{(1-\beta)H}{1 + \frac{H}{2\mu}} (\hat{n} \otimes \hat{n}) : \dot{\epsilon} \end{aligned} \tag{16}$$

Where sign ":" stands for double contraction operation of tensors and $\otimes$ is dyadic multiplication sign that $(a \otimes b)_{ijkl} = a_{ij}b_{kl}$. If $\beta = 1$, only isotropic hardening will function and if $\beta = 0$, only the kinematic hardening rule is applied. In DMD processes, as the material experiences thermal cycles, the material definition should be able to take into account the Bauschinger effect. Kinematic hardening (Prager hardening) is capable of handling the Bauschinger effect, however, isotropic hardening is not. Then, a middle range value for β ($0 < \beta < 1$) should be considered to take advantage of both hardening rules [208]. The thermal effect in the plasticity is considered through the determination of the yield stress as the criterion for checking if an element has reached the current yield limit or not.

3.3. Element activation methods

Unlike most of thermomechanical analysis techniques that the part is fully defined at the beginning of the analysis, a modeling method accounting for material addition is needed for the simulation DMD processes. Specially, as commercial software is used to generate FE-based models, it is essential to employ certain techniques to account for material addition. A few methods have been implemented in the application of commercial FE packages, e.g. ABAQUS, to incrementally add material or elements into an existing model. These methods are known as a) quiet element activation, b) inactive element activation, and c) hybrid element activation methods [121, 203]. Implementation of these techniques into commercial FE packages requires vast knowledge in finite element modeling and also in heat transfer, elasticity, and plasticity topics to develop suitable and valid subroutines and their integration into FE software package(s). The mentioned element activation procedures and their advantages and disadvantages are listed below [121, 202, 203]:

3.3.1. Quiet element activation method

In the quiet element activation method, the complete part including all nodes and elements exists in the model at the beginning of the analysis, however, the material properties of the non-deposited elements and layers are scaled down so that they will not interfere with the analysis. The quiet elements are activated and their material properties are changed into actual properties as the thermal source passes over them. The quiet activation method can be simply implemented in commercial FE packages such as ABAQUS and renumbering of nodes/elements is not needed in every increment as the number of elements and nodes are not changed. Since the elements' stiffness and mass matrices are not evolved, solver initialization in every increment is also not required. However, scaling down the material properties to account for the non-deposited elements/layers makes the stiffness and mass matrices ill-conditioned and also there is a large number of quiet elements at the beginning of the process which increases the number of the equations to be solved in every increment.

3.3.2. Inactive element activation method

In the inactive element activation method, only deposited elements/nodes exist in the model and non-deposited elements are added into the model in every solution increment as the heat source moves forward. Hence, there are no ill-conditioned stiffness and mass matrices in the analysis and the size of them are small at first. This may seem to be beneficial in the case of acquiring more precise responses, however, the implementation of the inactive element activation method into commercial software is not an easy task. Adding nodes and elements in every increment requires renumbering of the stiffness and mass matrices for the whole process time. Indeed, the computational effort for renumbering the nodes and elements and initializing the solver for every increment is bothersome.

3.3.3. Hybrid activation method

The hybrid activation method was later introduced to account for the depositing of new elements/layers by taking advantage of both activation methods [203]. In the hybrid activation method, the non-deposited layers are removed from the model. Only the depositing layer is present in the model and non-deposited elements of that layer are scaled down using the quite element method. The next layer is added to the model and the nodes/elements are renumbered based on the inactive element activation method and its non-deposited elements become quiet. The main advantage of this activation procedure is that smaller and less ill-conditioned stiffness matrices is generated and computational effort will be minimized. A number of research works have been conducted based on these activation methods [24, 51, 124, 203, 209, 210].

In the first paper, Michaleris [203] developed a 1D bar and 3D wall with pure heat transfer models based on the application of element activation methods and investigated their efficiency and accuracy thoroughly. In the case of the 1D problem using quiet element methods, different scaling factors for heat conductivity (S_k) and specific heat (S_{Cp}) were considered and results were compared with the exact solution of the heat transfer problem. The left half-length of the bar was selected to be active at all times and the other half was activated using quiet and inactive element activation methods. The heat source was applied to the left side of the bar from 0-0.1 time. It was presented in [203] that the energy leakage from the interface nodes (the nodes between the recently activated and not-activated elements) to the not-activated elements caused some error in temperature estimation at the first (T_{center}^{1}) and the last (T_{center}^{100}) increments when the body was cooled down to the room temperature. Hence, the author established another modification technique to the element activation mechanism that temperature (T_{center}^{n-1}) of the common nodes (that are shared with the previously activated elements) of the next element was reset to zero. Table 1 demonstrates the calculated temperatures for the first and last increments of the central point of the 1D bar using both quiet element activation method with different scaling factors and the inactive element activation method and corresponding errors. Q1-9 stands for the quiet element activation method and I1-4 represents the inactive element activation scheme. It should be noticed that the best combination of the scaling factors for the quiet activation method ought to yield accurate results for both first and last increments since the nodal temperature history is quite important in the determination of residual stresses in structural analysis. As it was demonstrated in Table 1, the results obtained from the inactive element activation method have lower error values as the resetting was applied to the newly activated elements. However, both methods are capable of predicting the temperature history of the central point of the bar.

Table 1 Effect of different activation methods on error of the estimated temperature of the bar center using quiet and inactive element activation methods [203]

Case	# of elements	S_k	S_{Cp}	T_{center}^{n-1} reset	T_{center}^{1} (% error)	T_{center}^{100} (% error)
exact	10	1	1	No	100	50
Q1	10	0.01	1	No	50.0000 (-50.0)	50.0000 (2.8×10^{-14})
Q2	10	0.0001	1	No	85.7959 (-14.204)	50.0000 (2.8×10^{-14})
Q5	10	0.0001	0.1	No	98.6704 (-1.3296)	52.6393 (5.2786)
Q6	10	0.0001	0.01	No	99.8347 (-0.1653)	53.6090 (7.2180)
Q7	100	0.0001	0.01	No	99.9016 (-0.0984)	53.2298 (6.4596)
Q8	10	0.0001	0.01	Yes	99.8347 (-0.1653)	49.9635 (-0.0729)
I1	10	-	-	No	100 (0)	55.0000 (10.0000)
I2	100	-	-	No	100 (0)	50.5000 (1.0000)
I3	10	-	-	Yes	100 (0)	50.0000 (-4.2×10^{-14})
I4	100	-	-	Yes	100 (0)	50.0000 (3.4×10^{-13})

Michaleris [203] also implemented the same procedure for building a 3D thin wall and compared the results by applying different element activation methods. Furthermore, the hybrid element activation procedure was also used for the material addition of the thin single-wall build. The results of the built wall using different element activation methods with corresponding computational time are presented in Table 2. WQ, WI, and WIQ are referred to as the case implemented quiet, inactive, and hybrid element activation methods, respectively. It should be noted that the error of the activation method for the built wall with inactive element activation method and temperature resetting which had the lowest value, was considered as the reference for comparison. Results showed that the hybrid element activation with temperature resetting provided reliable and accurate results considering the lowest computational time. As it was described in [203], more accurate results were obtained as the temperature resetting technique applied in the modeling procedure. However, in order to avoid any further complexity in developing FE-based models for complex shapes and large components with a few numbers of layers, the hybrid element activation technique demonstrated high efficiency and good approximation of the AM process. As discussed, the inactive element activation usage is bothersome when the commercial finite element packages are used and the computational time for node/element renumbering for each increment is increased. A number of research studies that used similar activation mechanisms were reported to account for material addition in DMD [30, 51, 121, 124, 197, 199, 201-203, 209, 211-217]. It should be mentioned that the element activation procedures have to be employed in both thermal and mechanical modeling regardless of using weakly-coupled or coupled approaches to account for material/element addition.

Table 2 Results for the built wall using different element activation method and their corresponding run time [203]

Case	Method	S_k	S_{Cp}	T_{center}^{n-1} reset	Max (% error)	Run time (s) with 1 core
WQ1	Quiet	0.000001	0.01	No	4.1234	7864
WQ2	Quiet	0.000001	0.01	Yes	0.3734	7587
WI1	Inactive	-	-	No	5.3056	8102
WI2	Inactive	-	-	Yes	Reference	8179
WIQ1	Inactive/quiet	0.000001	0.01	No	3.5323	6313
WIQ2	Inactive/quiet	0.000001	0.01	Yes	0.5242	6284

For the present study, the hybrid element activation technique was implemented in all the structures and for thermal and mechanical analyses. Layers were activated based on the inactive element activation technique and their elements were activated via the quite element activation technique. The material properties of the quiet elements were scaled down such that they did not interfere with the solution in the analysis. Two parameters including thermal conductivity and specific heat were scaled down based on the values obtained from the literature [24, 121, 203, 210]. Scaling coefficient of 10^{-9} and 10^{-2} were multiplied by the thermal conductivity and specific heat, respectively as recommended in the literature. On the other hand, only Young's modulus was scaled down with a factor of 10^{-9} for those elements that are quiet according to the literature [24, 121, 203, 210].

The criterion for activating the elements is based on their contact with the heat source. In other words, if the laser passes the elements, they become active and real material properties are assigned to them. This can be easily achieved by setting the dimensional criteria with respect to the moving laser’s location. The activation criteria were applied in UMATHT and UMAT subroutines for the thermal and mechanical analyses, respectively.

Chapter 4:

Machine learning and neural networks

Machine learning is a broad term and it is the most developed and extensively used branch of AI that includes all algorithms which are able to extract patterns from a given dataset and create a logical relationship between its inputs and outputs. ML enables the machine to learn from a set of data without being specifically programmed. ML was born in 1943 but it was mainly introduced in the research topics in 1990s in different fields such as image and voice recognition, traffic controls, medical examinations, marketing, weather forecasting, and the developing of self-driving cars [50]. In order to apply such techniques, the first step is to build a dataset. Dataset is referred to the sequence of numbers as inputs and their corresponding output(s).

The ML techniques and methods are categorized into three main classes based on the learning scheme. Supervised learning, unsupervised learning, and reinforced learning. Supervised learning is the most common type of ML algorithms that tries to find a logical relationship between labeled data which is called the training process. This method is well-suited for regression (e.g. distortion assessment of DMD parts) and classification problems (e.g. failure detection in none-destructive evaluation methods) and is commonly used in structural mechanics. However, the techniques and algorithms that are implemented in unsupervised learning are based n the unlabelled dataset. There are various machine learning techniques and approaches that are commonly used in the field of solid and structural mechanics such as Artificial Neural Networks (ANNs), Decision Trees (DT), Support Vector Machines (SVM), Random Forest (RF), etc. Unlike the massive dataset in the fields of image and speech recognition, reliable datasets in the filed of solid mechanics are very limited and often are confidential and exclusive to the companies that performed the tests and created the dataset. Therefore, the application of ML in solid mechanics is still in the first steps compared to other domains in the research community. On the other hand, the configuration of the dataset for a specific problem in structural mechanics is not straightforward and may require a lot of time to formulate and adjust the data to be able to apply ML concepts to them. However, by acquiring more datasets in the field and also by increasing the computational power of machines, researchers have become more interested in applying ML algorithms in solid mechanics. Some of the related applications of ML algorithms on structural mechanics are listed in the literature review to represent the importance of ML in developing novel and innovative approaches for solving real-time problems. A dataset should be sufficiently large and well-structured that represent the full characteristics of a problem thoroughly. Therefore, the FE analysis is adopted as the appropriate analysis tool for generating the datasets in the present dissertation.

Neural networks (NNs) are recognized among data scientist to be one of the most powerful ML algorithms that can extract non-linear and complex relationships between inputs and outputs of a system [218-239]. Generally, the NNs are developed into three categories based on the application:

- Artificial neural networks (ANNs). ANNs are recognized as commonly used NNs that can be implemented in both regression and classification problems. The ANNs generate deep neural networks that map the inputs to the outputs through a dense connection of neurons and several hidden layers between input/outputs. Any type of nonlinear relationship can be extracted with ANNs if the hyperparameters (which will be introduced in the following) are adjusted well [45, 240]. The ANNs utilize the forward propagation to estimate the output based on inputs, weights, biases, and activation functions, then use the backward propagation to calculate the error and minimize it by adjusting the weights and biases. This process is known as the training of the network. The backward propagation is performed by taking the derivative of the activation function. Therefore, if the number of hidden layers exceeds a certain limit (depending on the features of the dataset and type of selected activation function), the gradient of the activation function in the backward propagation vanishes through several layers and the training is not accomplished well. One of the important characteristics of the ANNs is that in order to use the trained network, the input must be in the same format/size as the training data. Different data sizes will raise an error in the network and no output will be generated. More details on generating an ANN and selection of hyperparameters are given in this chapter. Schematic representation of the ANN is shown in Figure 6.

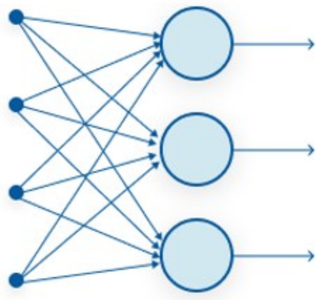

Figure 6 Artificial neural networks configuration

- Recurrent neural networks (RNNs). RNNs were developed to cover the shortcomings of the ANNs in certain applications where the data size/format is usually changed from one pair of input/output to another and deeper networks needs to be constructed. The RNNs are mostly used in sequential data series such as text data and audio data where the sequence and occurrence of the data/features are important. The RNNs are similar to ANNs with an extra connection to the hidden layer where data can be added to the existing input during the training and prediction. A schematic representation of the RNN is shown in Figure 7.

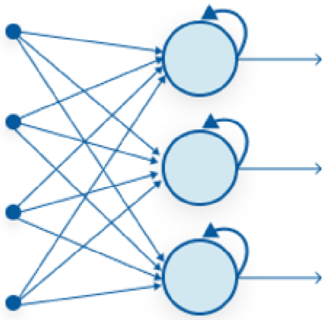

Figure 7 Recurrent neural networks configuration

- Convolution neural networks (CNNs). CNNs commonly consist of convolutional layers that may be called a filter/kernel, a pooling layer that is used for size reduction, and a fully connected deep neural network similar to ANN. The convolutional layers are a finite number of filters that mutate the inputs by extracting certain and relevant features of the data and creating different input data. The CNNs are mostly used in the field of image/facial recognition in an efficient way compared to ANNs. The volume of the computations to minimize the error is drastically reduced due to introduction of several convolutional layers to extract only the relevant data from input. Similar to the human's brain that can distinguish different items on a face such as a nose, eyes, mouth, …, the CNNs separate the items using the filters and also keeps the arrangement in order according to the original image. The schematic representation of the CNNs is shown in Figure 8.

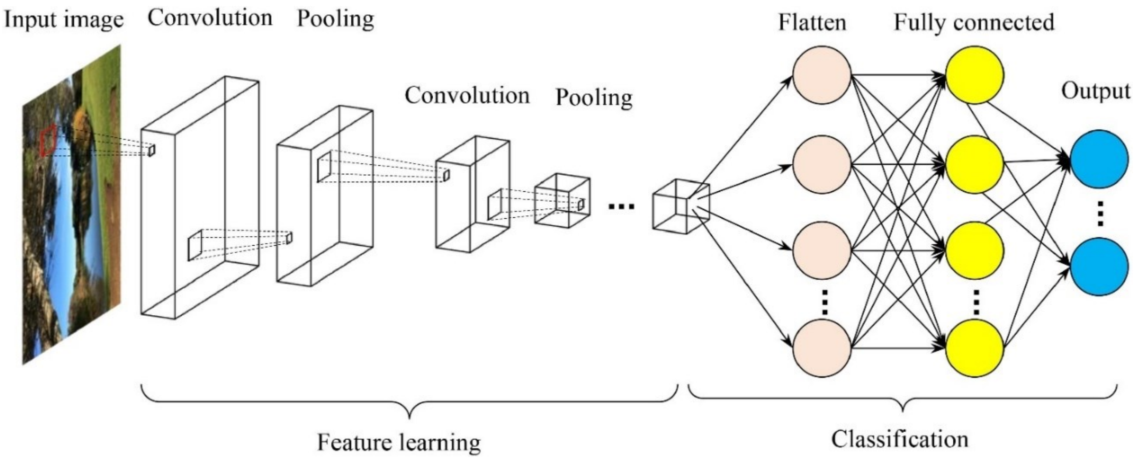

Figure 8 Schematic representation of convolutional neural networks [50]

According to the discussion above on the applications of the different NNs, it is concluded that the conventional ANNs are the best candidate for the regression problem stated in the present study. The ANN can figure out the impact of each feature/input with significant efficiency [222-227]. Artificial neural networks (ANN) are known as the most popular and powerful machine learning techniques that have been extensively used in different disciplines such as image recognition, financial markets, and weather forecasting.

One of the major shortcomings of all ML algorithms and ANNs is the lack of comprehensive data for the training step. If the dataset is biased and it cannot represent the general and overall features of the system, the ANNs will not recognize the relationship between the inputs and outputs of the system [229, 232-239]. The size of all input and output data needs to be exactly the same for training, validation, and testing. Therefore, the problem features have to be constructed in a way that complies with the structure of the built ANN [225-232]. The construction of the network itself and assigning the hyperparameters need lots of trials and errors to achieve an optimized network. These hyperparameters depend on the data set and cannot be identified based on a logical or theoretical method [234-237]. If the problem is the regression type, the ANNs can not be used for the extrapolation based on the training dataset [232, 233, 237-239].

Rosenblatt [241] presented a multi-layer artificial neuron that consisted of two mathematical operators:

$$z = \vec{w}^T \vec{x} + b \tag{17}$$

as the net input of the neuron and an activation function $\emptyset$, shown in Figure 9 (a). The ANN model can consist of several layers and a specific number of neurons in each layer. All the inputs are set in the input layer and the outputs are set in the output layer of the ANN. The ANN can contain one or multiple hidden layers with a predetermined number of neurons as shown in Figure 9 (b).

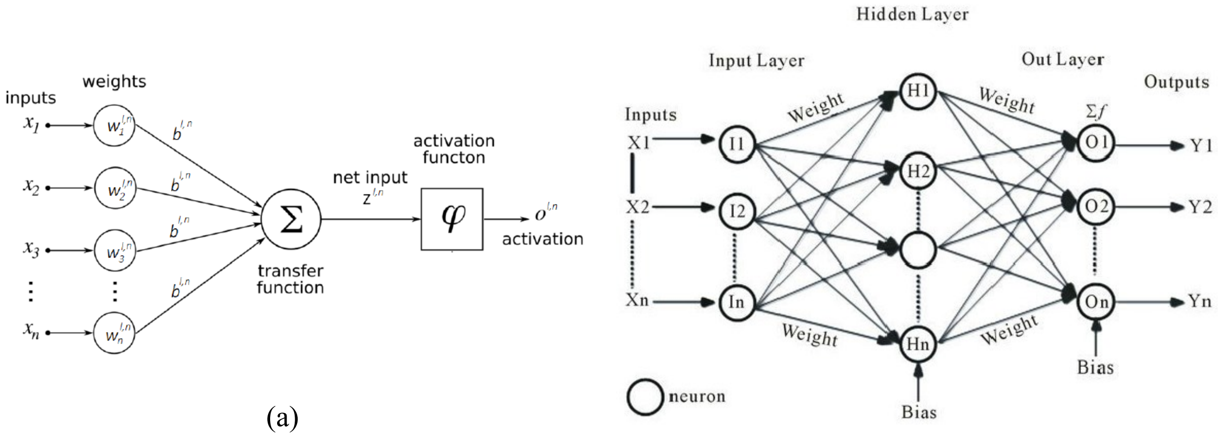

(a)

(b)

Figure 9 (a) Layout of multilayer neuron in artificial neural networks (b) Three layers artificial neural networks configuration with one hidden layer [46]

Based on the activation criterion defined for each layer, each neuron will remain silent or fire or become active. At first, initial values for weights and biases are considered. By feeding the input vector into the network, output will result. As the output is different from the actual output, an error function can be established and used for measuring the deviations from actual values. Thus, the network is trained by minimizing the error function that leads to adjusting the weights and biases. The gradient descent approach with backpropagation is used as an efficient training algorithm [46]. It minimizes the error by finding the local optima of the loss function. The general idea of gradient descent approach is given based on Taylor expansion [46]:

$$\begin{gathered} f(\vec{x}+h\vec{s}) = f(\vec{x}) + (\nabla f)^T \vec{s}h + o(h^2) \\ df = f(\vec{x}+h\vec{s}) - f(\vec{x}) \approx (\nabla f)^T \vec{s}h \\ \vec{s} = \nabla f \text{ as the optimal step direction} \end{gathered} \tag{18}$$

As f represents the loss function, h is the learning rate or step size, and $\vec{s}$ is the derivative of the loss function with respect to the inputs in the network. The derivative of the loss function with respect to any input variable in ANN can be expressed as [46]:

$$\delta^{n,l} = \frac{\partial f}{\partial z^{n,l}} \tag{19}$$

After calculation of $z^{n,l}$ for every input parameter, the optimal step direction ($\vec{s}$) is found. Then, based on the reverse computation (also known as backward propagation) in the network, starting from the output and reaching the input, the weights and biases are modified to minimize the loss function, consequently, the prediction error. The gradient descent algorithm with backpropagation in ANN is executed on the whole network and the outputs are stored in order to update the weights and biases for the next epoch. Once the network is properly trained, it can be used for prediction purposes. Some of the important factors in developing an ANN are related to the configuration of the network including:

- The number of hidden layers, number of neurons in each layer and number of epochs. The number of the hidden layers and also the neurons in each layer depend on the size of the input data and the level of the nonlinearity and complexity of the dataset. In order to have higher training accuracy and accurate predictions, the number of hidden layers and the neurons in each layer has to be adjusted in such a way that the network is capable of acknowledging the effect of each input parameter and the possible interplay between them. Nevertheless, by increasing the number of neurons in each layer excessively, the training accuracy will be declined. Excessive increase in the number of layers results in undermining the effect of each input in the ANN model. Consequently, the training accuracy is reduced.
- Selection of activation function: It is recommended to use a non-linear activation function

specially when dealing with non-linear and complex problems. Activation functions are used to determine whether the neuron will be active or mute. Sigmoid, hyperbolic tangent and rectified linear unit (ReLU) functions are the prominent activation functions with continuous and non-zero derivatives for the backpropagation process.

- Selection of the loss or cost function: In order to compute the error between the exact values of the outputs and the predictions from the ANN, a certain loss function should be used based on the problem. A mean squared loss function is the most popular function for regression problems. On the other hand, cross-entropy is known to be a better option for classification problems in which the likelihood of output is compared with the actual output.
- Specifying the learning rates. The learning rate is an important hyperparameter specified before training the network (shown as *h* in Eq. (18)). This value controls updating the weights and biases of the network and plays a major role in the convergence of training. The effect of the learning rate is demonstrated in Figure 10. It can be seen that very high learning rates develop an unbalanced condition for updating the weights and biases and minimizing the loss function. It can be interpreted that the higher learning rates skip the optima of the loss function. On the other hand, the low learning rate may not allow the loss function to reach the optima and end up with higher loss values. The optimum learning rate can be specified by observing the loss function as it continuously declined over the training process. However, there is no explicit method of determining the learning rate as it depends on multiple factors such as the data structure and its features, the activation function, and the loss function.

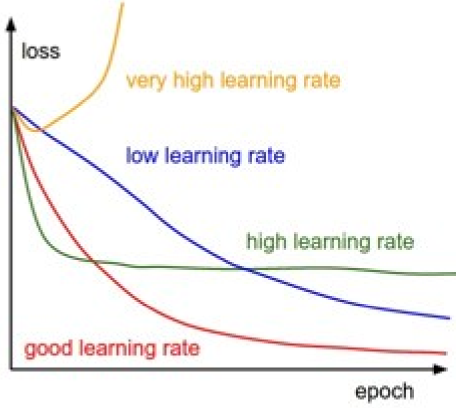

Figure 10 Effect of the learning rate in the training ANN [46]

- The computational time for training. One of the major factors in the application of ANNs is related to its high computational time. During the training, the data is fed into the network and the loss function is calculated. Then, the derivative of the loss function is computed with respect to each input. The backward propagation is used along with the learning rate to find the updated weights and biases. The whole optimization process is time-consuming especially when the data set and the numbers of its features are large.

- Overfitting and underfitting. One of the major problems of implementing the ANNs is related to the underfitting and overfitting of the network. Overfitting refers to the state that the trained network is only capable of making predictions for the data identical to the training data. In other words, the weights and biases are adjusted in such a way that can only map the trained network to its corresponding output. On the other hand, underfitting refers to the state that the network that is incapable of extracting the relationship between inputs and outputs. This may arise as a result of insufficient data or an inconsistent dataset.

In the next chapter, the methodology adopted to integrate the FE analysis with the ANNs is presented in detail and the ANN structure that was developed is discussed along with the data structure.

Chapter 5:

Methodology

According to the literature, there are numerous research studies that point out the shortcomings of the numerical analysis which is related to the computational time of the applying FE method to obtain the residual stresses for a complex part. It becomes even more susceptive when the part requires the application of the support structures. Support structures are substantial for building highly complex geometries. However, removing them after finishing the process imposes significant stresses on the remaining part. Furthermore, simulation of the support removal process is also challenging and it will certainly increase the computational time.

Developing a detailed FE model is crucial to obtain accurate results that could be used as reference datasets for comparison with the results of other phases of this dissertation. Therefore, a weakly-coupled thermomechanical approach was considered in the early stages of this study and different models based on various component shapes were built. The models are generated using Python scripts and implemented in the ABAQUS commercial FE package. This facilitates any modification to the geometry and boundary conditions of the models and makes the design more feasible. All the material properties and boundary conditions are considered temperature-dependent. Thermal boundary conditions including convection and radiation heat transfer are applied in the thermal analysis and all the translational degrees of freedom are applied in the mechanical analysis. As mentioned before, the thermal history of the nodes obtained from the thermal analysis is then applied in the mechanical analysis as the predefined field variables. Hence, the elements in the structural analysis only have translational degrees of freedom. The material properties of AISI 304L are given in Table 3. Furthermore, a constant density of 7800 (kgm^{-3}) was used for AISI 304L in the FE analysis.

It is noted that an accurate FE model of the DMD process requires very intensive calculations both in the thermal and mechanical analyses. However, it is not feasible to consider all the physical phenomena happening during a DMD process in FE modeling of the process. Therefore, some simplifications assumptions were made to enhance the computational efficiency as following:

1- The surfaces of the deposited layers (or parts) remained flat after deposition.
2- The effects of phase change and creep phenomena and resultant strains were neglected.
3- The density of the material was assumed to be constant at all temperatures.
4- Vaporization of the material in high temperatures was neglected.
5- The fluid-solid interactions inside the melt pool were neglected.\

As mentioned in the literature, there are various innovative techniques and methods to lower the computational effort of the time-consuming thermomechanical analysis such as DMD processes. Introducing the innovative and novel framework of integrating the finite element method with machine learning techniques is presented in this study to enhance the computational efficiency of the numerical analysis. In this chapter, the developed procedures to generate a novel and feasible method for improving the computational time of the thermomechanical process for the DMD process and calculating the residual stress distribution in several selected structures are introduced. The core part of this study is to integrate ML, specially ANNs, with the conventional FE analysis to achieve a robust framework to predict residual stresses in DMD processes. Furthermore, the adaptive meshing is also implemented prior to introducing the integration of ANNs-FE to show the capability of the adaptive meshing in reducing computational time and to compare its results with the computational time of the integrated ANN-FE method. In the following, the adaptive meshing is presented followed by the developed novel ANN-FE.

Table 3 Thermal and mechanical properties of AISI 304L [124]

Temperature (°C)	Specific Heat (J/Kg°C)	Conductivity (J/m°C)	Thermal Expansion ($\times 10^{-5}$/°C)	Yield Stress (MPa)	Young's Modulus (GPa)
20	462	14.6	1.70	319	198.5
100	496	15.1	1.74	279	193
200	512	16.1	1.80	238	185
300	525	17.9	1.86	217	176
400	540	18.0	1.91	198	167
600	577	20.8	1.96	177	159
800	604	23.9	2.02	112	151
1200	676	32.2	2.07	32	60
1300	692	33.7	2.11	19	20
1480	700	120	2.16	8	10

5.1. Verification of the finite element model

In order to make sure that the results obtained from the thermomechanical FE analysis are reliable and accurate, a verification step was considered based on the research conducted by Mukherjee et al. [24]. The authors have studied the formation and evaluation of residual stresses during the DMD process of IN 718. FE simulations were performed on a simple direct wall with 10 layers and a thick substrate made from the same material. The experimental tests were also performed to evaluate the residual stresses in two directions; longitudinal direction and stacking direction. The results of the FE simulations were found to be in good agreement with the experimental results. However, it should be noted that the experimental tests were only conducted on several points of the workpiece and recorded as the actual residual stresses. In the following, the thermal and mechanical properties of IN 718 were represented and implemented in the model validation of the present study [24].

Table 4 Thermal and mechanical properties of IN 718 [24]

Temperature (°K)	Young's modulus (GPa)	Thermal expansion coefficient ($\times 10^{-6}$)	Temperature (°K)	Yield stress (MPa)
300	156.3	11.7	300	308.9
477.6	144.9	12.8	588.7	246.3
699.8	131.4	14.1	810.9	226.1
922	124	14.6	1033.2	207.7
1144	107.7	15.7	1255.4	114
1366	68.95	16.6		
1672	23.79	16.7		

The density of the material was assumed to be constant (8100 kg/m^3). Temperature-dependent thermal conductivity and specific heat were considered in the model according to the following equation respectively [24]:

$$\begin{gathered} K = 0.56 + 2.9 \times 10^{-5}T - 7 \times 10^{-6}T^2 \\ C_p = 360.24 + 0.026T - 4 \times 10^{-6}T^2 \end{gathered} \tag{20}$$

T is the temperature in Kelvin. A laser power of 300 W with a scanning speed of 15mm/s was considered for the analysis according to the experiment. The length of each layer is 15 mm and its thickness is 0.67 mm according to [24]. In the following, the results of the validated FE model are presented and compared with the results obtained from [24].

Figure 11 demonstrates the comparison of the predicted results (S11) from the developed FE model and the original results obtained from [24]. The distribution pattern of S11 was captured very well compared to the results of the referenced article. The intersection of the top layer shows very high tensile residual stresses that is consistent with the results of the article.

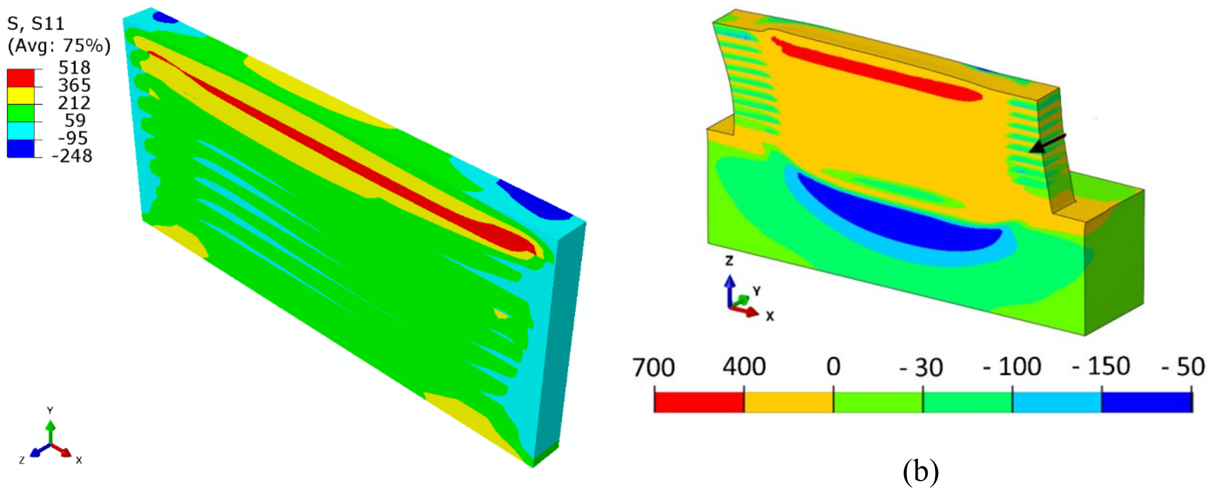

(a)

(b)

Figure 11 Comparison of S11 obtained from (a) developed finite element model and (b) Ref [24]

Figure 12 also represents a comparison of the predicted S22 from the developed FE model and results from the reference article [24]. The high compressive residual stresses at the lower layers and middle of the part were captured discreetly as well as high tensile residual stresses at both ends of the component. A smooth transition from the high residual tensile stresses to compressive stresses was observed in both developed FE model and the article's results.

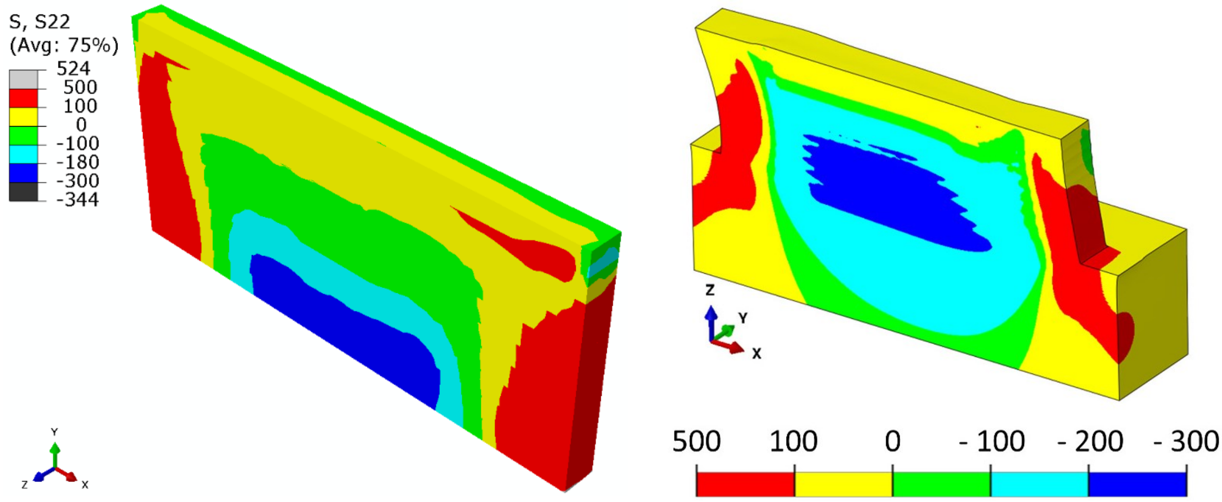

(a)

(b)

Figure 12 Comparison of the S22 obtained from (a) developed finite element model and (b) Ref [24]

The verification of the developed FE model was conducted and approved. Therefore, it can be applied to any material that follows temperature-dependent properties. Table 5 demonstrates the verification error of the developed FE model and the results from the reference [24]. The maximum error is associated with the S22 stress component. However, the predicted results from the developed FE model can accurately simulate the pattern of the stresses successfully.

Table 5 Comparison of the results obtained from the developed finite element model and reference [24]

		Developed FE model (MPa)	Mukherjee et al. [24] (MPa)	Error (%)
S11	Max	518	550 (approximate)	5.8%
	Min	-248	-270 (approximate)	8.1%
S22	Max	524	500	4.8%
	Min	-300	-344	12.7%

5.2. Adaptive meshing technique implementation

The number of elements in an FE analysis denotes the total degrees of freedom of a model and the computational effort. Therefore, one possible solution is to reduce the total degrees of freedom of a FE model. On the other hand, very fine mesh is required for the thermomechanical analysis to be able to handle severe thermal gradients and achieve accurate results. By continuation of the process and depositing the upper layers of a component, the lower layers are not affected by the thermal source and the thermal gradients are attenuated significantly. This allows the model to use coarser mesh sizes for those layers far from the heat source. Hence, an FE-based framework implementing an adaptive mesh-based approach is developed and explained in Figure 14. According to Figure 14 (a), a Python script is developed to generate the FE models for both thermal and mechanical analysis. Corresponding subroutines for each one of the thermal and mechanical models are developed to account for the element activation procedures (UMATHT subroutine for the thermal analysis and UMAT subroutine for the mechanical analysis) and applying moving heat source (DFLUX subroutine for the thermal analysis) with double ellipsoid Goldak's model [121].

The mesh coarsening process is performed in a layer-by-layer manner, as in the DMD process itself. After mechanical analysis for a particular layer e.g. the first layer is completed, the developed Python code is run to map the results of the finer mesh to the coarser mesh. The mapping process begins with extrapolating the solution results to the nodal point of the finer mesh. Then, based on the spatial locations of nodes of the coarse mesh, the results are interpolated to the nodes of the coarse mesh. Afterward, the values for stress and strain tensor are interpolated to the integration point of elements in the coarse mesh configuration using a linear shape function. Next, the field values e.g. stress components, are imported as predefined field variables for those coarsened layers in the new model and deposition of the new layer begins. Based on the temperature or stress gradients, the coarsening technique can be adjusted to be performed in certain intervals. If the temperature during the deposition is so high that it could melt the deposited layers, the coarsening better begins from the deposition of the third or fourth layer keeping the top deposited layer(s) with fine mesh to be able to handle the high temperature or high-stress gradients. For the selected material (AISI 304L) with 0.03% C that is categorized as low-carbon stainless steel, the criterion for coarsening was based on the phase transformation diagram represented in Figure 13. It is shown in the diagram that for temperatures below 300 °C and considering the carbon percentage, there is no phase transformation occuring in the material. Therefore, a threshold of 300 °C was considered as the criterion for the mesh coarsening of the lower layers when their elements did not reach temperatures beyond 300 °C. A schematic representation for implementing the adaptive mesh coarsening technique in the present study is illustrated in Figure 14 (b). It should be noted that all the thermomechanical procedures except the mesh-coarsening process are performed for different geometries with fine mesh.

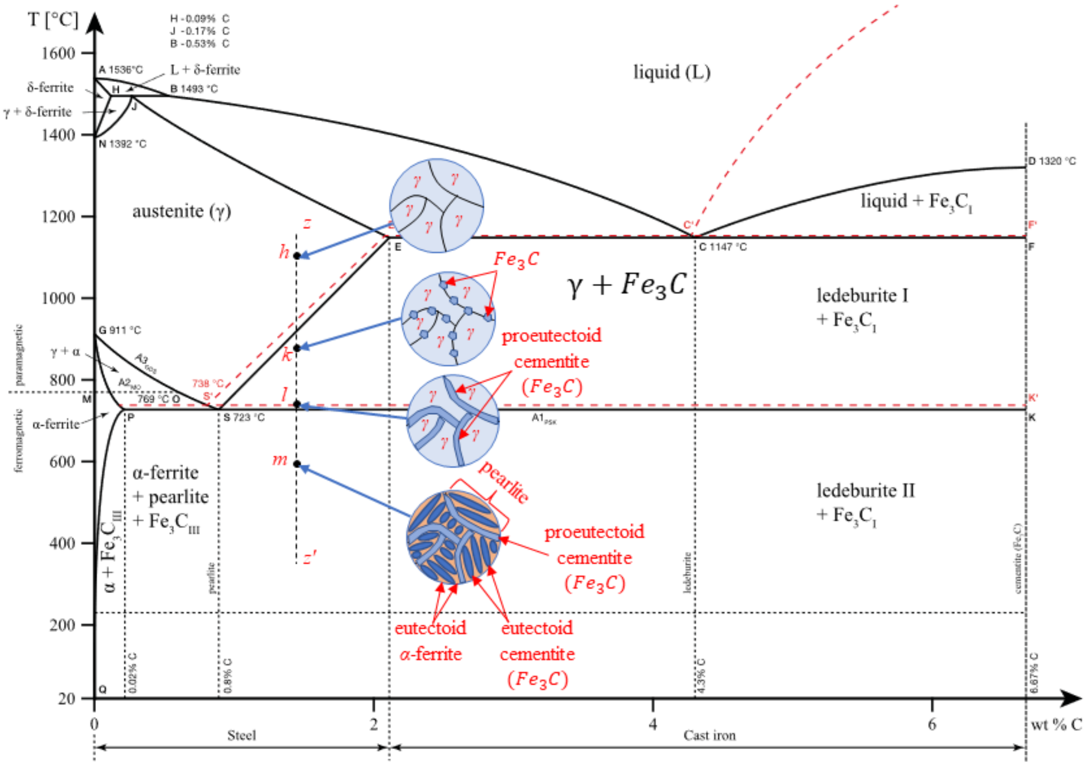

Figure 13 Phase diagram of Fe-%C [242]

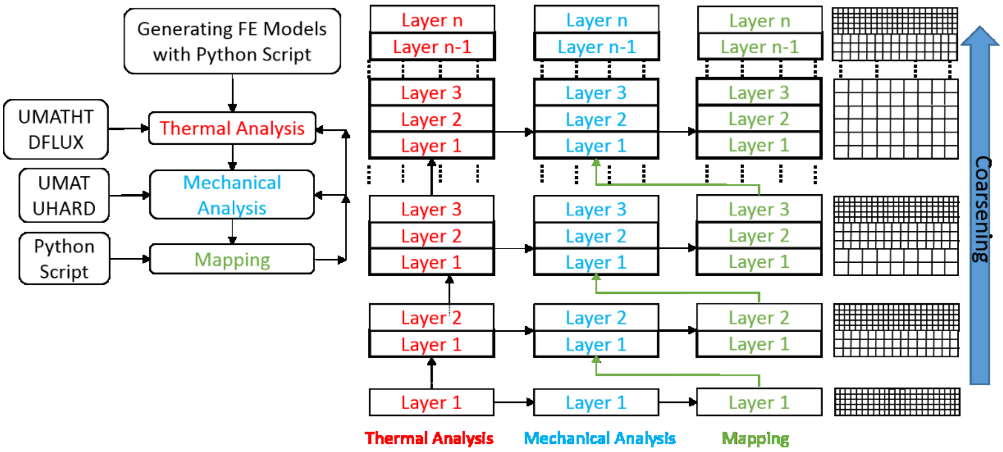

Figure 14 (a) Schematic representation of analysis sequences and (b) sequence of finite element approach for adaptive mesh-based model [124]

The thermal analysis is performed on the three configurations demonstrated in Figure 15 using ABAQUS/STANDARD. All selected three structural parts are 18-layers wall with a thickness of 1 (mm) per layer and with a length (or width) of 15 (mm). In order to account for the element addition and imposing temperature-dependent material in the FE analysis, the UMATHT subroutine is developed and implemented in conjunction with ABAQUS. A laser heat source with a power of 250 (w), beam radius of 0.5 (mm), and transverse speed of 11.25 (mm/s) was used and implemented by DFLUX subroutine. The process parameters are summarized in Table 6. The hybrid element activation technique [124, 243] is adopted to optimize the efficiency of the FE process. All the layers meshed with 5 elements in the thickness direction using linear brick elements (C3D8T) to ensure that the developed FE model is capable of handling high thermal gradients. The material properties of AISI 304L are given in Table 3. Furthermore, a constant density of 7800 (kgm^{-3}) was used for AISI 304L in the FE analysis.

Table 6 Process parameters for the finite element simulations of all structures

Laser power	Scanning speed	Beam radius	Layer thickness
250 w	15 mm/s	0.5 mm	1 mm

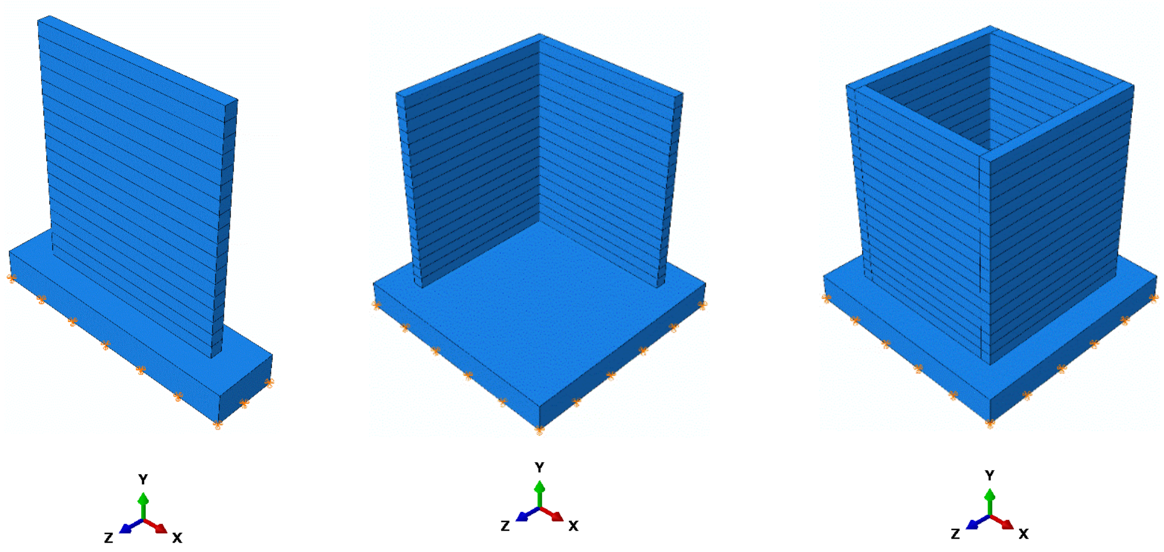

(a) (b) (c)

Figure 15 The three geometries (a) wall, (b) L-shape wall, and (c) rectangular wall for employing the novel approach of integrating the artificial neural networks and finite element analysis

5.3. Integrating finite element analysis and artificial neural networks

Different structural geometries demonstrated in Figure 16 are considered for the development of an integrated modeling framework. For all these geometric structures, the following modeling steps are conducted to develop the proposed ANN-FE framework:

1- Detailed thermomechanical FE-based modeling is performed using ABAQUS/STANDARD commercial package for the parts with 12 and 18 layers; the structures with 12 layers are selected because the 12 layers in the stacking direction can create all the possibilities for elements under cyclic thermal conditions. On the other hand, the full spectrum of the cyclic thermal conditions is not reachable when lower layers (e.g. 6-8-10) are adapted as the training structures.

2- The training and testing datasets are extracted for both 12-layers and 18-layers structural parts. The input data include the temperature history of the elements and their spatial coordinates and the output data consists of the stress components for elements of the structures; the thermal history and spatial coordinates of the elements are chosen on the basis that a comprehensive dataset should include all important features of the system. Therefore, according to the stated problem, the cyclic behavior of the process and its effects on the formation of residual stresses should be addressed in a way that the ANN can extract the relationship. The spatial coordinates are also involved in the input data as the representative of the geometrical effects and boundary conditions impact the magnitude/type of the residual stresses.

3- The features of the ANN are configured based on the size and structure format of the dataset obtained from the 12-layers structure. Then, the ANN is constructed and trained with the training dataset obtained from the 12-layers parts (for each structure);

4- The size of the input dataset for 18-layers structures is restructured to fit the format and size of the trained ANN.

5- After restructuring, the temperature history of each element with its spatial coordinates is fed into the trained ANN to predict the stress components of the corresponding elements. By comparing the difference between the actual (FE analysis) and predicted (ANN-FE) stress values for each element, the prediction error is evaluated for every element.

A schematic representation of the novel approach of integrating the ANN with FE analysis to predict the stress distribution of simple structural parts is illustrated in Figure 17. In the scope of this study, the input data should provide a meaningful description and comprehensive features of material deposition in the DMD process. In this problem, the input data are the thermal history and spatial coordinates of the elements/nodes, and the stress/strain distribution and nodal displacements are the outputs. For simplicity, only the stress distribution is considered as the output. According to Figure 17, after training the ANN is completed, the input dataset for the testing purpose or making a prediction is extracted from the thermal analysis results of 18-layers parts. Since the trained networks for each one of the parts are based on a certain input size, the input data extracted from the 18-layers model should be restructured or adjusted so that it can be fed into the trained network. For instance, the total analysis time steps for the 12-layers wall is 13 (s) which results in an input vector of size of 654 and the ANN is trained based on this data structure. However, the total analysis time steps for an 18-layers wall is 19 (s) which creates an input vector of size of 954. Considering that the ANN is trained based on the 12-layers data for each part, a restructure step is essential to make the input data for 18-layers parts compatible with their corresponding trained ANN. It should be noted that the restructuring must be executed in such a way that the thermal cycles of the elements would not be affected. Therefore, a Python script is developed in order to change the structure of the input data for every element in every layer. Except for the elements in the first layer, the elements in the other layers are constrained to take the effect of the previous layer deposition. For instance, for the extraction of the thermal history of an element in the third layer in the 18-layers wall, the thermal history of the element during deposition of the second layer is also included. However, because the element in the third layer would not exist when the second layer was deposited, the thermal history of the element in the third layer

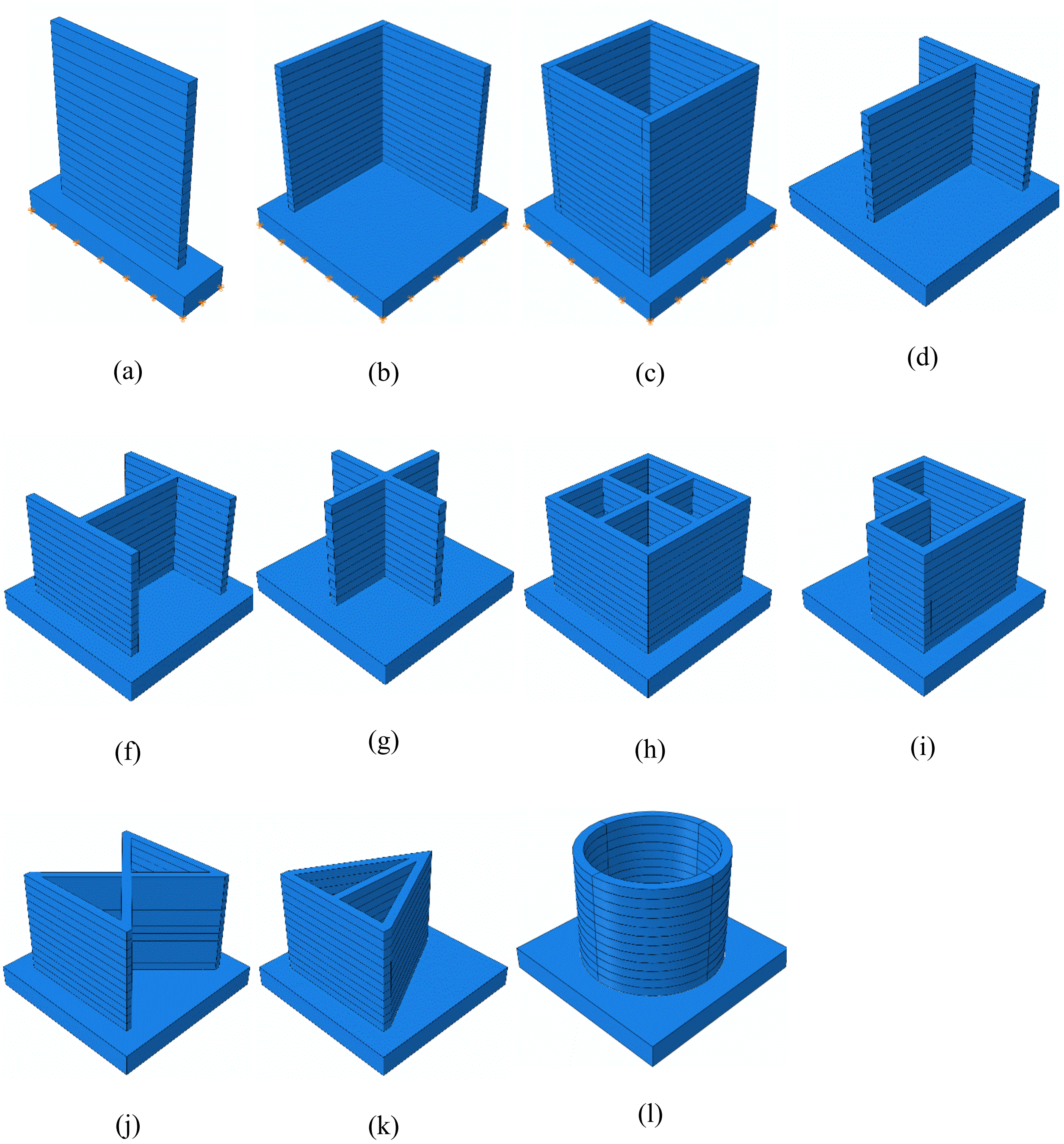

(a) (b) (c) (d)

(f) (g) (h) (i)

(j) (k) (l)

Figure 16 The selected geometries (a) wall, (b) L-shape wall, (c) Box, (d) T-shape wall, (e) S-shape wall, (f) H-shape- wall, (g) Plus-shape wall, (h) BoxPlus-shape wall, (i) Semi-Box- shape wall, (j) Hourglass-shape wall, (k) arrow-shape wall, and (l) cylinder for employing the novel approach of integrating the artificial neural networks and finite element analysis

was put to room temperature during the timespan of the second layer deposition. Finally, after the input datasets of all structural parts are extracted, they are fed into the corresponding trained network for each of the structures and prediction of the stress distribution is accomplished. The error of predicting the residual stress is calculated using the actual data obtained from thermomechanical FE analysis of 18-layers parts as:

$$Error_{\sigma} = \left| \frac{\sigma_{prediction} - \sigma_{FE}}{\sigma_{prediction}} \right| \tag{21}$$

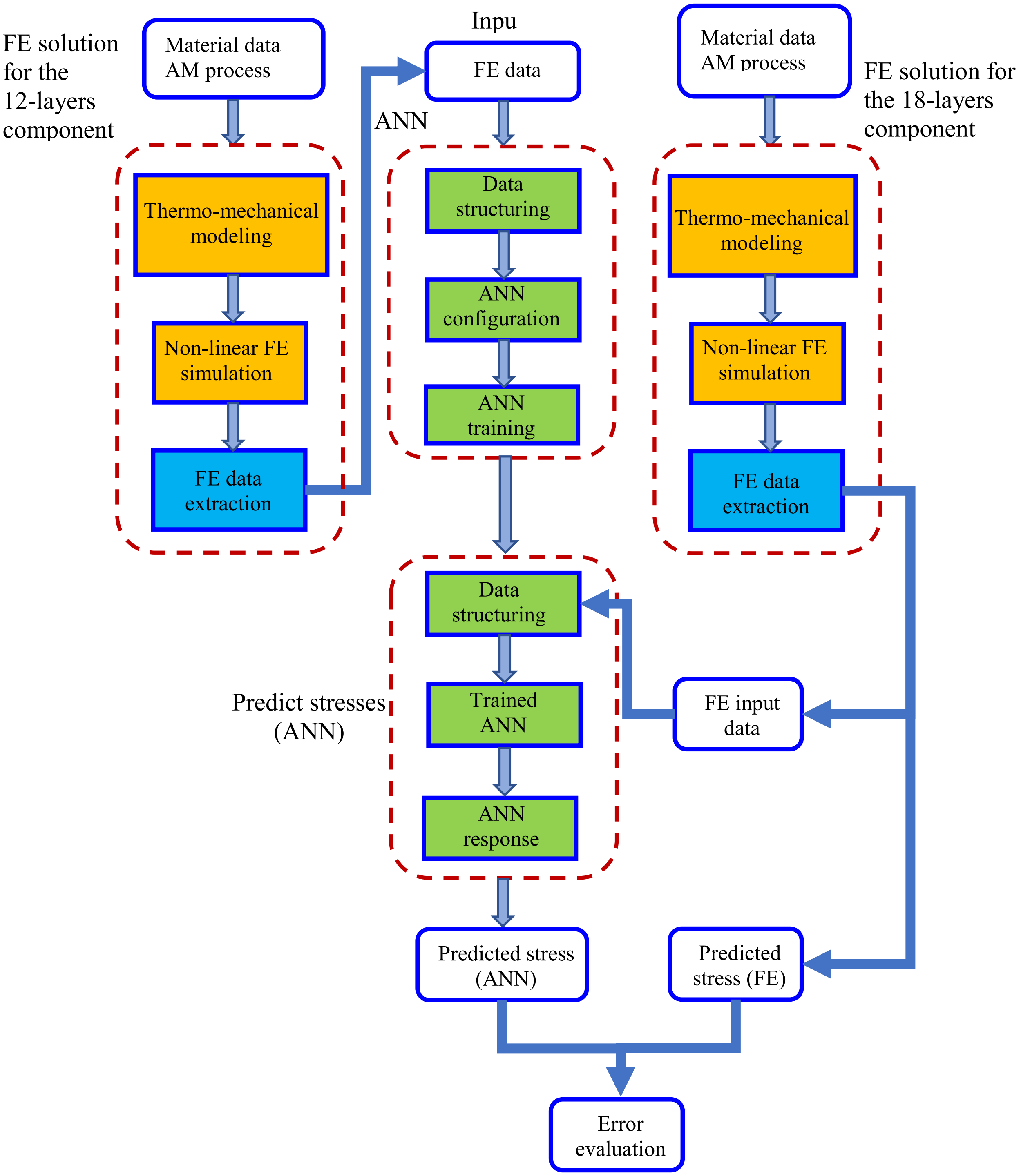

Figure 17 Schematic algorithm of employing the novel approach of integrating artificial neural networks and finite element analysis of direct metal deposition parts

The constructed neural network for the present study consists of two hidden layers with a different number of neurons for each layer (based on the structure) and shown in Figure 18. For every element in the structure, the thermal cycles and corresponding stress components are recorded and entered in the data set.

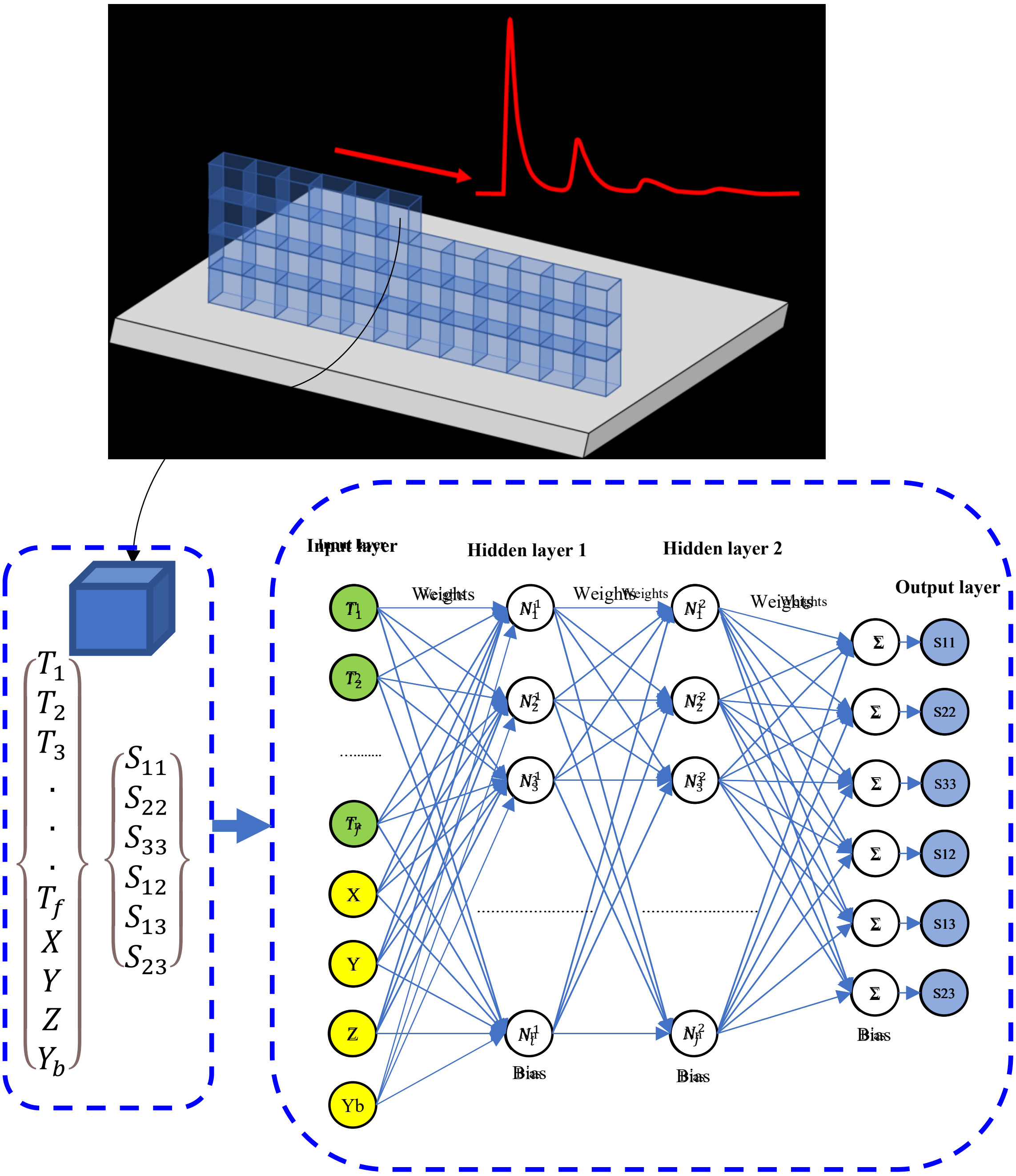

Figure 18 Schematic demonstration of the constructed artificial neural network

The mathematical formulation of the implemented ANN for the present study can be presented in Eq. (21):

$$S_{kl} = \sum_{m=1}^{6} w_{m,j} ReLU \left(\sum_{p=1}^{j} w_{p,i} ReLU \left(\sum_{r=1}^{i} w_{r,n} \vec{X}_n + b_r \right) + b_p \right) + b_m \tag{22}$$

$$ReLU(X) = \begin{cases} x & x > 0 \\ 0 & x \leq 0 \end{cases}$$

$$\vec{X} = \{T_1, T_2, T_3, \cdots, T_f, X, Y, Z, Y_b\}^T$$

Where, S_{kl} ($k, l = 1, 2, 3$) are the stress components as the outputs of the network, w and b represent the weights and biases corresponding to each neuron in each layer. The indices n, i, and j are the length of the input vector $\vec{X}$, the number of neurons in the first hidden layer, and number of neurons in the second hidden layer, respectively. $ReLU$ (rectified linear unit) is a nonlinear activation function defined for each layer to decide whether the neurons remain silent or become active.

At first, initial values for weights and biases are considered. By feeding the input vector of data into the network, the stress outputs are evaluated. Because the calculated stresses are different from the actual stress values, an error function (e.g. mean square error) can be established for measuring the deviations. Afterward, the network is trained by adjusting the weights and biases to minimize the error function.

The hyperparameters such as the number of hidden layers, number of neurons in each layer, activation function in each layer, loss function, number of epochs, learning rate, and a certain method for optimizing the weights and biases are selected by the user in order to establish an ANN. Furthermore, a certain criterion should be adopted to prevent overfitting and underfitting during the training. Features of the artificial neural network implemented in the training step for all the structures shown in Figure 16 are as follow:

- The number of the hidden layers and also the neurons in each layer depend on the size of the input data and the level of the nonlinearity and complexity of the dataset. In order to have higher training accuracy and accurate predictions, the number of hidden layers and the neurons in each layer has to be adjusted in such a way that the network is capable of acknowledging the effect of each input parameter and the possible interplay among them. An excessive increase in the number of layers and neurons in each layer results in excessive computational time for the training. For all structures, only two hidden layers with a different number of neurons presented in Table 7 are used.
- ReLU function in the hidden layers and linear function (also called identity) in the output layer is used as the activation functions in the generated network. It is recommended to use a non-linear activation function especially when dealing with non-linear and complex problems [244, 245];

Table 7 Number of neurons in the hidden layers of the artificial neural networks for the different structures

12-layers structural parts	Number of neurons for the first and the second hidden layer
Straight wall	2048 -1024
L-shape wall	4096 – 2048
Rectangular box wall	8196 – 4096
T-shape wall	8196 – 4096
H-shape wall	8196 – 4096
Plus-shape wall	8196 – 4096
BoxPlus-shape wall	8196 – 4096
Semi-Box shape wall	8196 – 4096
Hourglass-shape wall	8196 – 4096
Arrow-shape wall	8196 – 4096
Cylinder	4096-2048

- Mean squared error (MSE) is used as the loss function to evaluate the error between the predicted values from the network and the actual output. The mean squared loss function is the most popular function for regression problems;
- The number of epochs of 1000 – 2000 epochs are used in the training step for the three structures. This value is adjusted based on the training rate of the network and is chosen in such a way that a training accuracy higher than 95% would be achieved for every structure;
- A learning rate of 10^{-3} is chosen based on the performance of the network during the training. By keeping all other hyperparameters constant, the learning rate was varied over a range of 10^{-4} – 10^{-2} and it was noticed that the loss value improved continuously over time for values around 10^{-3}. Higher values such as 10^{-2} made the training unstable and lower values such as around 10^{-4} increased the number of epochs for the training.

In order to construct a reliable ANN without encountering underfitting or overfitting, the hyperparameters are adjusted in such a way that the loss function keeps improving during the training. The dataset for the training of each structure (12 layers) is divided into two parts with a percentage of 75% and 25% for training and validation, respectively. The training data (75%) is used to optimize the weights and biases and to improve the loss function for the training. On the other hand, the network is used to predict the results for the 25% of the validation data to show the network capability. The validation loss and accuracy values are obtained at the end of each epoch. By comparing the loss functions for the training and validation, the performance of the network can be observed and improved. Overfitting happens when the training loss value keeps improving but the validation loss value is deteriorating. Furthermore, the learning rate plays a major role in the configuration of the hyperparameters. The learning rate is varied to obtain the optimum loss function improvement. All this procedure is performed on all the structures to ensure that the overfitting is not happening. Thereafter, the trained network is used for the prediction of residual stresses in 18-layers structures. The underfitting is not a case for the present study since the data set is sufficient and it can capture all the possibilities that may happen in a DMD process.

Figure 19 shows the loss function diagram over the training of the ANN developed for the L-shape structure. Approximately 75% of the data are used for the training and 25% are considered for the validation. As it is seen, the mean squared error (blue color) is continuously reduced through the training and it reaches a stable condition after about 250 epochs. The mean squared error is also calculated for the validation data to evaluate the training performance and avoid undesired overfitting. As it is shown, the validation loss (red color) constantly declined over the training and it is in a very close range of the training loss. It demonstrates that the structure of the network along with its hyperparameters are selected appropriately.

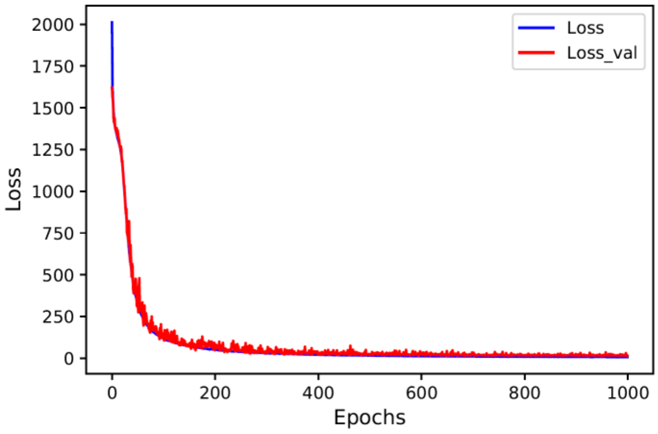

Figure 19 Comparison of loss function for the training and validation data

The accuracy of the training and validation of L-wall structure is shown in Figure 20 to demonstrate the capability of the trained network in the prediction of new input data that are never used for the training. The accuracy seems to be fluctuating during the training, however, it reaches a stable condition after 500 epochs, approximately 96.4% that is considered a good accuracy.

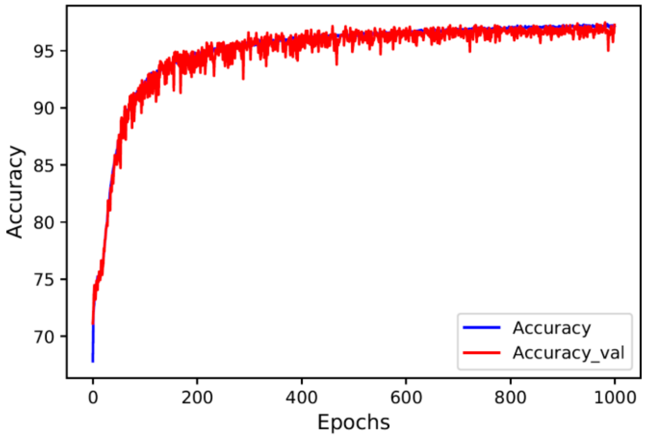

Figure 20 Comparison of accuracy for the training and validation data

Generating a well-structured and comprehensive dataset is crucial for employing any ANN and performing the training step. The data structure is the most important factor in any ML algorithm and has a significant impact on the performance of the developed ML algorithm. Input and output data have to be constructed in such a way they can demonstrate the physics of the problem. A schematic representation of the data structure is shown in Figure 21. According to Figure 21, the input data size for the simple wall becomes 668. For all the elements in the structure, a sequence of thermal histories and the geometrical factors are considered as the features of that element. Based on the time increments (0.3) specified for the structure, every element in its own layer has 50 temperatures plus 1 temperature at the beginning of the step (in ABAQUS it is called time zero of the step). Therefore, each element will have 51 records of temperature from its own layer. Considering the number of layers which is 12, the total number of increments for each layer will become 12*51. On the other hand, an additional step with 51 increments was considered for cooling the structure which will be added to the time increments of each element (12*51 + 51). By adding the extra 5 geometrical components as X, Y, Z, Yb, and an extra factor for representing the first layer (1 for the first layer and 0 for other layers), the total number of input sizes for the training and testing of the simple wall structure becomes 668. A similar procedure was implemented for generating the data set for other structures as well.

For generating the training and the testing dataset, FE analysis with fine-mesh is adopted to perform the thermomechanical analysis of DMD deposition of AISI 304L on all different parts in order to extract nodal temperature history and final stress distribution of the medium. A Python script was developed for the extraction and post-processing of the results. The training dataset is extracted based on the thermomechanical analysis of 12-layers structures for all structural parts. The 12-layers structures can cover all the possibilities of thermal cycles that happen in large components such as 18-layers. For clarification, the data size used for the training of the ANN for all the structures is listed in Table 8.

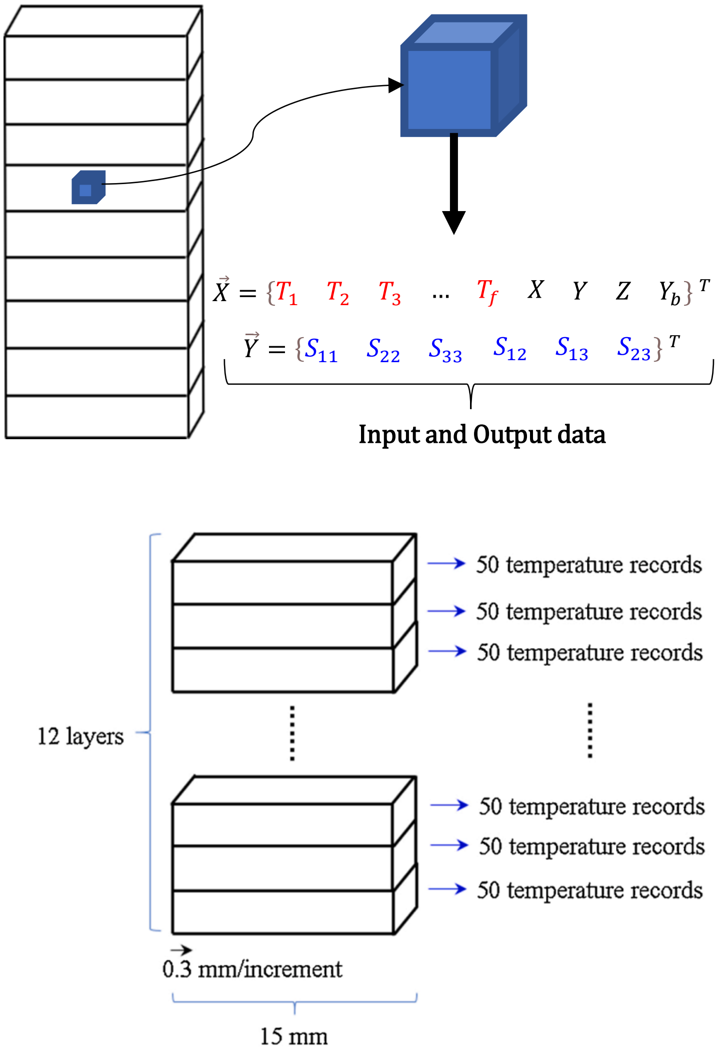

Figure 21 Schematic representation of the data structure for training the artificial neural network for the Wall structure (a) the structure (b) the input and output data structure (c) temperature history of an element

Table 8 Size of the input/output data for the different structures

Structures	Size of the input/output data
Straight wall	668
L-shape wall	1318
Rectangular box wall	2618
T-shape wall	2618

H-shape wall	2618
Plus-shape wall	2618
BoxPlus-shape wall	3918
Semi-Box shape wall	2618
Hourglass-shape wall	2618
Arrow-shape wall	2618
Cylinder	2618

Chapter 6:

Results and discussion

The results of the two applied approaches (adaptive mesh-based technique and integrated ANN-FE approaches) for improving the computational time of the FE analysis of DMD products are presented in this section. The adaptive mesh-based FE analyses are applied only L-shape wall to show the capability of the adaptive mesh-based technique and also compare the results of the structure with the results of the novel ANN-FE for the simple structure.

The results obtained from both adaptive mesh technique and ANN-FE methods are presented in the contour format of the ABAQUS via developing a post-processing Python code to easily map the predicted results to the corresponding structure. Demonstrating the predicted results in the same format as ABAQUS better represents the predicted responses of the two methods and makes it easier to observe the critical locations (large magnitudes of stress) or the location of the highest error. Furthermore, it simplifies the comparison of the results of ABAQUS with the predictions. The error is calculated based on Eq. (20) and the error plot is also shown in the contour format as ABAQUS on the corresponding structure. Moreover, the scatter error is plotted for the mid-surfaces of the structures for different sides to show the ranges of the error in an interactive format. Because the number of elements for each side of the structures is too much, the scatter error cannot be shown for all the elements and was only demonstrated for the mid-surfaces of each side of the structures. Alternatively, the histogram analysis was performed on the scatter errors for all the elements of the structures and the results are illustrated to assess the capability of the proposed novel integrated ANN-FE.

In the following, the result of the adaptive mesh-based technique on an L-shape wall is presented followed by the results of the proposed novel approach. The computational times are listed in a table along with specific characteristics of the obtained results. The accuracy of the predicted results is discussed using the error plots and also making a direct comparison of the residual stress distribution for all the structures. A comprehensive discussion is presented at the end of this chapter to assess the performance of the proposed method in capturing the residual stress field with the improvement in the computational times for each structure.

For clarification, S11 is the stress in direction 1 (X-direction) and S22 is the stress in direction 2 (Y-direction or the stacking direction).

6.1. Results of the adaptive mesh-based technique

The computational time and the results of the adaptive-mesh-based model vs. fine mesh analysis for the 18-layers L-shape wall is shown in Table 9 and Figure 22, respectively. An 18-layer L-shape part made from AISI 304 L was built using both the conventional and adaptive mesh-based models in order to assess the capability and accuracy of the proposed approach. Both models were generated with the same thermal and mechanical features and also the same process parameters. Each L-shape layer with a length of equally 15 (mm) and a thickness and width of 1 (mm) was built using laser power of 250 (W), beam radius of 0.5 (mm), and traverse speed of 15 (mm/s). All the layers were built considering a cooling time approximately equal to the deposition time of each layer. The adaptive meshing is used in four steps to coarsen the fine mesh (five elements in thickness) to the coarse mesh (three elements in thickness) of each layer. Eight-node linear heat transfer and structural brick element were used for thermal and structural analysis, respectively. The bottom layer is fixed to act as a substrate for the model.

Figure 22 represents S11 (or σ_{xx}) and S22 (or σ_{yy}) contours of the stress distribution for the adaptive mesh and fine meshes. The adaptive meshing on areas with consistent stress distribution demonstrates reasonable performance shown in Figure 22. The stress pattern remains almost the same for those areas, and the stress values are also found to be very close to the fine mesh ones. On the other hand, very local stresses with high stress gradients are not mapped appropriately since the new coarse mesh is incapable of capturing very localized stress gradients. The S11 is almost near zero (−58 to 58 MPa) for both approaches in the middle of the wall. However, stress distribution in the stacking direction (S22) illustrates high compressive values which could be important in the fatigue performance of the DMD-processed parts.

Table 9 Comparison of computational time between the fine mesh and adaptive mesh

Adaptive mesh	Layers No.	1-3	4-6	7-9	10-12	13-15	16-18	Total (hour)
	Run time (hour)	1:50	2:35	3:20	3:50	4:15	4:20	20:10 + 2:00 (mapping time)
Fine mesh	Layers No.	1-18						
	Run time (hour)	58:30						58:30

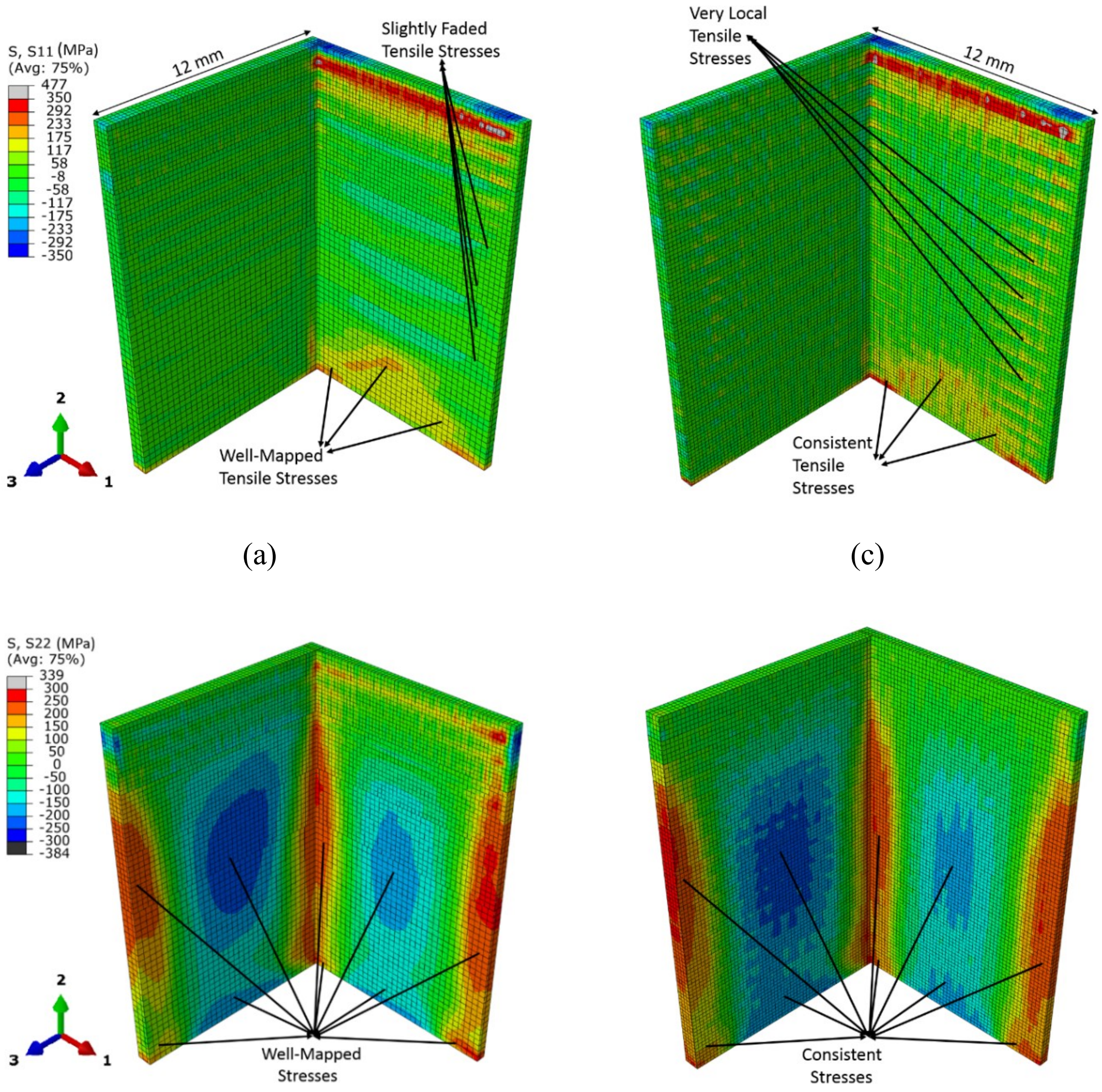

(a) (c)

(b) (d)

Figure 22 Adaptive-mesh based finite element model distribution of stress in (a) longitudinal direction (S11) (b) stacking direction (S22) and FE results of fine mesh in (c) longitudinal direction (S11) (d) stacking direction (S22)

6.2. Results of integrating machine learning with finite element analysis of direct metal deposition parts

The novel approach of integrating ANN and FE-based analysis is developed and tested on the sample parts shown in Figure 16. In order to show the capability of the proposed novel method in the prediction of residual stress distribution, the error scatter calculated using Eq. (20) and presented for each structure. Furthermore, the histogram diagram indicating the percentage of elements having different ranges of error is provided to exhibit the performance of the proposed novel approach. For clarification, S11 is the stress in direction 1 (X-direction) and S22 is the stress in the direction 2 (Y-direction or the stacking direction). As it is not practically possible to show the prediction error of different stress components for all the elements of the part, only the mid-surface of the FE models was used to demonstrate the error scatter and histogram analysis. The results of different structures are listed according to Figure 16.

Similar to the results shown for the adaptive mesh-based technique, all the predicted results from the novel ANN-FE approach are depicted in contour formats to make it clear to interpret the results and compare them with the results of the detailed FE analysis. Except for the adaptive mesh-based technique that a Core i7 desktop PC with 16 GB RAM was used to perform the analysis, the High-Performance Computing (HPC) cluster-based computer named "SPEED" was used for all the structures to perform the FE analysis as well as the training the ANN. The machine includes 24 nodes, each with 32 cores with 512 GB of RAM to perform the calculations. The machine is based on Linux 7 and it requires no extra software to be able to link the ABAQUS with the Fortran compiler. In a normal Windows-based computer, "Visual Studio" should be installed to be able to run a subroutine-based analysis in ABAQUS and it may increase the computational time.

6.2.1. 18-layers wall

Figure 23 shows the S11 distribution of the 18-layers wall part. Figure 23(a), (b), and (c) represent the result of the detailed FE analysis, the prediction obtained from the ANN, and the error evaluation of S11 distribution over the 18-layers wall, respectively. Figure 23 (d) and (e) show the error scatter in 2D and 3D spaces and Figure 23 (f) indicates the histogram analysis of error in the mid-surface of the 18-layers wall. By comparing Figure 23 (a) and (b), it is evident that the distribution pattern of S11 across the whole medium is consistent in both cases. The positive residual stress zone at the bottom of the wall where it is connected to the substrate is captured accurately in the novel integrated ANN-FE approach. In the upper layers, the negative S11 values predicted using ANN-FE are also in good agreement with the FE results. It is important to note that at the critical locations where S11 has its highest magnitude (top layer), the predicted results are very close to the FE results and the error percentage is less than 2% for that region. A limited number of elements with higher error values indicated by the red zone in Figure 23 (c) correspond to the relatively low-stress zone (S11<120 MPa) and it can be considered negligible. The error scatter of S11 shown in Figure 23 (d and e) represents a very limited number of elements that have higher error values than 15%. This can be clarified by histogram analysis for the error represented in Figure 23 (f). Approximately 12% of the elements show a prediction error higher than 15% and the majority of elements in the higher stress zones show lower error percentages.

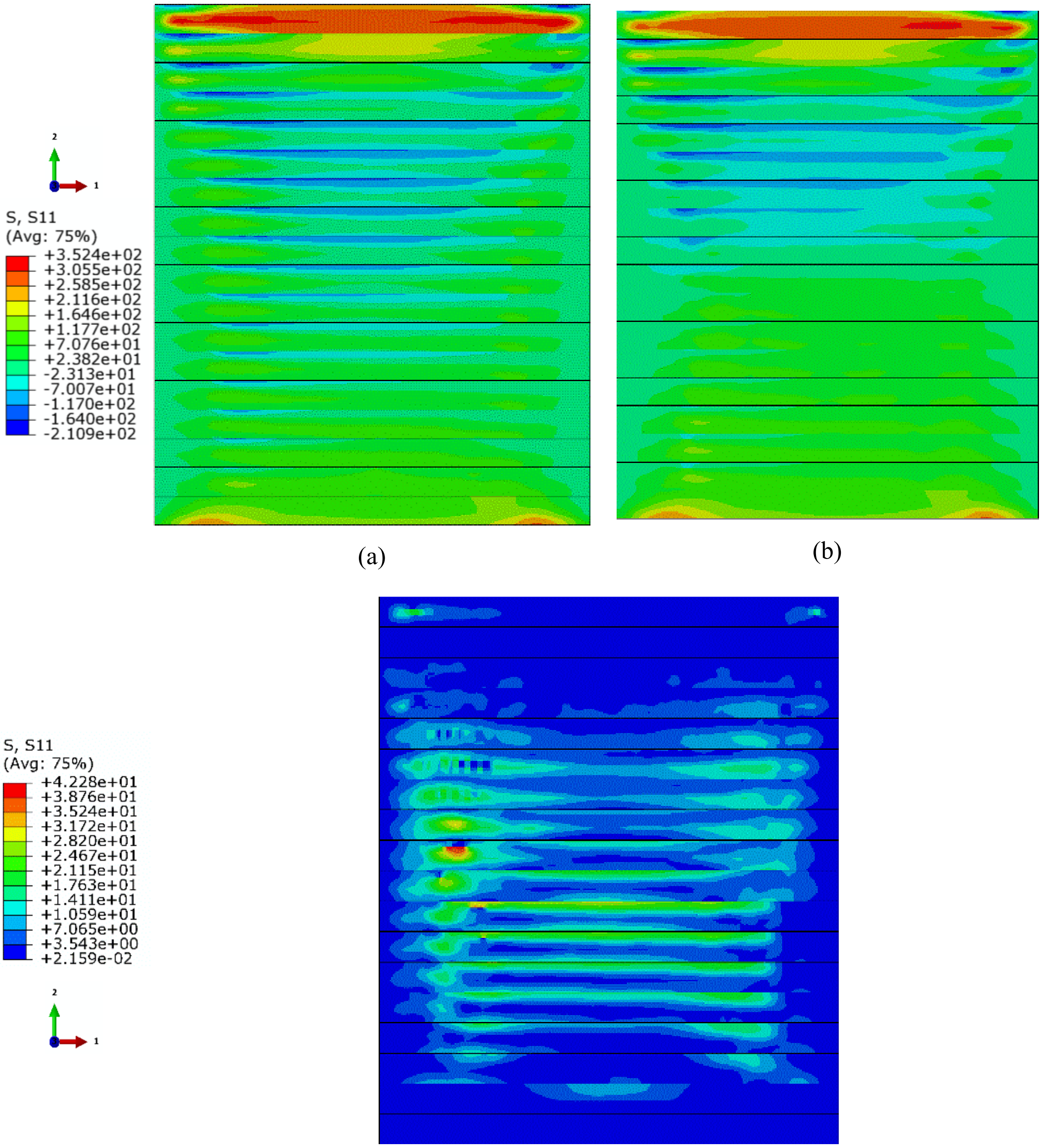
2
1
S, S11
(Avg: 75%)
+3.524e+02
+3.055e+02
+2.585e+02
+2.116e+02
+1.646e+02
+1.177e+02
+7.076e+01
+2.382e+01
-2.313e+01
-7.007e+01
-1.170e+02
-1.640e+02
-2.109e+02
S, S11
(Avg: 75%)
+4.228e+01
+3.876e+01
+3.524e+01
+3.172e+01
+2.820e+01
+2.467e+01
+2.115e+01
+1.763e+01
+1.411e+01
+1.059e+01
+7.065e+00
+3.543e+00
+2.159e-02
2
1

(a) (b)

(c)

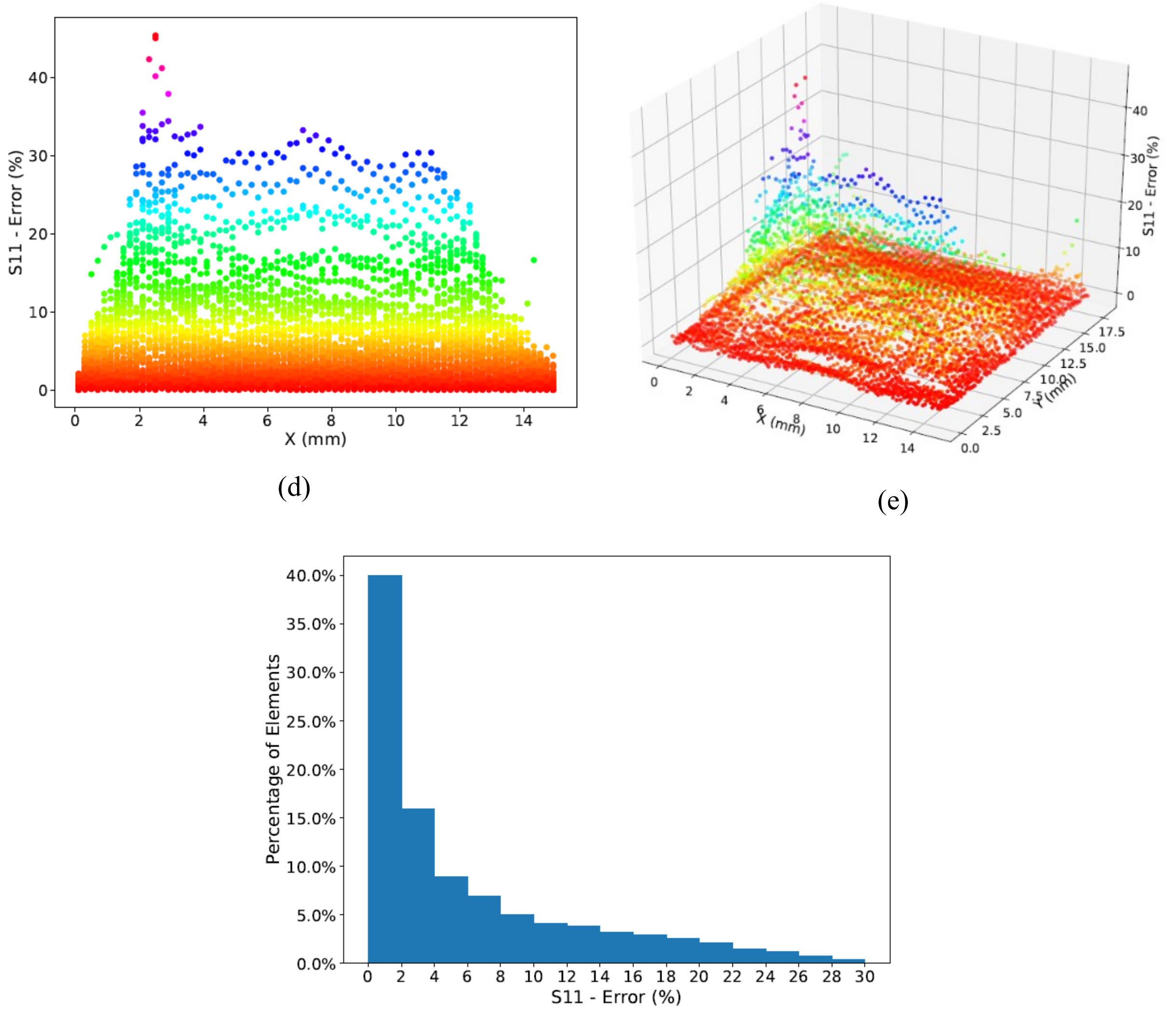

(d)

(e)

(f)

Figure 23 S11 distribution of 18-layers wall (in MPa) (a) finite element analysis (b) integrated ANN-FE (c) error value (%) (d) 2D error scatter (e) 3D error scatter (f) histogram of the error

Figure 24 shows the results of S22 (stress component in the stacking direction or along axis 2) distribution over the mid-surface of the 18-layers wall. Figure 24 (a) and (b) show the results of FE and integrated ANN-FE method, respectively. By comparing the results from the detailed FE analysis and the prediction, it is noted that the overall distribution of S22 is consistent in both stress contours. The tensile residual stresses are captured accurately in both ends of the part by implementing the integrated ANN-FE method. And, high compressive stress zone is also anticipated meticulously in the middle of the part by using the integrated ANN-FE approach. A very smooth transition from tensile to compressive residual stresses is observed in the predicted results. Top layers of the part show very small residual stresses (approximately -50 to 50 MPa) that is consistent with the FE results. The error contour is also demonstrated in Figure 24 (c) for the mid-surface of the 18-layers part. The blue color on the error contour shows the area with an error of less than 2%. It is evident that the prediction error is low for the majority of the elements in the mid-surface. The middle area of the part with green color shows an error of approximately less than 12%. Only a limited number of elements show an error higher than 10% which is very rare. For a better representation of the error, the error scatter is calculated and presented in Figure 24 (d) and (e) in 2D and 3D, respectively. A large portion of the elements is associated with the red and yellow colors in the scatter diagrams which correspond to an error value of less than 5%. Less than approximately 9% of the elements exhibit a prediction error higher than 10% as shown by the histogram analysis of the error depicted in Figure 24 (f).

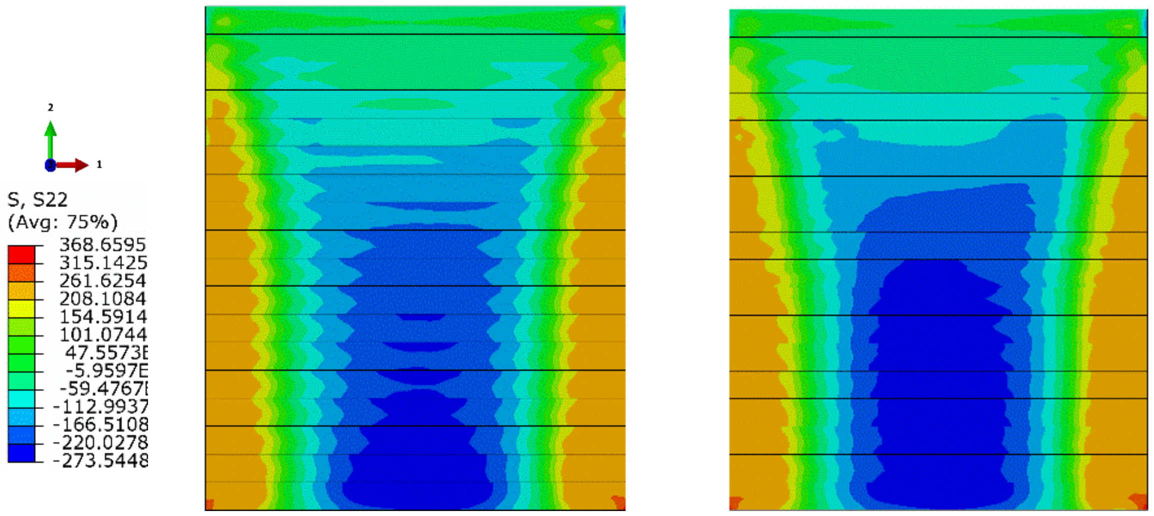

(a) (b)

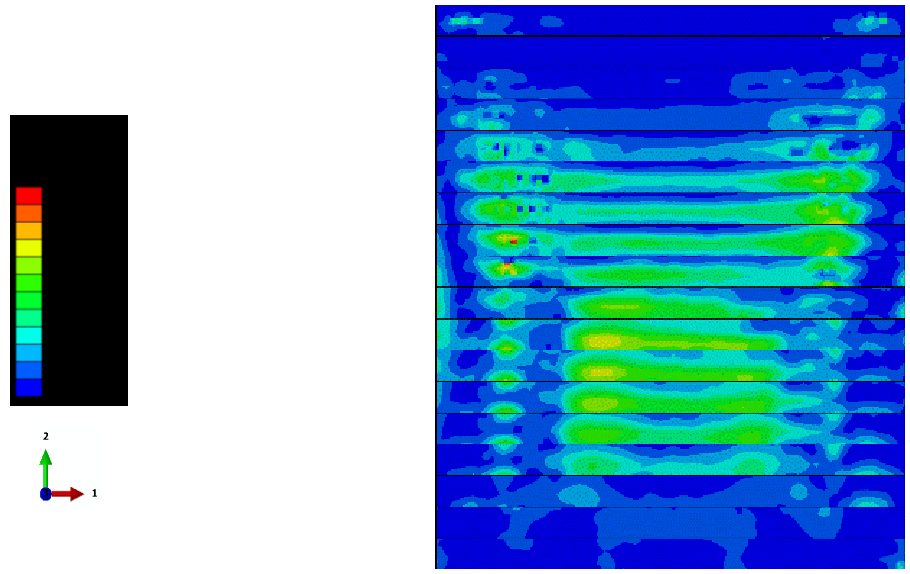

(c)

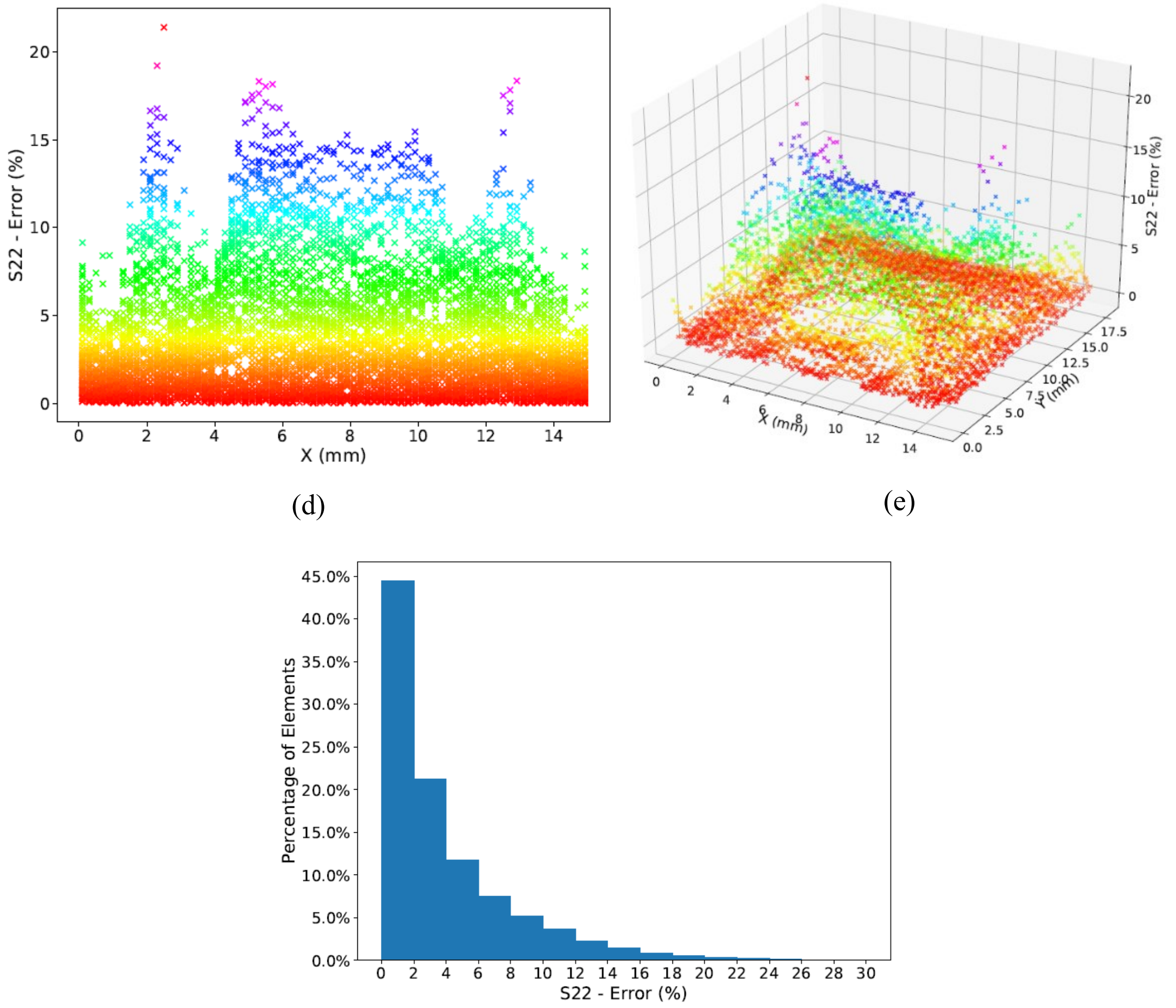

(d)

(e)

(f)

Figure 24 S22 distribution of 18-layers wall (in MPa) (a) finite element analysis (b) integrated ANN-FE (c) error value (%) (d) 2D error scatter (e) 3D error scatter (f) histogram of the error

6.2.2. 18-layers L-wall

Figure 25 shows the S11 distribution for the 18 layers L-wall. Figure 25 (a) and (b) demonstrate the distribution of S11 obtained from the FE analysis and integrated ANN-FE method for the whole medium, respectively. The mid-surface of the right-hand side of the L-wall is cut to show prediction errors in mid-plane of the body. On the other hand, the left-hand side is kept thoroughly to show the stress distribution on the free surface of the medium. By comparing these two contours, it is noticed that the prediction made by the integrated ANN-FE method is consistent with the results from the FE analysis. The highest tensile residual stresses are captured well in the integrated ANN-FE model; the top layer presents very high tensile residual stresses that are smooth in the middle part of the layer. Moreover, the high tensile residual stresses are predicted at the intersection and right end of the L-wall which is consistent with the FE results for S11. Also, the residual stresses are faded at the right end of the medium and at the intersection of the L-wall which is predicted accurately in the integrated ANN-FE model. Figure 25 (c) shows the error evaluation of the L-wall in the form of a contour. As it is shown, only a few elements show the highest error which can be neglected. All the regions with blue color represent the area with an error of less than 5%. To further quantify the prediction errors, the error scatter of the elements for the mid-surface of the right-hand side of the L-wall is calculated and shown in Figure 25 (d) and (e) in 2D and in 3D space, respectively. All the red and yellow points on an error scatter diagrams correspond to the error of less than 10%. Furthermore, the histogram analysis is also performed to analyze the percentage of the elements based on the error ranges. Approximately only 6% of the elements show errors higher than 15%. According to Figure 25 (c), the middle plane of the right-hand side of the L-wall that is demonstrated by light green and light blue colors corresponds to the S11 ranges of -50 to 50 MPa that is counted as the low-stress state and can be considered negligible.

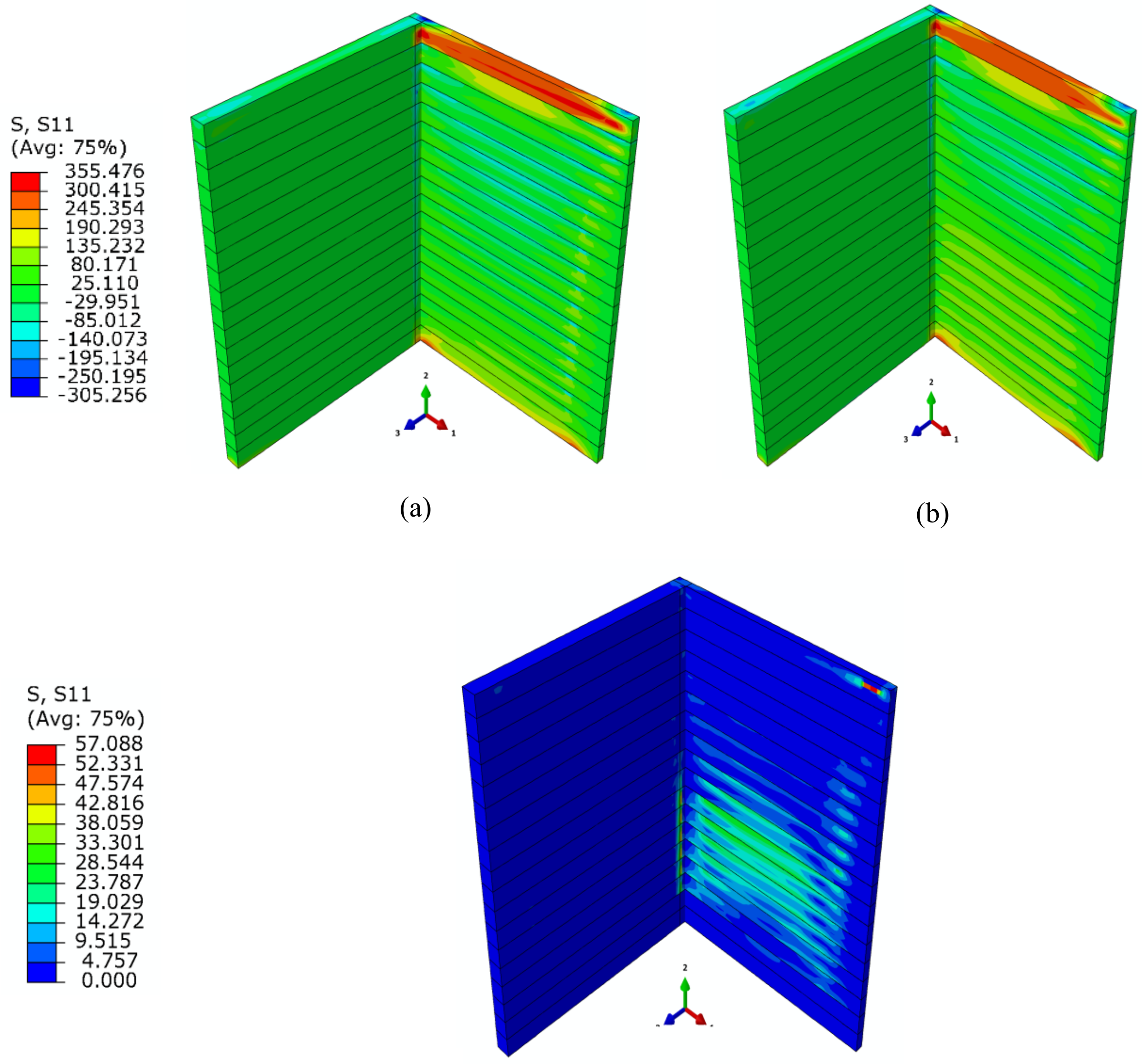

(a)

(b)

(c)

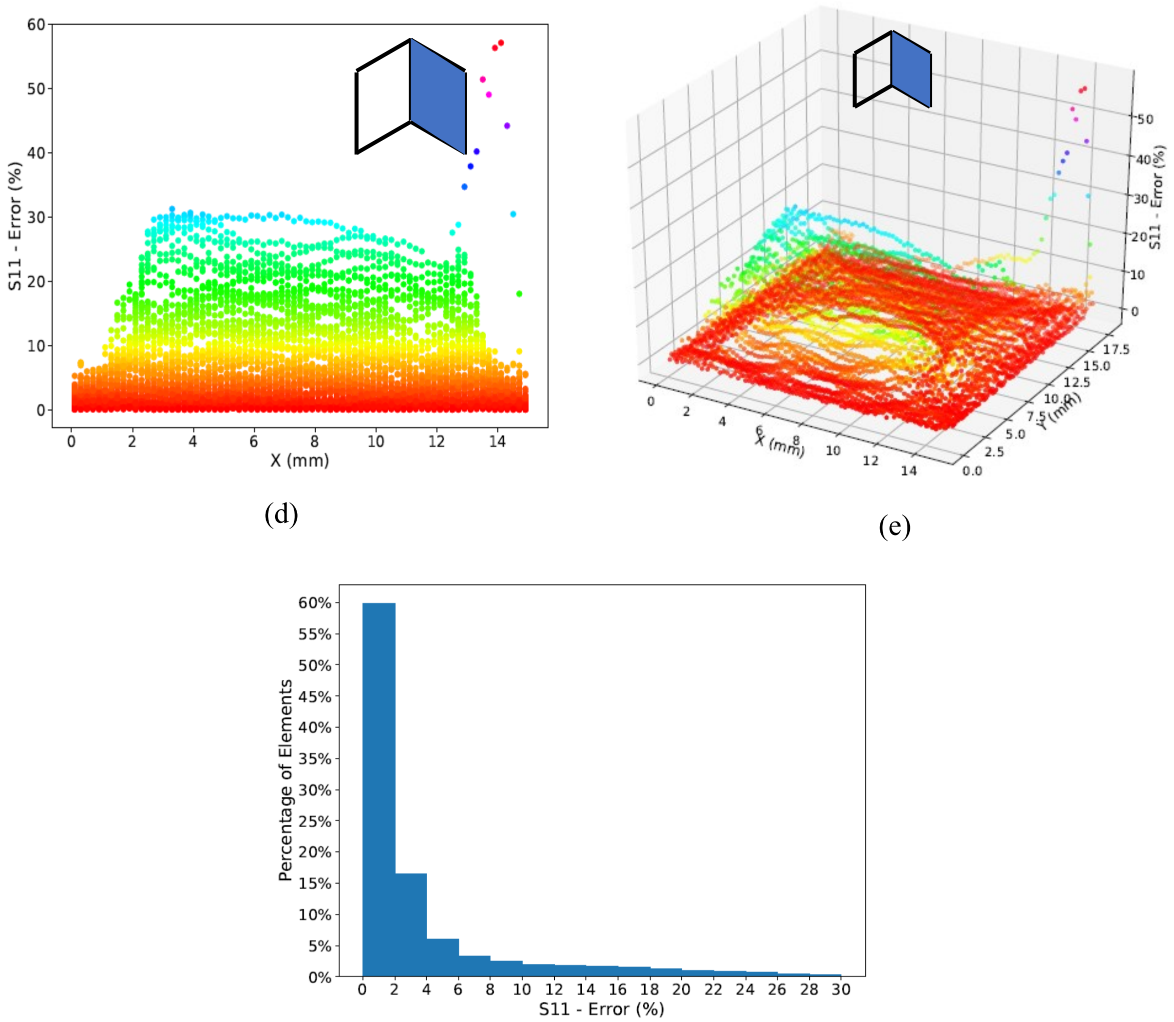

(d)

(e)

(f)

Figure 25 S11 distribution of 18-layers L-wall (in MPa) (a) finite element analysis (b) integrated ANN-FE (c) error value (%) (d) 2D error scatter of the right side (e) 3D error scatter of the right side (f) histogram of the error

Figure 26 shows the results for the prediction of S22 (stress component in the stacking direction or direction 2) of the mid-surface plane of the right-hand side and the free-surface of the left-hand side of the 18-layers L-wall structure. Figure 26 (a) and (b) show the S22 distribution in the form of contour obtained from the FE analysis and integrated ANN-FE method, respectively. By comparing the two contours, it is evident that the stress distribution pattern is consistent in both contours; both ends and the intersection of the L-wall depict the high tensile residual stresses and the middle part of the sides represents the highest compressive residual stresses. There is a very smooth transition zone in which the tensile residual stresses are changed into compressive residual stresses. The error evaluation of the predicted results by employing the integrated ANN-FE was performed and the results are shown in contour form in Figure 26 (c). As it can be seen from the contour, at the right-hand side of the structure showing the S11 error distribution in the mid-surface, the maximum error is approximately 10% shown by the light green color. On the other hand, the left-hand side of the part that represents the free surface of the structure, a limited number of elements show error values of approximately 24%. To better present the capability of the novel integrated ANN-FE method, the error scatter evaluated for the right-hand side of the structure in 2D and 3D in Figure 26 (d) and (e), respectively. All the red, yellow, and green colors in the scatter diagrams show an error value of less than 10%. It expresses that the very high fraction of elements has a prediction error of less than 10% that is considered to be acceptable accuracy. Histogram analysis demonstrates the percentage of the elements with a certain error range for the right-hand side of the L-wall structure. It can be seen that approximately 2.5% of the elements exhibit error values greater than 10% by using the novel integrated ANN-FE approach.

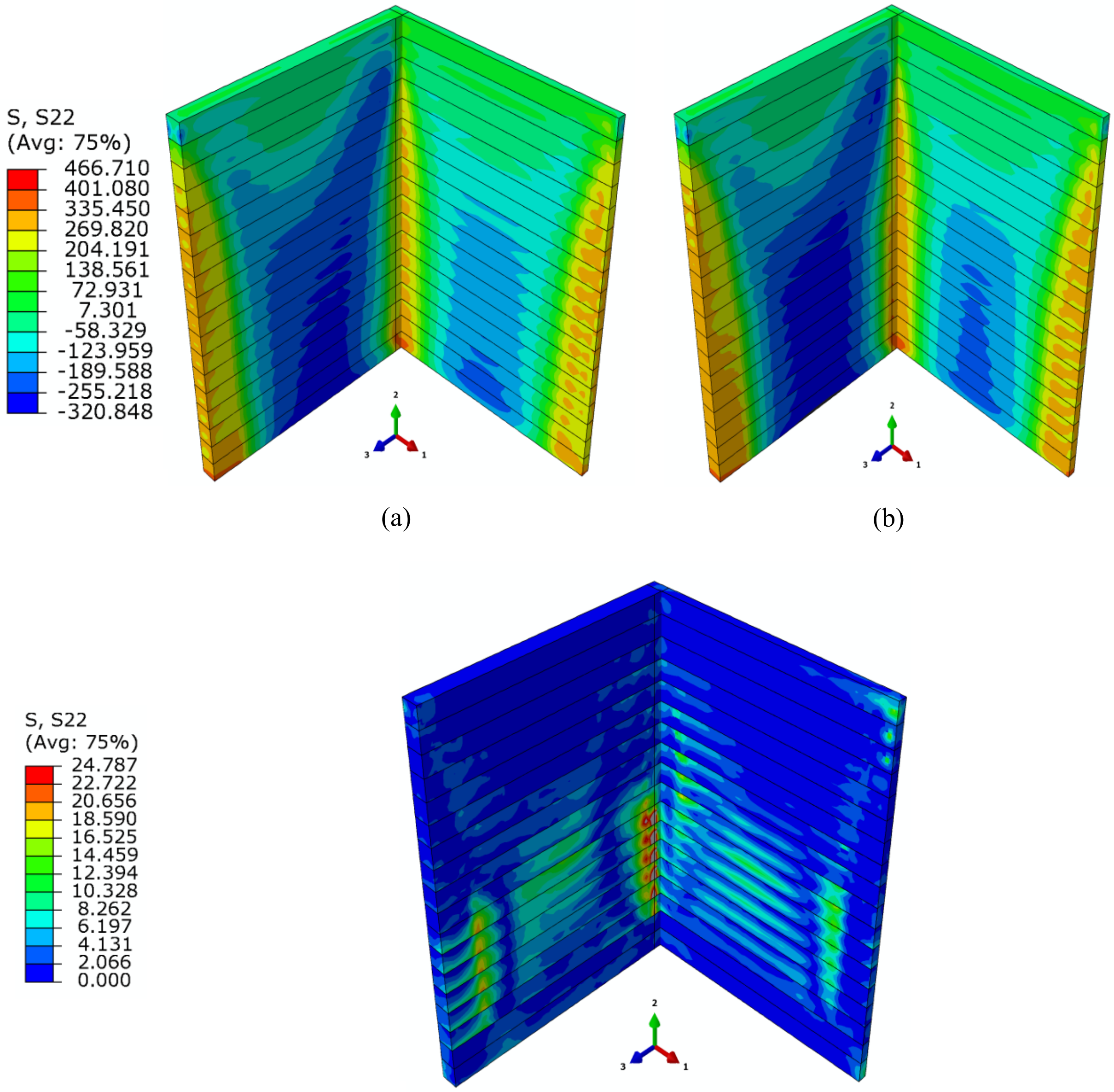

(a)

(b)

(c)

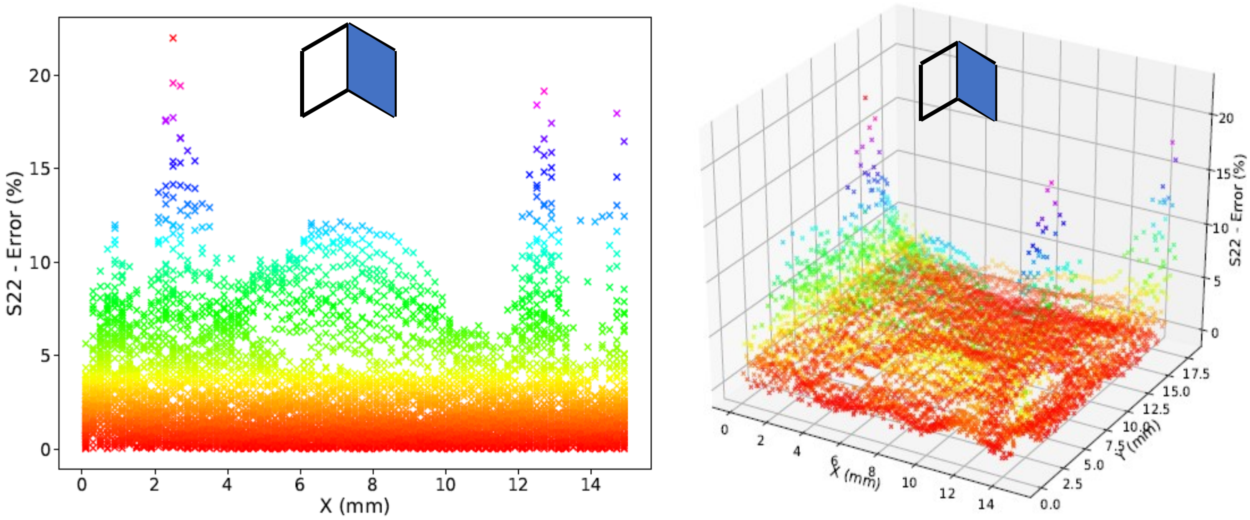

(d) (e)

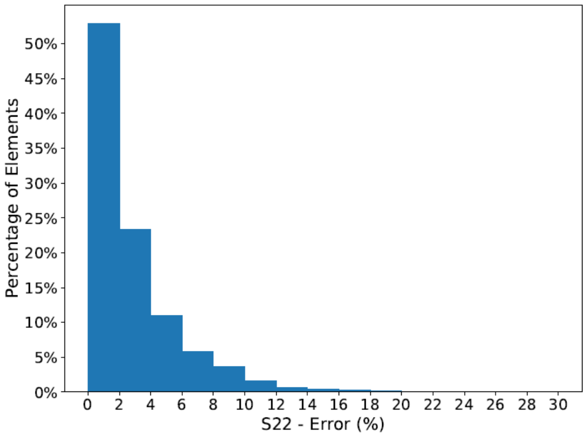

(f)

Figure 26 S22 distribution of 18-layers L-wall (in MPa) (a) finite element analysis (b) ANN prediction (c) error value (%) (d) 2D error scatter (e) 3D error scatter (f) histogram of the error

6.2.3. 18-layers rectangular box

Figure 27 shows the stress results obtained from the FE analysis and the novel integrated ANN-FE method for the 18-layers rectangular box. Figure 27 (a) and (b) demonstrate the S11 (stress component in direction 1) obtained from the detailed finite element analysis and integrated ANN-FE approach, respectively. As it is depicted, the overall residual stress distribution and its pattern are consistent in both contours especially in the top layer and the bottom of the box where the positive residual stresses are high. By evaluating the prediction error from the ANN-FE method, it can be concluded that a significant number of elements show error values of less than 3.5% which is shown by the blue colors in Figure 27 (c). The high error values, approximately 42%, correspond to the limited number of elements located on the top surface of the 18th layer shown in Figure 27 (c). Areas with the light green color also represent the error values of approximately 20%, however, considering the S11 values in those areas (-6 to 117 MPa), the error is not counted as a significant drawback of employing the integrated ANN-FE. Furthermore, the error scatter is evaluated for the outer surface of the shown side in Figure 27 (d) and (e) in 2D and 3D, respectively. The error scatter shows that the high volume of elements illustrate error value of lower than 15% considering the complexity of the box structure. By assessing the histogram analysis for the elements, it is seen that approximately 5% of the elements on the surface of the shown side have error values higher than 15%. Therefore, the light green area in Figure 27 (c) is not a considerable portion of the elements and the employed integrated ANN-FE method shows a high capability of predicting the residual stresses in the rectangular box.

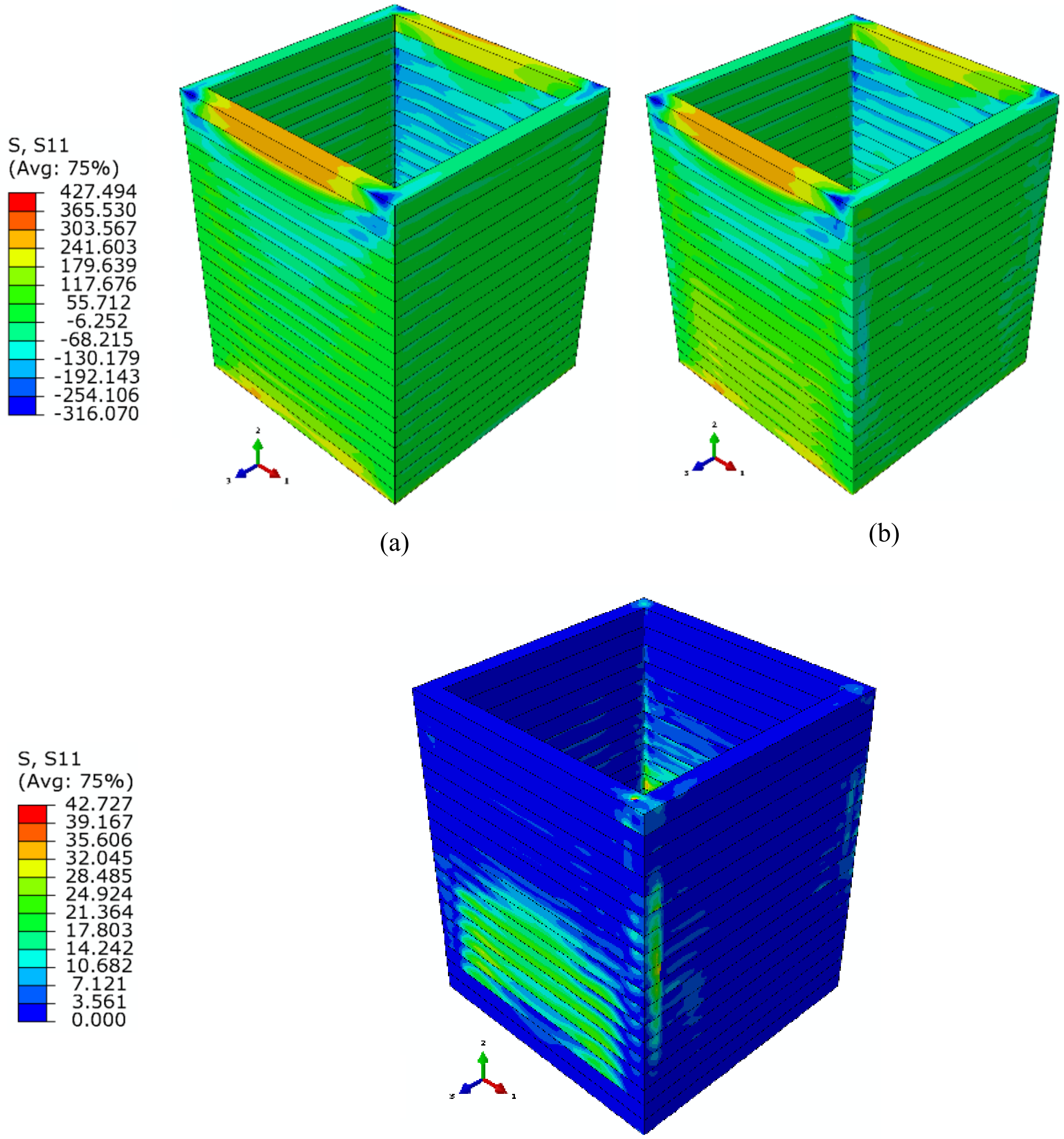

(a)

(b)

(c)

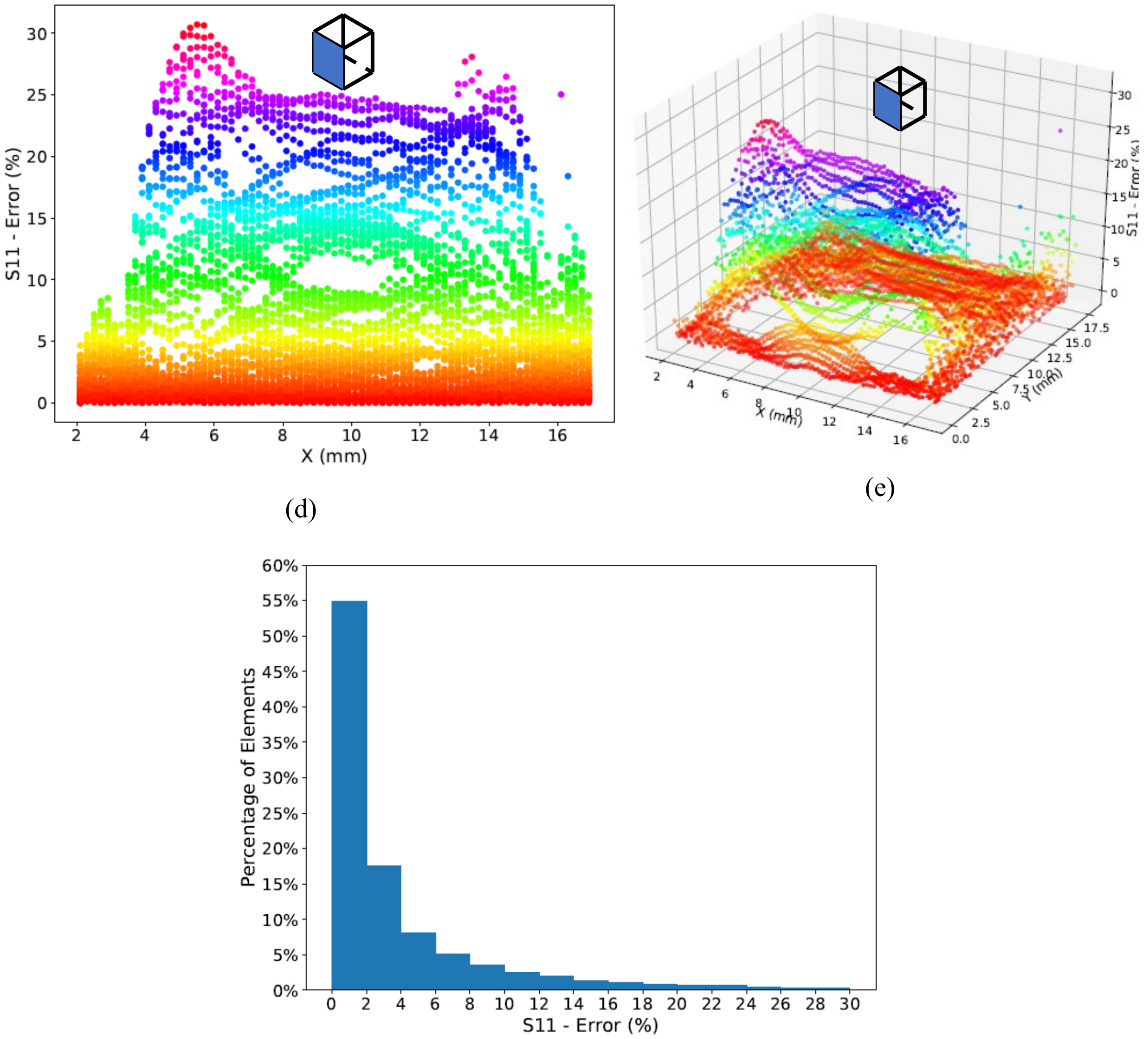

(d)

(e)

(f)

Figure 27 S11 distribution of 18-layers rectangular box (in MPa) (a) finite element analysis (b) ANN prediction (c) error value (%) (d) 2D error scatter (e) 3D error scatter (f) histogram of the error

Figure 28 shows the S22 distribution (stress component in the stacking direction or direction 2) for the rectangular box structure. Figure 28 (a) and (b) show the S22 obtained from FE analysis and the novel integrated ANN-FE approach, respectively. The distribution pattern in both cases is consistent and the high tensile and compressive residual stresses are captured well in the ANN-FE approach. The S22 distribution over the whole medium is smooth. The corners show tensile residual stresses followed by a smooth transition to compressive residual stresses in the middle of the part. Higher compressive stresses are observed in the inner side of the box and the prediction made from the integrated ANN-FE approach is in good agreement with the results of the detailed FE analysis. The error evaluation in the form of contour also provided for assessing the accuracy of the employed integrated ANN-FE approach and shown in Figure 28 (c). The majority of the elements demonstrate low error values and are depicted with blue color (error <3.7%). The high error of 44% is regarded as one or two elements on the inner side and can be neglected in the accuracy assessment of the proposed novel approach. However, the area near the corners of the box represents higher errors than other zones. But, by comparing the scatter analysis of the error represented in Figure 28 (d) and (e), it is evident that the number of elements with an error greater than 15% is limited. Histogram analysis of S22 error is shown in Figure 28 (f). Only 8% of the elements show a prediction error higher than 15%. As mentioned before, a high fraction of elements has a low prediction error as it is supported by the histogram analysis.

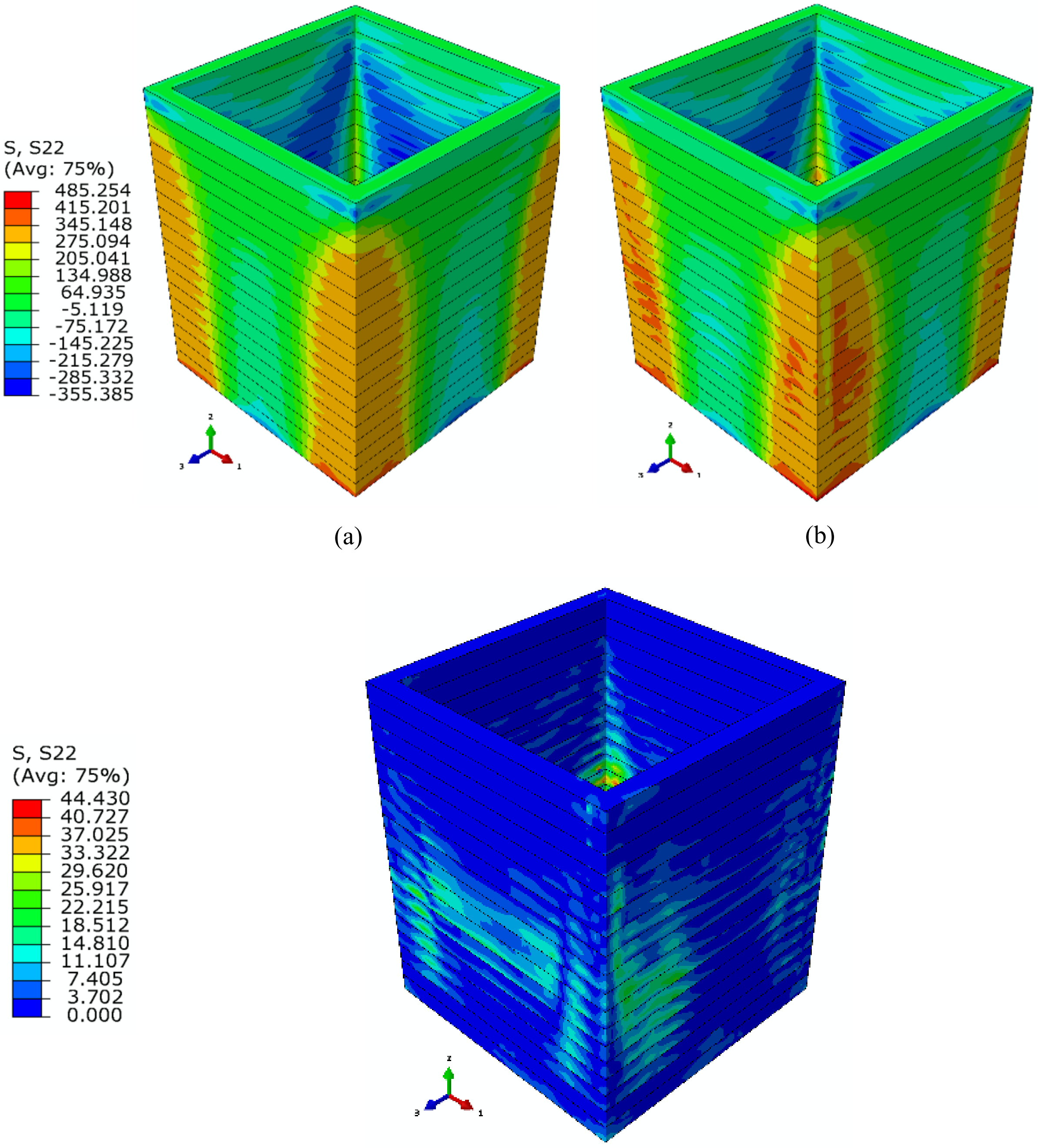

(a) (b)

(c)

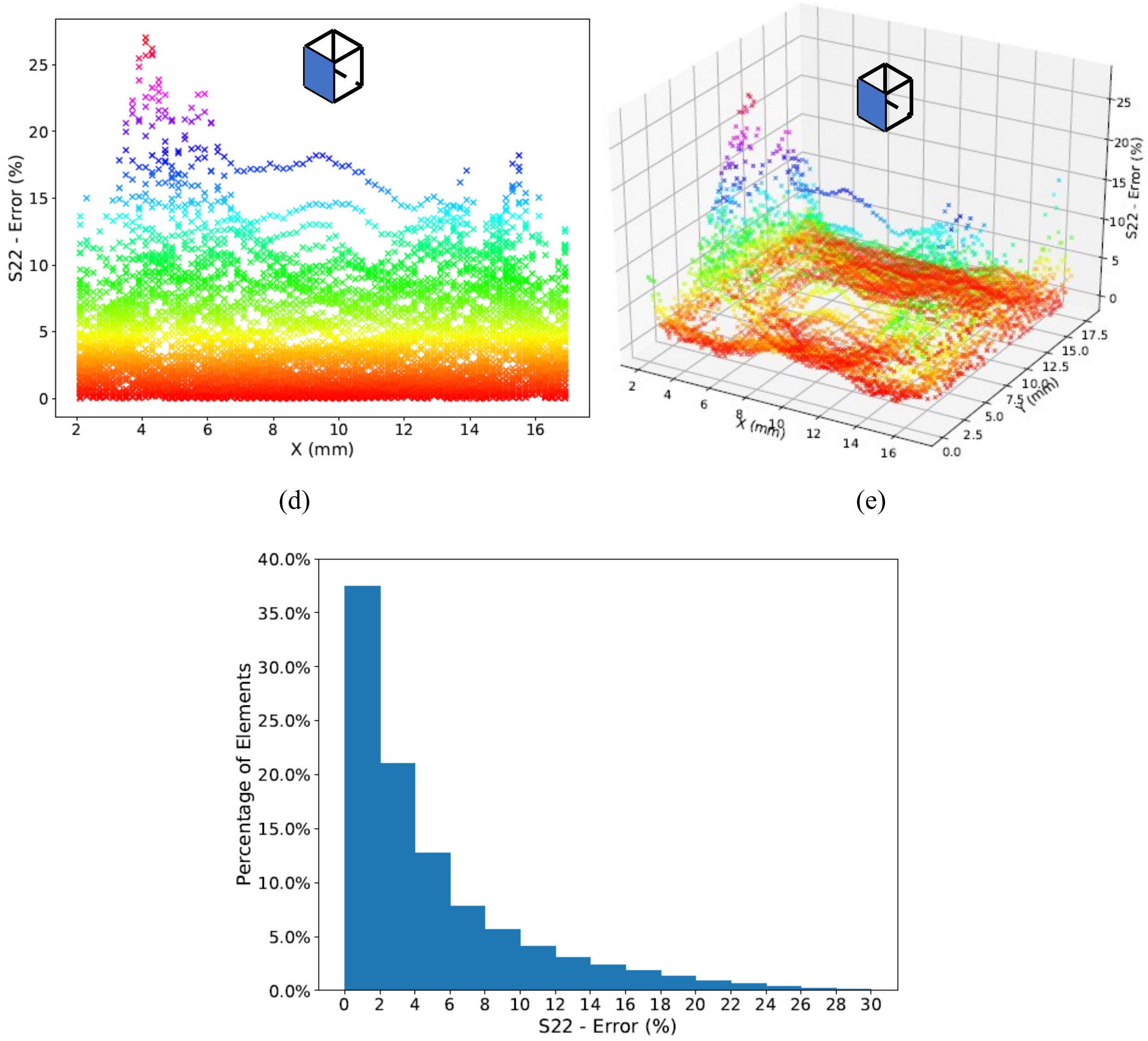

(d) (e)

(f)

Figure 28 S22 distribution of 18-layers rectangular box (in MPa) (a) finite element analysis (b) ANN prediction (c) error value (%) (d) 2D error scatter (e) 3D error scatter (f) histogram of the error

6.2.4. 18-layers T-shape

Figure 29 shows the S11 distribution for the 18 layers T-shape wall. Figure 29 (a) and (b) show the distribution of S11 calculated from the FE analysis and novel integrated ANN-FE method for the structure, respectively. By comparing these two contours, it is noted that the prediction made by the integrated ANN-FE method is consistent with the results from the detailed FE analysis. The highest tensile residual stresses are captured well in the integrated ANN-FE model; the top layer presents very high tensile residual stresses at the intersection of the two sides and the transition from the high residual tensile stresses to compressive stresses are smooth in the middle part of the layer of the backside (X-Y plane). Moreover, the high compressive residual stresses are predicted at the sides of the back side on the top layers followed by a smooth transition in the opposite stacking direction into the tensile residual stresses on the sides of the first layer where the structure is separated from the substrate. Figure 29 (c) shows the error evaluation of the T-shape wall in the form of a contour. As it was pointed out earlier for other structures, the error was calculated based on Eq. (20) and the results were depicted in the contour format as the output results of ABAQUS. As it is shown, only a few elements show the highest error which can be neglected and most of the elements are shown in blue color which represents an error of about 5%. However, the middle part of the back side; from the 3d layer up to 10th layer, demonstrates an error of about 20%. However, according to Figure 29 (a), the high error area is associated with the elements whose stress state is not critical (green color) and the S11 component varies between -50 to 50 MPa, approximately. To have a better representation of elements with high error values shown in green color, the mid-plane of the back side is cut and the scatter error of S11 component is extracted and shown in Figure 29 (d) and (e) in 2D and 3D, respectively. Elements with the blue and purple colors shown in the scatter diagram have an error of higher than 15% in the mid-plane of the back side, which is limited. The majority of the elements with red and yellow colors demonstrate an error of less than 5%.

Furthermore, the histogram analysis is also performed to correlate the percentage of the elements with their error ranges and shown in Figure 29 (f). Approximately only 7% of the elements show errors higher than 15%. This represents the capability of the novel proposed integrated ANN-FE framework.

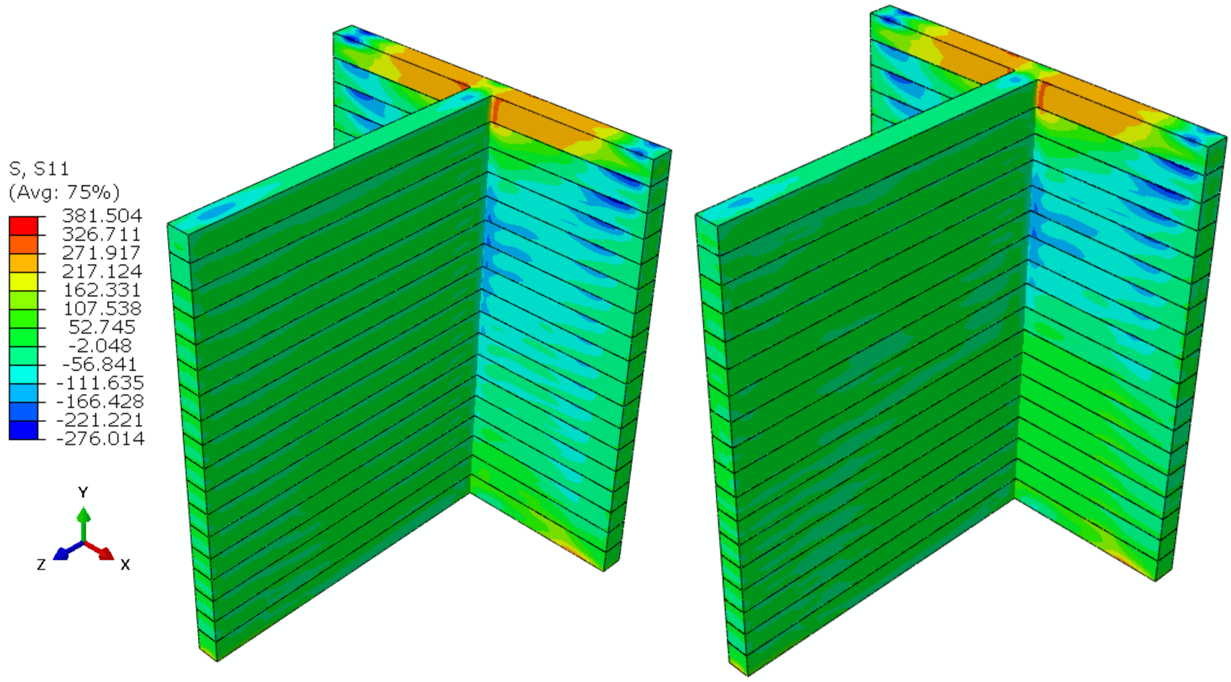

(a)

(b)

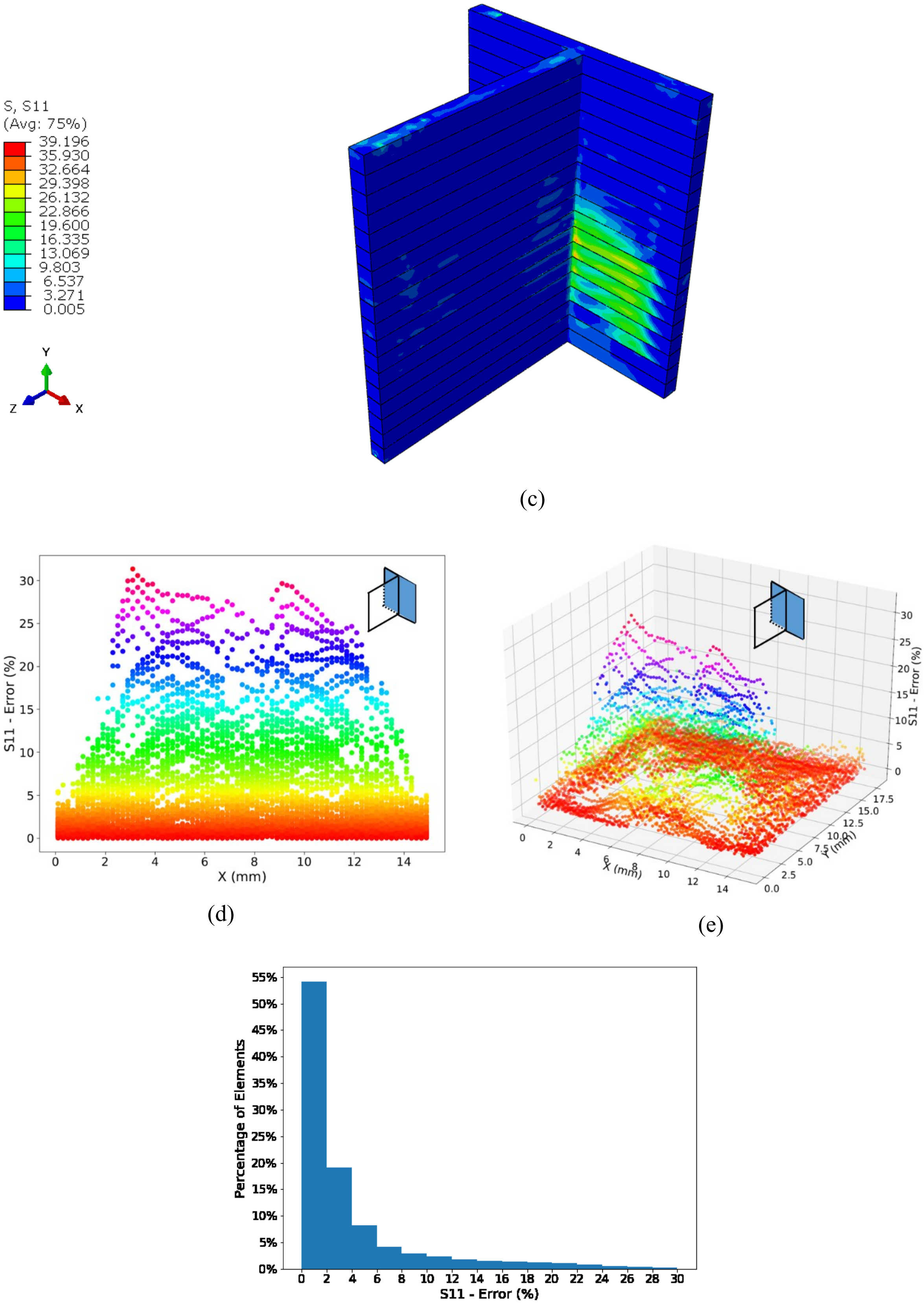

(c)

(d)

(e)

(f)

Figure 29 S11 distribution of 18-layers T-shape wall (in MPa) (a) finite element analysis (b) ANN prediction (c) error value (%) (d) 2D error scatter (X-Y plane) (e) 3D error scatter (X-Y plane) (f) histogram of the error

Figure 30 shows the results for the prediction of S22 (stress component in the stacking direction or direction 2) of the 18-layers T-shape wall structure. Figure 30 (a) and (b) illustrate the S22 distribution in the form of contour evaluated from the FE analysis and integrated ANN-FE method, respectively. According to Figure 30 (a) and (b), the stress distribution pattern is consistent in both contours; all three ends of the structure demonstrate the tensile residual stress in the stacking direction that is smoothened into the lower tensile residual stresses in the middle parts of both sides and then, the high compressive residual stress state is dominant in the central part of the workpiece. The intersection of the two sides demonstrates a relatively low-stress state (-60 to 60 MPa). Furthermore, the high amplitude residual stresses are faded in the stacking direction and turn into the low-stress state on the top layers smoothly. The prediction error is calculated and shown in Figure 30 (c) in the contour format for the whole structure. The majority of the elements with blue colors represent a prediction error of less than 4% and only a very localized areas shown in red and yellow colors demonstrates an error higher than 15%. To better show the capabilities of the proposed new method of integrated ANN-FE, the scatter error of the predictions is obtained according to Eq. (20) and demonstrated for the mid-plane of the back side (X-Y plane) of the structure as shown in Figure 30 (d) and (e). All the elements in the mid-plane show a prediction error value of less than 15%. A very limited number of elements in the mid-plane of the back side represent the error of over 10% that is shown with the dark blue and purple colors. Furthermore, the histogram analysis was utilized to show the percentages of the element with their associated error ranges for the whole structure and shown in Figure 30 (f). Approximately 2% of the elements in the whole structure show a prediction error of more than 15% according to the histogram analysis.

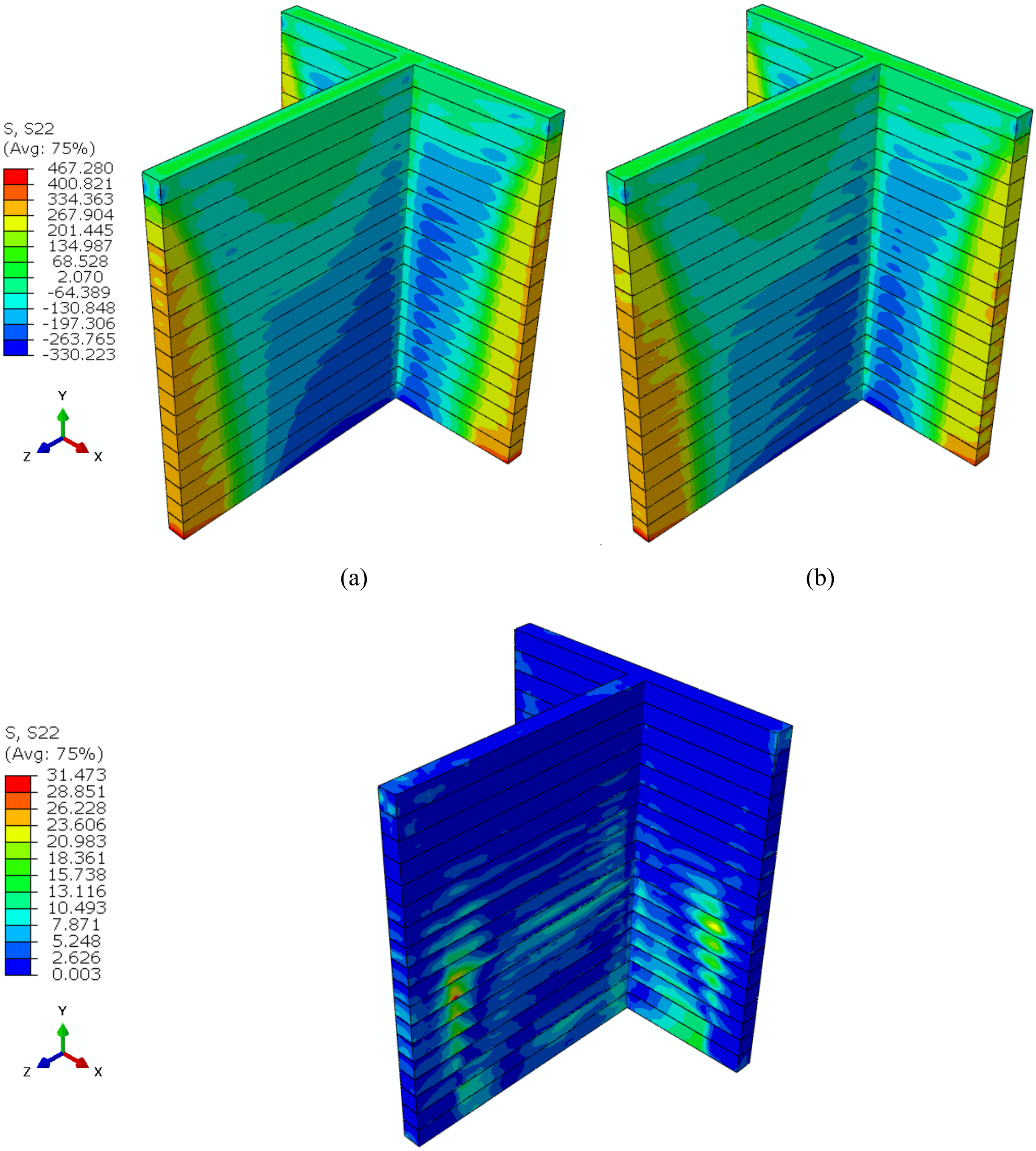
S, S22
(Avg: 75%)
467.280
400.821
334.363
267.904
201.445
134.987
68.528
2.070
-64.389
-130.848
-197.306
-263.765
-330.223
Y
Z
X
S, S22
(Avg: 75%)
31.473
28.851
26.228
23.606
20.983
18.361
15.738
13.116
10.493
7.871
5.248
2.626
0.003
Y
Z
X

(a)

(b)

(c)

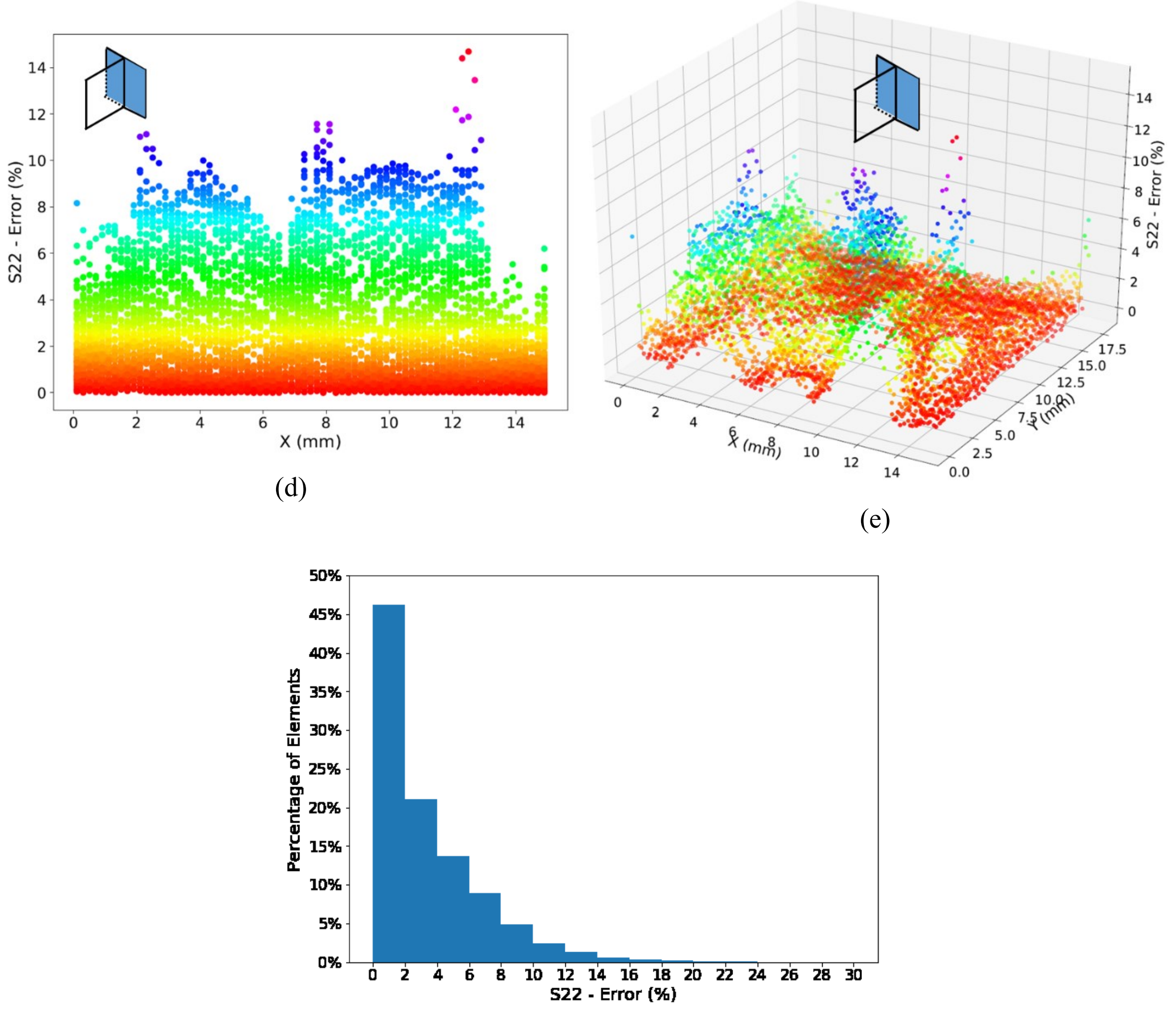

(d)

(e)

(f)

Figure 30 S22 distribution of 18-layers t-shape wall (in MPa) (a) finite element analysis (b) ANN prediction (c) error value (%) (d) 2D error scatter (X-Y plane) (e) 3D error scatter (X-Y plane) (f) histogram of the error

The results of the longitudinal stress in the Z direction (S33) are provided in the supplementary results along with the scatter error diagrams for the Y-Z plane.

6.2.5. 18-layers H-shape

Figure 31 shows the stress results obtained from the FE analysis and the novel integrated ANN-FE method for the 18-layers H-shape wall. Figure 31 (a) and (b) demonstrate the S11 (stress component in direction X) obtained from the detailed finite element analysis and integrated ANN-FE approach, respectively. As it is depicted, the distribution of the residual stress and its pattern are consistent in both contours in the top and bottom layers of the structure where the tensile residual stresses are high. Very local and high tensile residual stresses were captured substantially in the integrated ANN-FE method. Furthermore, the local compressive residual stresses were also predicted in the ANN-FE method in the outer elements of the back plane and at the ends of the top layer. However, there are high compressive residual stresses on the outer elements of the front plane. The predicted error of the whole structure is calculated using Eq. (20) and illustrated in the contour format in Figure 31 (c) to facilitate the comparison of the results of the FE analysis and ANN-FE results. By evaluating the prediction error from the ANN-FE method, it can be concluded that a significant number of elements show error values of less than 7% which is shown by blue colors in Figure 31 (c). The high error values, approximately 45%, correspond to the limited number of elements located on the front plane of the structure and on the middle layers. It should be noted that most of these elements are located on the outer surface or on the free surface of the structure. Areas with the light green color also represent the error values of above 20%, however, considering the S11 values in those areas (-45 to 95 MPa), the error is not counted as a significant drawback. Furthermore, the error scatter is evaluated for the outer surface of the shown side in Figure 31 (d) and (e) in 2D and 3D, respectively. The error scatter shows that a large number of elements demonstrate an error of lower than 15% considering the complexity of the H-shape structure. By assessing the histogram analysis for the H-shape wall, it is seen that approximately 17% of the elements have error values higher than 15%. Therefore, the light green area in Figure 31 (c) is not a considerable portion of the elements and the employed integrated ANN-FE method shows a high capability of predicting the residual stresses in the rectangular box.

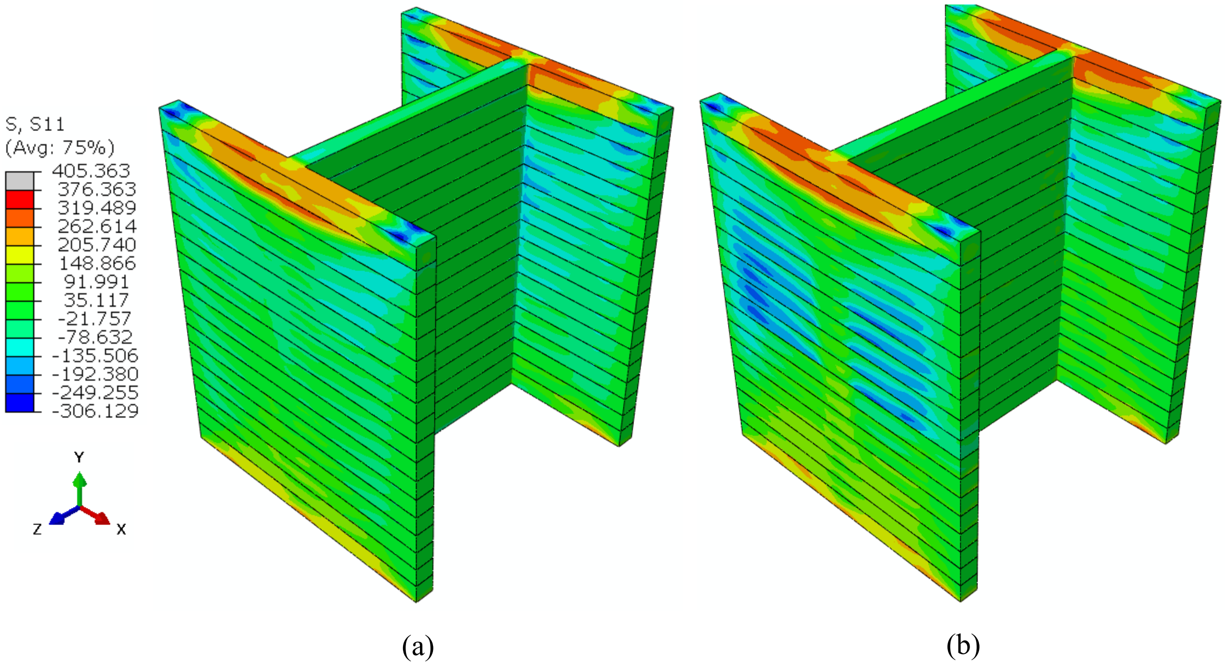

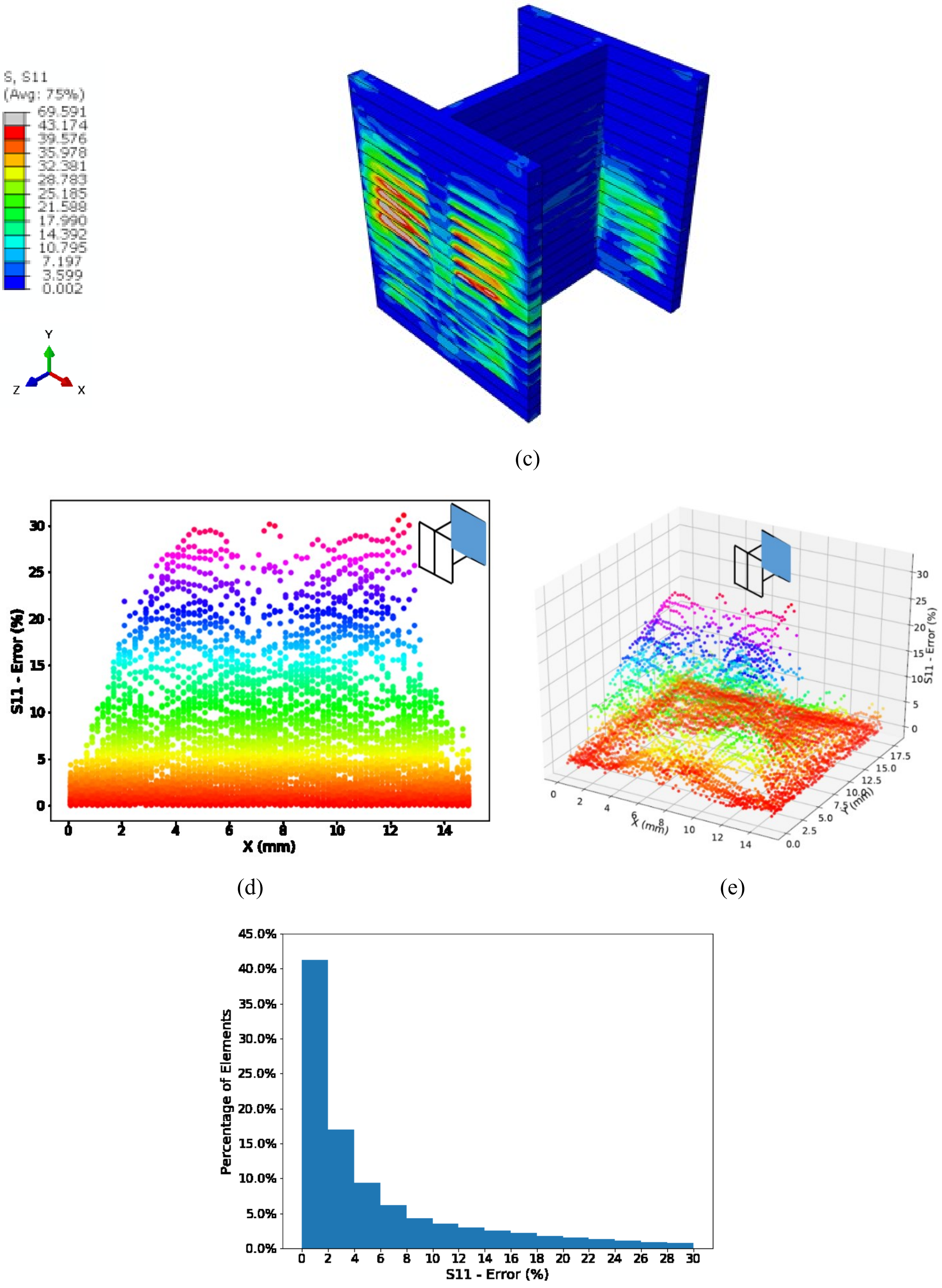

(c)

(d)

(e)

(f)

Figure 31 S11 distribution of 18-layers H-shape wall (in MPa) (a) finite element analysis (b) ANN prediction (c) error value (%) (d) 2D error scatter (X-Y plane - back) (e) 3D error scatter (X-Y plane - back) (f) histogram of the error

Figure 32 shows the S22 distribution (stress component in the stacking direction or direction Y) for the H-shape structure. Figure 32 (a) and (b) show the S22 obtained from FE analysis and the novel integrated ANN-FE approach, respectively. The distribution pattern in both contours is consistent; the high tensile residual stresses are found in both cases in the ends of the edges and also in the middle of the front plane of the structure. On the front plane, the high tensile residual stresses are smoothly converted to a low stress zone shown by the green color in Figure 32 (a) and (b) and then, a relatively high tensile residual stress zone is formed in both the FE and ANN-FE results for the S22. Furthermore, the midplane of the part represents high compressive residual stresses in the central portions of the Y-Z plane which is gradually converted into a low stress state zone shown by the green color. Also, a smooth mutation of high tensile stresses into compressive stresses is observed in the back plane of the specimen that is accurately captured by the ANN-FE method. To better demonstrate the capability of the ANN-FE approach, the 3D error of the predicted results is displayed in the contour format shown in Figure 32 (c). The majority of the elements shown with the blue color represent the areas with less than 10% prediction error. However, there is a significantly large area in the middle of the front plane showing very high (greater than 100%) error in the prediction as shown in Figure 32 (b). Based on the stress level in that area (-21 to 55 MPa) from Figure 32 (b), it is seen that the actual stresses in the stacking direction is not significant value and the high prediction error will have no considerable impact on the capabilities of the proposed method. But, by comparing the scatter analysis of the error represented in Figure 28 (d) and (e), it is noticeable that the number of elements with an error greater than 15% is very limited. Histogram analysis of S22 error is shown in Figure 28 (f). Approximately 12% of the elements show a prediction error higher than 15%. As mentioned before, a high fraction of elements has a low prediction error as it is supported by the histogram analysis.

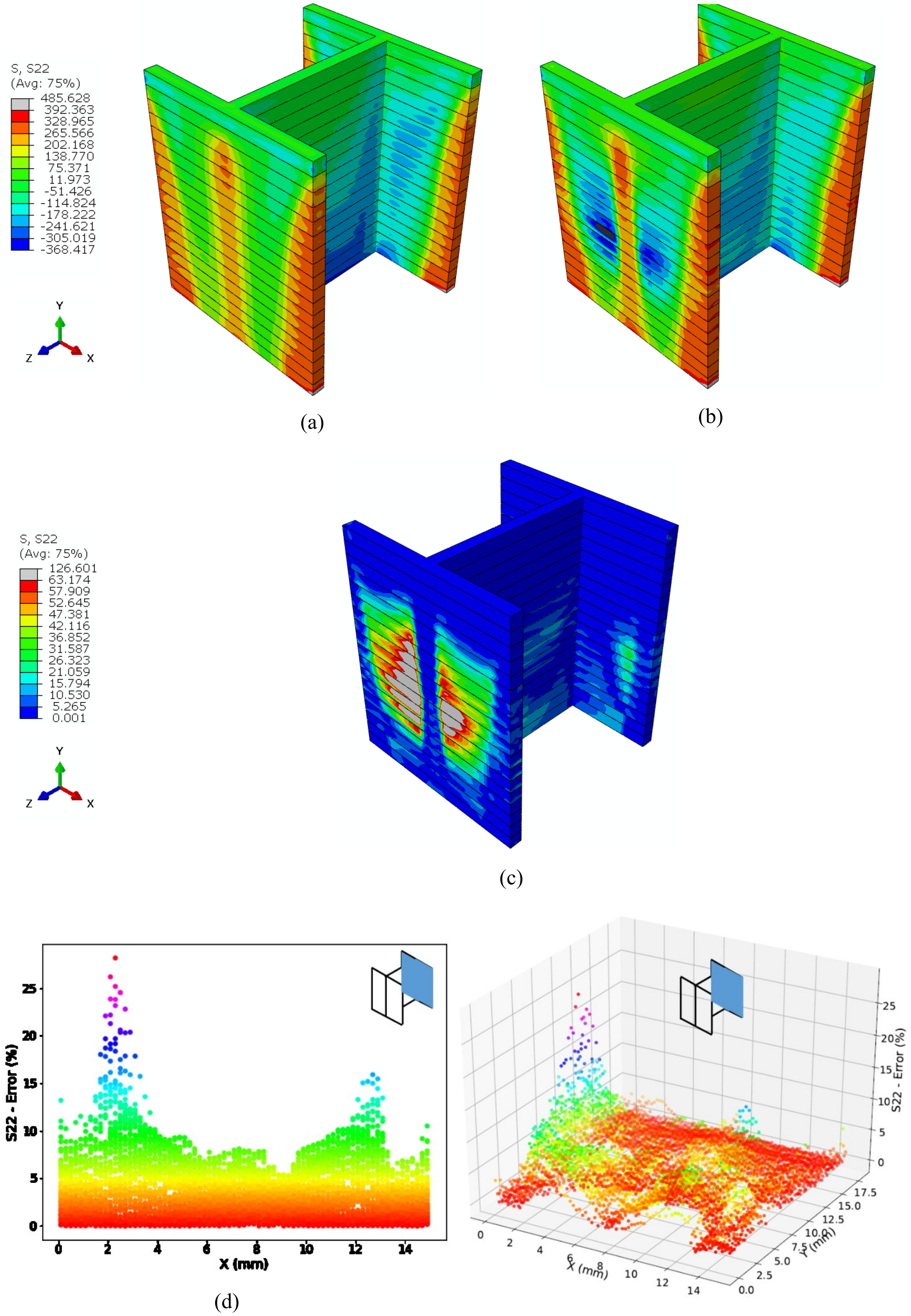
S, S22
(Avg: 75%)
485.628
392.363
328.965
265.566
202.168
138.770
75.371
11.973
-51.426
-114.824
-178.222
-241.621
-305.019
-368.417
Y
Z
X
S, S22
(Avg: 75%)
126.601
63.174
57.909
52.645
47.381
42.116
36.852
31.587
26.323
21.059
15.794
10.530
5.265
0.001
Y
Z
X
S22 - Error (%)
X (mm)
0
2
4
6
8
10
12
14
5
10
15
20
25
X (mm)
Y (mm)
S22 - Error (%)
0.0
2.5
5.0
7.5
10.0
12.5
15.0
17.5

(a)

(b)

(c)

(d)

(e)

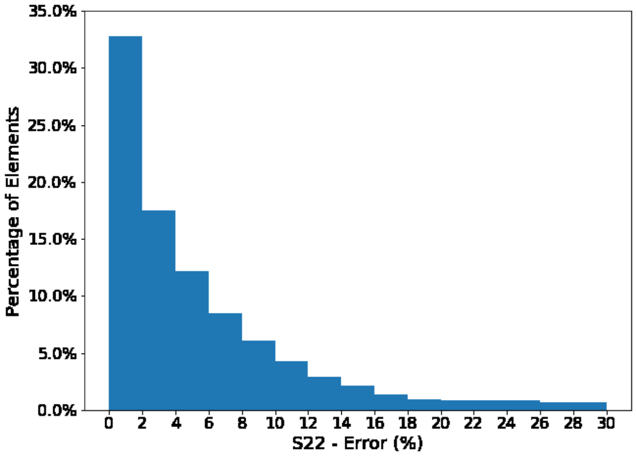

(f)

Figure 32 S22 distribution of 18-layers H-shape wall (in MPa) (a) finite element analysis (b) ANN prediction (c) error value (%) (d) 2D error scatter (X-Y plane - back) (e) 3D error scatter (X-Y plane - back) (f) histogram of the error

Additional results for the S33 distribution of the part along with error scatter for the other two mid-planes, Y-Z plane and X-Y plane (front), are provided in the supplementary section.

6.2.6. 18-layers Plus-shape

Figure 33 shows the S11 distribution for the 18 layers Plus-shape wall. Figure 33 Figure 29(a) and (b) show the distribution of S11 calculated from the FE analysis and novel integrated ANN-FE method for the structure, respectively. The predicted results from the integrated ANN-FE approach mimic the FE analysis results. The residual stress distribution of S11 component is well captured in the prediction via ANN-FE. The highest tensile stresses are observed in the tip layer with a smooth transition to the local compressive stresses at the ends of the (X-Y) plane. The intersection of the two planes is a low-stress state zone and local compressive stress is noticed right at the center of the intersection. The S11 component of stress becomes negative on the outer surface of the (X-Y) plane on the 13th up to 17th layers. Furthermore, both ends of the first layer demonstrate high tensile residual stresses that are substantially well captured in the ANN-FE analysis as well. In order to better perceive the ANN-FE capabilities, the prediction error in a contour form is presented in Figure 33 (c). Most of the elements illustrate the blue color showing the error values of less than 4% and the green color representing the error values of approximately 20% denoted to the region with a very low stress-state. Large error values are observedd at the bottom of the first layer, however, that area is also associated with the low-stress state zone. This show the significant performance of the ANN-FE model in the prediction of the residual stress in the X direction. To have a better representation of elements with high error values shown in green color, the mid-plane of the X-Y plane is cut and the scatter error of S11 component is extracted and shown in Figure 33 (d) and (e) in 2D and 3D, respectively. Elements with red and yellow colors represent error values less than 15% and the green dots show the elements with error values up to 30%. Blue and purple dots show prediction error values of higher than 30% which are very limited. Furthermore, the histogram analysis is also conducted to associate the percentage of the elements with their error ranges and shown in Figure 33 (f). Approximately only 8% of the elements show errors higher than 15%.

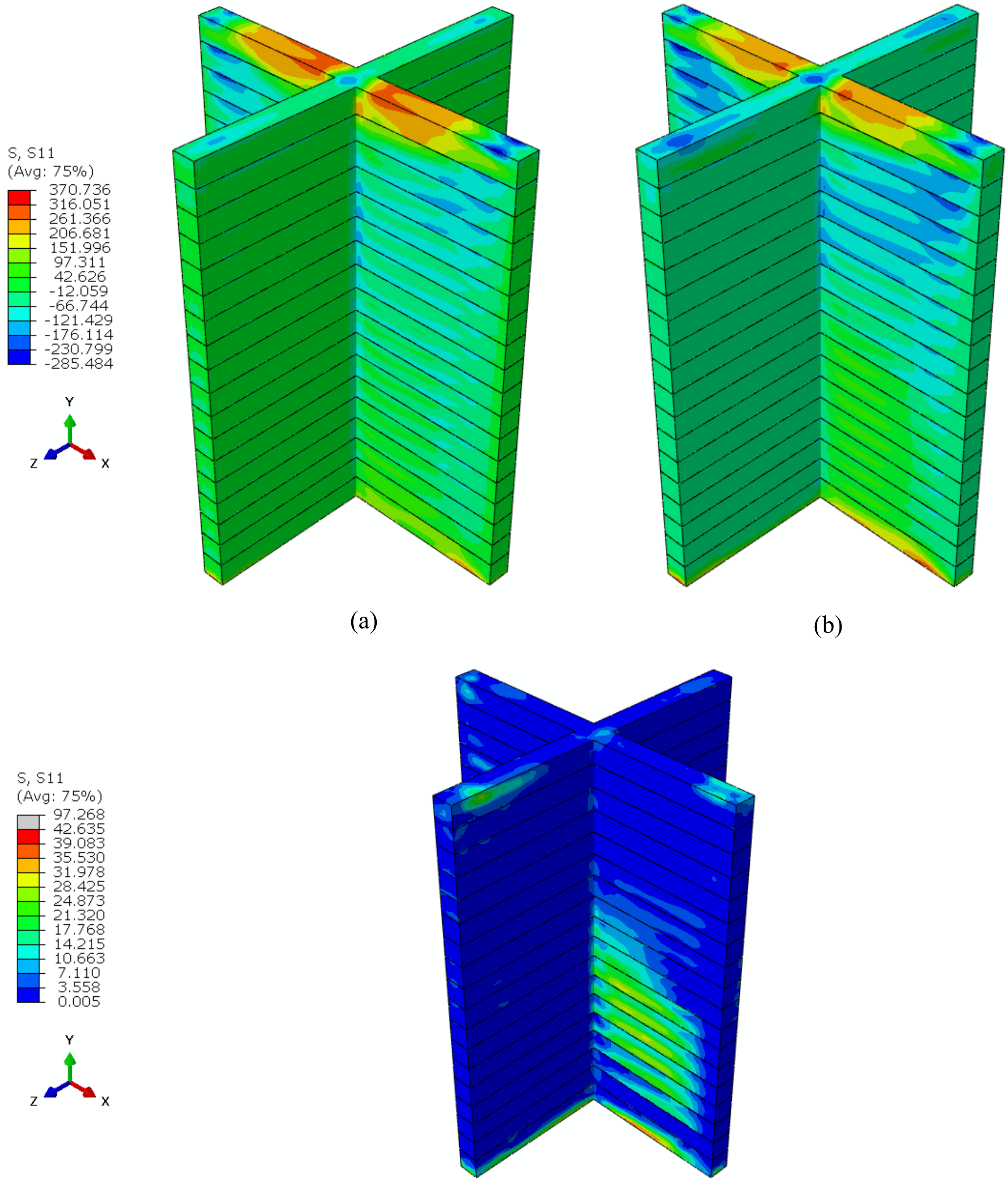

(a) (b)

(c)

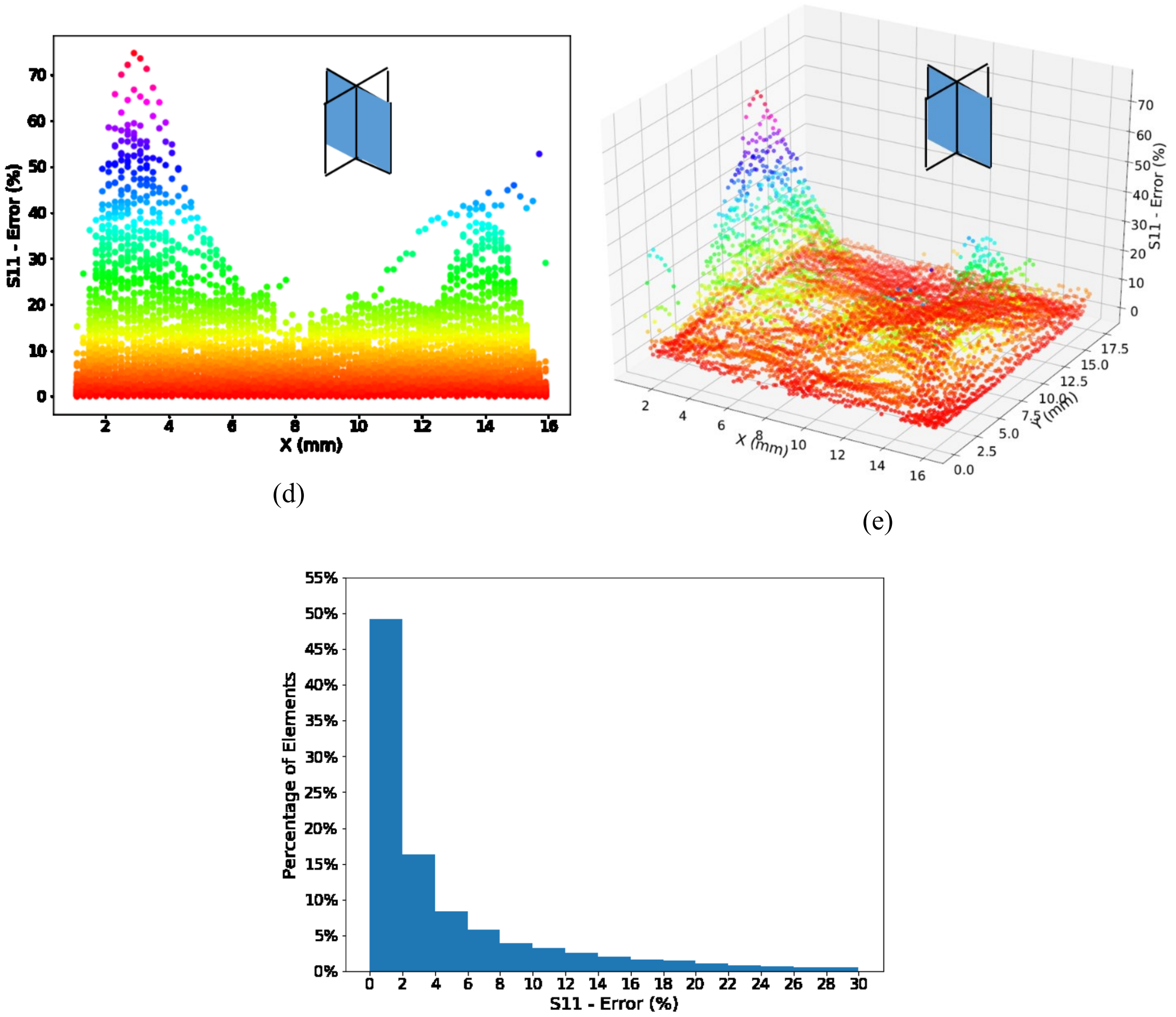

(d)

(e)

(f)

Figure 33 S11 distribution of 18-layers Plus-shape wall (in MPa) (a) finite element analysis (b) ANN prediction (c) error value (%) (d) 2D error scatter (X-Y) plane (e) 3D error scatter (X-Y) plane (f) histogram of the error

Figure 34Figure 26 shows the results for predicting S22 (stress component in the stacking direction or direction Y) of the 18-layers Plus-shape wall structure. Figure 34 (a) and (b) show the S22 distribution in the form of contour obtained from the FE analysis and integrated ANN-FE method, respectively. The middle part of the structure shows the highest compressive stresses in the stacking direction in both the FE and ANN-FE analyses. The distribution of the S22 stress is well captured in the ANN-FE analysis. According to Figure 34, the compressive residual stress in the sacking direction I the central regions is gradually changed to the low-stress state area shown with green color and then, it is smoothly changed to high tensile residual stress at the ends of the structure. Especially, in the first layer, the highest tensile residual stresses are depicted in both approaches. The S22 stress gradually faded into a low-stress state by going in the stacking direction that is captured well in the ANN-FE model as well. Very local compressive stresses on the mid-layers are demonstrated in the result of the ANN-FE analysis showing the reliability of the ANN-FE model in predicting the detailed stress distribution of the DMD parts. The contour format of the residual stresses in the stacking direction s illustrated in Figure 34 (c). The blue colors in the error contour show the regions with an error of less than 5% in the prediction of S22. Very local areas of green color (error<20%) and red color (error<30%) are observed which are related to the low-stress states. Only the elements at the bottom parts of the first layer show high error values and the area is high stress state. However, the number of elements in the area is very limited. The 2D and 3D error scatter of S22 are represented in Figure 34 (d) and (e) to better show the elements with the high error rates in the X-Y plane. As can be seen, the red and yellow dots represent the elements with less than 10% error in predicting S22. The blue and purple dots associate with the elements with higher than 20% error are very rare. The histogram analysis is also conducted for the whole structure for the prediction error of S22 and shown in Figure 34 (f). The histogram expresses that the very high fraction of elements has a prediction error of less than 15% that is considered to be acceptable accuracy. Approximately 6% of the elements show an error of higher than 15% that shows the prediction capability of the ANN-FE.

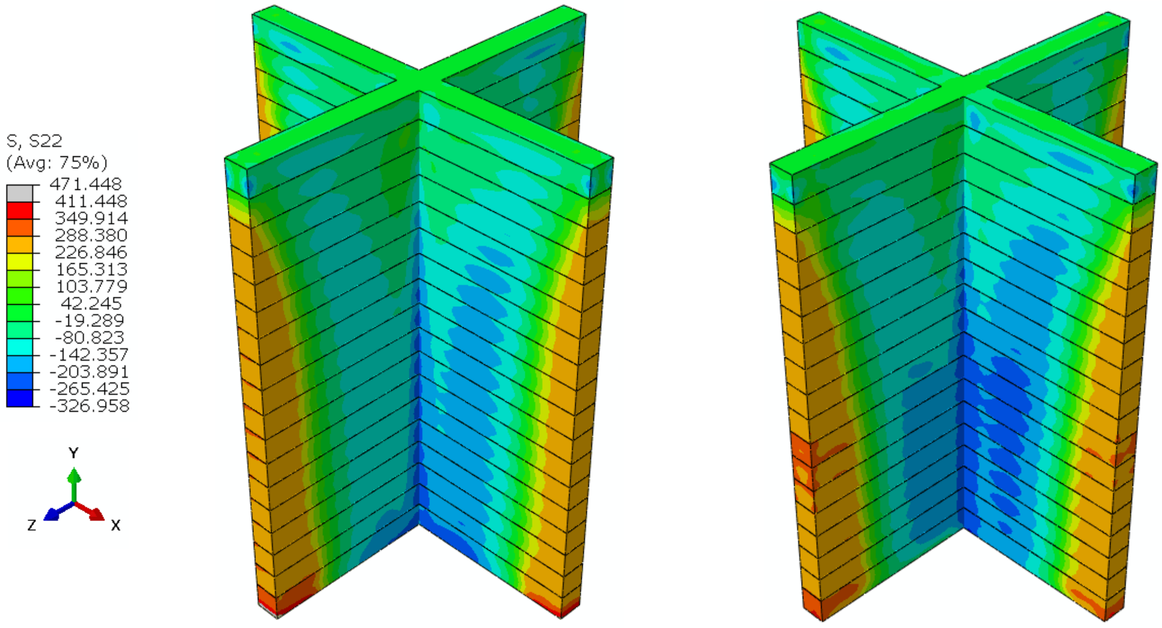

(a)

(b)

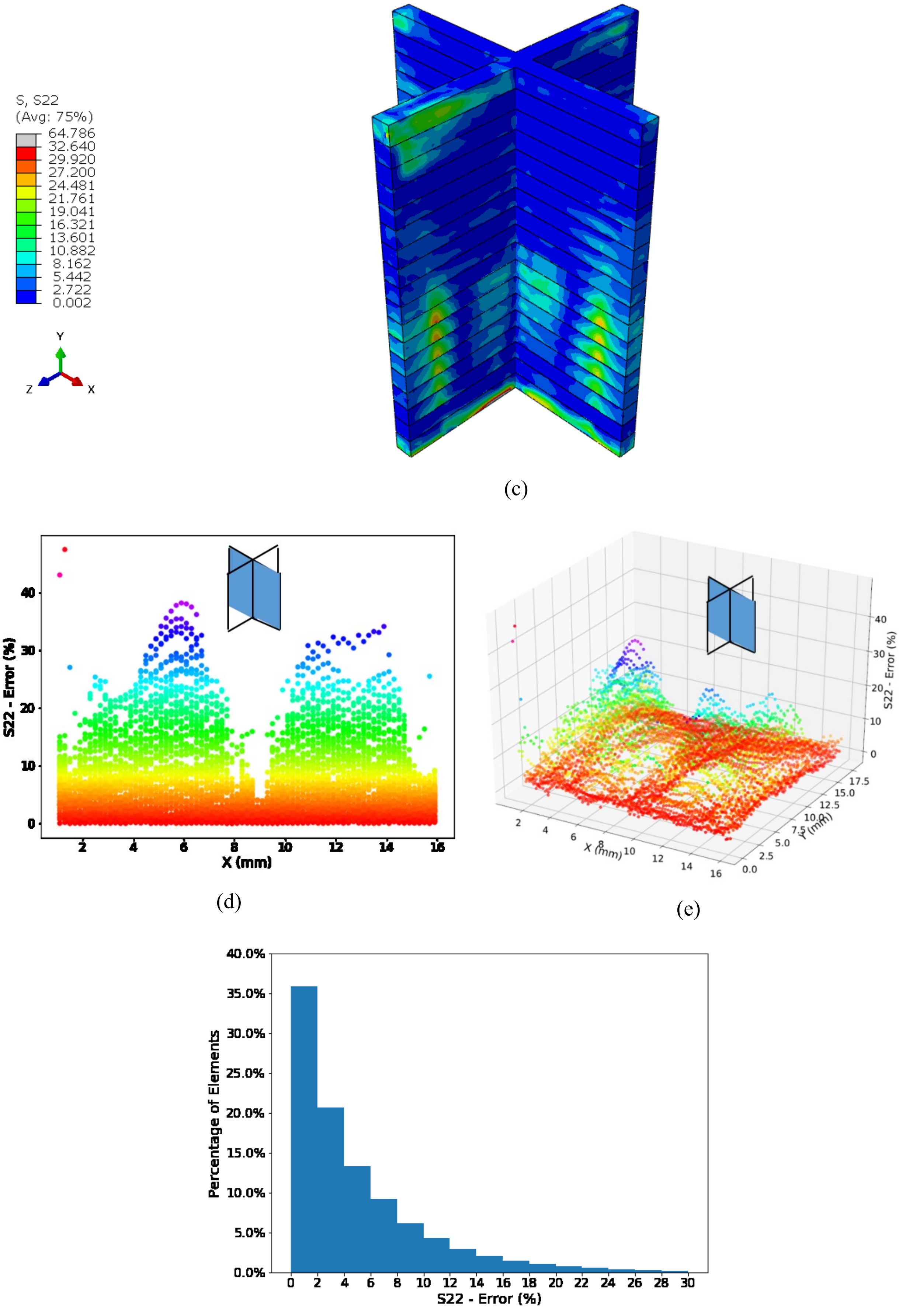
S, S22
(Avg: 75%)
64.786
32.640
29.920
27.200
24.481
21.761
19.041
16.321
13.601
10.882
8.162
5.442
2.722
0.002
Y
Z
X
S22 - Error (%)
X (mm)
0
10
20
30
40
2
4
6
8
10
12
14
16
X (mm)
Y (mm)
0.0
2.5
5.0
7.5
10.0
12.5
15.0
17.5
Percentage of Elements
S22 - Error (%)
0.0%
5.0%
10.0%
15.0%
20.0%
25.0%
30.0%
35.0%
40.0%
0
2
4
6
8
10
12
14
16
18
20
22
24
26
28
30

(c)

(d)

(e)

(f)

Figure 34 S22 distribution of 18-layers Plus-shape wall (in MPa) (a) finite element analysis (b) ANN prediction (c) error value (%) (d) 2D error scatter (X-Y) plane (e) 3D error scatter (X-Y) plane (f) histogram of the error

Additional results of the Plus-shape for the Y-Z plane are provided in the supplementary section.

6.2.7. 18-layers BoxPlus-shape

Figure 35 shows the stress results obtained from the FE analysis and the proposed integrated ANN-FE method for the 18-layers BoxPlus structure. Figure 35 (a) and (b) demonstrate the S11 (stress component in direction X) obtained from the detailed finite element analysis and integrated ANN-FE approach, respectively. As it is depicted, the overall residual stress distribution and its pattern are consistent in both contours especially in the top layer and the bottom layer of the BoxPlus structure where the tensile residual stresses are high. The tensile residual stresses in the X-direction are dominant on the top layer and they are slightly faded and converted into the low-stress state zone at the center of the specimen. Furthermore, the high tensile residual stresses were accurately captured at the bottom of the first layer in the ANN-FE analysis. Very local compressive stresses were also evaluated in the outer surfaces of the top layer and well-captured in the ANN-FE analysis as well. The 3D contour of the prediction error was calculated according to Eq. (20) and presented in Figure 35 (c). A vast number of elements that are shown in blue color are associated with a prediction error value of less than 5%. Some of the elements shown with the green color represent a prediction error of approximately 17% and a very limited number of elements demonstrated a prediction error of more than 20% as shown in red color. To better present the performance of the novel ANN-FE method, the 2D and 3D error scatter diagrams are built for the mid-plane of the X-Y front surface and presented in Figure 35 (d) and (e), respectively. As can be seen, a very limited number of elements show error values of more than 20%. The high values of the error are related to the areas with a very local stress state that contains very few elements. Finally, the histogram analysis was performed on the error data for the structure and shown in Figure 35 (f). The total number of elements with error values greater than 15% is limited to about 5% of the elements.

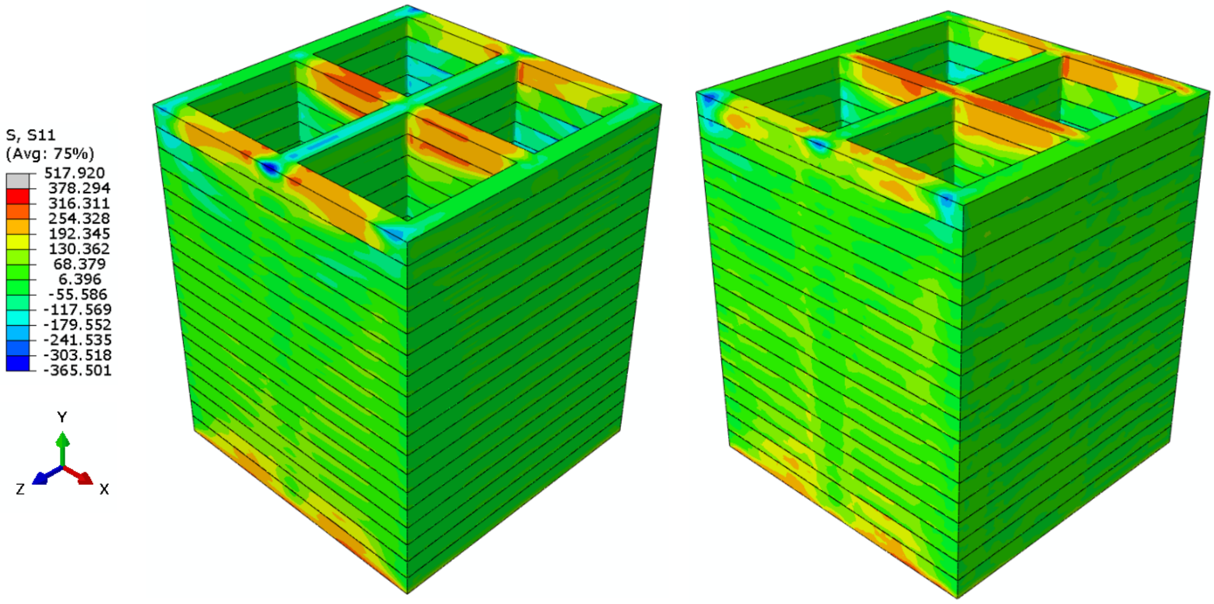
S, S11
(Avg: 75%)
517.920
378.294
316.311
254.328
192.345
130.362
68.379
6.396
-55.586
-117.569
-179.552
-241.535
-303.518
-365.501
Y
Z
X

(a)

(b)

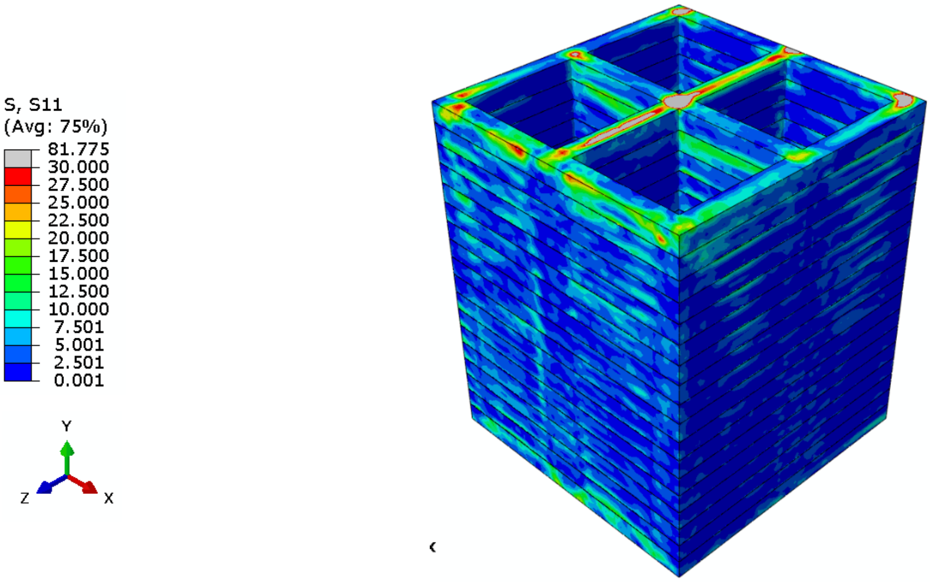
S, S11
(Avg: 75%)
81.775
30.000
27.500
25.000
22.500
20.000
17.500
15.000
12.500
10.000
7.501
5.001
2.501
0.001
Y
Z
X

(c)

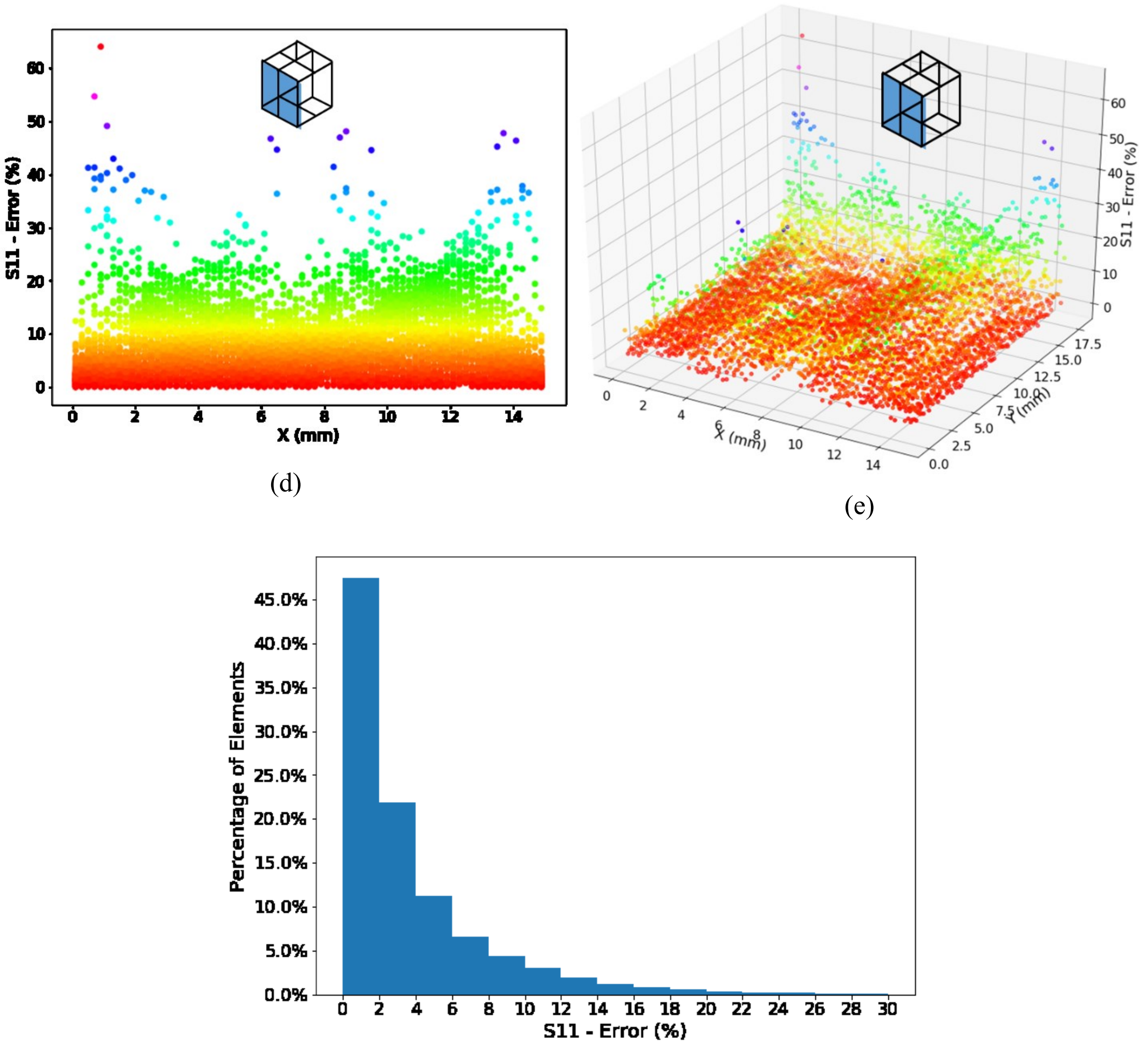

(d)

(e)

(f)

Figure 35 S11 distribution of 18-layers BoxPlus structure (in MPa) (a) finite element analysis (b) ANN prediction (c) error value (%) (d) 2D error scatter (X-Y plane - front) (e) 3D error scatter (X-Y plane - front) (f) histogram of the error

Figure 36 shows the S22 distribution (stress component in the stacking direction or direction Y) for the 18-layers BoxPlus structure. Figure 28 Figure 36 (a) and (b) show the S22 evaluated from FE analysis and the proposed integrated ANN-FE approach, respectively. The distribution pattern in both cases is similar and consistent. The high tensile residual stresses are found at the bottom layer of the structure for both FE and ANN-FE results of the S22 distribution. The middle parts of the surfaces represent slightly high tensile residual stresses with a gradual smoothing of the stresses toward the compressive residual stresses in the inner side of the structure. The low-stress state shown with green color is captured well in the ANN-FE as well. However, the area in between the layers represents higher error values. The 3D contour of the error for the whole structure is shown in Figure 36 (c). The free surfaces of the structure, e.g. front surface, shows high prediction error, however, the prediction error declined in the mid-side of the planes into the thickness. The 2D and 3D scatter error of the stress in the stacking direction are obtained and shown in Figure 36 (d) and (e). The majority of the dots are illustrated with red and yellow colors showing the prediction error of less than 10%. The green colors represent a prediction error of less than 33%. However, the blue and purple colors are associated with errors larger than 33%. The reason for the high error seems to be issued by the insufficient number of neurons for each layer in the constructed neural networks. Alternatively, the error could be caused from the low number of hidden layers. Due to the restriction of the time and the computational power of the utilized machine, an excessive number of neurons would result in a very high training time. Therefore, the implemented neural network was kept as similar to the other structures. The histogram analysis was also performed for the entire structure and the results are shown in Figure 36 (f). Approximately 12% of the elements show a prediction error higher than 15%. Although the constructed neural network is not sufficient for the structure, the fraction of the elements that have higher than acceptable error ranges is not significantly high.

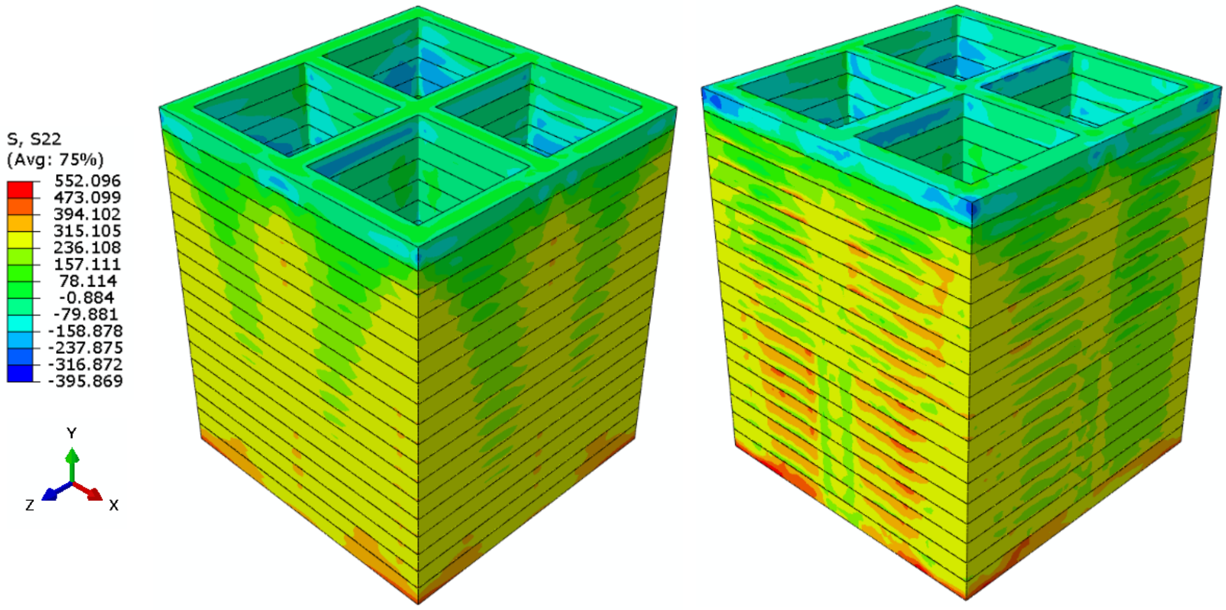

(a) (b)

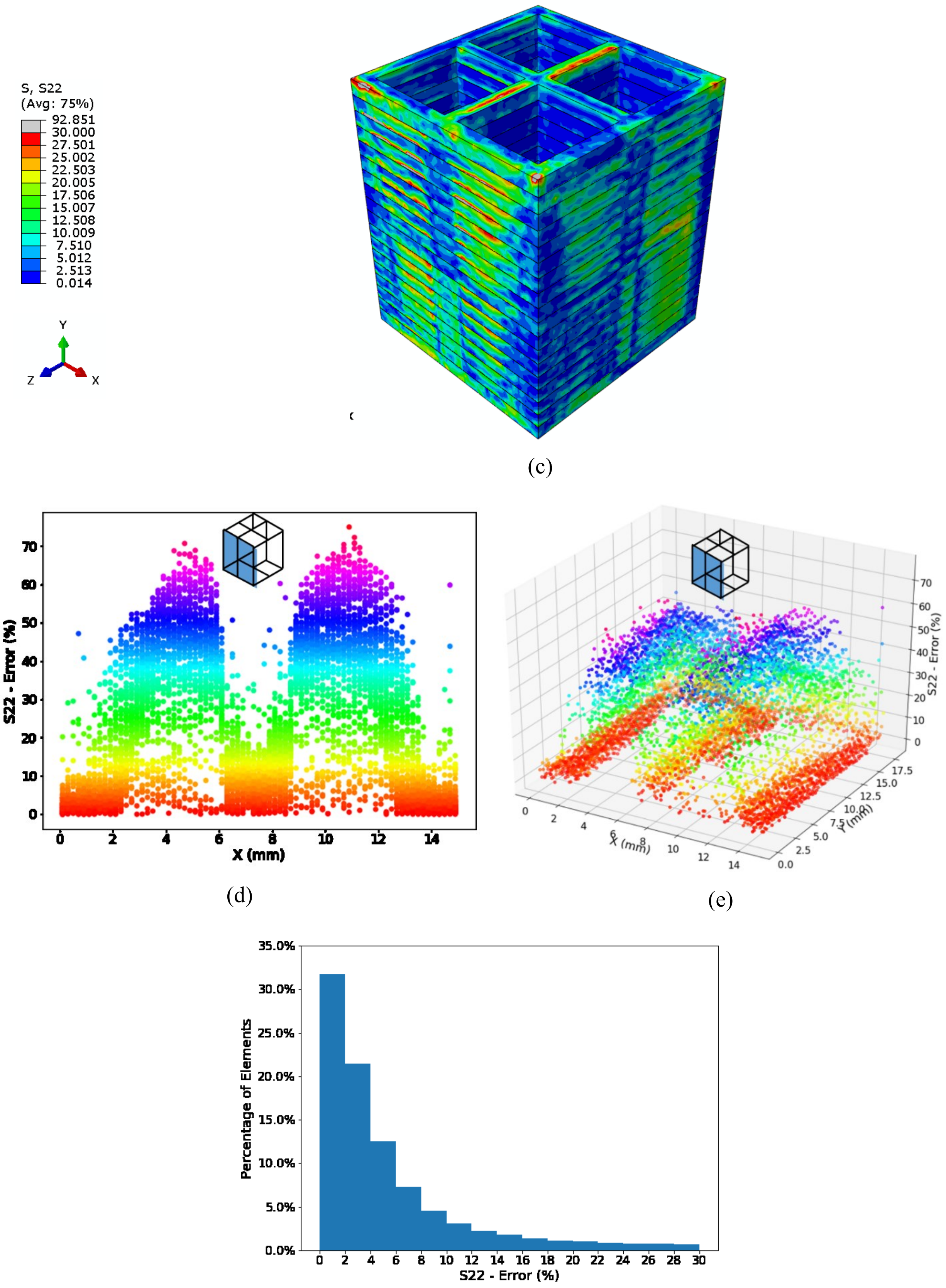

(c)

(d)

(e)

(f)

Figure 36 S22 distribution of 18-layers BoxPlus structure (in MPa) (a) finite element analysis (b) ANN prediction (c) error value (%) (d) 2D error scatter (X-Y plane - front) (e) 3D error scatter (X-Y plane - front) (f) histogram of the error

The additional results for the 18-layers BoxPlus structure are provided in the supplementary section.

6.2.8. 18-layers SemiBox-shape

Figure 37 shows the S11 distribution for the 18-layers SemiBox structure. Figure 37 (a) and (b) represent the S11 distribution obtained from the detailed FE analysis and ANN-FE approach, respectively. The residual stress distribution pattern is very similar and consistent in both contours and the critical location of the part associated with the highest tensile and compressive stresses is captured well in the ANN-FE results. The highest tensile residual stresses are observed in the lower layers of the front surfaces. On the top 5 layers, the compressive stress is observed both in the FE analysis results and ANN-FE results. A smooth transition of S11 from compressive to tensile is observed in the mid parts of the front surfaces and well captured in the ANN-FE. The 3D error in the form of a contour is represented for the longitudinal stress component as shown in Figure 37 (c). Most of the elements demonstrate a prediction error of less than 3% shown with blue color. The green color in the contour denotes to the elements with errors less than approximately 16%. A very localized area on the front surfaces of the top layer and mid-layers illustrates high prediction errors. However, the area is a low-stress state area whose stress values range from -5 to 70 MPa. 2D and 3D representation of the scattered error are shown in Figure 37 (d) and (e) for the back plate, respectively. All the red and yellow dots are associated with the elements with less than 10% error and only a very limited number of elements shown in the green, blue, and purple show an error greater than 10%. The histogram analysis is performed on the prediction data of all elements and the result is shown in Figure 37 (f). As can be seen, approximately 5% of the elements in the structure demonstrate a prediction error of S11 higher than 15%. Hence, it is concluded that the proposed integrated ANN-FE method is capable of predicting the stress distribution of the structure well enough.

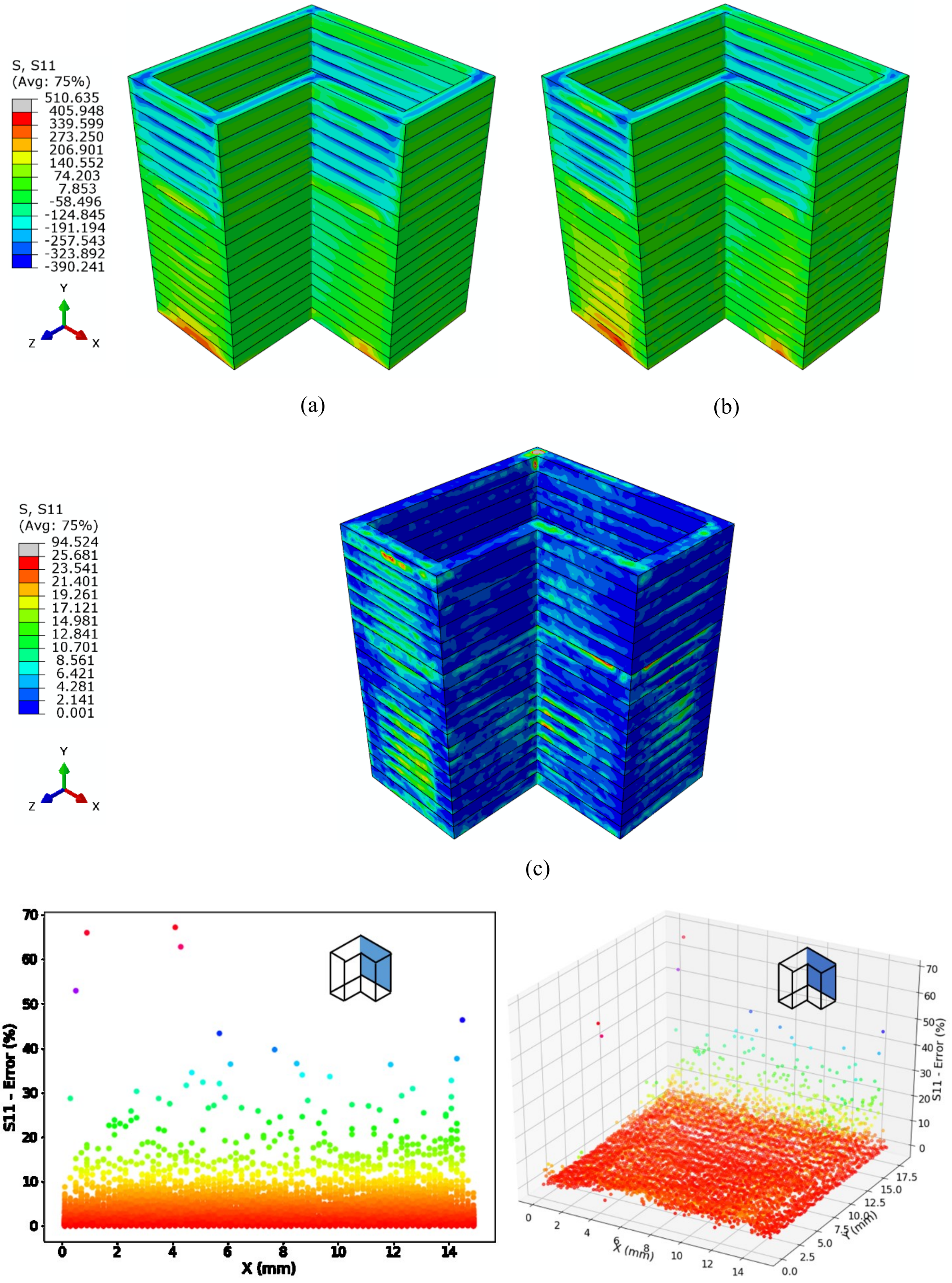
S, S11
(Avg: 75%)
510.635
405.948
339.599
273.250
206.901
140.552
74.203
7.853
-58.496
-124.845
-191.194
-257.543
-323.892
-390.241
Y
Z
X
S, S11
(Avg: 75%)
94.524
25.681
23.541
21.401
19.261
17.121
14.981
12.841
10.701
8.561
6.421
4.281
2.141
0.001
Y
Z
X
S11 - Error (%)
70
60
50
40
30
20
10
0
X (mm)
0
2
4
6
8
10
12
14
X (mm)
Y (mm)
S11 - Error (%)
0.0
2.5
5.0
7.5
10.0
12.5
15.0
17.5

(a) (b)

(c)

(d) (e)

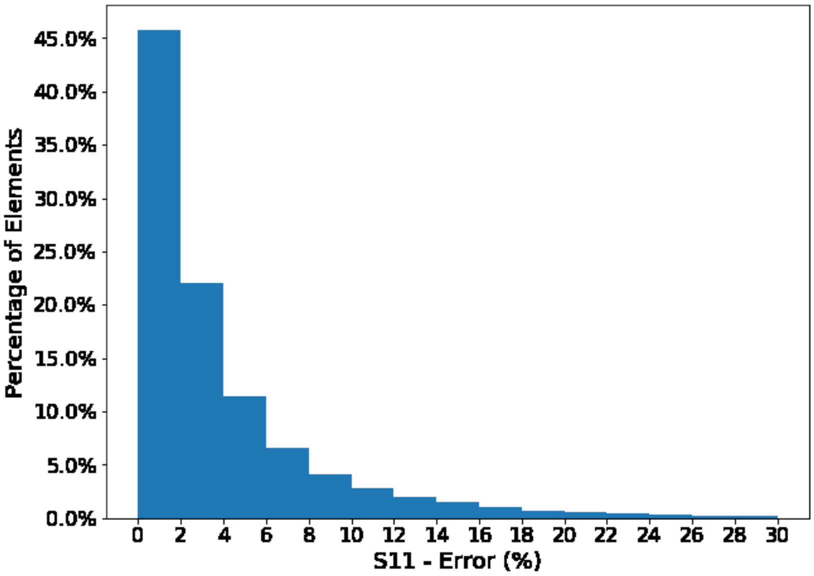

(f)

Figure 37 S11 distribution of 18-layers SemiBox wall (in MPa) (a) finite element analysis (b) ANN prediction (c) error value (%) (d) 2D error scatter (X-Y plane - back) (e) 3D error scatter (X-Y plane - back) (f) histogram of the error

Figure 38 shows the results for the prediction of S22 (stress component in the stacking direction or direction 2) of the 18-layers SemiBox structure. Figure 38 (a) and (b) show the S22 distribution in the form of contour obtained from the FE analysis and integrated ANN-FE method, respectively. By comparing the two contours, it is noticeable that the stress distribution pattern is consistent in both contours. The high residual stress states are well captured in the ANN-FE approach. The central parts of the structure show the low-stress state zone closely followed by the high compressive stresses and then, the low-stress state and a very smooth transition into the high tensile stress region in the corners. The pattern is very consistent between the FE and ANN-FE for that small region that proves the high potential of the ANN-FE method. Furthermore, the corners of the structure show the high tensile residual stress state smoothened into low-stress state region in the middle of the surfaces. By going in the stacking direction, the tensile residual stresses are faded and turned into compressive stresses in the top layers. The inner surfaces of the structure are also proving the very consistent prediction of the ANN-FE compared to the FE results. Figure 38 (c) shows the 3D representation of the S22 error in the contour format for the entire structure. The blue elements represent error values of less than 4% and the green areas demonstrate a prediction error of less than 17%. Very limited number of elements on the free surfaces of the front surfaces show the red color representing more than approximately 20% error. The scatter error for the S22 prediction is obtained in 2D and 3D and shown in Figure 38 (d) and (e) for the mid-surface of the X-Y plane (back), respectively. The majority of the elements shown with the red and yellow dots exhibit error values of less than 10%. A few and a limited number of elements show error in the prediction of the S22 higher than 15%. The histogram analysis performed on the entire data of the structure predict the S22 error and is shown in Figure 38 (f). The elements with errors higher than 15% are approximately 20% of the whole elements of the structure. However, a limited number of the elements representing high errors are associated with the low stress state zones. Furthermore, the incomplete geometry of the structures is thought to have a significant impact on the constructed network. In other words, the dataset for training the network is not sufficiently comprehensive and may cause higher prediction errors for the structure with semi-walls. It should be noted that the transition of the stresses I the stacking direction is drastic considering a very small area in the small surfaces of the part.

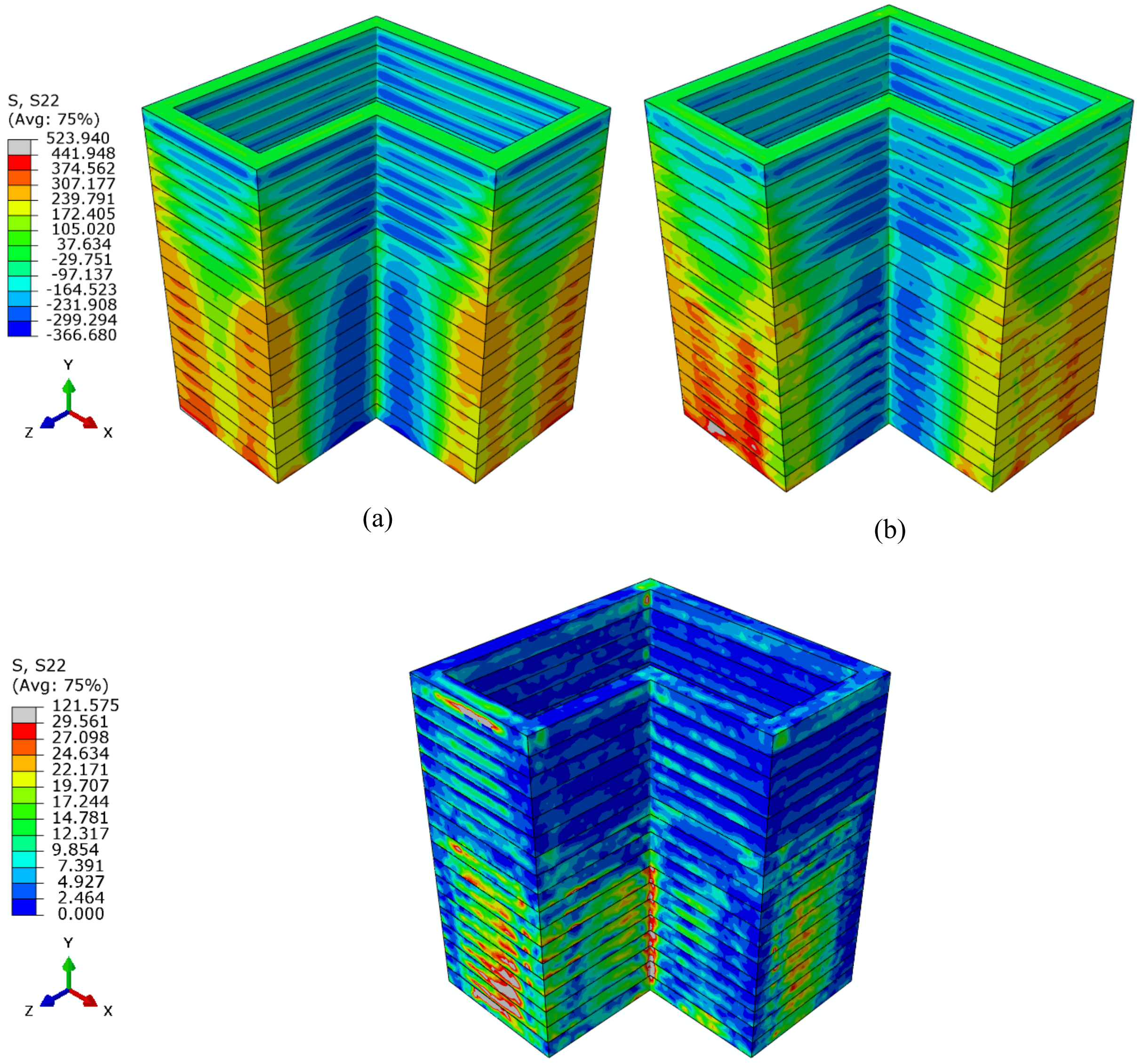

(a)

(b)

(c)

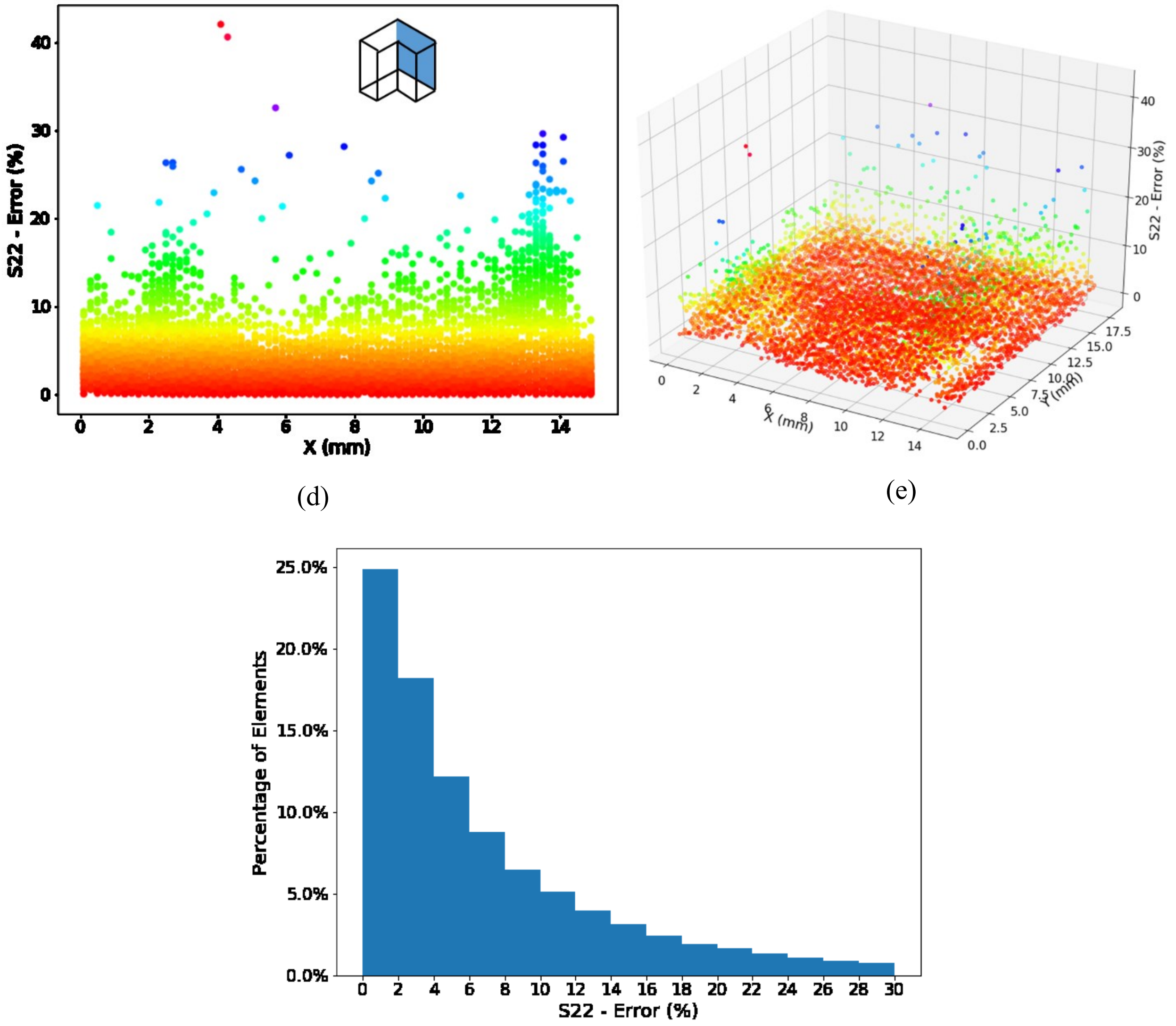

(d)

(e)

(f)

Figure 38 S22 distribution of 18-layers SemiBox wall (in MPa) (a) finite element analysis (b) ANN prediction (c) error value (%) (d) 2D error scatter (X-Y plane - back) (e) 3D error scatter (X-Y plane - back)

(f) histogram of the error

Supplementary results for the other planes are provided in the supplementary section.

6.2.9. 18-layers Hourglass-shape

Figure 39 shows the stress results obtained from the FE analysis and the novel integrated ANN-FE method for the 18-layers Hourglass-shape wall. Figure 39 (a) and (b) demonstrate the S11 (stress component in direction X) obtained from the detailed finite element analysis and integrated ANN-FE approach, respectively. As it is depicted, the overall residual stress distribution and its pattern are consistent in both contours especially in the top layer and the bottom layers of the structure where the highest residual tensile stresses are present. The stresses at the bottom layer where the structure is attached to the substrate is caught well in the integrated ANN-FE method. The smooth transition of the high tensile stresses into the low-stress state shown with the green color is captured in the ANN-FE model. The 3D error contour is shown of S11 is shown in Figure 39 (c) for the entire elements. It is seen that the blue color represents the elements with the error less than 5% and also the green color demonstrates the elements with an error of less than 20%, approximately. Only vel areas on the top layer illustrate high errors more than 20% which is not significant in the analysis of the structure's response to the thermal loads. To further investigate the capabilities of the proposed method on this structure, the scatter error of S11 in the mid-plane of the front surface is obtained and shown in Figure 39 (d) and (e). The red dots show the elements with an error of less than 15% and the yellow dots stand for the elements with approximately 20% error. The green and purple dots exhibit the elements with higher than 20% error. Finally, to quantify the error percentages of the element, the histogram analysis is performed and shown in Figure 39 (f). Approximately 20% of the elements represent the error in predicting S11 greater than 15%. It should be noted that most of the high errors occur in the area with a lower stress state which means the high prediction error of those locations has no significant impact on the performance of the proposed ANN-FE model.

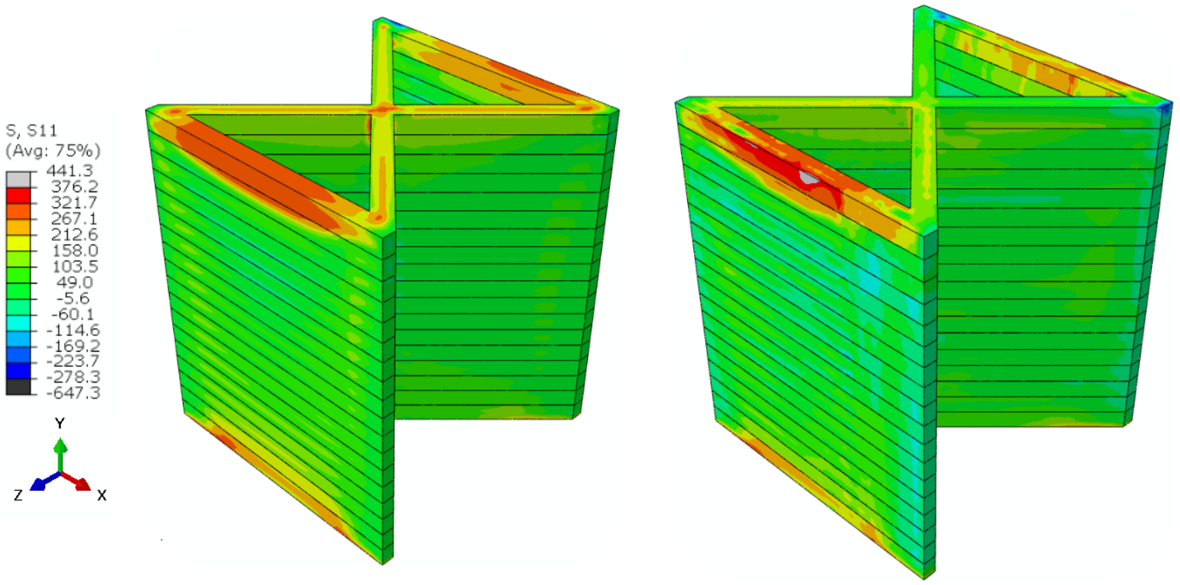

(a)

(b)

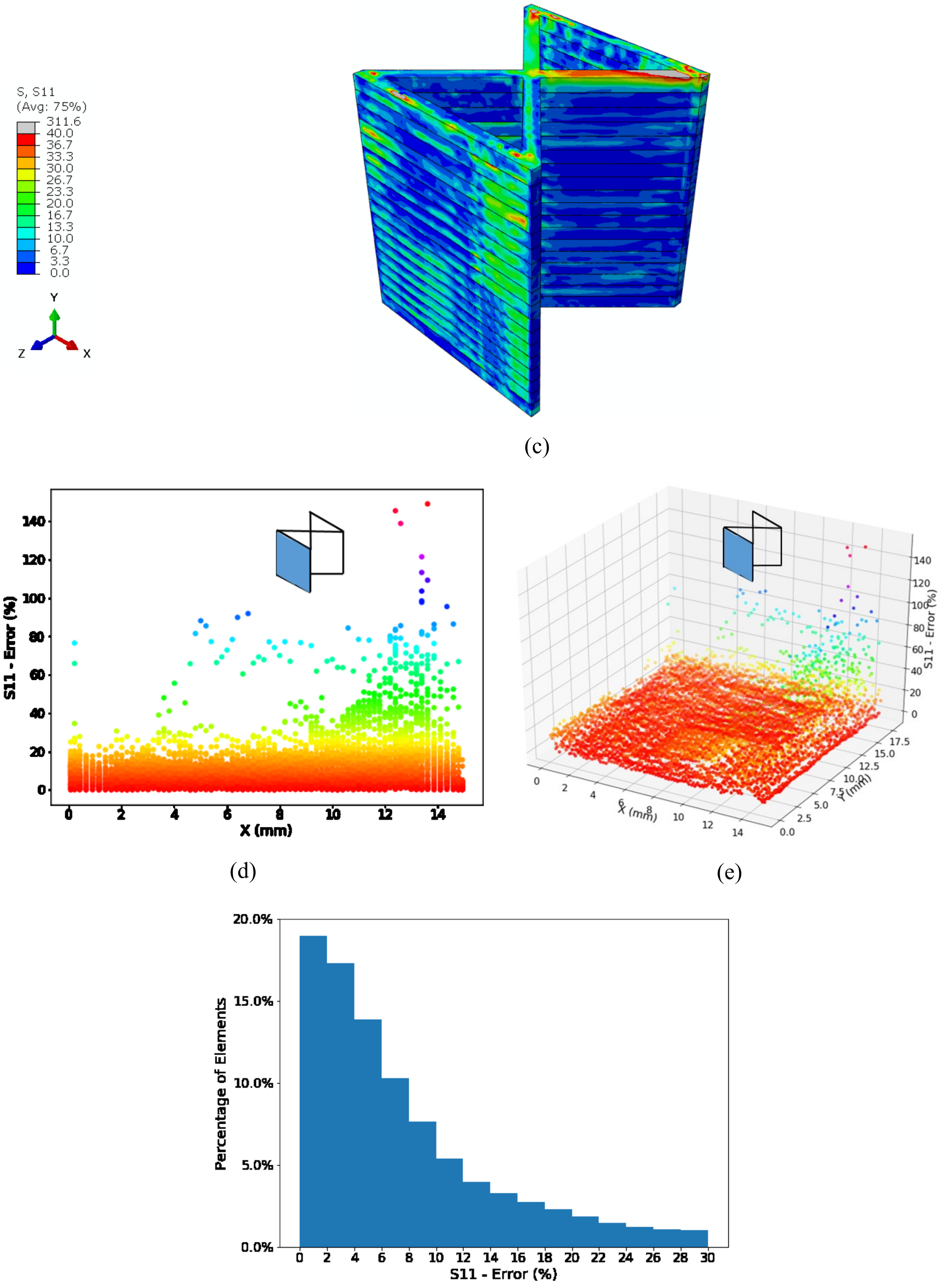

(c)

(d)

(e)

(f)

Figure 39 S11 distribution of 18-layers Hourglass-shape wall (in MPa) (a) finite element analysis (b) ANN prediction (c) error value (%) (d) 2D error scatter (X-Y plane - front) (e) 3D error scatter (X-Y plane - front) (f) histogram of the error

Figure 40 shows the S22 distribution (stress component in the stacking direction or direction Y) for the Hourglass-shape structure. Figure 28 (a) and (b) show the S22 obtained from FE analysis and the novel integrated ANN-FE approach, respectively. The distribution pattern in both cases is consistent and the high tensile and compressive residual stresses are captured well in the ANN-FE approach. The S22 distribution over the whole medium is smooth. The corners show tensile residual stresses followed by a smooth transition to low-stress state in the middle of the part. The transition from the very high tensile residual stresses into the low stress state and then into the high compressive stresses in the central regions of the part is well captured in the ANN-FE approach. The error evaluation in the form of contour also provided for assessing the accuracy of the employed integrated ANN-FE approach and shown in Figure 40 (c). The majority of the elements shown in blue color demonstrate the perdition error of less than 3% for S22. The green color also represents the elements with an error of less than 14%. Very limited area of the contour shown a high error rate greater than 15% and are shown with red color. However, by comparing the result of the S22 distribution, the area with high error rates is considered the low-stress state region. Hence, the greater error percentage for that area has no significant impact on the feasibility of the design process. The scatter error is also calculated and prepared for the mid-plane of the front surface and shown in Figure 40 (d) and (e), respectively. By analyzing the scatter error diagrams, it is noted that most of the elements have error values of less than 15%. The red and yellow dots represent the elements with an error of less than 10%. Moreover, the green color is associated with the elements with less than 16% prediction error. Furthermore, a histogram analysis of S22 error is conducted and shown in Figure 40 (f). Only 8% of the elements show a prediction error higher than 15% according to the histogram analysis that shows the high capability of the ANN-FE analysis.

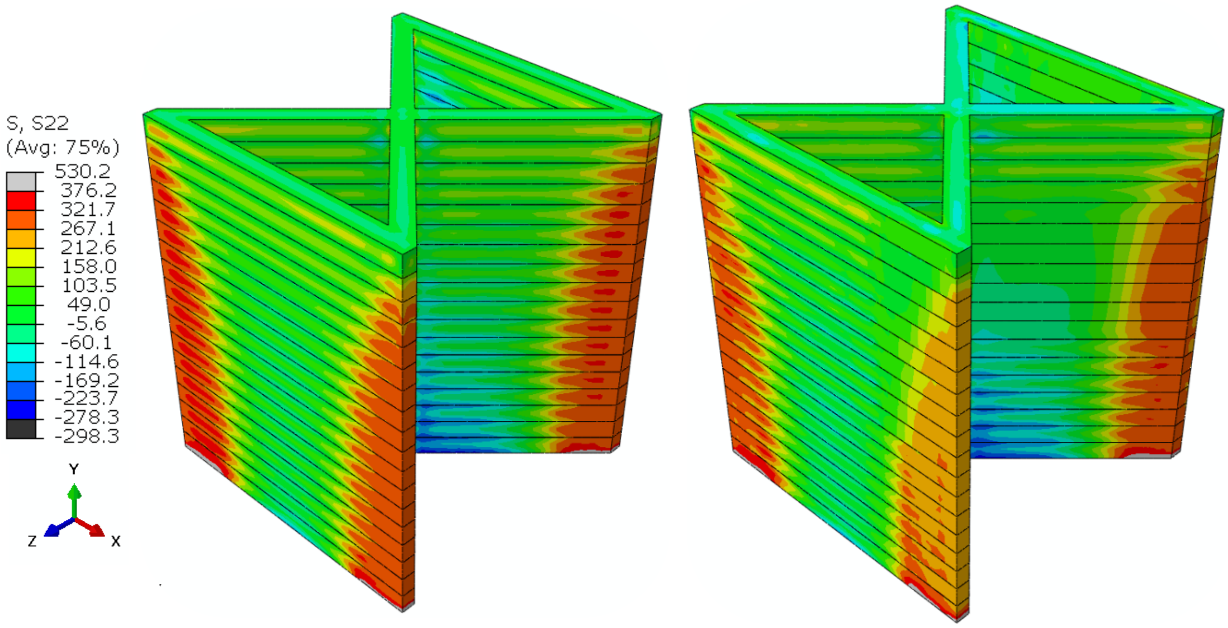
S, S22
(Avg: 75%)
530.2
376.2
321.7
267.1
212.6
158.0
103.5
49.0
-5.6
-60.1
-114.6
-169.2
-223.7
-278.3
-298.3
Y
Z
X

(a)

(b)

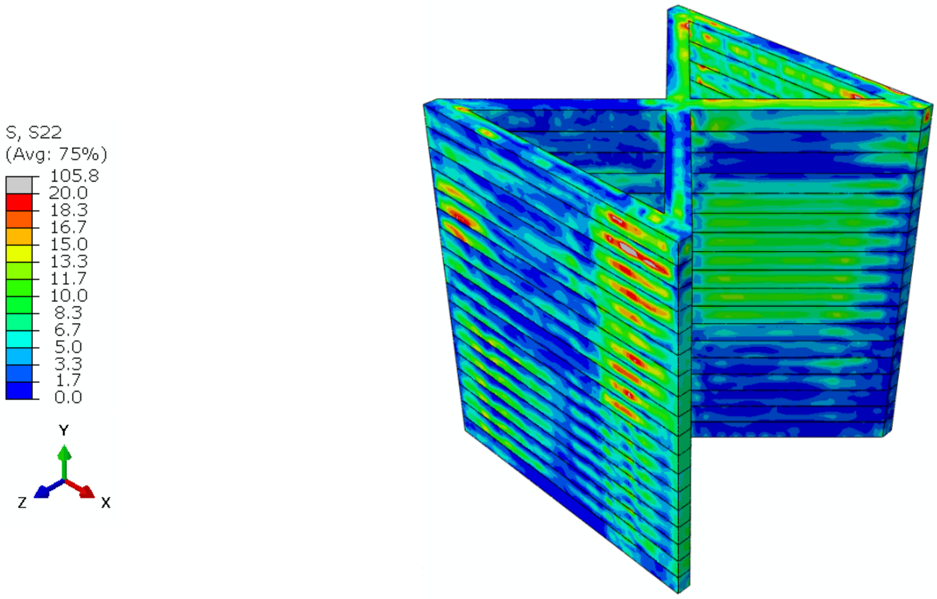
S, S22
(Avg: 75%)
105.8
20.0
18.3
16.7
15.0
13.3
11.7
10.0
8.3
6.7
5.0
3.3
1.7
0.0
Y
Z
X

(c)

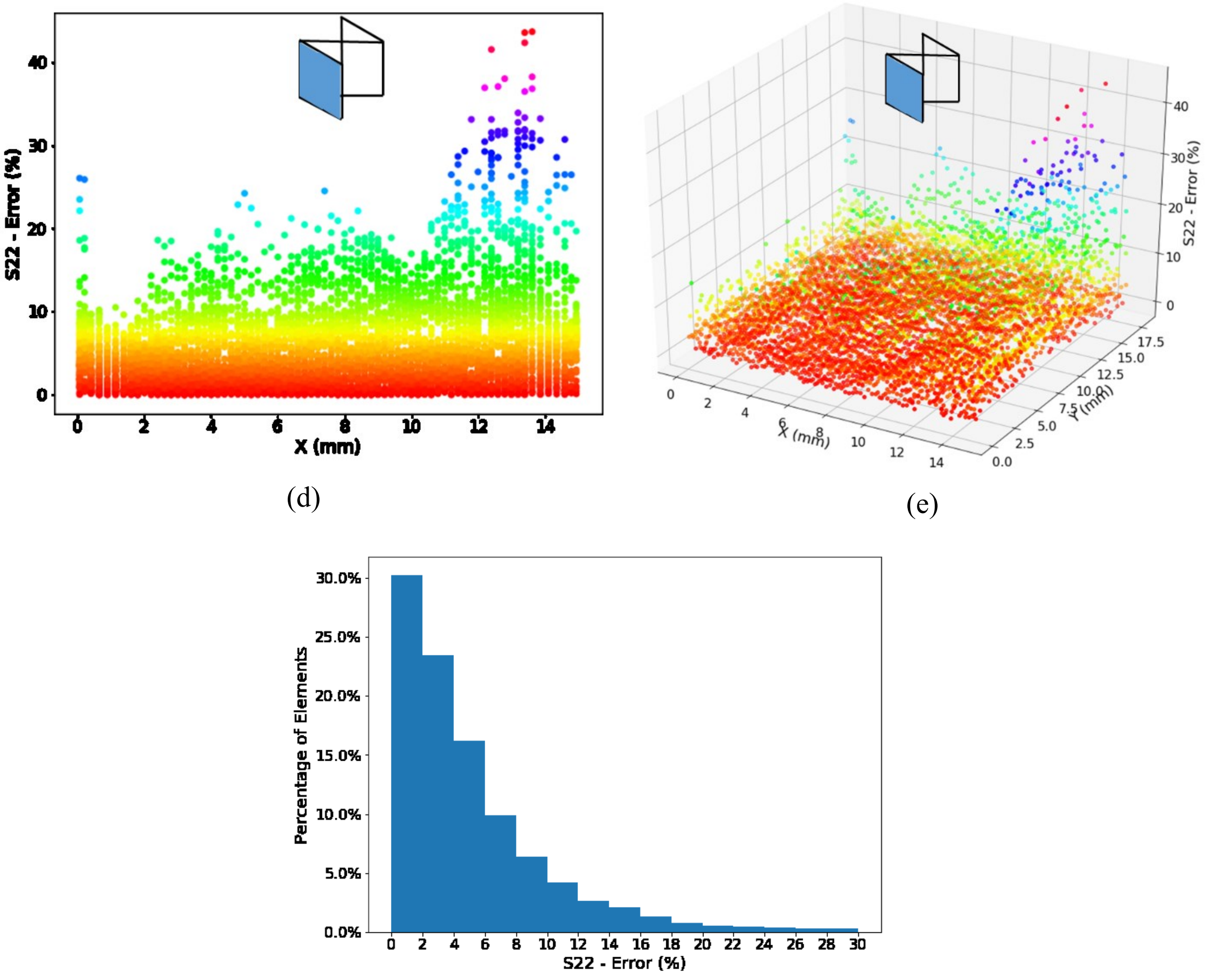

(d)

(e)

(f)

Figure 40 S22 distribution of 18-layers Hourglass-shape (in MPa) (a) finite element analysis (b) ANN prediction (c) error value (%) (d) 2D error scatter (X-Y plane - front) (e) 3D error scatter (X-Y plane - front) (f) histogram of the error

Supplementary results for the other planes are provided in the supplementary section.

6.2.10. 18-layers Arrow-shape

Figure 41 shows the S11 distribution for the 18-layers Arrow-shape wall. Figure 41 (a) and (b) demonstrate the distribution of S11 obtained from the FE analysis and integrated ANN-FE method, respectively, for the whole structure. The S11 distribution and pattern of the predicted results obtained from the ANN-FE agree well with the results of the FE analysis. The high compressive residual stress region on the top layer and on the narrow side of the arrow is captured well in the ANN-FE analysis. Furthermore, the high residual tensile stresses on the top layer are detected. The area at the intersection of the X-Y and Y-Z planes becomes low-stress state zone and by mowing away from the center, the S11 is gradually transitioned into high residual tensile stresses. Finally, the S11 is smoothly turned into the compressive stresses at the two corners. Moreover, the high residual tensile stresses are noted at the bottom layer of the structure at the corners. All these phenomena are captured well in the ANN-FE results proving the potential capabilities of the implemented method. The 3D error in the format of the contour is obtained from the error calculations and depicted in Figure 41 (c). The blue colors show the elements with very low error amplitudes, i.e. less than 2%. It is noted that the red color demonstrates the elements with a maximum of 15% error. Several locations of the part such as corners illustrate the highest error magnitudes, however, the area is very limited to several elements. In order to better present the fraction of elements with high errors, the 2D and 3D scatter diagrams are prepared and shown in Figure 41 (d) and (e), respectively. As can be seen, almost all of the elements are shown in red color with less than 10% error. The green dots representing the elements with approximately 20% error are scares in the figure. The blue and purple colors can be considered negligible as they are just a few elements. The histogram analysis is performed for the error data of all the elements in the structure and shown in Figure 41 (f). Approximately 5% of the elements exhibit a higher error than 15%. Hence, majority of the elements of the whole structure have very small error values in predicting S11 and this proves the capability of the proposed novel method.

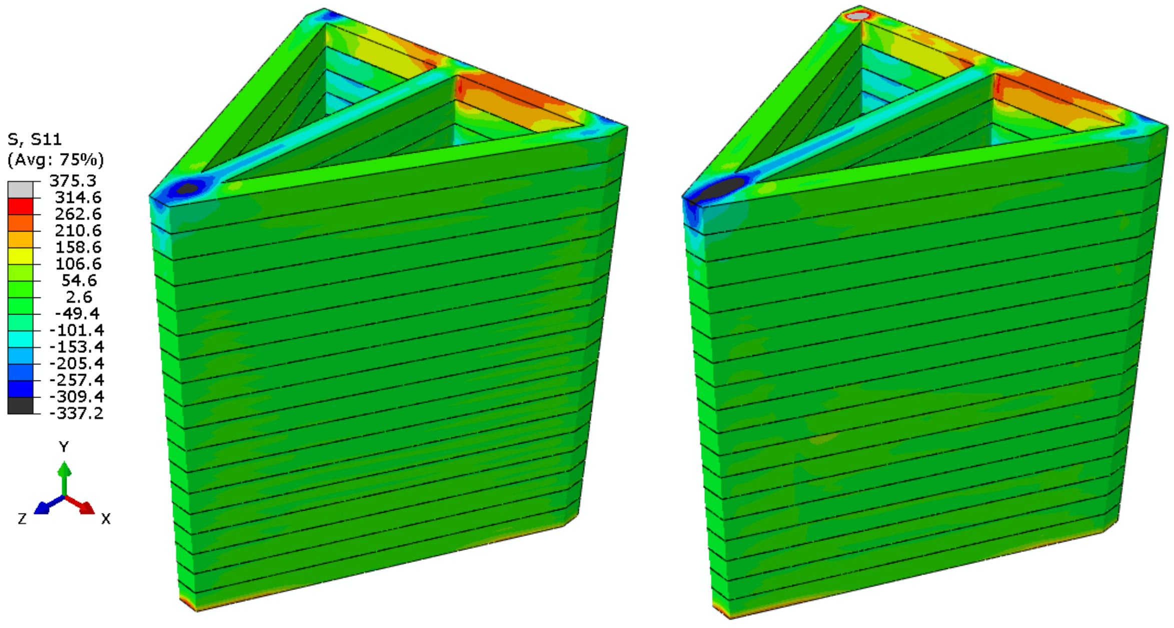

(a) (b)

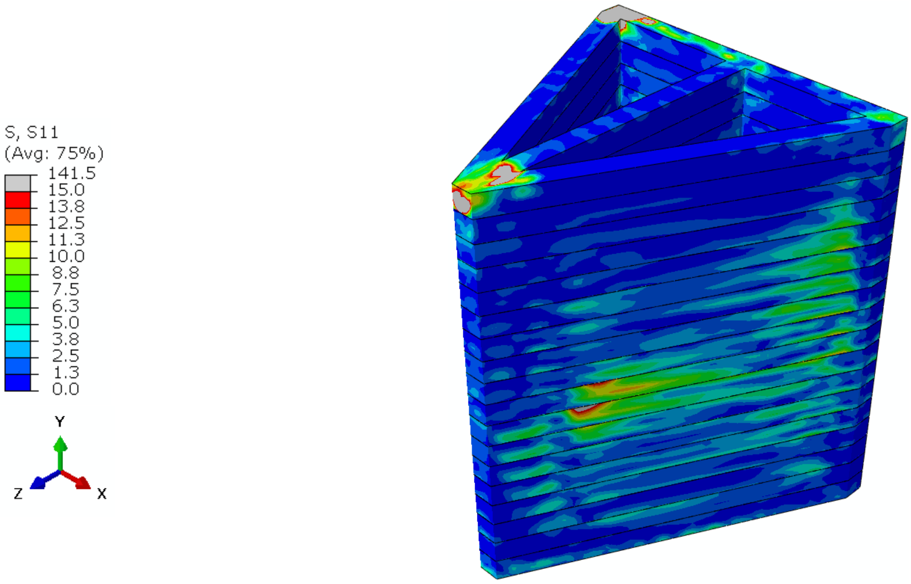

(c)

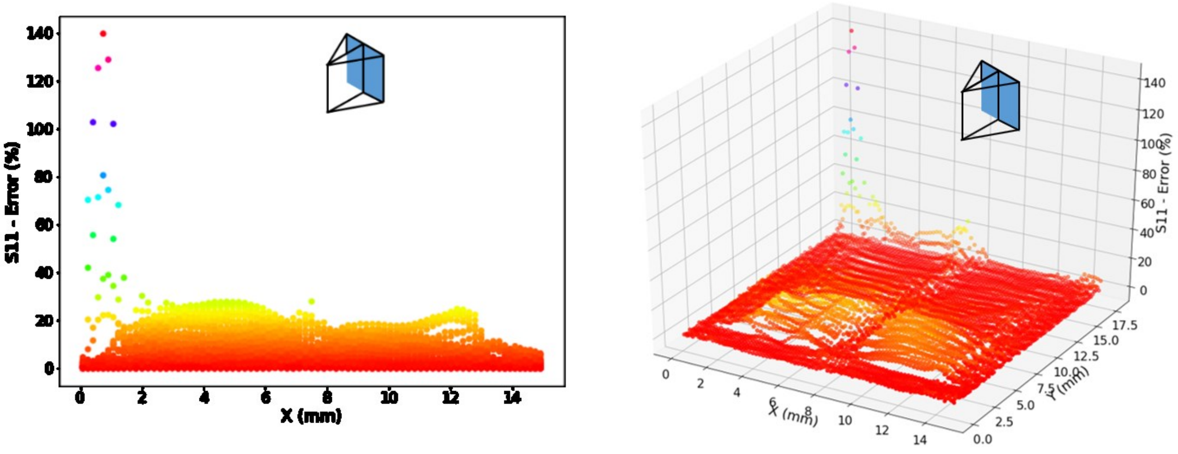

(d)

(e)

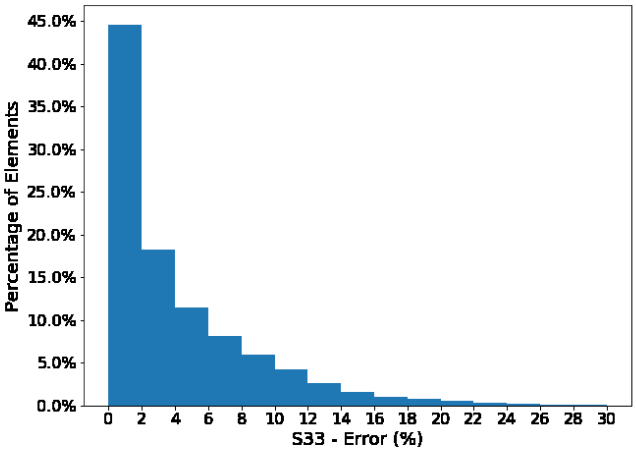

(f)

Figure 41 S11 distribution of 18-layers Arrow-shape wall (in MPa) (a) finite element analysis (b) ANN prediction (c) error value (%) (d) 2D error scatter (X-Y plane) (e) 3D error scatter (X-Y plane) (f) histogram of the error

Figure 42 shows the results for the prediction of S22 (stress component in the stacking direction or direction Y) of the 18-layers Arrow-shape structure. Figure 42 (a) and (b) show the S22 distribution in the form of contour obtained from the FE analysis and integrated ANN-FE method, respectively. It is noted that the high residual tensile stresses (S22) at the corners of the structure are captured well in the ANN-FE method as well as the stresses at the inner surfaces of the structure, i.e. in the inner side of the X-Y plane. High compressive residual stresses are formed in the predicted results from the integrated ANN-FE method that is not consistent with the results of the FE analysis. The high compressive stresses act on the free surface of the slope plane of the structure. However, the smooth transition of the residual stresses from the tensile to low-stress state and then to the local compressive stresses are observed in the top layers near the corners. Figure 42 (c) shows the calculated error in the contour format for the whole structure for the S22 stress component. As expected, very large error values are seen in the outer surface of the structure as a result of excessive compressive stresses predicted in the ANN-FE method. In order to quantify a number of elements that are associated with the high error rates shown in the contour, the 2D and 3D scatter errors are calculated and presented in Figure 42 (d) and (e), respectively. The majority of the elements with the red and yellow colors depict a prediction error of less than 10%. However, the green color dots represent the elements with 15-30% error in predicting the S22. A limited number of elements show an error beyond 30%. The histogram analysis is performed for the error data for S22 prediction and presented in Figure 42 (f). Approximately 7% of the elements are shown with error values greater than 15%. Although a considerable number of elements show large errors, most of the elements have error values in the acceptable range of 15%.

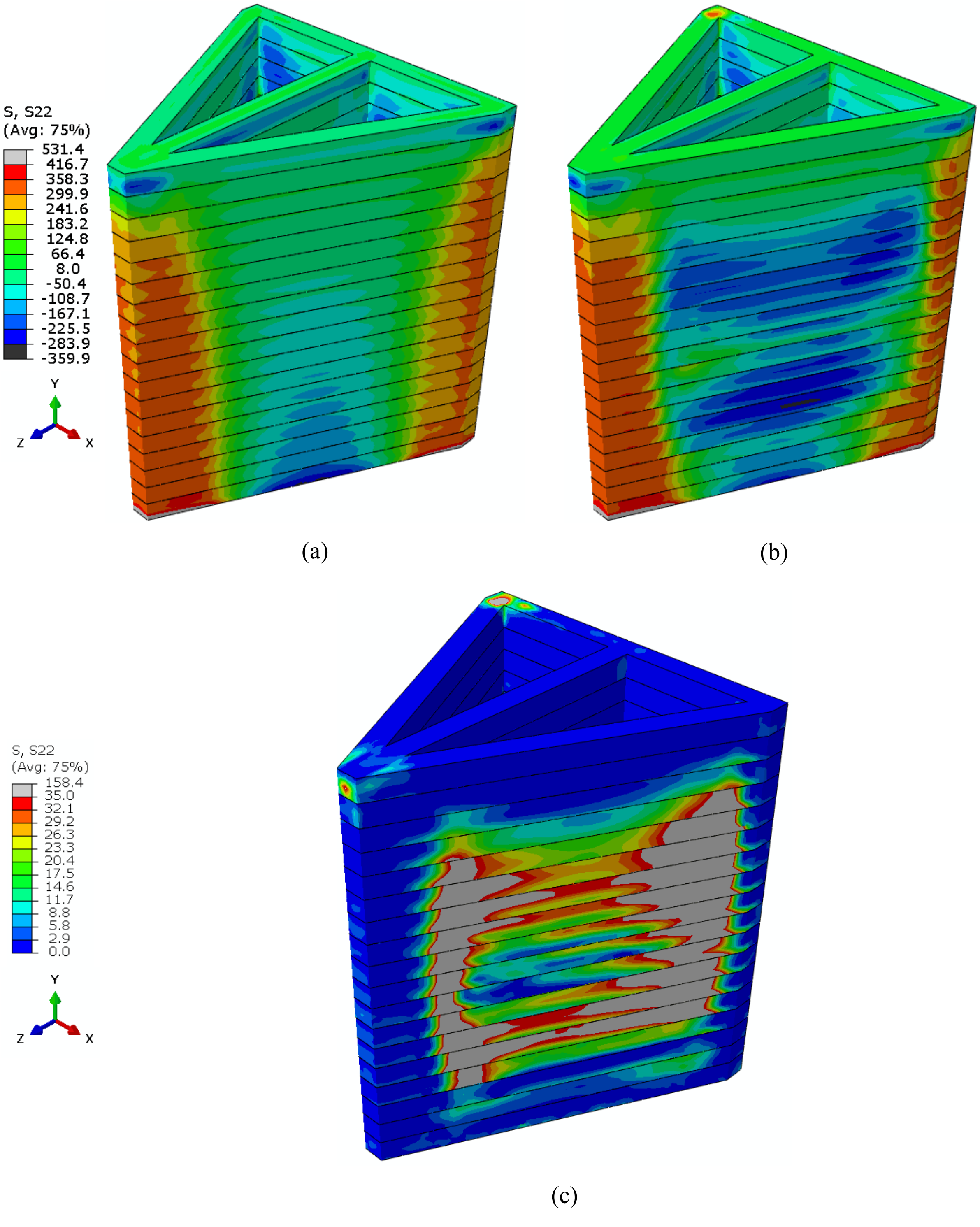
S, S22
(Avg: 75%)
531.4
416.7
358.3
299.9
241.6
183.2
124.8
66.4
8.0
-50.4
-108.7
-167.1
-225.5
-283.9
-359.9
Y
Z
X
S, S22
(Avg: 75%)
158.4
35.0
32.1
29.2
26.3
23.3
20.4
17.5
14.6
11.7
8.8
5.8
2.9
0.0
Y
Z
X

(a)

(b)

(c)

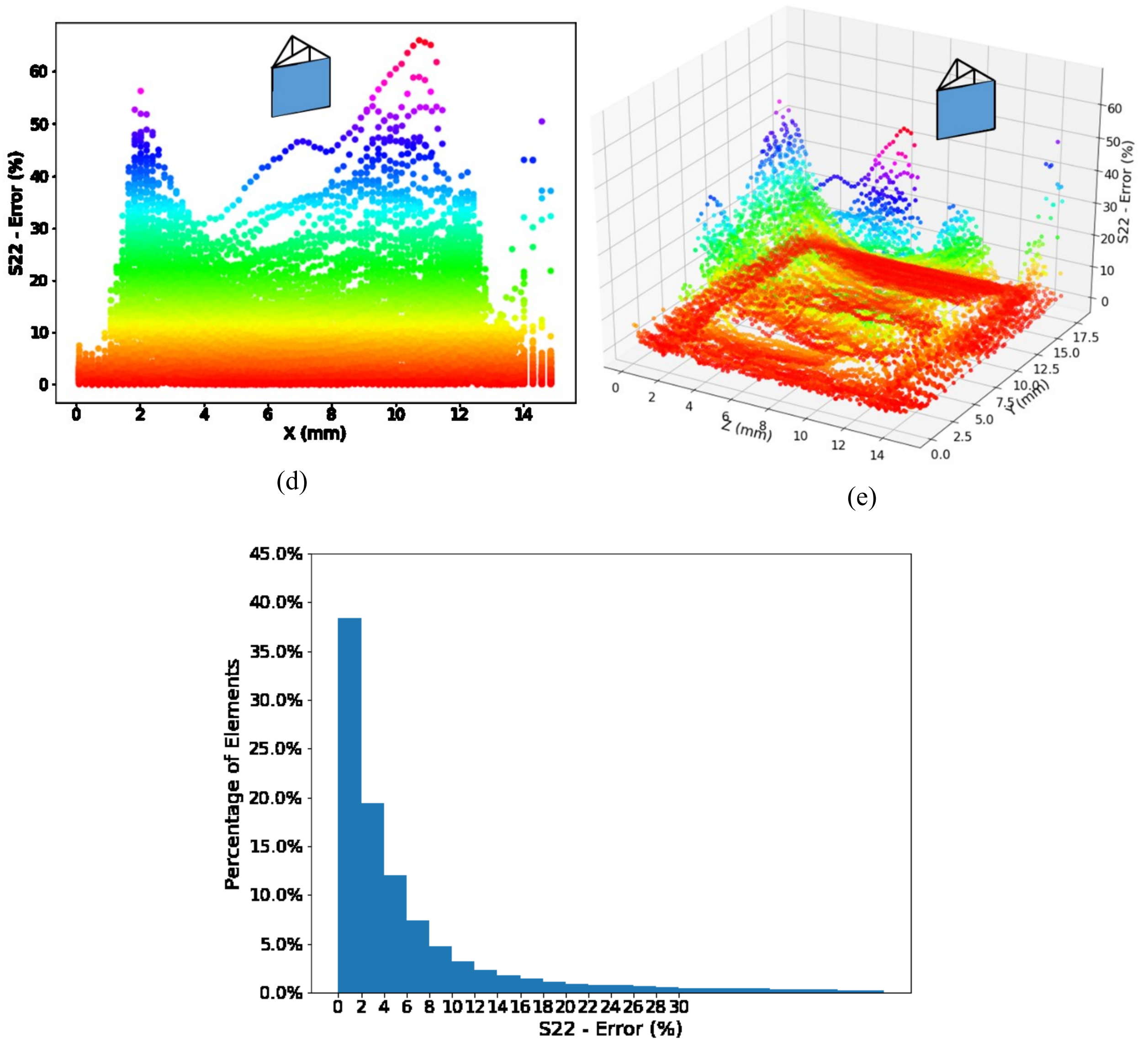

(d)

(e)

(f)

Figure 42 S22 distribution of 18-layers rectangular box (in MPa) (a) finite element analysis (b) ANN prediction (c) error value (%) (d) 2D error scatter (e) 3D error scatter (f) histogram of the error

Supplementary results for the other planes are provided in the supplementary section.

6.2.11. 18-layers cylinder

Figure 43 shows the stress results obtained from the FE analysis and the novel integrated ANN-FE method for the 18-layers cylinder. Figure 43 (a) and (b) demonstrate the S11 (stress component in direction X) obtained from the detailed finite element analysis and integrated ANN-FE approach, respectively. The residual stress distribution in the X-direction is well captured I the integrated ANN-FE analysis when the two contours are compared. The high residual tensile stresses are determined at the bottom of the first layer where it is attached to the substrate. The inner surfaces of the cylinder are shown to have high compressive residual stresses followed by a smooth transition into the low-stress state zone which is again, well captured in the ANN-FE analysis. The top layer seems to have tensile residual stresses in the thickness of the layer as shown in Figure 43 (c). Similar to the other structures, the 3D error of predicting S11 is obtained in contour format and depicted in Figure 43 (d). Most of the elements are shown in blue color that is associated with the estimation error of less than 4% in the longitudinal direction. The green color is also correlated with the error magnitudes of less than 15%. Very limited elements such as at the bottom of the first layer shown in red demonstrate an error higher than 15%. The histogram analysis of the prediction error for S11 is depicted in Figure 43 (e). The histogram analysis shows that the majority of the elements have a prediction error less than 15%. Approximately 3% of the elements show errors higher than 15% which is considered a very good accuracy.

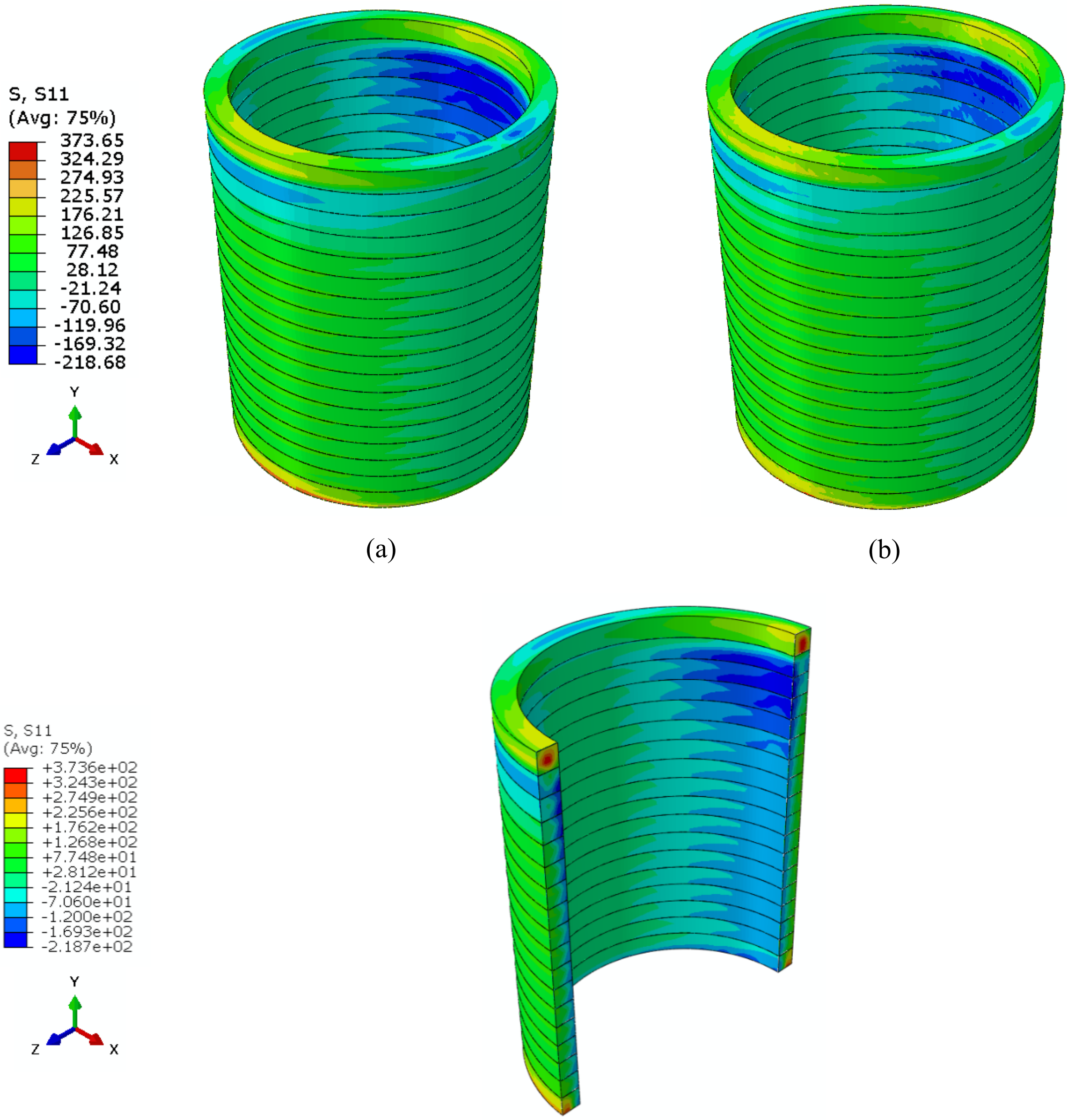

(a) (b)

(c)

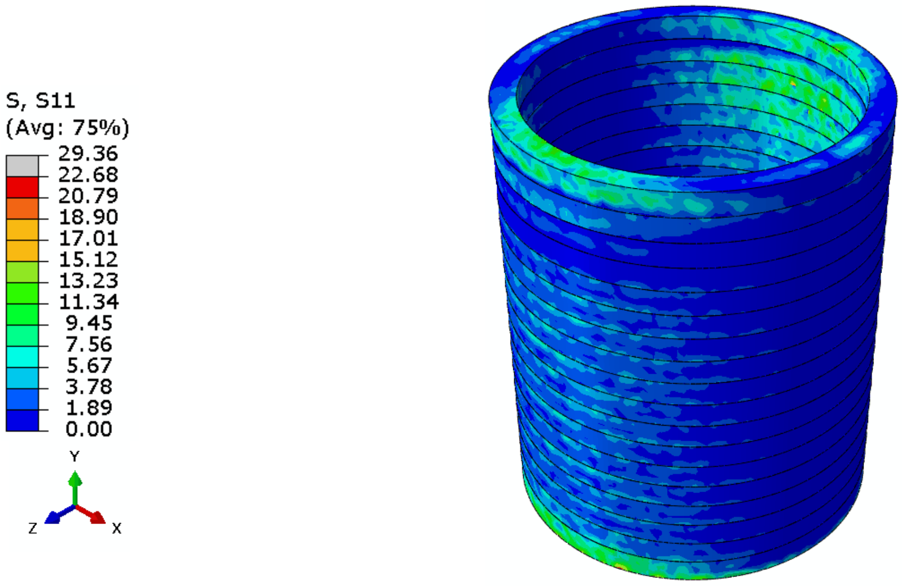

(d)

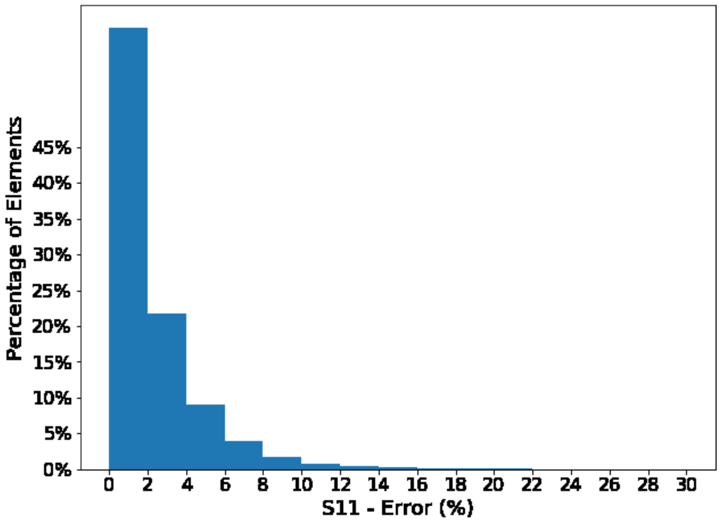

(e)

Figure 43 S11 distribution of 18-layers Cylinder (in MPa) (a) finite element analysis (b) ANN prediction (c) cut-view of the part (d) error value (%) (e) histogram of the error

Figure 44 shows the S22 distribution (stress component in the stacking direction or direction Y) for the 18-layers cylinder. Figure 44 (a) and (b) show the S22 obtained from FE analysis and the novel integrated ANN-FE approach, respectively. The stresses in the stacking direction (Y) is well captured in the integrated ANN-FE method as can be seen by comparing the two contours. The high residual tensile stresses are found on the outer free surface of the cylinder. On the other hand, high compressive residual stresses are formed in the inner free surface of the cylinder. The ANN-FE is capable of predicting the smooth transition of the S22 stress through the thickness of the cylinder. The residual tensile stresses are changed into almost ow stress state zone on the top three layers which are again captured by the ANN-FE approach. The mid part of the outer surface demonstrates a bit of underestimation of the S22 stress and is shown with a light green color in Figure 44 (b). The 3D error in the form of a contour is prepared for S22 as well to show the error distribution of predicting S22 and presented in Figure 44 (c). The top layers shown in blue color demonstrate the minimum error (<3%). And, most of the elements that are shown with green color illustrate an error of approximately 12%. Very localized regions and very limited elements show prediction error of higher than 15% that are shown in red color. The 3D error scatter calculated for the mid-plane of the cylinder and shown in Figure 44 (d). All the red, yellow, and green dots present the elements with a prediction error of less than 7%. Furthermore, dots with blue colors show the elements with an error of less than 15%. And, dots with the purple color show the elements with errors higher than 15%. The histogram analysis is performed on the error data of the S22 and depicted in Figure 44 (e). The histogram analysis shows that about 6% of the elements have a prediction error of higher than 15% which is an acceptable range in an analysis.

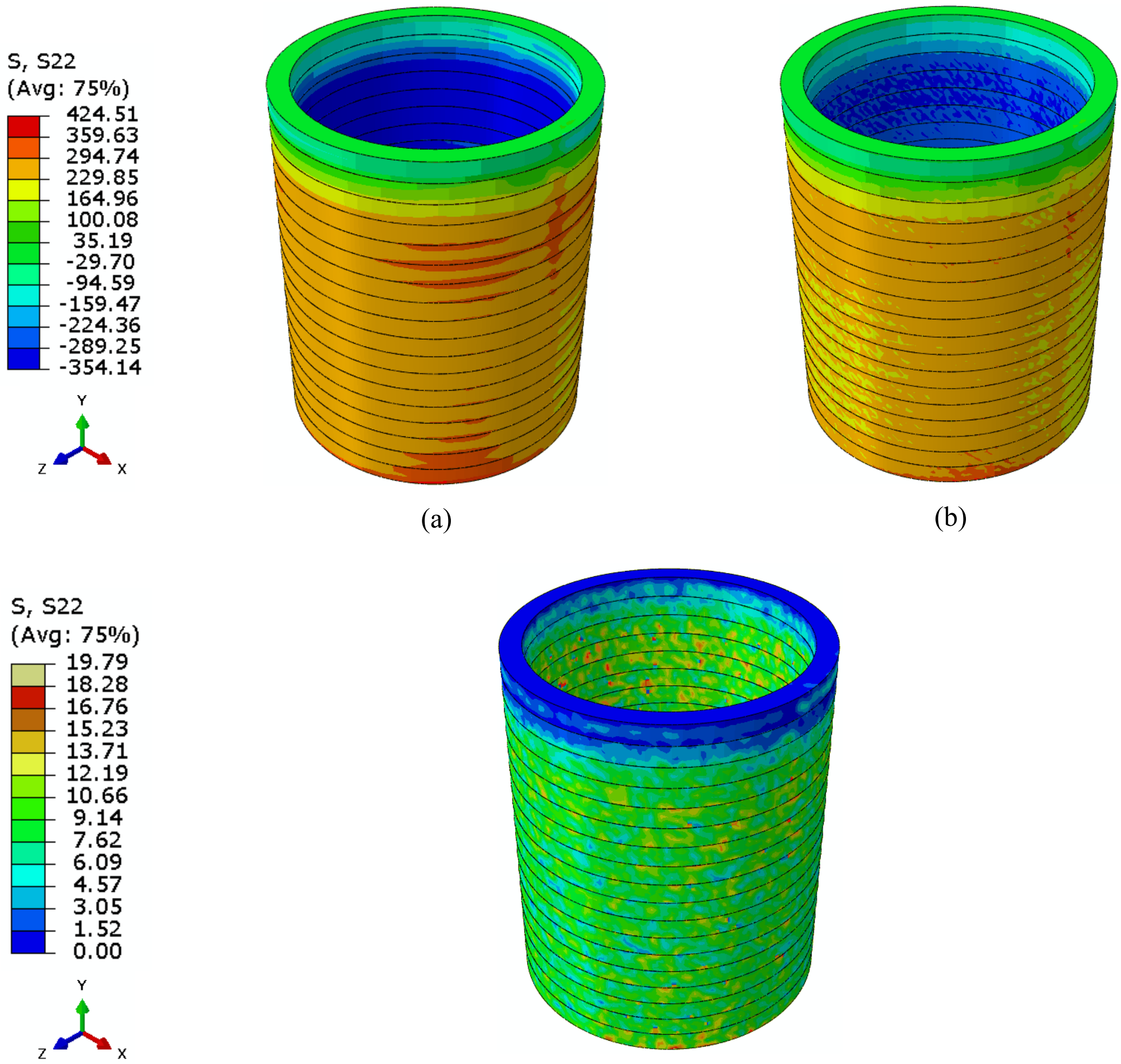

(a) (b)

(c)

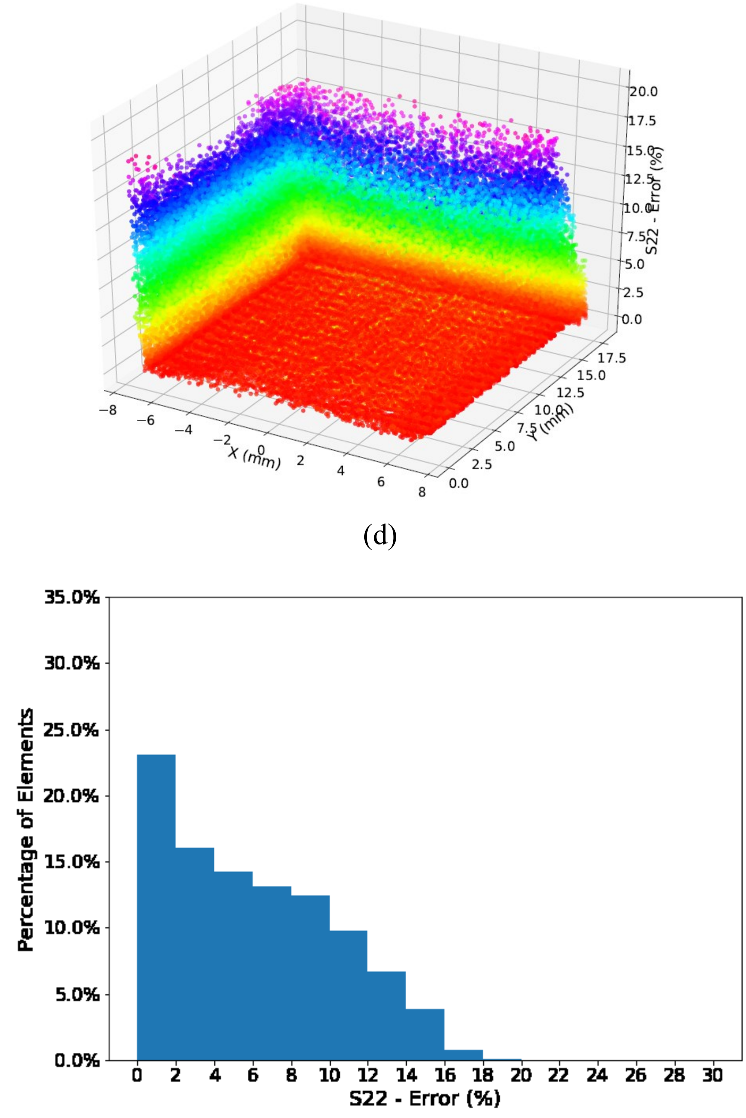

(d)

(e)

Figure 44 S22 distribution of 18-layers Cylinder (in MPa) (a) finite element analysis (b) ANN prediction (c) error value (%) (d) 3D error scatter (e) histogram of the error

6.3. Summary and discussion

A summary of the error analysis for the selected structures considered in the present study is provided in Table 10. The percentages of the elements with a prediction error of higher than 15% for all the structures are summarized in the table. As mentioned in section 5.3, different artificial neural networks were constructed for each structure with different neurons based on the length of the input data of the structure. However, by comparing the results of different structures, no simple explanation can be made to justify the variety of the element percentages whose errors exceed the allowable error rate. For some cases developed at the early stages of this research, i.e. simple wall, a fraction of the elements with higher than 15% error exceeds more complex structures investigated in the present study. For instance, for the S11 of the wall structure, about 12% of the elements demonstrate an error higher than 15%. On the other hand, for BoxPlus shape structure which is more complex than the simple wall, the fraction of the elements that exceed the acceptable error ranges is about 5%. This can certainly be associated with the low and insufficient number of neurons and epochs considered for the simple wall for training of the network.

Moreover, the structures that are similar to each other, such as T-shape and wall, exhibit approximately the same behavior in terms of the number of elements that have error values of more than 15%. The percentages for these two structures are quite comparable which seems sensible. This means that the implemented ANN-FE approach is able to correlate the geometries that are similar to one another. By comparing the results shown in Table 10, it can be realized that the geometries with less complexity and irregularities have fewer elements exhibiting errors beyond 15%. For instance, the results obtained for Hourglass, SemiBox, and H-shape demonstrate higher fraction of elements with errors beyond the allowable range. Based on the data structure fed into the network, it is concluded that the lack of sufficient data related to the geometrical complexities' effect causes this error.

To the best knowledge of the author, there is no theoretical and straightforward methodology for determining and implementing a number of neurons and hidden layers while constructing the ANN. Therefore, the training step of implementing the ANN-FE approach should be repeated until better performance of the ANN is achieved. This may be the main drawback of employing ANN for prediction purposes.

The main objective of the present study is to improve the computational time of predicting the residual stresses in the DMD fabricated parts. Therefore, the computational times of both method, conventional detailed FE analysis and the proposed novel approach of integrating ANN-FE, will be presented and discussed.

The computational time of the FE is associated with both thermal and mechanical FE analyses. The time for developing models with Python scripts is not considered in the computational time of the FE analysis. On the other hand, the computational time of the novel ANN-FE approach is mainly dominated by the training time for the ANN and the time for generating data sets and importing them into the network is not considered in the computational time of the ANN-FE. Considering that after the training is performed for a given data set, the prediction time for the test data is quick; less than a minute! Also, the time for generating the 3D contours of the predicted data from the ANN-FE is not considered since it is very quick; less than a few seconds. However,

Table 10 Percentage of elements in each structure with the prediction error higher than 15%

Structure	Percentage of the elements	
	S11/S33	S22
Straight wall	12	4
L-wall	6	3
Box	5	8
T-shape	7	2
H-shape	17	12
Plus-shape	8	6
BoxPlus-shape	5	12
SemiBox-shape	5	20
Hourglass-shape	20	8
Arrow-shape	5	7
Cylinder	3	6

it requires developing post-processing codes for accessing the predicted data and assigning them to the contour obtained from the ABAQUS.

The computational time of both methods for each structure is listed in Table 11 along with the percentage of improvement in the computational time. The training time of the ANN is different for every structure based on the size of the dataset, the number of hidden layers, the number of neurons in each layer of the network, and the number of epochs for training the network. By comparing the computational time of the thermomechanical FE analysis and the novel ANN-FE integrated approach for every part, it is evident that the computational time for all the parts has improved significantly. It is worth noting that the computational time of the proposed novel ANN-FE method is significantly improved compared to the FE analysis. The greatest improvement in the computational time belongs to T-shape structure with about 8.9 improvements. And, the lowest improvement in the computational time belongs to the Plus-shape wall with approximately 3.8 times improvement. It is noted for the complex structures with very high computational time, the improvement is about 6 times which is considered a great achievement. As mentioned, the computational time of the novel integrated ANN-FE model is governed by the training time of the ANNs. However, once the network is trained, it can be used for any type of prediction regarding the study of the effect of process parameters on the residual distribution of the DMD fabricated part with the same geometry. In other words, for any combination of the process parameters, a simple pure heat transfer analysis is performed to obtain the temperature history of the elements, then, it will be fed into the trained network to predict the residual stress distribution of the DMD part. Therefore, the computational time will be significantly lower since there is no need for training the network anymore. Therefore, by having a well-trained artificial neural network, the computational time of predicting the residual stress distribution is governed by the thermal analysis which is very quick compared to the complex mechanical analysis. This means the integrated ANN-FE approach is most beneficial for complex shapes with a higher number of elements which makes the thermomechanical FE analysis more time-consuming.

Table 11 Comparison of computational time between FE-based model and ANN-FE model

Structure	Computational time (hour)		Improvement in calculation time
	FE analysis	Integrated ANN-FE	
Straight wall	26	6	4.3
L-wall	69	12	5.7
Box	128	20	6.4
T-shape	58	6.5	8.9
H-shape	76.5	10	7.6
Plus-shape	27	7	3.8
BoxPlus-shape	159	28	5.6
SemiBox-shape	135	22	6.1
Hourglass-shape	130	20.5	6.3
Arrow-shape	128	21	6
Cylinder	66	10	6.6

The computational time of the simple wall structure via using the Core i7 desktop PC with 16 GB RAM and also improvement in the computational time is given in Table 12. As can be seen, an improvement of about 3 times was achieved in the application of the adaptive mesh-based technique to reduce the computational time. However, because of the demanding process of applying the method to a complex structure, the technique was not applied to complex structures.

Table 12 Comparison of run time between fine mesh and adaptive mesh

Adaptive mesh	Layers No.	1-3	4-6	7-9	10-12	13-15	16-18	Total (hour)
	Run time (hour)	1:50	2:35	3:20	3:50	4:15	4:20	20:10 + 2:00 (mapping)
Fine mesh	Layers No.	1-18						
	Run time (hour)	58:30						58:30

The developed method demonstrated significant improvement in the computational time and consistent results with the FE analysis. However, it has certain limits and shortcomings in the early stages of development. Some of the main limitations are listed as follow:

- The developed novel approach can only be used for the cases with single-track laser. It means that the developed method was not applicable to multiple tracks deposition processes at this stage.
- The developed method was applied to the simplified and straight wall structures. As the continuation of the research, the method can be examined for its capabilities for practical and more complex components.
- As a part of this research, the developed novel approach was applied to AISI 304L. However, it was not applied to other materials to evaluate its capabilities in the residual stress prediction of other materials.
- A unique ANNs was constructed, trained, and used for each structure which makes the process more inclusive of the geometrical complexities. Therefore, a single comprehensive ANN was not developed as a general tool for predicting residual stresses.

6.4. Conclusion

A novel approach of integrating ANNs with the well-known FE analysis is developed and proposed in the current thesis to introduce the concept of machine learning into the field of assessing the thermomechanical response of metal alloys as in direct metal deposition processes. Prediction of the residual stress distribution of the DMD fabricated parts using the conventional

FE method is very time-consuming especially when a large-scale structure is to be investigated. Therefore, a novel method of ANN-FE is proposed to equip the design team with a reliable and efficient tool to assess the thermomechanical response of a part. The adaptive mesh-based technique is also employed in the present study to make a good comparison of the results considering the computational time of determining the residual stress distributions for DMD parts.

The novel approach of integrated ANN-FE is applied to several structures to predict the residual stresses within their medium and to study the improvement in the computational time of the analysis as the method was used. Detailed FE analyses are performed using ABAQUS commercial package to accurately obtain the residual stress distributions of the parts and use the results as the comparing reference to the results of the ANN-FE. In order to develop the novel approach, FE analyses are performed on 12-layers and 18-layers structural parts and the temperature history of elements alongside the final stress distribution of elements are recorded. The training dataset is obtained with the results of 12-layers structures. Afterward, the ANNs are trained for each structure and the predictions are made with the input data from the 18-layers structure. Finally, the results from the FE analyses and predictions from ANN are compared and the error value and the distribution of the error is evaluated. The most valuable outcomes of the present study are listed in the following:

- The results of the original FE analysis and the results obtained from applying the novel integrated ANN-FE approach to the structures are in good agreement and the stress distribution pattern obtained from the integrated ANN-FE approach is consistent with the result of the detailed FE analysis.
- The ANN algorithms show the promising capability of being employed in the field of solid mechanics and for the prediction and evaluation of residual stresses in the DMD process.
- A very limited number of elements showed a prediction error higher than 15%. For the cases considered in the present study, the 18-layers L-wall and cylinder showed more accurate results than the other structures; the percentage of elements with a prediction error higher than 15% was approximately 6 and 3% for S11 and 3 and 6% for S22, respectively.
- The more complex structures such as hourglass and H-shape structures considered in the study demonstrated higher prediction accuracy.
- The computational time for predicting the residual stresses improved significantly by employing the proposed integrated ANN-FE method; an improvement factor of approximately 8.9 is achieved for the T-shape structure. And, the lowest factor of improvement, 3.8, is associated with the Plus-shape structure. Most of the structures with a very large number of

elements such as the BoxPlus structure have proved to show about 6 times improvement in the computational time of predicting the residual stresses. It is truly beneficial to reduce the computational time of the structure from several days to several hours especially when the product is still on the early stages of development.

- The integrated ANN-FE can offer a significant improvement in the computational time of predicting the residual stress distribution of complex structures fabricated by the DMD process.

6.5. Future works

There are several scopes that can be extended based on the findings of this research as listed in the following:

1- The proposed method of integrated ANN-FE can be applied to the structures that were assumed to be constructed with only one laser pass in the thickness. However, real components may need several passes in the thickness direction to build the requested CAD file. Therefore, the model can be developed to test its capabilities in the prediction of residual stresses in thick and bulky structures.

2- The applied ANN-FE model showed significant improvement in the computational time of predicting the residual stress distribution inside a medium. However, reducing the training time and utilizing GPU-based machines may improve the training time of the network, hence, further improving the computational time.

3- The feed-forward artificial neural network was implemented in this research and the results for the accuracy of the results were in the acceptable ranges considering that the applied method is in the early stage of development. However, the training accuracy and also prediction of the stresses can be improved by employing other ML algorithms, such as LSTM, that are more advanced and may yield better predictions.

4- The data structure implemented in this research to catch the behavior of the material under thermal loads and boundary conditions may be improved/shortened to reduce the computational time of the ANN-FE. However, building a comprehensive data set that can include all states of the material for different structures and boundary conditions requires lots of effort and time.

5- A comprehensive ANNs can be developed and constructed for all of the structures that can predict the residual stresses regardless of the shape of the structure. Therefore, a general framework can be developed to address the limitation of the presented research regarding a unique ANN for each structure.

6- The concept of the inherent strain can also be integrated with ML to improve its shortcomings in estimating the residual stress distribution of very large and complex structures.

7- Experimental studies can also be performed and integrated with ML to act as the data generation method. However, it requires a lot of equipment to build the component and test it for extracting the residual stresses inside the medium.

References

[1] Carroll BE, Palmer TA, Beese AM. Anisotropic tensile behavior of Ti–6Al–4V components fabricated with directed energy deposition additive manufacturing. Acta Materialia. 2015;87:309-20.

[2] Murr LE, Gaytan SM, Ramirez DA, Martinez E, Hernandez J, Amato KN, et al. Metal fabrication by additive manufacturing using laser and electron beam melting technologies. Journal of Materials Science & Technology. 2012;28:1-14.

[3] Altenburg SJ, Straße A, Gumenyuk A, Maierhofer C. In-situ monitoring of a laser metal deposition (LMD) process: Comparison of MWIR, SWIR and high-speed NIR thermography. Quantitative InfraRed Thermography Journal. 2022;19:97-114.

[4] Chatterjee A, Sprague E, Mazumder J, Misra A. Hierarchical microstructures and deformation behavior of laser direct-metal-deposited Cu–Fe alloys. Materials Science and Engineering: A. 2021;802:140659.

[5] Ahn D-G. Directed energy deposition (DED) process: state of the art. International Journal of Precision Engineering and Manufacturing-Green Technology. 2021;8:703-42.

[6] Li B, Zheng H, Han C, Zhou K. Nanotwins-containing microstructure and superior mechanical strength of a Cu–9Al–5Fe–5Ni alloy additively manufactured by laser metal deposition. Additive Manufacturing. 2021;39:101825.

[7] Feenstra D, Banerjee R, Fraser H, Huang A, Molotnikov A, Birbilis N. Critical review of the state of the art in multi-material fabrication via directed energy deposition. Current Opinion in Solid State and Materials Science. 2021;25:100924.

[8] Wei C, Zhang Z, Cheng D, Sun Z, Zhu M, Li L. An overview of laser-based multiple metallic material additive manufacturing: from macro-to micro-scales. International Journal of Extreme Manufacturing. 2020;3:012003.

[9] Xie J, Lu H, Lu J, Song X, Wu S, Lei J. Additive manufacturing of tungsten using directed energy deposition for potential nuclear fusion application. Surface and Coatings Technology. 2021;409:126884.

[10] Ansari M, Jabari E, Toyserkani E. Opportunities and challenges in additive manufacturing of functionally graded metallic materials via powder-fed laser directed energy deposition: A review. Journal of Materials Processing Technology. 2021;294:117117.

[11] Svetlizky D, Das M, Zheng B, Vyatskikh AL, Bose S, Bandyopadhyay A, et al. Directed energy deposition (DED) additive manufacturing: Physical characteristics, defects, challenges and applications. Materials Today. 2021;49:271-95.

[12] Caiazzo F, Caggiano A. Laser direct metal deposition of 2024 Al alloy: trace geometry prediction via machine learning. Materials. 2018;11:444.

[13] Li Y, Sun Y, Han Q, Zhang G, Horváth I. Enhanced beads overlapping model for wire and arc additive manufacturing of multi-layer multi-bead metallic parts. Journal of Materials Processing Technology. 2018;252:838-48.

[14] Zhai P, Wang T, Jiang H, Wan J, Wei Y, Wang L, et al. 3D Artificial Solid-Electrolyte Interphase for Lithium Metal Anodes Enabled by Insulator–Metal–Insulator Layered Heterostructures. Advanced Materials. 2021;33:2006247.

[15] Blakey-Milner B, Gradl P, Snedden G, Brooks M, Pitot J, Lopez E, et al. Metal additive manufacturing in aerospace: A review. Materials & Design. 2021;209:110008.

[16] Chen L-Y, Liang S-X, Liu Y, Zhang L-C. Additive manufacturing of metallic lattice

structures: Unconstrained design, accurate fabrication, fascinated performances, and challenges. Materials Science and Engineering: R: Reports. 2021;146:100648.

[17] Vafadar A, Guzzomi F, Rassau A, Hayward K. Advances in metal additive manufacturing: a review of common processes, industrial applications, and current challenges. Applied Sciences. 2021;11:1213.

[18] Ghanavati R, Naffakh-Moosavy H. Additive manufacturing of functionally graded metallic materials: A review of experimental and numerical studies. Journal of Materials Research and Technology. 2021;13:1628-64.

[19] Jandyal A, Chaturvedi I, Wazir I, Raina A, Haq MIU. 3D printing–A review of processes, materials and applications in industry 4.0. Sustainable Operations and Computers. 2022;3:33-42.

[20] Gu D, Shi X, Poprawe R, Bourell DL, Setchi R, Zhu J. Material-structure-performance integrated laser-metal additive manufacturing. Science. 2021;372:eabg1487.

[21] Pragana J, Sampaio R, Bragança I, Silva C, Martins P. Hybrid metal additive manufacturing: A state–of–the-art review. Advances in Industrial and Manufacturing Engineering. 2021;2:100032.

[22] Liang X, Cheng L, Chen Q, Yang Q, To AC. A modified method for estimating inherent strains from detailed process simulation for fast residual distortion prediction of single-walled structures fabricated by directed energy deposition. Additive Manufacturing. 2018;23:471-86.

[23] Romano S, Brückner-Foit A, Brandão A, Gumpinger J, Ghidini T, Beretta S. Fatigue properties of AlSi10Mg obtained by additive manufacturing: Defect-based modelling and prediction of fatigue strength. Engineering Fracture Mechanics. 2018;187:165-89.

[24] Mukherjee T, Zhang W, DebRoy T. An improved prediction of residual stresses and distortion in additive manufacturing. Computational Materials Science. 2017;126:360-72.

[25] Olabi A, Hashmi M. Stress relief procedures for low carbon steel (1020) welded components. Journal of materials processing technology. 1996;56:552-62.

[26] Rossini N, Dassisti M, Benyounis K, Olabi A-G. Methods of measuring residual stresses in components. Materials & Design. 2012;35:572-88.

[27] Tebedge N, Alpsten G, Tall L. Residual-stress measurement by the sectioning method. Experimental Mechanics. 1973;13:88-96.

[28] Withers PJ, Bhadeshia H. Residual stress. Part 1–measurement techniques. Materials science and Technology. 2001;17:355-65.

[29] Hoye N, Li HJ, Cuiuri D, Paradowska AM. Measurement of residual stresses in titanium aerospace components formed via additive manufacturing. Materials Science Forum: Trans Tech Publ; 2014. p. 124-9.

[30] Ding J, Colegrove P, Mehnen J, Ganguly S, Almeida PS, Wang F, et al. Thermo-mechanical analysis of Wire and Arc Additive Layer Manufacturing process on large multi-layer parts. Computational Materials Science. 2011;50:3315-22.

[31] Colegrove PA, Coules HE, Fairman J, Martina F, Kashoob T, Mamash H, et al. Microstructure and residual stress improvement in wire and arc additively manufactured parts through high-pressure rolling. Journal of Materials Processing Technology. 2013;213:1782-91.

[32] Wu AS, Brown DW, Kumar M, Gallegos GF, King WE. An experimental investigation into additive manufacturing-induced residual stresses in 316L stainless steel. Metallurgical and Materials Transactions A. 2014;45:6260-70.

[33] An K, Yuan L, Dial L, Spinelli I, Stoica AD, Gao Y. Neutron residual stress measurement

and numerical modeling in a curved thin-walled structure by laser powder bed fusion additive manufacturing. Materials & design. 2017;135:122-32.

[34] Cao J, Gharghouri MA, Nash P. Finite-element analysis and experimental validation of thermal residual stress and distortion in electron beam additive manufactured Ti-6Al-4V build plates. Journal of Materials Processing Technology. 2016;237:409-19.

[35] Simson T, Emmel A, Dwars A, Böhm J. Residual stress measurements on AISI 316L samples manufactured by selective laser melting. Additive Manufacturing. 2017;17:183-9.

[36] Ahmad B, van der Veen SO, Fitzpatrick ME, Guo H. Residual stress evaluation in selective-laser-melting additively manufactured titanium (Ti-6Al-4V) and inconel 718 using the contour method and numerical simulation. Additive Manufacturing. 2018;22:571-82.

[37] Knowles C, Becker T, Tait R. Residual stress measurements and structural integrity implications for selective laser melted Ti-6Al-4V: general article. South African Journal of Industrial Engineering. 2012;23:119-29.

[38] Wang Y, Li Q, Qian L, Yang Y. A modified inherent strain model with consideration of the variance of mechanical properties in metal additive manufacturing. Journal of Manufacturing Processes. 2021;72:115-25.

[39] Setien I, Chiumenti M, van der Veen S, San Sebastian M, Garciandía F, Echeverría A. Empirical methodology to determine inherent strains in additive manufacturing. Computers & Mathematics with Applications. 2019;78:2282-95.

[40] Zeng K, Pal D, Gong H, Patil N, Stucker B. Comparison of 3DSIM thermal modelling of selective laser melting using new dynamic meshing method to ANSYS. Materials Science and Technology. 2015;31:945-56.

[41] Olleak A, Xi Z. Efficient lpbf process simulation using finite element modeling with adaptive remeshing for distortions and residual stresses prediction. Manufacturing Letters. 2020;24:140-4.

[42] Pal D, Patil N, Kutty KH, Zeng K, Moreland A, Hicks A, et al. A generalized feed-forward dynamic adaptive mesh refinement and derefinement finite-element framework for metal laser sintering—Part II: Nonlinear thermal simulations and validations. Journal of Manufacturing Science and Engineering. 2016;138.

[43] Patil N, Pal D, Khalid Rafi H, Zeng K, Moreland A, Hicks A, et al. A generalized feed forward dynamic adaptive mesh refinement and derefinement finite element framework for metal laser sintering—part I: formulation and algorithm development. Journal of Manufacturing Science and Engineering. 2015;137.

[44] Baiges J, Chiumenti M, Moreira CA, Cervera M, Codina R. An Adaptive Finite Element strategy for the numerical simulation of Additive Manufacturing processes. Additive Manufacturing. 2021;37:101650.

[45] Lempitsky V, Zisserman A. Learning to count objects in images. Advances in neural information processing systems. 2010;23.

[46] Gulikers T. An Integrated Machine Learning and Finite Element Analysis Framework, Applied to Composite Substructures including Damage. 2018.

[47] Bontha S, Klingbeil NW. Effect of a distributed heat source on melt pool geometry and microstructure in beam-based solid freeform fabrication. 2006 International Solid Freeform Fabrication Symposium2006.

[48] Tapia G, Elwany AH, Sang H. Prediction of porosity in metal-based additive manufacturing using spatial Gaussian process models. Additive Manufacturing. 2016;12:282-90.

[49] Ren K, Chew Y, Zhang Y, Bi G, Fuh J. Thermal analyses for optimal scanning pattern evaluation in laser aided additive manufacturing. Journal of Materials Processing Technology. 2019;271:178-88.

[50] Thai H-T. Machine learning for structural engineering: A state-of-the-art review. Structures: Elsevier; 2022. p. 448-91.

[51] Hajializadeh F, Ince A. Integration of artificial neural network with finite element analysis for residual stress prediction of direct metal deposition process. Materials Today Communications. 2021;27:102197.

[52] Hajializadeh F, Ince A. Finite element–based numerical modeling framework for additive manufacturing process. Material Design & Processing Communications. 2019;1:e28.

[53] Free JA, Goff RFP. Predicting residual stresses in multi-pass weldments with the finite element method. Computers & structures. 1989;32:365-78.

[54] Krol T, Seidel C, Schilp J, Hofmann M, Gan W, Zaeh M. Verification of structural simulation results of metal-based additive manufacturing by means of neutron diffraction. Physics Procedia. 2013;41:849-57.

[55] Liu R, Kumar A, Chen Z, Agrawal A, Sundararaghavan V, Choudhary A. A predictive machine learning approach for microstructure optimization and materials design. Scientific reports. 2015;5:1-12.

[56] Chen Q, Liang X, Hayduke D, Liu J, Cheng L, Oskin J, et al. An inherent strain based multiscale modeling framework for simulating part-scale residual deformation for direct metal laser sintering. Additive Manufacturing. 2019;28:406-18.

[57] Zhang Z-D, Ibhadode O, Ali U, Dibia CF, Rahnama P, Bonakdar A, et al. Topology optimization parallel-computing framework based on the inherent strain method for support structure design in laser powder-bed fusion additive manufacturing. International Journal of Mechanics and Materials in Design. 2020;16:897-923.

[58] Cheng L, Liang X, Bai J, Chen Q, Lemon J, To A. On utilizing topology optimization to design support structure to prevent residual stress induced build failure in laser powder bed metal additive manufacturing. Additive Manufacturing. 2019;27:290-304.

[59] Schoinochoritis B, Chantzis D, Salonitis K. Simulation of metallic powder bed additive manufacturing processes with the finite element method: A critical review. Proceedings of the Institution of Mechanical Engineers, Part B: Journal of Engineering Manufacture. 2017;231:96-117.

[60] Chen S-g, Wu Q, Gao H-j, Gao Z-h, Li X. Effect of solid-state phase transformation on residual stress of selective laser melting Ti6Al4V. Materials Science and Engineering: A. 2021;819:141299.

[61] Denlinger ER, Michaleris P. Effect of stress relaxation on distortion in additive manufacturing process modeling. Additive Manufacturing. 2016;12:51-9.

[62] Hussein A, Hao L, Yan C, Everson R. Finite element simulation of the temperature and stress fields in single layers built without-support in selective laser melting. Materials & Design (1980-2015). 2013;52:638-47.

[63] Hibbitt HD, Marcal PV. A numerical, thermo-mechanical model for the welding and subsequent loading of a fabricated structure. Computers & Structures. 1973;3:1145-74.

[64] Zhao X, Iyer A, Promoppatum P, Yao S-C. Numerical modeling of the thermal behavior and residual stress in the direct metal laser sintering process of titanium alloy products. Additive

Manufacturing. 2017;14:126-36.

[65] Gu D, He B. Finite element simulation and experimental investigation of residual stresses in selective laser melted Ti–Ni shape memory alloy. Computational Materials Science. 2016;117:221-32.

[66] Ueda Y, Fukuda K, Kim YC. New measuring method of axisymmetric three-dimensional residual stresses using inherent strains as parameters. 1986.

[67] Dalaee MT, Gloor L, Leinenbach C, Wegener K. Experimental and numerical study of the influence of induction heating process on build rates Induction Heating-assisted laser Direct Metal Deposition (IH-DMD). Surface and Coatings Technology. 2020;384:125275.

[68] Kumar SP, Elangovan S, Mohanraj R, Narayanan VS. Significance of continuous wave and pulsed wave laser in direct metal deposition. Materials Today: Proceedings. 2021;46:8086-96.

[69] Chen B, Su Y, Xie Z, Tan C, Feng J. Development and characterization of 316L/Inconel625 functionally graded material fabricated by laser direct metal deposition. Optics & Laser Technology. 2020;123:105916.

[70] Pant P, Chatterjee D, Samanta SK, Nandi T, Lohar AK. A bottom-up approach to experimentally investigate the deposition of austenitic stainless steel in laser direct metal deposition system. Journal of the Brazilian Society of Mechanical Sciences and Engineering. 2020;42:1-10.

[71] Mirkoohi E, Dobbs JR, Liang SY. Analytical modeling of residual stress in direct metal deposition considering scan strategy. The International Journal of Advanced Manufacturing Technology. 2020;106:4105-21.

[72] Mianji Z, Kholopov A, Binkov I, Kiani A. Numerical simulation of thermal behavior and experimental investigation of thin walls during direct metal deposition of 316L stainless steel powder. Lasers in Manufacturing and Materials Processing. 2021;8:426-42.

[73] Soffel F, Eisenbarth D, Hosseini E, Wegener K. Interface strength and mechanical properties of Inconel 718 processed sequentially by casting, milling, and direct metal deposition. Journal of Materials Processing Technology. 2021;291:117021.

[74] Yan L, Chen Y, Liou F. Additive manufacturing of functionally graded metallic materials using laser metal deposition. Additive Manufacturing. 2020;31:100901.

[75] Sibisi PN, Popoola A, Arthur NK, Pityana SL. Review on direct metal laser deposition manufacturing technology for the Ti-6Al-4V alloy. The International Journal of Advanced Manufacturing Technology. 2020;107:1163-78.

[76] Pant P, Chatterjee D, Samanta SK, Lohar AK. Experimental and numerical analysis of the powder flow in a multi-channel coaxial nozzle of a direct metal deposition system. Journal of Manufacturing Science and Engineering. 2021;143.

[77] Zhang H, Zhu L, Xue P. Laser direct metal deposition of variable width thin-walled structures in Inconel 718 alloy by coaxial powder feeding. The International Journal of Advanced Manufacturing Technology. 2020;108:821-40.

[78] Gokhale NP, Kala P. Thermal analysis of TIG-WAAM based metal deposition process using finite element method. Materials Today: Proceedings. 2021;44:453-9.

[79] Chen M, Lu Y, Wang Z, Lan H, Sun G, Ni Z. Melt pool evolution on inclined NV E690 steel plates during laser direct metal deposition. Optics & Laser Technology. 2021;136:106745.

[80] Zhu Z, Chen B, Gou G, Zhang Z, Ma C, Gao W. Effect of solid state phase transformation on the residual stress in multi-pass weld plates of S355J2W steel. International Journal of Modern

Physics B. 2019;33:1940046.

[81] Jiang W, Wang B, Gong J, Tu S. Finite element analysis of the effect of welding heat input and layer number on residual stress in repair welds for a stainless steel clad plate. Materials & Design. 2011;32:2851-7.

[82] Barsoum Z, Lundbäck A. Simplified FE welding simulation of fillet welds–3D effects on the formation residual stresses. Engineering Failure Analysis. 2009;16:2281-9.

[83] Ahn J, He E, Chen L, Wimpory R, Kabra S, Dear J, et al. FEM prediction of welding residual stresses in fibre laser-welded AA 2024-T3 and comparison with experimental measurement. The International Journal of Advanced Manufacturing Technology. 2018;95:4243-63.

[84] Cho J, Lee B, Moon Y, Van Tyne C. Investigation of residual stress and post weld heat treatment of multi-pass welds by finite element method and experiments. Journal of materials processing technology. 2004;155:1690-5.

[85] Jiang W, Zhang Y, Woo W. Using heat sink technology to decrease residual stress in 316L stainless steel welding joint: Finite element simulation. International journal of pressure vessels and piping. 2012;92:56-62.

[86] Nasir NSM, Razab MKAA, Mamat S, Iqbal M. Review on welding residual stress. stress. 2006;2:8-10.

[87] Deng D, Kiyoshima S, Ogawa K, Yanagida N, Saito K. Predicting welding residual stresses in a dissimilar metal girth welded pipe using 3D finite element model with a simplified heat source. Nuclear Engineering and Design. 2011;241:46-54.

[88] Bao R, Zhang X, Yahaya NA. Evaluating stress intensity factors due to weld residual stresses by the weight function and finite element methods. Engineering Fracture Mechanics. 2010;77:2550-66.

[89] Deng D, Murakawa H, Liang W. Numerical and experimental investigations on welding residual stress in multi-pass butt-welded austenitic stainless steel pipe. Computational Materials Science. 2008;42:234-44.

[90] Xie X-f, Jiang W, Luo Y, Xu S, Gong J-M, Tu S-T. A model to predict the relaxation of weld residual stress by cyclic load: Experimental and finite element modeling. International Journal of Fatigue. 2017;95:293-301.

[91] Deng D, Murakawa H. Prediction of welding distortion and residual stress in a thin plate butt-welded joint. Computational Materials Science. 2008;43:353-65.

[92] Zhang W, Jiang W, Zhao X, Tu S-T. Fatigue life of a dissimilar welded joint considering the weld residual stress: Experimental and finite element simulation. International Journal of Fatigue. 2018;109:182-90.

[93] Ogawa K, Deng D, Kiyoshima S, Yanagida N, Saito K. Investigations on welding residual stresses in penetration nozzles by means of 3D thermal elastic plastic FEM and experiment. Computational materials science. 2009;45:1031-42.

[94] Wikander L, Karlsson L, Nasstrom M, Webster P. Finite element simulation and measurement of welding residual stresses. Modelling and Simulation in Materials Science and Engineering. 1994;2:845.

[95] Rong Y, Xu J, Huang Y, Zhang G. Review on finite element analysis of welding deformation and residual stress. Science and Technology of Welding and Joining. 2018;23:198-208.

[96] Deng D, Kiyoshima S. FEM prediction of welding residual stresses in a SUS304 girth-welded pipe with emphasis on stress distribution near weld start/end location. Computational Materials

Science. 2010;50:612-21.

[97] Deng D. FEM prediction of welding residual stress and distortion in carbon steel considering phase transformation effects. Materials & Design. 2009;30:359-66.

[98] Bian P, Shi J, Shao X, Du J. Evolution of cyclic thermal stress in selective laser melting of 316L stainless steel: a realistic numerical study with experimental verification. The International Journal of Advanced Manufacturing Technology. 2019;104:3867-82.

[99] Parry L, Ashcroft I, Wildman R. Geometrical effects on residual stress in selective laser melting. Additive Manufacturing. 2019;25:166-75.

[100] Heigel J, Michaleris P, Reutzel EW. Thermo-mechanical model development and validation of directed energy deposition additive manufacturing of Ti–6Al–4V. Additive manufacturing. 2015;5:9-19.

[101] Hodge N, Ferencz R, Solberg J. Implementation of a thermomechanical model for the simulation of selective laser melting. Computational Mechanics. 2014;54:33-51.

[102] Van Belle L, Vansteenkiste G, Boyer JC. Comparisons of numerical modelling of the Selective Laser Melting. Key engineering materials: Trans Tech Publ; 2012. p. 1067-72.

[103] Wang Z, Denlinger E, Michaleris P, Stoica AD, Ma D, Beese AM. Residual stress mapping in Inconel 625 fabricated through additive manufacturing: Method for neutron diffraction measurements to validate thermomechanical model predictions. Materials & Design. 2017;113:169-77.

[104] Matsumoto M, Shiomi M, Osakada K, Abe F. Finite element analysis of single layer forming on metallic powder bed in rapid prototyping by selective laser processing. International Journal of Machine Tools and Manufacture. 2002;42:61-7.

[105] Nickel A, Barnett D, Prinz F. Thermal stresses and deposition patterns in layered manufacturing. Materials Science and Engineering: A. 2001;317:59-64.

[106] Klingbeil NW, Beuth JL, Chin R, Amon C. Residual stress-induced warping in direct metal solid freeform fabrication. International Journal of Mechanical Sciences. 2002;44:57-77.

[107] Kruth J-P, Froyen L, Van Vaerenbergh J, Mercelis P, Rombouts M, Lauwers B. Selective laser melting of iron-based powder. Journal of materials processing technology. 2004;149:616-22.

[108] Chin R, Beuth J, Amon C. Successive deposition of metals in solid freeform fabrication processes, Part 1: thermomechanical models of layers and droplet columns. J Manuf Sci Eng. 2001;123:623-31.

[109] Roberts IA. Investigation of residual stresses in the laser melting of metal powders in additive layer manufacturing. 2012.

[110] Arni R, Gupta S. Manufacturability analysis of flatness tolerances in solid freeform fabrication. J Mech Des. 2001;123:148-56.

[111] Zaeh M, Branner G, Krol T. A three dimensional FE-model for the investigation of transient physical effects in Selective Laser Melting. Innovative developments in design and manufacturing: CRC Press; 2009. p. 433-42.

[112] Lundbäck A, Pederson R, Colliander MH, Brice C, Steuwer A, Heralic A, et al. Modeling and experimental measurement with synchrotron radiation of residual stresses in laser metal deposited Ti-6Al-4V. Proceedings of the 13th World Conference on Titanium; Venkatesh, V, Pilchak, AL, Allison, JE, Ankem, S, Boyer, R, Christodoulou, J, Fraser, HL, Imam, MA, Kosaka, Y, Rack, HJ, et al, Eds2016. p. 1279-82.

[113] Denlinger ER, Irwin J, Michaleris P. Thermomechanical modeling of additive

manufacturing large parts. Journal of Manufacturing Science and Engineering. 2014;136.

[114] Li C, Liu J, Fang X, Guo Y. Efficient predictive model of part distortion and residual stress in selective laser melting. Additive Manufacturing. 2017;17:157-68.

[115] Parry L, Ashcroft I, Wildman RD. Understanding the effect of laser scan strategy on residual stress in selective laser melting through thermo-mechanical simulation. Additive Manufacturing. 2016;12:1-15.

[116] Ghosh S, Choi J. Three-dimensional transient finite element analysis for residual stresses in the laser aided direct metal/material deposition process. Journal of laser applications. 2005;17:144-58.

[117] Vasinonta A, Beuth JL, Griffith M. Process maps for predicting residual stress and melt pool size in the laser-based fabrication of thin-walled structures. 2007.

[118] Megahed M, Mindt H-W, N'Dri N, Duan H, Desmaison O. Metal additive-manufacturing process and residual stress modeling. Integrating Materials and Manufacturing Innovation. 2016;5:61-93.

[119] Srivastava S, Garg RK, Sharma VS, Sachdeva A. Measurement and mitigation of residual stress in wire-arc additive manufacturing: A review of macro-scale continuum modelling approach. Archives of Computational Methods in Engineering. 2021;28:3491-515.

[120] Neiva E, Badia S, Martín AF, Chiumenti M. A scalable parallel finite element framework for growing geometries. Application to metal additive manufacturing. International Journal for Numerical Methods in Engineering. 2019;119:1098-125.

[121] Denlinger ER, Irwin J, Michaleris P. Thermomechanical modeling of additive manufacturing large parts. Journal of Manufacturing Science and Engineering. 2014;136:061007.

[122] Kollmannsberger S, Özcan A, Carraturo M, Zander N, Rank E. A hierarchical computational model for moving thermal loads and phase changes with applications to selective laser melting. Computers & Mathematics with Applications. 2018;75:1483-97.

[123] Gouge M, Denlinger E, Irwin J, Li C, Michaleris P. Experimental validation of thermo-mechanical part-scale modeling for laser powder bed fusion processes. Additive Manufacturing. 2019;29:100771.

[124] Hajializadeh F, Ince A. Finite Element based Numerical Modeling Framework for Additive Manufacturing Process. Mat Design Process Comm. 2019:1-7.

[125] Francois MM, Sun A, King WE, Henson NJ, Tourret D, Bronkhorst CA, et al. Modeling of additive manufacturing processes for metals: Challenges and opportunities. Current Opinion in Solid State and Materials Science. 2017;21:198-206.

[126] Ou W, Knapp G, Mukherjee T, Wei Y, DebRoy T. An improved heat transfer and fluid flow model of wire-arc additive manufacturing. International Journal of Heat and Mass Transfer. 2021;167:120835.

[127] Takezawa A, To AC, Chen Q, Liang X, Dugast F, Zhang X, et al. Sensitivity analysis and lattice density optimization for sequential inherent strain method used in additive manufacturing process. Computer Methods in Applied Mechanics and Engineering. 2020;370:113231.

[128] Liang X, Dong W, Hinnebusch S, Chen Q, Tran HT, Lemon J, et al. Inherent strain homogenization for fast residual deformation simulation of thin-walled lattice support structures built by laser powder bed fusion additive manufacturing. Additive Manufacturing. 2020;32:101091.

[129] Bugatti M, Semeraro Q. Limitations of the inherent strain method in simulating powder bed

fusion processes. Additive Manufacturing. 2018;23:329-46.

[130] Liang X, Dong W, Chen Q, To AC. On incorporating scanning strategy effects into the modified inherent strain modeling framework for laser powder bed fusion. Additive Manufacturing. 2021;37:101648.

[131] Sun L, Gao H, Pan S, Wang J-X. Surrogate modeling for fluid flows based on physics-constrained deep learning without simulation data. Computer Methods in Applied Mechanics and Engineering. 2020;361:112732.

[132] McBride K, Sundmacher K. Overview of surrogate modeling in chemical process engineering. Chemie Ingenieur Technik. 2019;91:228-39.

[133] Tiglio M, Villanueva A. Reduced order and surrogate models for gravitational waves. Living Reviews in Relativity. 2022;25:1-97.

[134] Fei C-W, Li H, Lu C, Han L, Keshtegar B, Taylan O. Vectorial surrogate modeling method for multi-objective reliability design. Applied Mathematical Modelling. 2022;109:1-20.

[135] Hess MW, Quaini A, Rozza G. A data-driven surrogate modeling approach for time-dependent incompressible navier-stokes equations with dynamic mode decomposition and manifold interpolation. arXiv preprint arXiv:220110872. 2022.

[136] Kudela J, Matousek R. Recent advances and applications of surrogate models for finite element method computations: a review. Soft Computing. 2022:1-25.

[137] Alizadeh R, Allen JK, Mistree F. Managing computational complexity using surrogate models: a critical review. Research in Engineering Design. 2020;31:275-98.

[138] Bhosekar A, Ierapetritou M. Advances in surrogate based modeling, feasibility analysis, and optimization: A review. Computers & Chemical Engineering. 2018;108:250-67.

[139] Box GE, Draper NR. Empirical model-building and response surfaces: John Wiley & Sons; 1987.

[140] Vickers NJ. Animal communication: when i'm calling you, will you answer too? Current biology. 2017;27:R713-R5.

[141] Forrester AI, Keane AJ. Recent advances in surrogate-based optimization. Progress in aerospace sciences. 2009;45:50-79.

[142] Moustapha M, Sudret B, Bourinet J-M, Guillaume B. Quantile-based optimization under uncertainties using adaptive Kriging surrogate models. Structural and multidisciplinary optimization. 2016;54:1403-21.

[143] Xing J, Luo Y, Gao Z. A global optimization strategy based on the Kriging surrogate model and parallel computing. Structural and Multidisciplinary Optimization. 2020;62:405-17.

[144] Zhang X, Wang L, Sørensen JD. REIF: a novel active-learning function toward adaptive Kriging surrogate models for structural reliability analysis. Reliability Engineering & System Safety. 2019;185:440-54.

[145] Tresidder E, Zhang Y, Forrester A. Acceleration of building design optimisation through the use of kriging surrogate models. Proceedings of building simulation and optimization. 2012:1-8.

[146] Huang Z, Wang C, Chen J, Tian H. Optimal design of aeroengine turbine disc based on kriging surrogate models. Computers & structures. 2011;89:27-37.

[147] Gaspar B, Teixeira AP, Soares CG. Assessment of the efficiency of Kriging surrogate models for structural reliability analysis. Probabilistic Engineering Mechanics. 2014;37:24-34.

[148] Park J, Sandberg IW. Universal approximation using radial-basis-function networks. Neural

computation. 1991;3:246-57.

[149] Buhmann MD. Radial basis functions: theory and implementations: Cambridge university press; 2003.

[150] Rippa S. An algorithm for selecting a good value for the parameter c in radial basis function interpolation. Advances in Computational Mathematics. 1999;11:193-210.

[151] Mulgrew B. Applying radial basis functions. IEEE signal processing magazine. 1996;13:50-65.

[152] Park J, Sandberg IW. Approximation and radial-basis-function networks. Neural computation. 1993;5:305-16.

[153] Musavi MT, Ahmed W, Chan KH, Faris KB, Hummels DM. On the training of radial basis function classifiers. Neural networks. 1992;5:595-603.

[154] Yang GR, Wang X-J. Artificial neural networks for neuroscientists: A primer. Neuron. 2020;107:1048-70.

[155] Hassoun MH. Fundamentals of artificial neural networks: MIT press; 1995.

[156] Abraham A. Artificial neural networks. Handbook of measuring system design. 2005.

[157] Hopfield JJ. Artificial neural networks. IEEE Circuits and Devices Magazine. 1988;4:3-10.

[158] Jain AK, Mao J, Mohiuddin KM. Artificial neural networks: A tutorial. Computer. 1996;29:31-44.

[159] Yegnanarayana B. Artificial neural networks: PHI Learning Pvt. Ltd.; 2009.

[160] Mesgarpour M, Mir M, Alizadeh R, Abad JMN, Borj EP. An evaluation of the thermal behaviour of a lithium-ion battery pack with a combination of pattern-based artificial neural networks (PBANN) and numerical simulation. Journal of Energy Storage. 2022;47:103920.

[161] Dimitriadou S, Nikolakopoulos KG. Artificial neural networks for the prediction of the reference evapotranspiration of the Peloponnese Peninsula, Greece. Water. 2022;14:2027.

[162] Abellán García J, Fernandez Gomez J, Torres Castellanos N. Properties prediction of environmentally friendly ultra-high-performance concrete using artificial neural networks. European Journal of Environmental and Civil Engineering. 2022;26:2319-43.

[163] Wang C, Xu S, Liu J, Yang J, Liu C. Building an improved artificial neural network model based on deeply optimizing the input variables to enhance rutting prediction. Construction and Building Materials. 2022;348:128658.

[164] Gupta P, Kumar P, Rao SM. Artificial neural network model for single-phase real gas ejectors. Applied Thermal Engineering. 2022;201:117615.

[165] Bas E, Egrioglu E, Kolemen E. Training simple recurrent deep artificial neural network for forecasting using particle swarm optimization. Granular Computing. 2022;7:411-20.

[166] Matel E, Vahdatikhaki F, Hosseinyalamdary S, Evers T, Voordijk H. An artificial neural network approach for cost estimation of engineering services. International journal of construction management. 2022;22:1274-87.

[167] Tam VW, Butera A, Le KN, Da Silva LC, Evangelista AC. A prediction model for compressive strength of CO2 concrete using regression analysis and artificial neural networks. Construction and Building Materials. 2022;324:126689.

[168] Böttcher L, Antulov-Fantulin N, Asikis T. AI Pontryagin or how artificial neural networks learn to control dynamical systems. Nature communications. 2022;13:1-9.

[169] Veza I, Afzal A, Mujtaba M, Hoang AT, Balasubramanian D, Sekar M, et al. Review of artificial neural networks for gasoline, diesel and homogeneous charge compression ignition engine. Alexandria Engineering Journal. 2022.

[170] Bhatt AN, Shrivastava N. Application of artificial neural network for internal combustion engines: a state of the art review. Archives of Computational Methods in Engineering. 2022;29:897-919.

[171] Silvestrini S, Lavagna M. Deep Learning and Artificial Neural Networks for Spacecraft Dynamics, Navigation and Control. Drones. 2022;6:270.

[172] Koeppe A, Padilla CAH, Voshage M, Schleifenbaum JH, Markert B. Efficient numerical modeling of 3D-printed lattice-cell structures using neural networks. Manufacturing Letters. 2018;15:147-50.

[173] Liang L, Liu M, Martin C, Sun W. A deep learning approach to estimate stress distribution: a fast and accurate surrogate of finite-element analysis. Journal of The Royal Society Interface. 2018;15:20170844.

[174] Mortazavi S, Ince A. An artificial neural network modeling approach for short and long fatigue crack propagation. Computational Materials Science. 2020;185:109962.

[175] Zhang M, Sun C-N, Zhang X, Goh PC, Wei J, Hardacre D, et al. High cycle fatigue life prediction of laser additive manufactured stainless steel: A machine learning approach. International Journal of Fatigue. 2019;128:105194.

[176] Singh A, Cooper D, Blundell N, Gibbons G, Pratihar D. Modelling of direct metal laser sintering of EOS DM20 bronze using neural networks and genetic algorithms. Proceedings of the 37th international MATADOR conference: Springer Science & Business Media; 2012. p. 395.

[177] Jiang J, Hu G, Li X, Xu X, Zheng P, Stringer J. Analysis and prediction of printable bridge length in fused deposition modelling based on back propagation neural network. Virtual and Physical Prototyping. 2019;14:253-66.

[178] Lu Z, Li D, Lu B, Zhang A, Zhu G, Pi G. The prediction of the building precision in the Laser Engineered Net Shaping process using advanced networks. Optics and Lasers in Engineering. 2010;48:519-25.

[179] Mozaffar M, Paul A, Al-Bahrani R, Wolff S, Choudhary A, Agrawal A, et al. Data-driven prediction of the high-dimensional thermal history in directed energy deposition processes via recurrent neural networks. Manufacturing letters. 2018;18:35-9.

[180] Xiong J, Zhang G, Hu J, Wu L. Bead geometry prediction for robotic GMAW-based rapid manufacturing through a neural network and a second-order regression analysis. Journal of Intelligent Manufacturing. 2014;25:157-63.

[181] Garg A, Lam JSL, Savalani M. A new computational intelligence approach in formulation of functional relationship of open porosity of the additive manufacturing process. The International Journal of Advanced Manufacturing Technology. 2015;80:555-65.

[182] Garg A, Lam JSL. Measurement of environmental aspect of 3-D printing process using soft computing methods. Measurement. 2015;75:210-7.

[183] Douard A, Grandvallet C, Pourroy F, Vignat F. An example of machine learning applied in additive manufacturing. 2018 IEEE International Conference on Industrial Engineering and Engineering Management (IEEM): IEEE; 2018. p. 1746-50.

[184] Aoyagi K, Wang H, Sudo H, Chiba A. Simple method to construct process maps for additive manufacturing using a support vector machine. Additive manufacturing. 2019;27:353-62.

[185] Zhang W, Mehta A, Desai PS, Higgs III CF. Machine learning enabled powder spreading process map for metal additive manufacturing (AM). 2017 International Solid Freeform Fabrication Symposium: University of Texas at Austin; 2017.

[186] Kappes B, Moorthy S, Drake D, Geerlings H, Stebner A. Machine learning to optimize additive manufacturing parameters for laser powder bed fusion of Inconel 718. Proceedings of the 9th international symposium on superalloy 718 & derivatives: Energy, aerospace, and industrial applications: Springer; 2018. p. 595-610.

[187] Chowdhury S, Anand S. Artificial neural network based geometric compensation for thermal deformation in additive manufacturing processes. International Manufacturing Science and Engineering Conference: American Society of Mechanical Engineers; 2016. p. V003T08A6.

[188] Li Z, Zhang Z, Shi J, Wu D. Prediction of surface roughness in extrusion-based additive manufacturing with machine learning. Robotics and Computer-Integrated Manufacturing. 2019;57:488-95.

[189] Sosnovik I, Oseledets I. Neural networks for topology optimization. Russian Journal of Numerical Analysis and Mathematical Modelling. 2019;34:215-23.

[190] Pilania G, Wang C, Jiang X, Rajasekaran S, Ramprasad R. Accelerating materials property predictions using machine learning. Scientific reports. 2013;3:1-6.

[191] Gu GX, Chen C-T, Buehler MJ. De novo composite design based on machine learning algorithm. Extreme Mechanics Letters. 2018;18:19-28.

[192] Song J, Peters J, Noor A, Michaleris P. Sensitivity analysis of the thermomechanical response of welded joints. International Journal of Solids and Structures. 2003;40:4167-80.

[193] Darcourt C, Roelandt J, Rachik M, Deloison D, Journet B. Thermomechanical analysis applied to the laser beam welding simulation of aeronautical structures. Journal de Physique IV (Proceedings): EDP sciences; 2004. p. 785-92.

[194] Sawant S, Muliana A. A thermo-mechanical viscoelastic analysis of orthotropic materials. Composite Structures. 2008;83:61-72.

[195] Alshorbagy A, Alieldin S, Shaat M, Mahmoud F. Finite element analysis of the deformation of functionally graded plates under thermomechanical loads. Mathematical Problems in Engineering. 2013;2013.

[196] Ngo TD, Kashani A, Imbalzano G, Nguyen KT, Hui D. Additive manufacturing (3D printing): A review of materials, methods, applications and challenges. Composites Part B: Engineering. 2018;143:172-96.

[197] Roberts IA, Wang C, Esterlein R, Stanford M, Mynors D. A three-dimensional finite element analysis of the temperature field during laser melting of metal powders in additive layer manufacturing. International Journal of Machine Tools and Manufacture. 2009;49:916-23.

[198] Song J, Shanghvi J, Michaleris P. Sensitivity analysis and optimization of thermo-elasto-plastic processes with applications to welding side heater design. Computer methods in applied mechanics and engineering. 2004;193:4541-66.

[199] Raghavan N, Dehoff R, Pannala S, Simunovic S, Kirka M, Turner J, et al. Numerical modeling of heat-transfer and the influence of process parameters on tailoring the grain morphology of IN718 in electron beam additive manufacturing. Acta Materialia. 2016;112:303-14.

[200] Yang Y, Jamshidinia M, Boulware P, Kelly S. Prediction of microstructure, residual stress, and deformation in laser powder bed fusion process. Computational Mechanics. 2018;61:599-615.

[201] Yan L, Zhang Y, Liou F. A conceptual design of residual stress reduction with multiple shape laser beams in direct laser deposition. Finite Elements in Analysis and Design. 2018;144:30-7.

[202] Denlinger ER, Heigel JC, Michaleris P. Residual stress and distortion modeling of electron beam direct manufacturing Ti-6Al-4V. Proceedings of the Institution of Mechanical Engineers, Part B: Journal of Engineering Manufacture. 2015;229:1803-13.

[203] Michaleris P. Modeling metal deposition in heat transfer analyses of additive manufacturing processes. Finite Elements in Analysis and Design. 2014;86:51-60.

[204] Kwon YW, Bang H. The finite element method using MATLAB: CRC press; 2018.

[205] Fu G, Gu J, Lourenco MI, Duan M, Estefen SF. Parameter determination of double-ellipsoidal heat source model and its application in the multi-pass welding process. Ships and offshore structures. 2015;10:204-17.

[206] Manvatkar V, De A, DebRoy T. Heat transfer and material flow during laser assisted multi-layer additive manufacturing. Journal of Applied Physics. 2014;116:124905.

[207] Svensson L, Gretoft B, Bhadeshia H. An analysis of cooling curves from the fusion zone of steel weld deposits. Scand J Metall. 1986;15:e103.

[208] Borja RI. Plasticity: Springer; 2013.

[209] DebRoy T, Wei H, Zuback J, Mukherjee T, Elmer J, Milewski J, et al. Additive manufacturing of metallic components–process, structure and properties. Progress in Materials Science. 2018;92:112-224.

[210] Jayanath S, Achuthan A. A Computationally Efficient Finite Element Framework to Simulate Additive Manufacturing Processes. Journal of Manufacturing Science and Engineering. 2018;140:041009.

[211] Bontha S, Klingbeil NW. Effect of a distributed heat source on melt pool geometry and microstructure in beam-based solid freeform fabrication. Proceedings 2006 Solid Freeform Fabrication Symposium, Austin, TX2006.

[212] Liu J. Phase transformations and stress evolution during laser beam welding and post heat treatment of TiAl-alloys: Helmholtz-Zentrum Geesthacht, Zentrum für Material-und Küstenforschung; 2015.

[213] Chae HM. A Numerical and Experimental Study for Residual Stress Evolution in Low Alloy Steel during Laser Aided Additive Manufacturing Process. 2013.

[214] Gouge M, Michaleris P, Denlinger E, Irwin J. The Finite Element Method for the Thermo-Mechanical Modeling of Additive Manufacturing Processes. Thermo-Mechanical Modeling of Additive Manufacturing: Elsevier; 2018. p. 19-38.

[215] Yang Q, Zhang P, Cheng L, Min Z, Chyu M, To AC. Finite element modeling and validation of thermomechanical behavior of Ti-6Al-4V in directed energy deposition additive manufacturing. Additive Manufacturing. 2016;12:169-77.

[216] Yang Y, Jamshidinia M, Boulware P, Kelly S. Prediction of microstructure, residual stress, and deformation in laser powder bed fusion process. Computational Mechanics. 2018:1-17.

[217] Xiong Y, Hofmeister WH, Cheng Z, Smugeresky JE, Lavernia EJ, Schoenung JM. In situ thermal imaging and three-dimensional finite element modeling of tungsten carbide–cobalt during laser deposition. Acta Materialia. 2009;57:5419-29.

[218] Khatir S, Tiachacht S, Thanh C-L, Bui TQ, Wahab MA. Damage assessment in composite laminates using ANN-PSO-IGA and Cornwell indicator. Composite Structures. 2019;230:111509.

[219] Albu A, Precup R-E, Teban T-A. Results and challenges of artificial neural networks used for decision-making and control in medical applications. Facta Universitatis Series: Mechanical Engineering. 2019;17:285-308.

[220] Abualigah L, Elaziz MA, Khasawneh AM, Alshinwan M, Ibrahim RA, Al-qaness MA, et al. Meta-heuristic optimization algorithms for solving real-world mechanical engineering design problems: a comprehensive survey, applications, comparative analysis, and results. Neural Computing and Applications. 2022:1-30.

[221] Karthikeyan S, Lakshmi K, Gobhinath S. Design and implementation of SEPIC converter based nine-level MLI fed IM with PI, FLC, and ANN controller. Recent Trends in Mechanical Engineering: Springer; 2021. p. 621-31.

[222] Liu D, Wang Y. Multi-fidelity physics-constrained neural network and its application in materials modeling. Journal of Mechanical Design. 2019;141.

[223] Nirala A, Soren S, Kumar N, Shrivastava Y, Kamal R, Al-Mansour AI, et al. Assessing the Mechanical Properties of a New High Strength Aluminum Hybrid MMC Based on the ANN Approach for Automotive Application. Materials. 2022;15:2015.

[224] Gomes GF, Mendez YAD, da Silva Lopes Alexandrino P, da Cunha SS, Ancelotti AC. A review of vibration based inverse methods for damage detection and identification in mechanical structures using optimization algorithms and ANN. Archives of computational methods in engineering. 2019;26:883-97.

[225] Mouloodi S, Rahmanpanah H, Martin C, Gohari S, Burvill C, Davies HM. The use of deep learning algorithms to predict mechanical strain from linear acceleration and angular rates of motion recorded from a horse hoof during exercise. International Journal of Mechanical Sciences. 2022;216:106972.

[226] Paturi UMR, Cheruku S, Reddy N. The role of artificial neural networks in prediction of mechanical and tribological properties of composites—a comprehensive review. Archives of Computational Methods in Engineering. 2022:1-41.

[227] Efkolidis N, Hernandez CG, Talon JLH, Kyratsis P. Modelling and Prediction of Thrust Force and Torque in Drilling Operations of Al7075 Using ANN and RSM Methodologies. Strojniski Vestnik/Journal of Mechanical Engineering. 2018;64.

[228] Gunerkar RS, Jalan AK, Belgamwar SU. Fault diagnosis of rolling element bearing based on artificial neural network. Journal of Mechanical Science and Technology. 2019;33:505-11.

[229] Shahid N, Rappon T, Berta W. Applications of artificial neural networks in health care organizational decision-making: A scoping review. PloS one. 2019;14:e0212356.

[230] Radha Krishnan B, Vijayan V, Parameshwaran Pillai T, Sathish T. Influence of surface roughness in turning process—an analysis using artificial neural network. Transactions of the Canadian Society for Mechanical Engineering. 2019;43:509-14.

[231] Pavlenko I, Trojanowska J, Ivanov V, Liaposhchenko O. Scientific and methodological approach for the identification of mathematical models of mechanical systems by using artificial neural networks. International Conference on Innovation, Engineering and Entrepreneurship: Springer; 2018. p. 299-306.

[232] Sun G, Wang S. A review of the artificial neural network surrogate modeling in aerodynamic design. Proceedings of the Institution of Mechanical Engineers, Part G: Journal of Aerospace Engineering. 2019;233:5863-72.

[233] Zhang W, Zhang R, Wu C, Goh ATC, Lacasse S, Liu Z, et al. State-of-the-art review of soft computing applications in underground excavations. Geoscience Frontiers. 2020;11:1095-106.

[234] Huu PN, Minh QT. An ANN-based gesture recognition algorithm for smart-home applications. KSII Transactions on Internet and Information Systems (TIIS). 2020;14:1967-83.

[235] Monticeli FM, Neves RM, Ornaghi Júnior HL. Using an artificial neural network (ANN) for prediction of thermal degradation from kinetics parameters of vegetable fibers. Cellulose. 2021;28:1961-71.

[236] Kalantary S, Jahani A, Jahani R. MLR and ANN approaches for prediction of synthetic/natural nanofibers diameter in the environmental and medical applications. Scientific Reports. 2020;10:1-10.

[237] Marinković Z, Crupi G, Caddemi A, Marković V, Schreurs DMP. A review on the artificial neural network applications for small-signal modeling of microwave FETs. International Journal of Numerical Modelling: Electronic Networks, Devices and Fields. 2020;33:e2668.

[238] Abiodun OI, Jantan A, Omolara AE, Dada KV, Umar AM, Linus OU, et al. Comprehensive review of artificial neural network applications to pattern recognition. IEEE Access. 2019;7:158820-46.

[239] Abiodun OI, Jantan A, Omolara AE, Dada KV, Mohamed NA, Arshad H. State-of-the-art in artificial neural network applications: A survey. Heliyon. 2018;4:e00938.

[240] Shi B, Bai X, Yao C. An end-to-end trainable neural network for image-based sequence recognition and its application to scene text recognition. IEEE transactions on pattern analysis and machine intelligence. 2016;39:2298-304.

[241] Rosenblatt F. Principles of neurodynamics. perceptrons and the theory of brain mechanisms. Cornell Aeronautical Lab Inc Buffalo NY; 1961.

[242] Callister Jr WD, Rethwisch DG. Callister's materials science and engineering: John Wiley & Sons; 2020.

[243] Hajializadeh F, Ince A. Short review on modeling approaches for metal additive manufacturing process. Material Design & Processing Communications. 2020;2:e56.

[244] Aggarwal CC. Neural networks and deep learning. Springer. 2018;10:978-3.

[245] Cybenko G. Approximation by superpositions of a sigmoidal function. Mathematics of control, signals and systems. 1989;2:303-14.

[246] Manual AU. Abaqus user manual. Abacus. 2020.

Appendix A: Supplementary results

T-shape wall

S33 – (Y-Z) plane

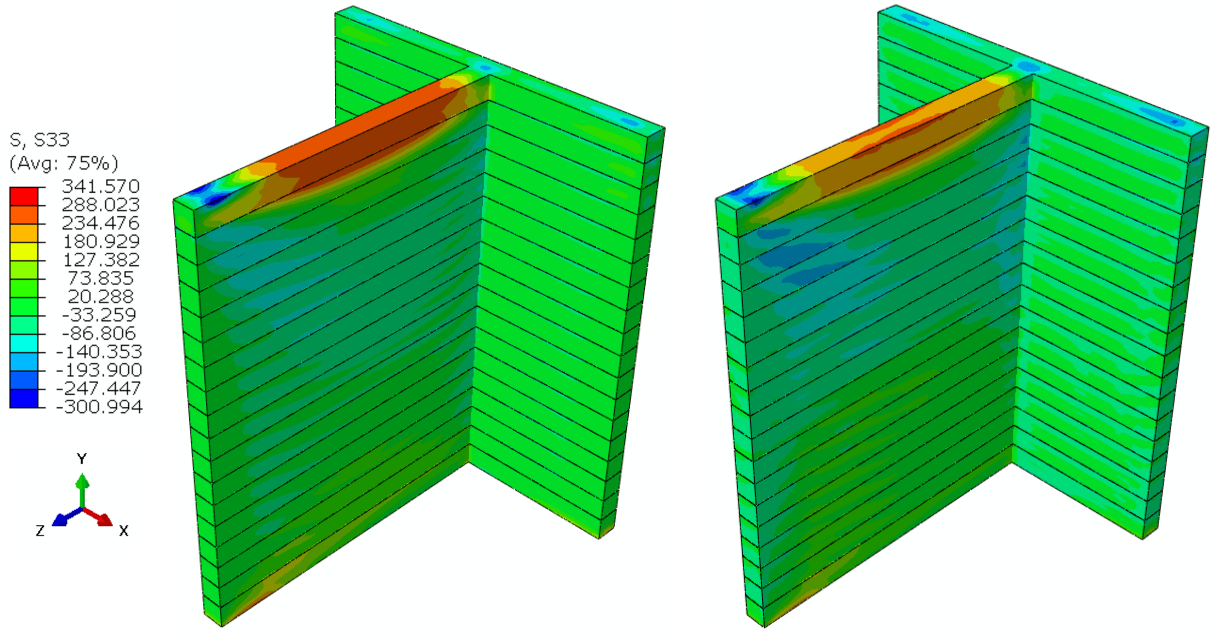

(a) (b)

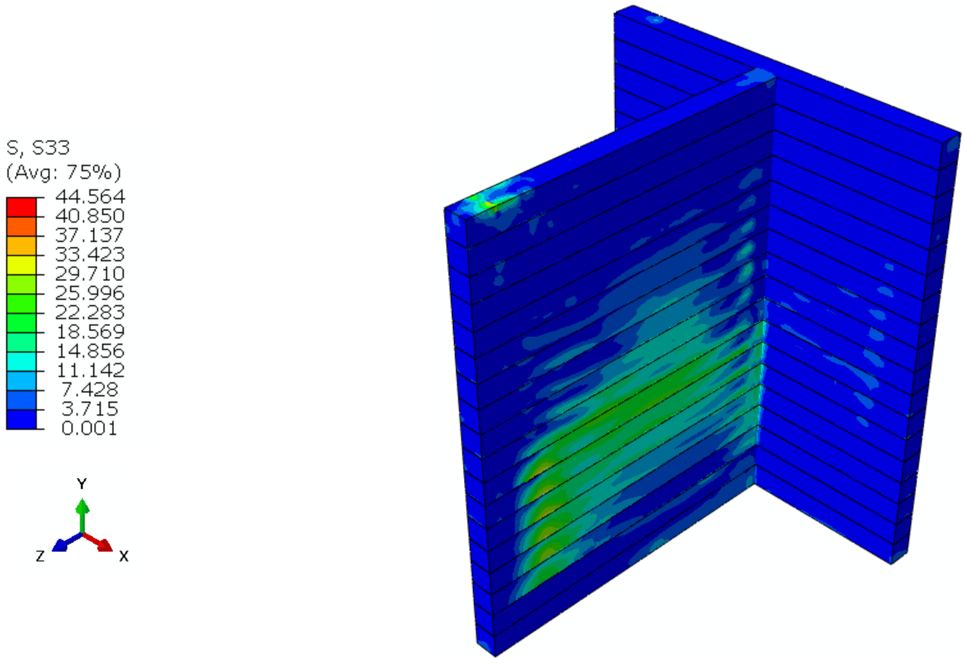

(c)

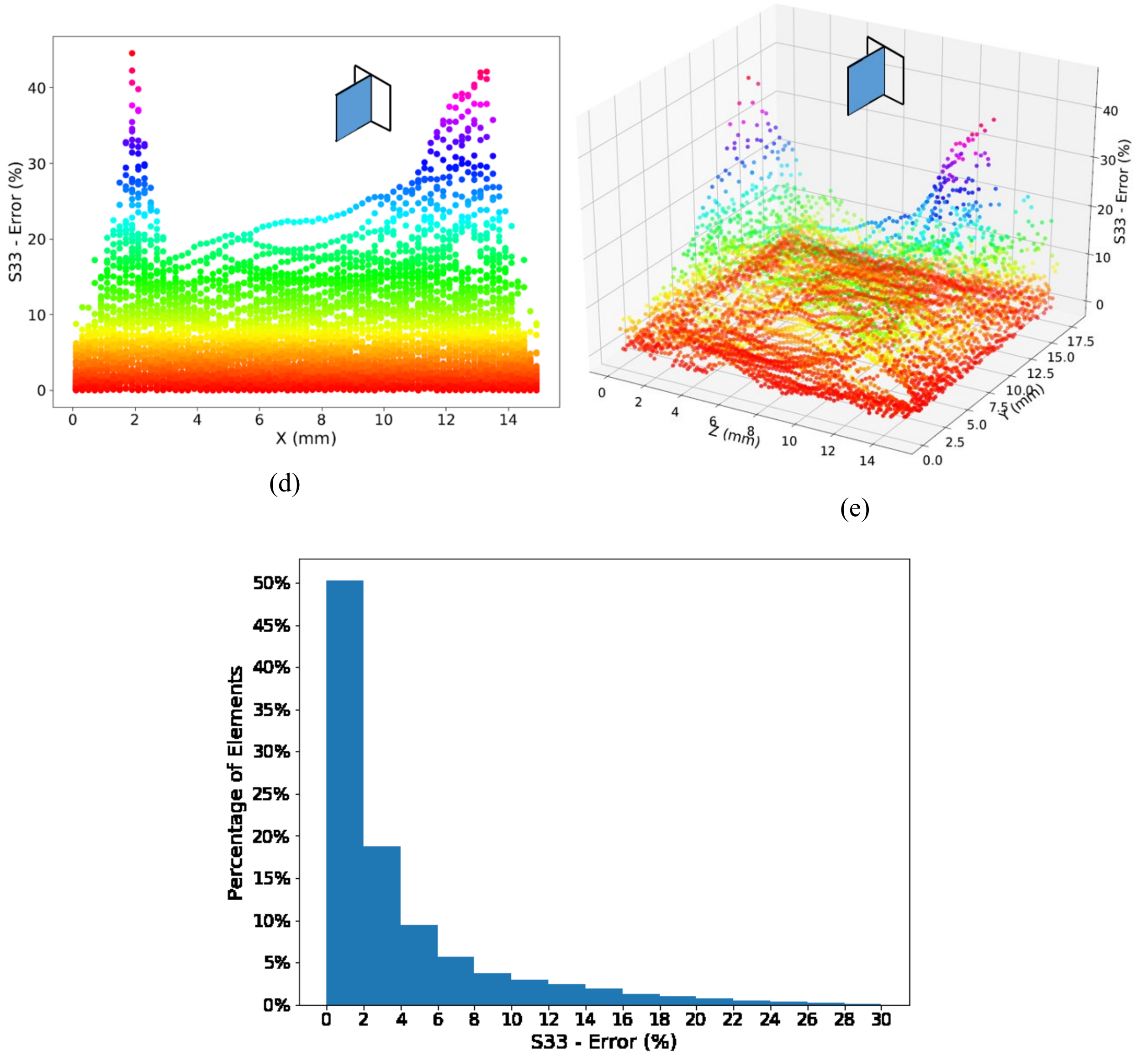

(d)

(e)

(f)

Figure 45 S33 distribution of 18-layers T-shape wall (in MPa) (a) FINITE ELEMENT analysis (b) ANN prediction (c) error value (%) (d) 2D error scatter (Y-Z plane) (e) 3D error scatter (Y-Z plane) (f) histogram of the error

S22 – (Y-Z) plane

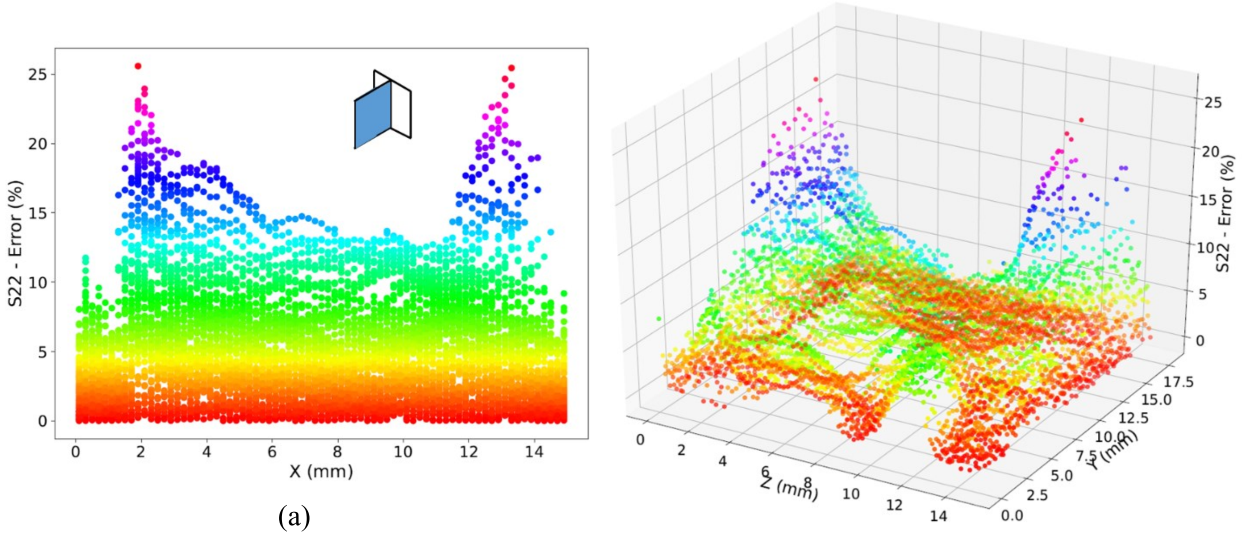

(a)

(b)

Figure 46 S22 distribution of 18-layers T-shape wall (Y-Z plane) (in MPa) (a) 2D error scatter (b) 3D error scatter

H-shape wall

S33 – (Y-Z) plane

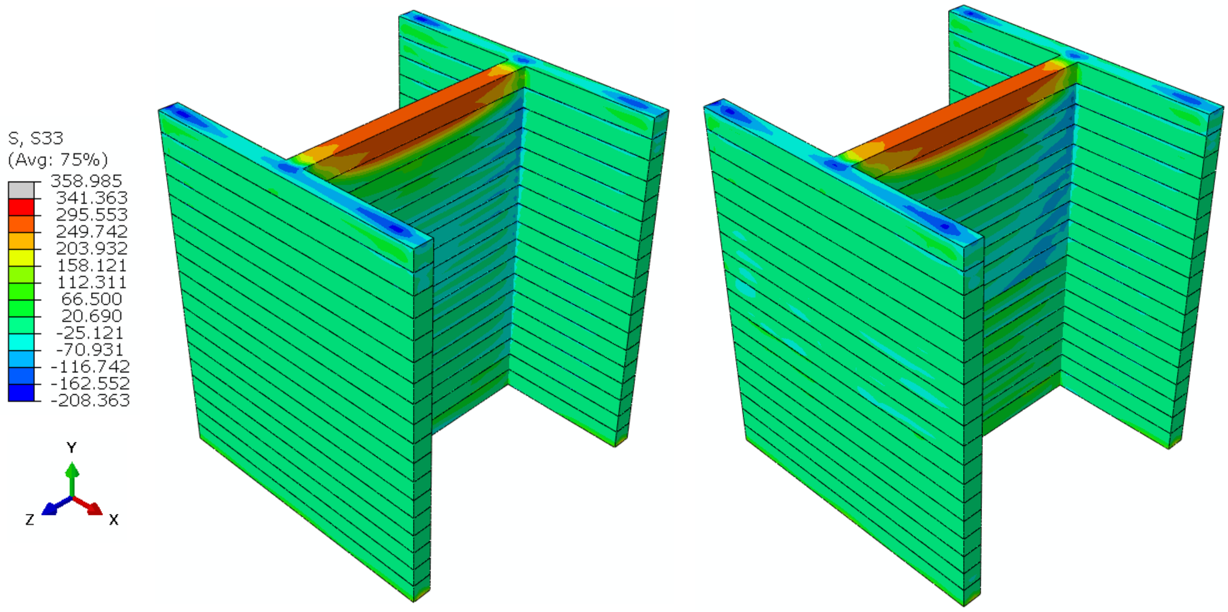

(a) (b)

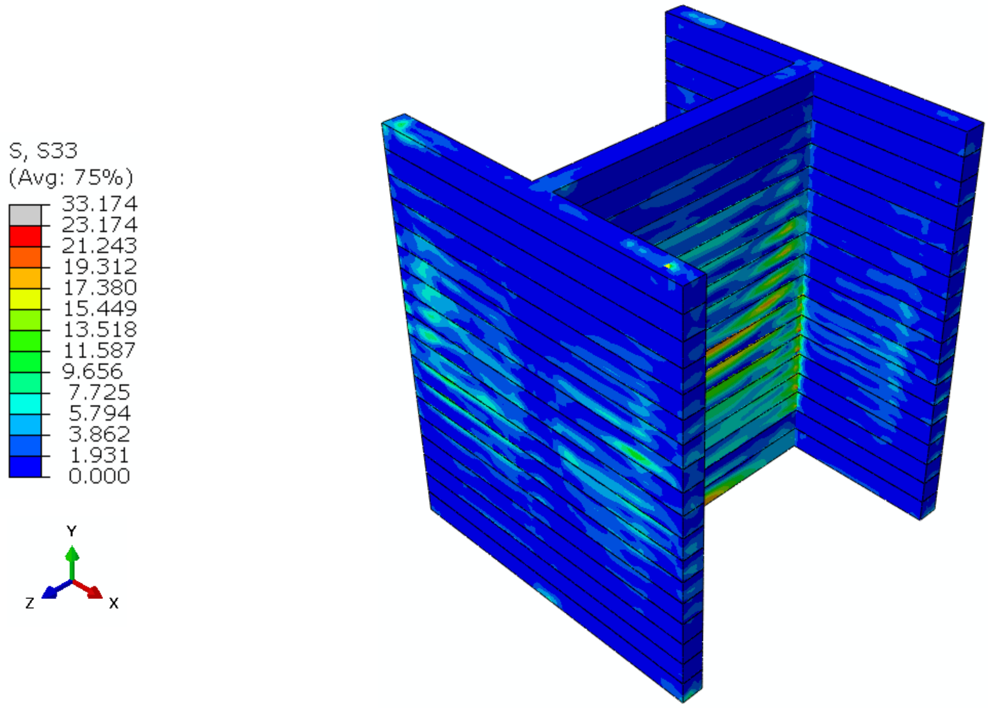

(c)

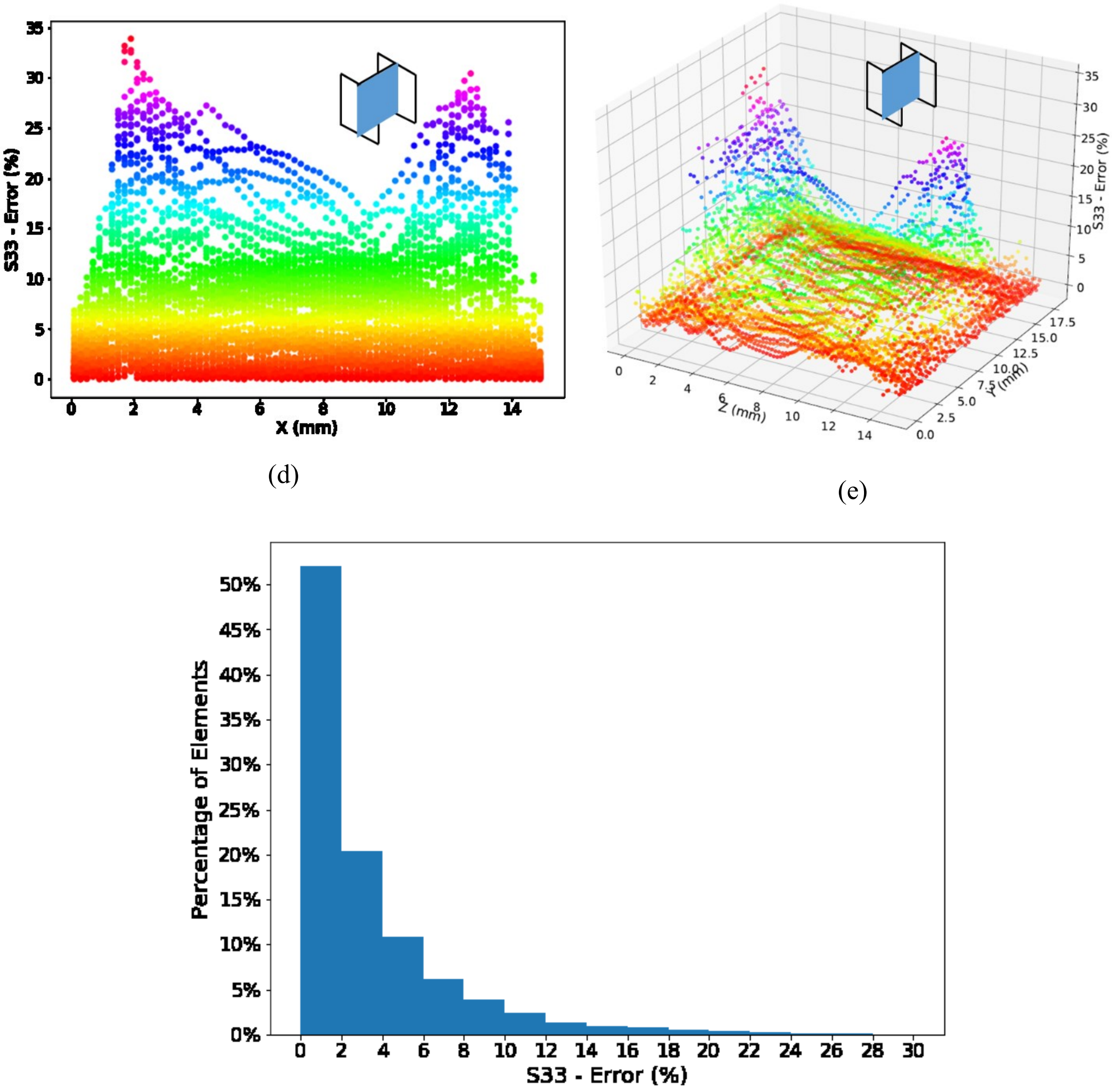

(d)

(e)

(f)

Figure 47 S33 distribution of 18-layers H-shape wall (in MPa) (a) FINITE ELEMENT analysis (b) ANN prediction (c) error value (%) (d) 2D error scatter (Y-Z plane) (e) 3D error scatter (Y-Z plane) (f) histogram of the error

S11 – (X-Y) plane - front

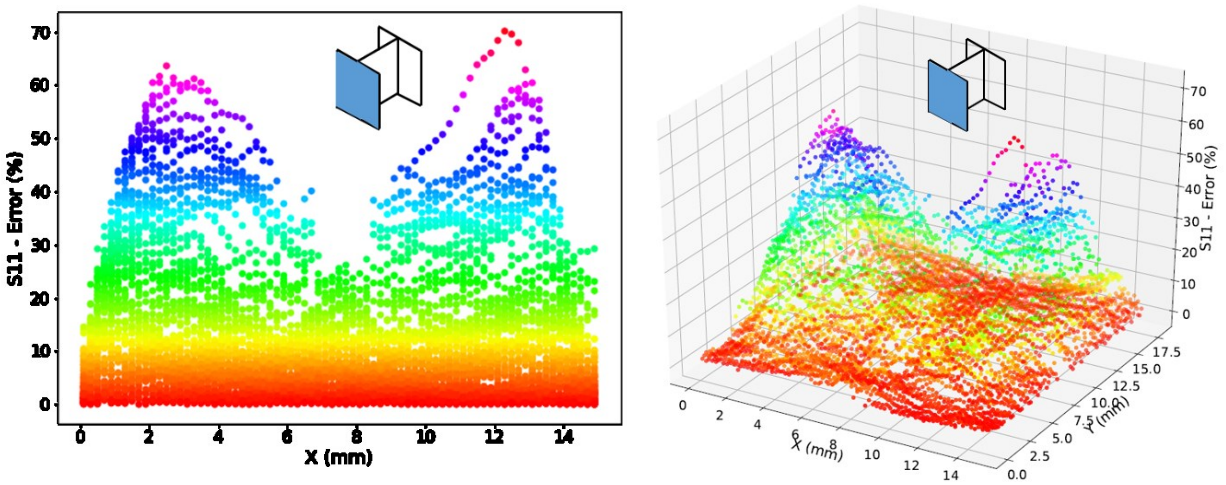

(a)

(b)

Figure 48 S11 distribution of 18-layers H-shape wall (a) 2D error scatter (X-Y plane - front) (b) 3D error scatter (X-Y plane - front)

S22 – (X-Y) plane - front

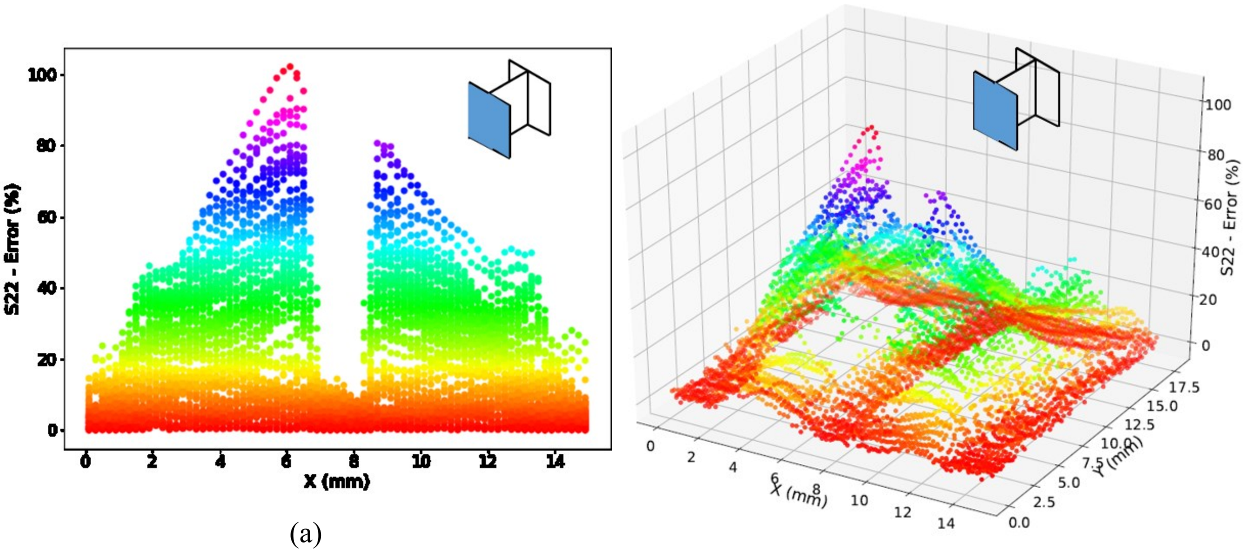

(a)

(b)

Figure 49 S22 distribution of 18-layers H-shape wall (a) 2D error scatter (X-Y plane - front) (b) 3D error scatter (X-Y plane - front)

Plus-shape wall

S33 – (Y-Z) plane

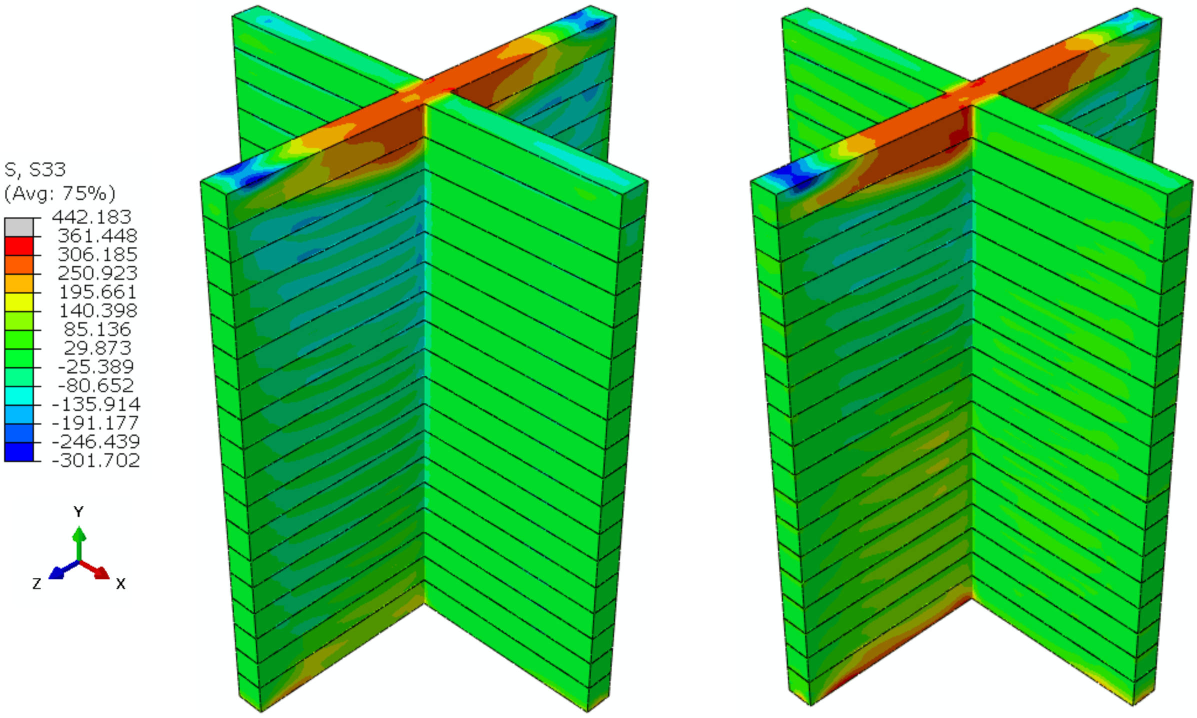

(a) (b)

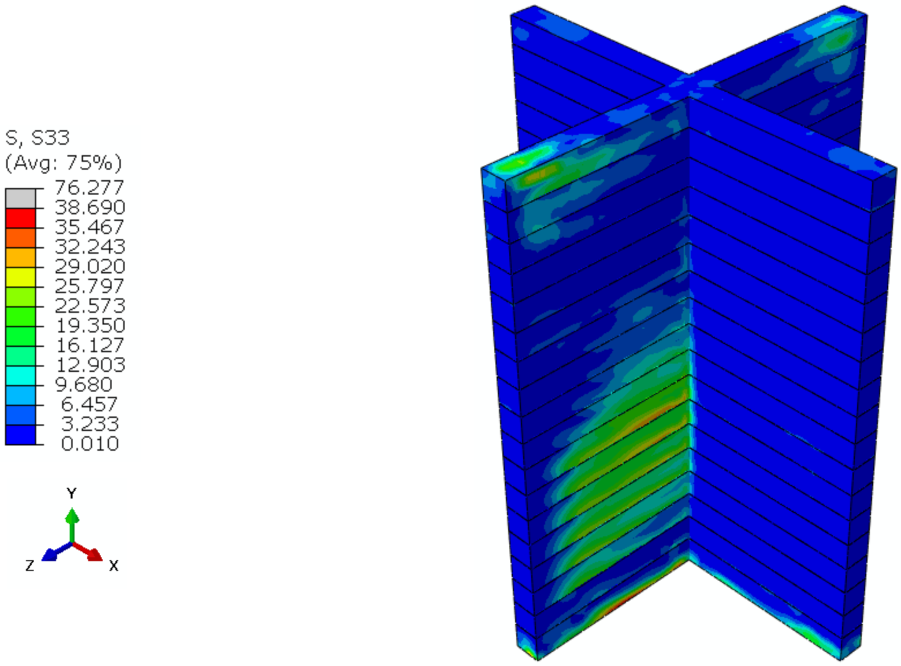

(c)

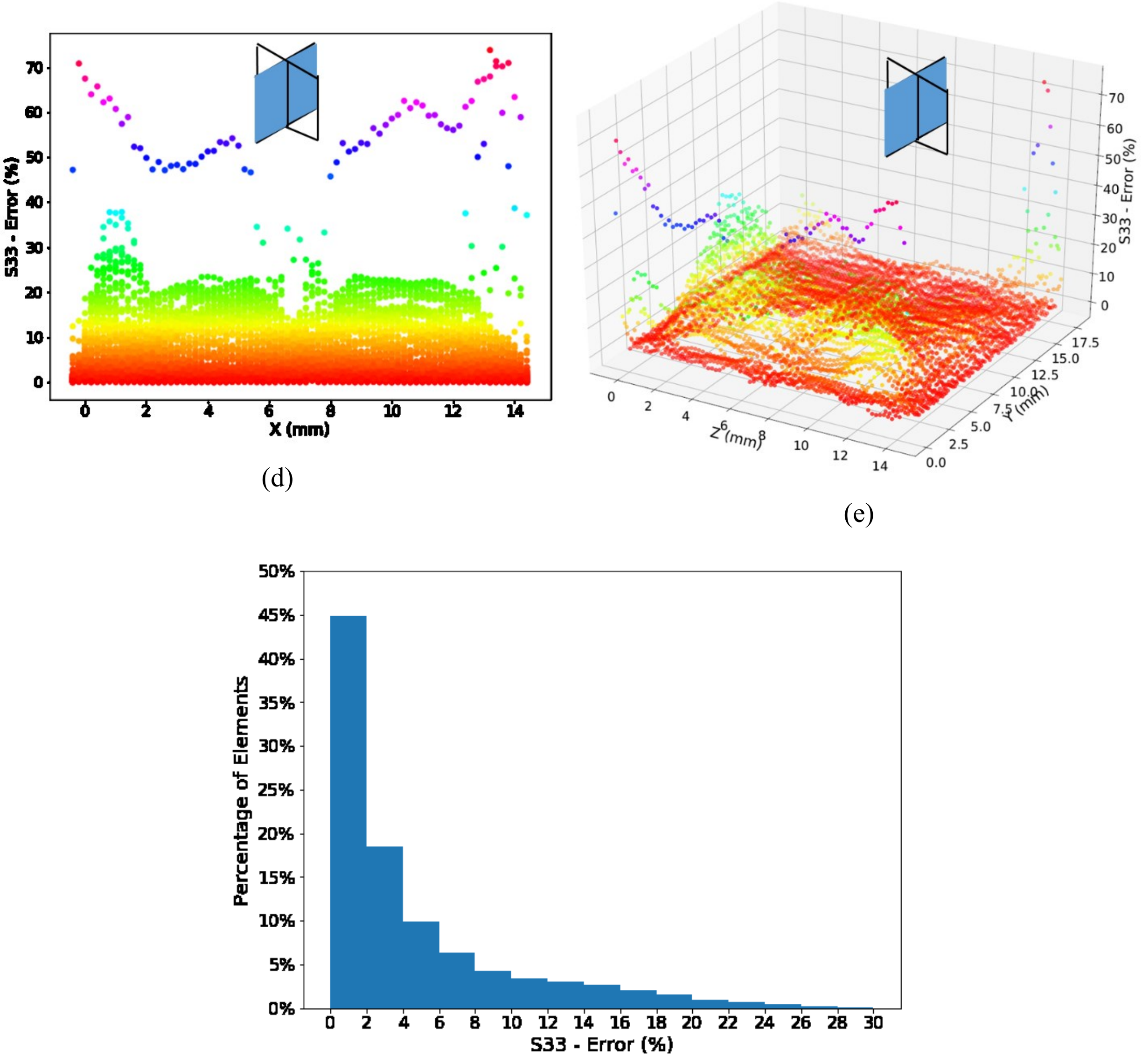

(d)

(e)

(f)

Figure 50 S33 distribution of 18-layers Plus-shape wall (in MPa) (a) FINITE ELEMENT analysis (b) ANN prediction (c) error value (%) (d) 2D error scatter (Y-Z) plane (e) 3D error scatter (Y-Z) plane (f) histogram of the error

S22 - (Y-Z) plane

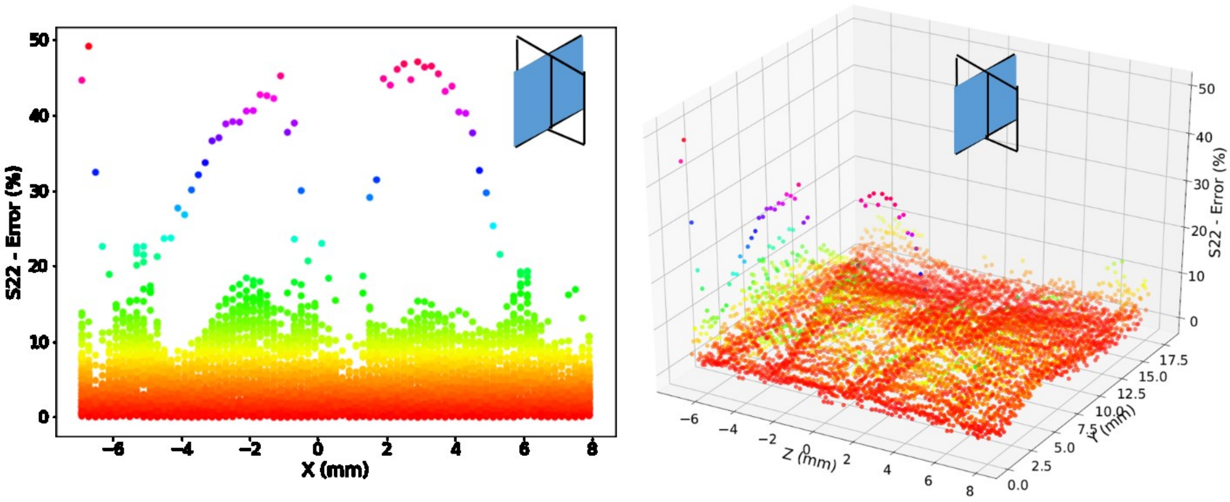

(d)

(e)

Figure 51 S22 distribution of 18-layers Plus-shape wall (a) 2D error scatter (Y-Z) plane (b) 3D error scatter (Y-Z) plane

BoxPlus shape wall

S11 – (X-Y) plane – back

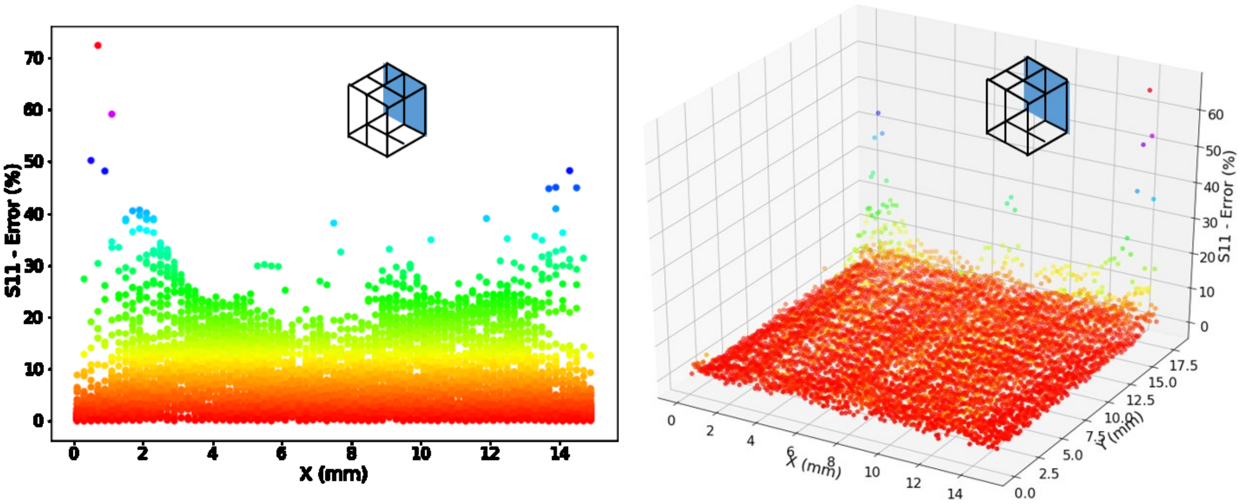

(a)

(b)

Figure 52 S11 distribution of 18-layers BoxPlus structure (a) 2D error scatter (X-Y plane - back) (b) 3D error scatter (X-Y plane - back)

S22 – (X-Y) plane – back

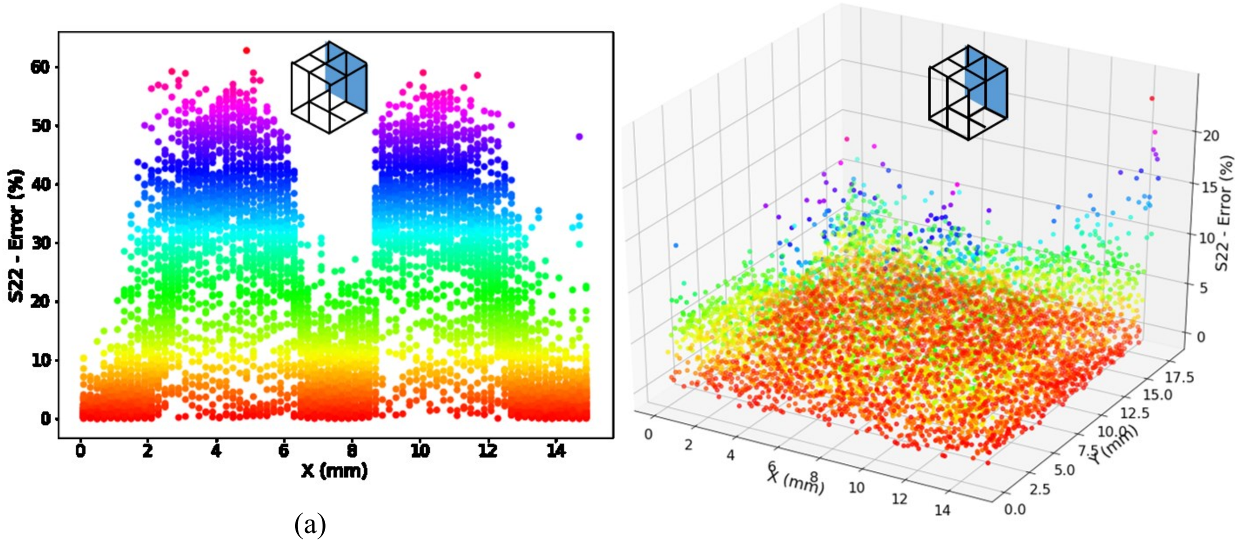

(a)

(b)

Figure 53 S22 distribution of 18-layers BoxPlus structure (a) 2D error scatter (X-Y plane - back) (b) 3D error scatter (X-Y plane - back)

S33- (Y-Z) plane – right

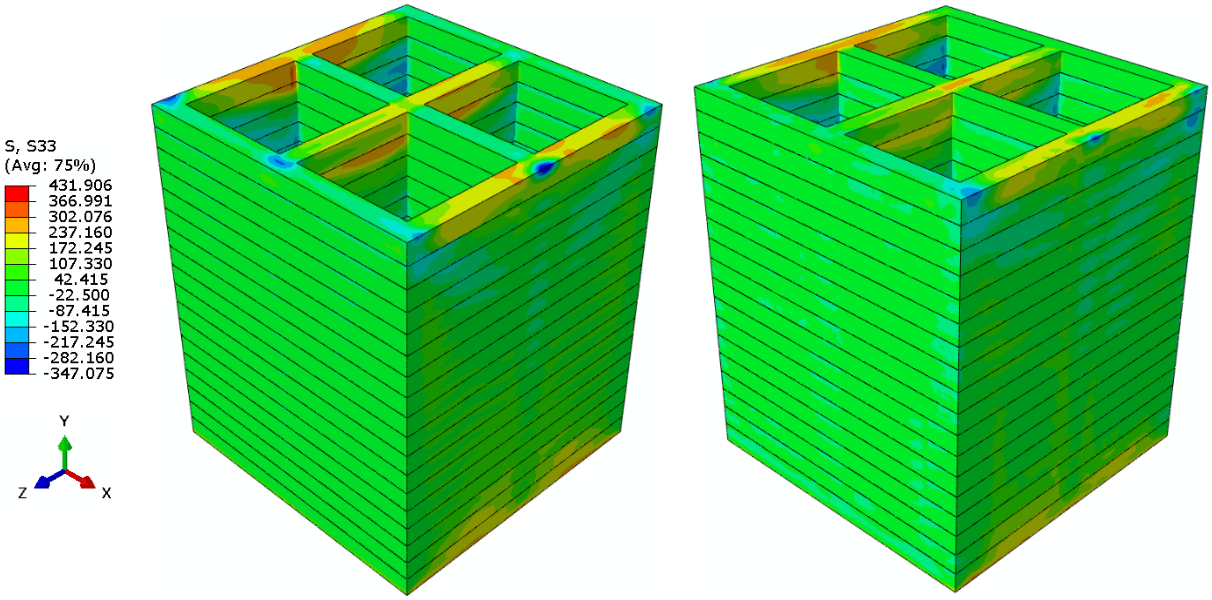

(a) (b)

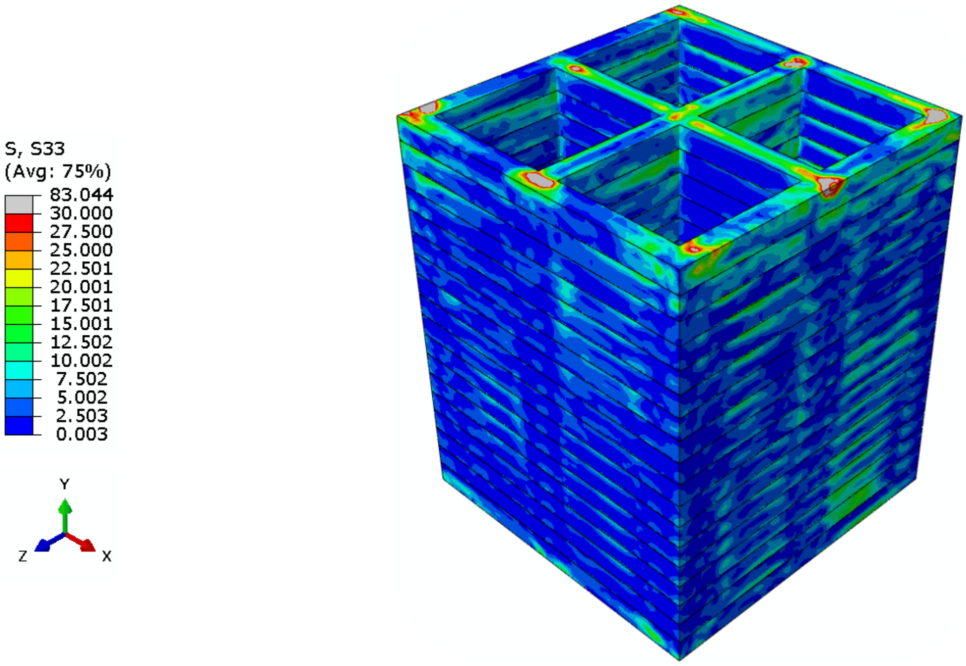

(c)

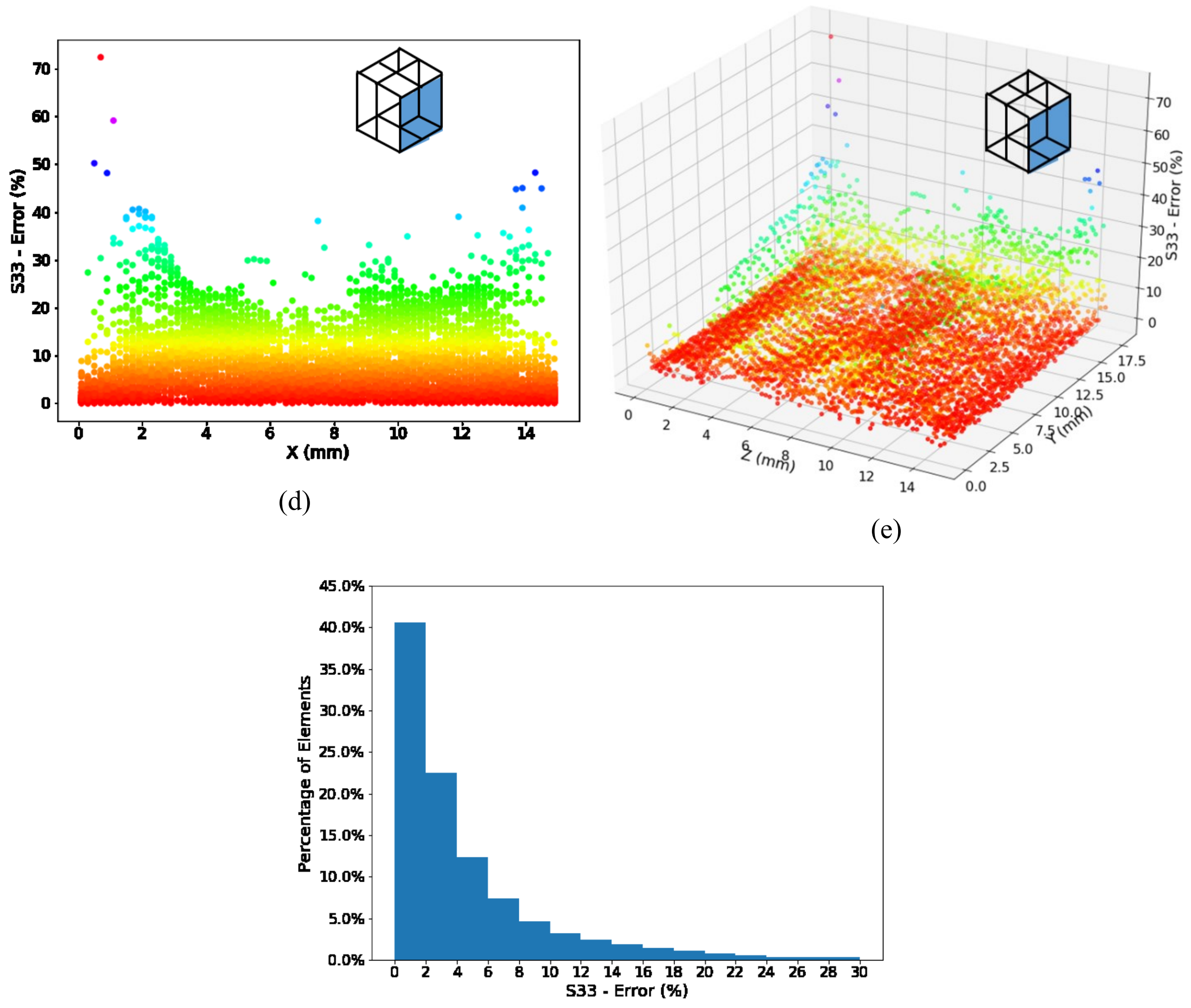

(d)

(e)

(f)

Figure 54 S33 distribution of 18-layers BoxPlus structure (in MPa) (a) FINITE ELEMENT analysis (b) ANN prediction (c) error value (%) (d) 2D error scatter (Y-Z plane - right) (e) 3D error scatter (Y-Z plane - right) (f) histogram of the error

S22 – (Y-Z) plane - right

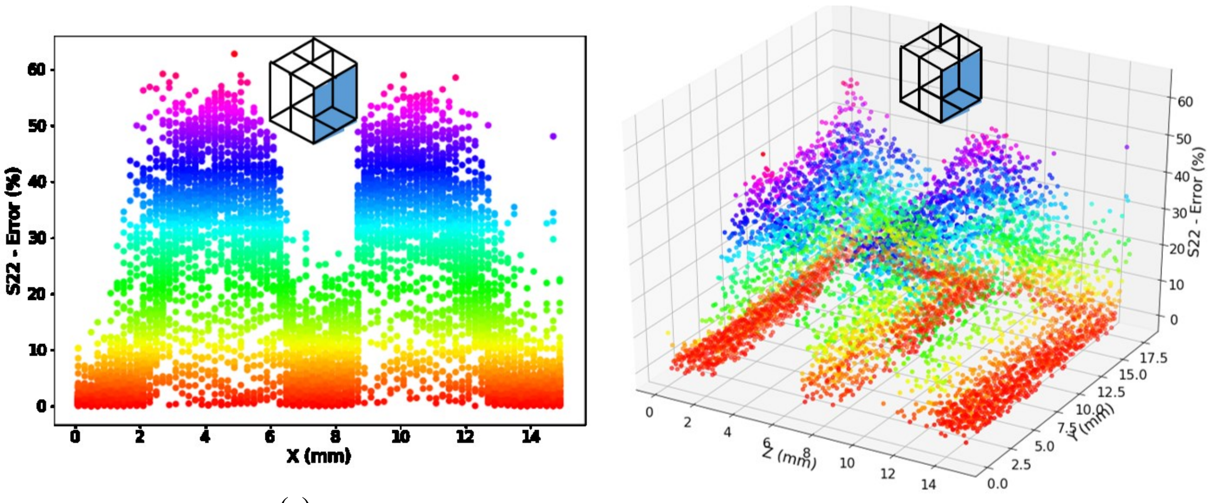

(a)

(b)

Figure 55 S22 distribution of 18-layers BoxPlus structure (a) 2D error scatter (Y-Z plane - right) (b) 3D error scatter (Y-Z plane - right)

S33 - (Y-Z) plane – left

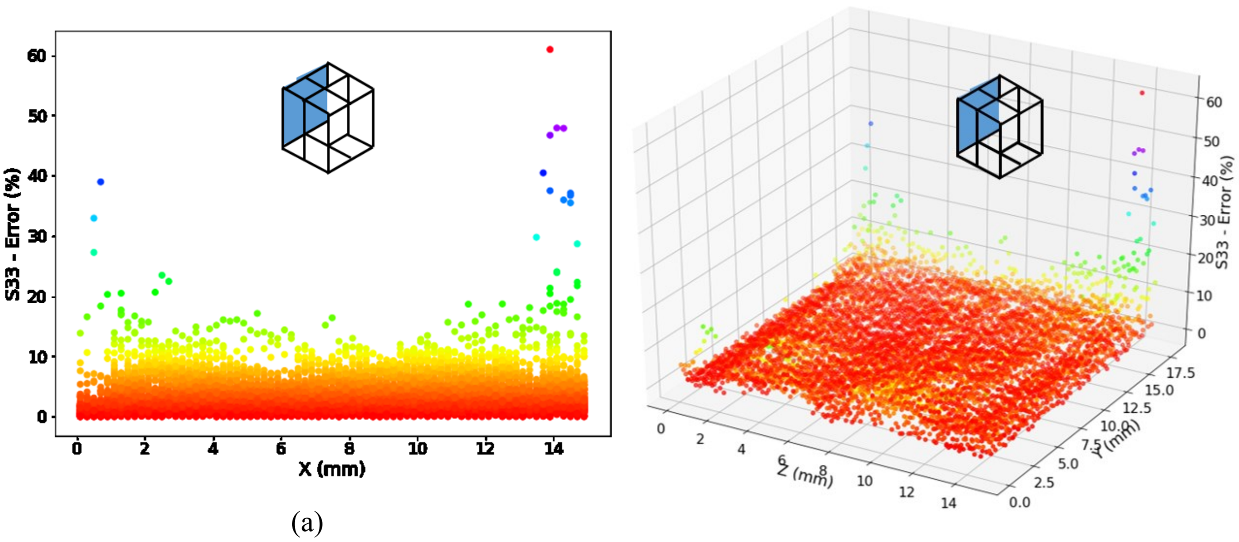

(a)

(b)

Figure 56 S33 distribution of 18-layers BoxPlus structure (a) 2D error scatter (Y-Z plane - left) (b) 3D error scatter (Y-Z plane - left)

S22 - (Y-Z) plane – left

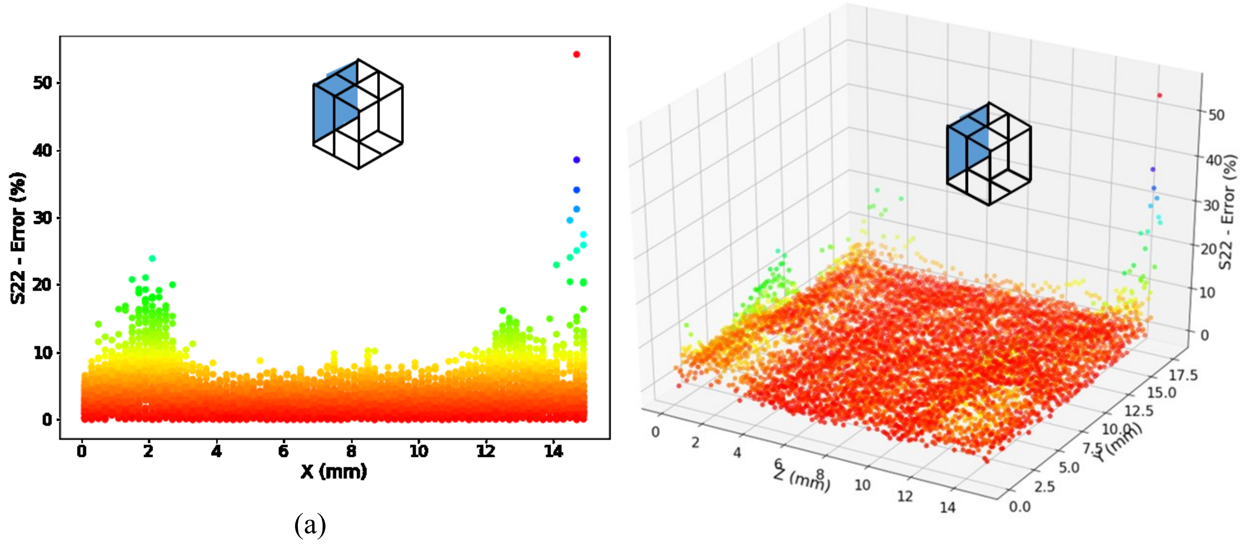

(a)

(b)

Figure 57 S22 distribution of 18-layers BoxPlus structure (a) 2D error scatter (Y-Z plane - left) (b) 3D error scatter (Y-Z plane - left)

S11 – (X-Y) plane – middle

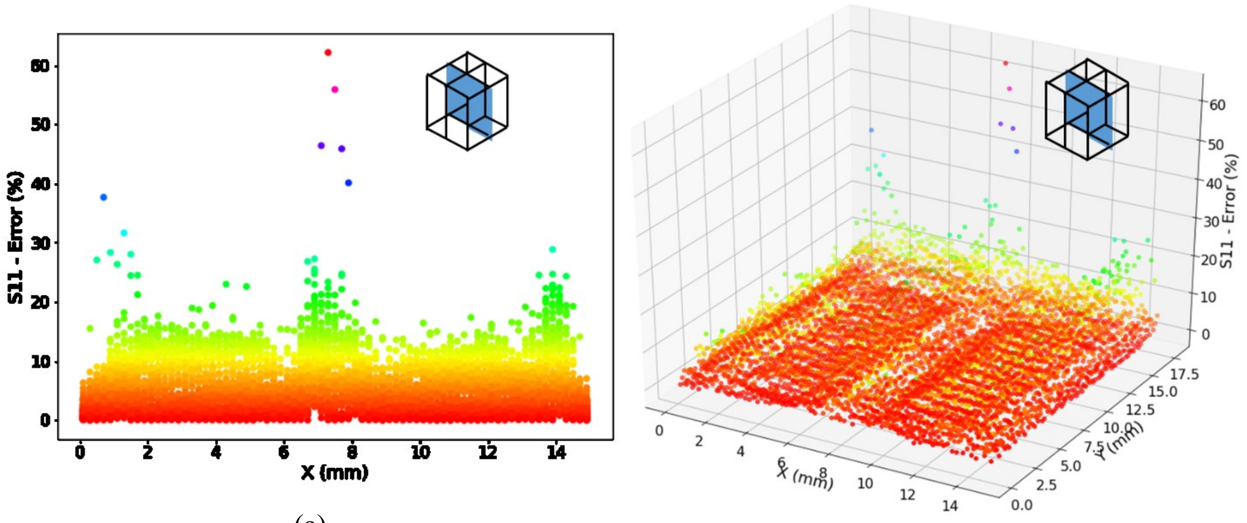

(a)

(b)

Figure 58 S11 distribution of 18-layers BoxPlus structure (a) 2D error scatter (X-Y plane - middle) (b) 3D error scatter (X-Y plane - middle)

S22 – (X-Y) plane – middle

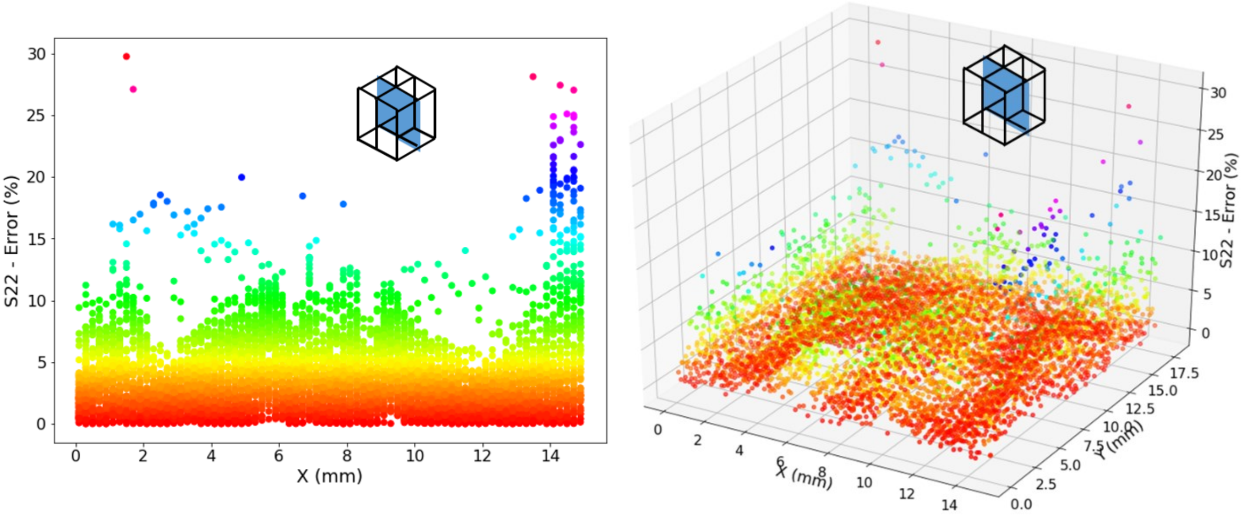

(a)

(b)

Figure 59 S22 distribution of 18-layers BoxPlus structure (a) 2D error scatter (X-Y plane - middle) (b) 3D error scatter (X-Y plane - middle)

S33 - (Y-Z) plane – middle

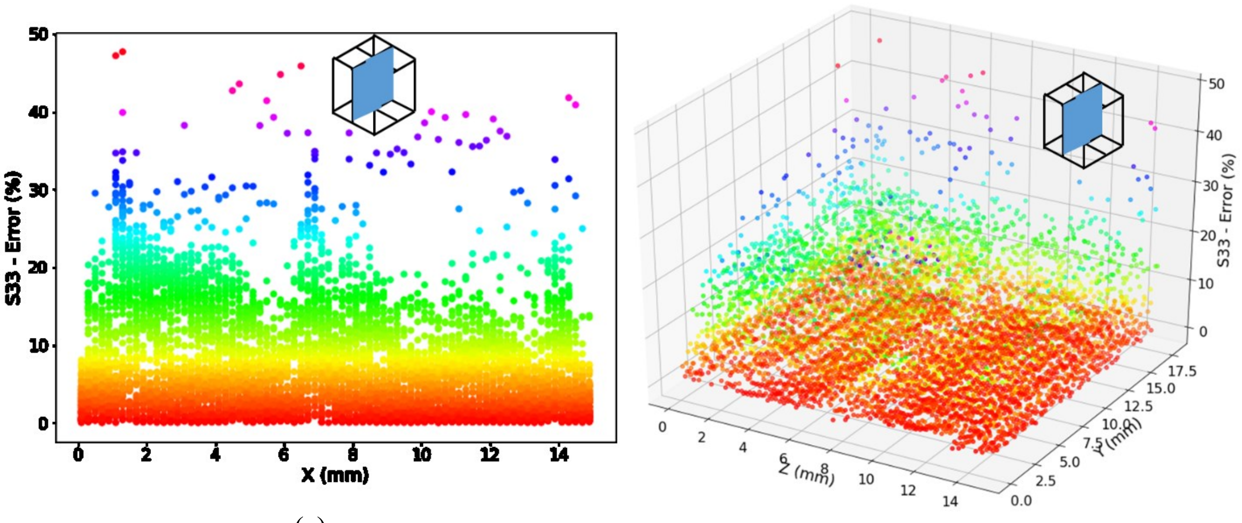

(a)

(b)

Figure 60 S33 distribution of 18-layers BoxPlus structure (a) 2D error scatter (Y-Z plane - middle) (b) 3D error scatter (Y-Z plane - middle)

S22 - (Y-Z) plane – middle

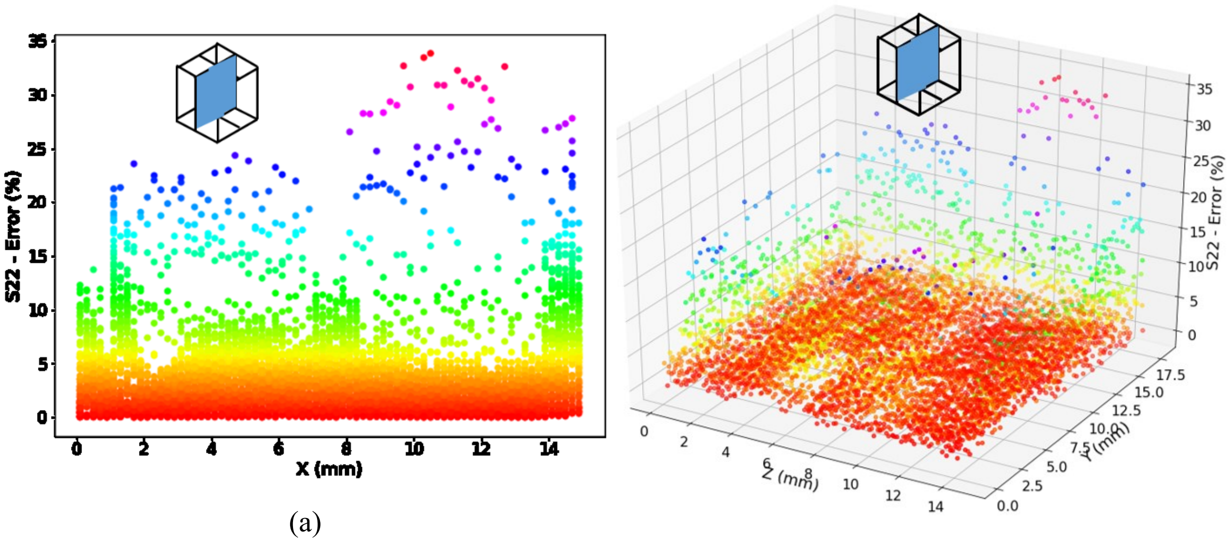

(a)

(b)

Figure 61 S22 distribution of 18-layers BoxPlus structure (a) 2D error scatter (Y-Z plane - middle) (b) 3D error scatter (Y-Z plane - middle)

SemiBox wall

S33 – (Y-Z) plane – right

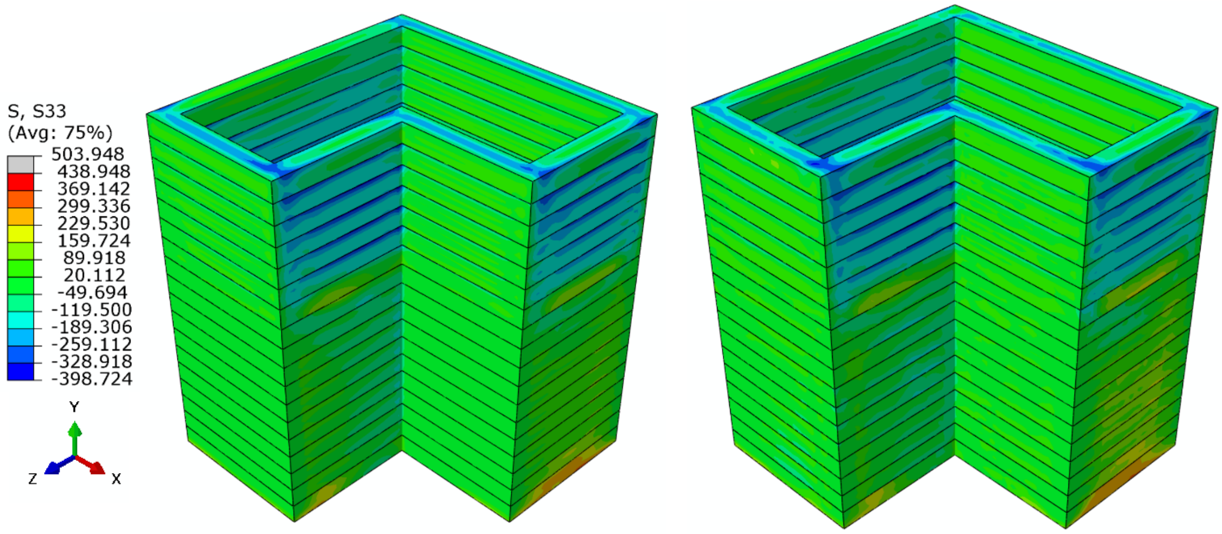

(a)

(b)

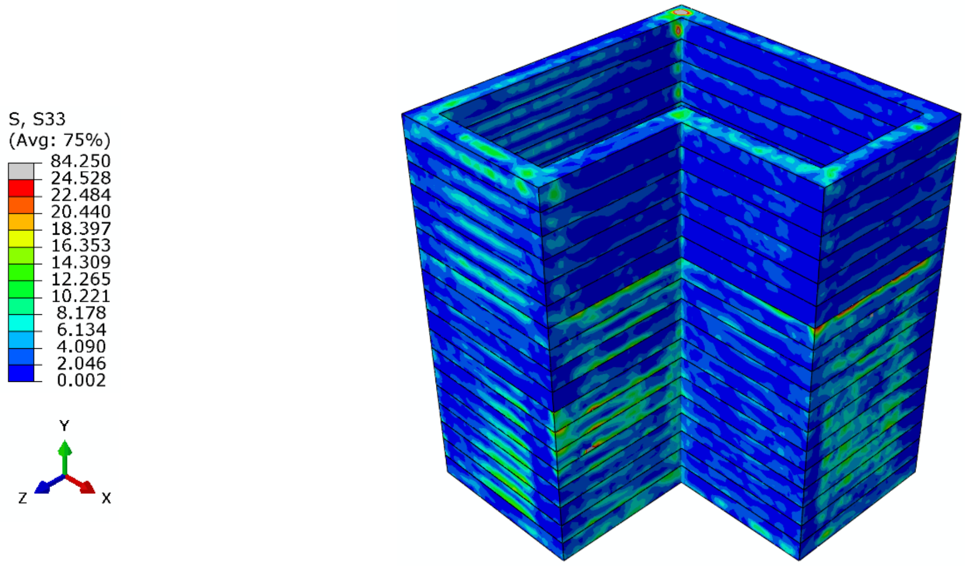

(c)

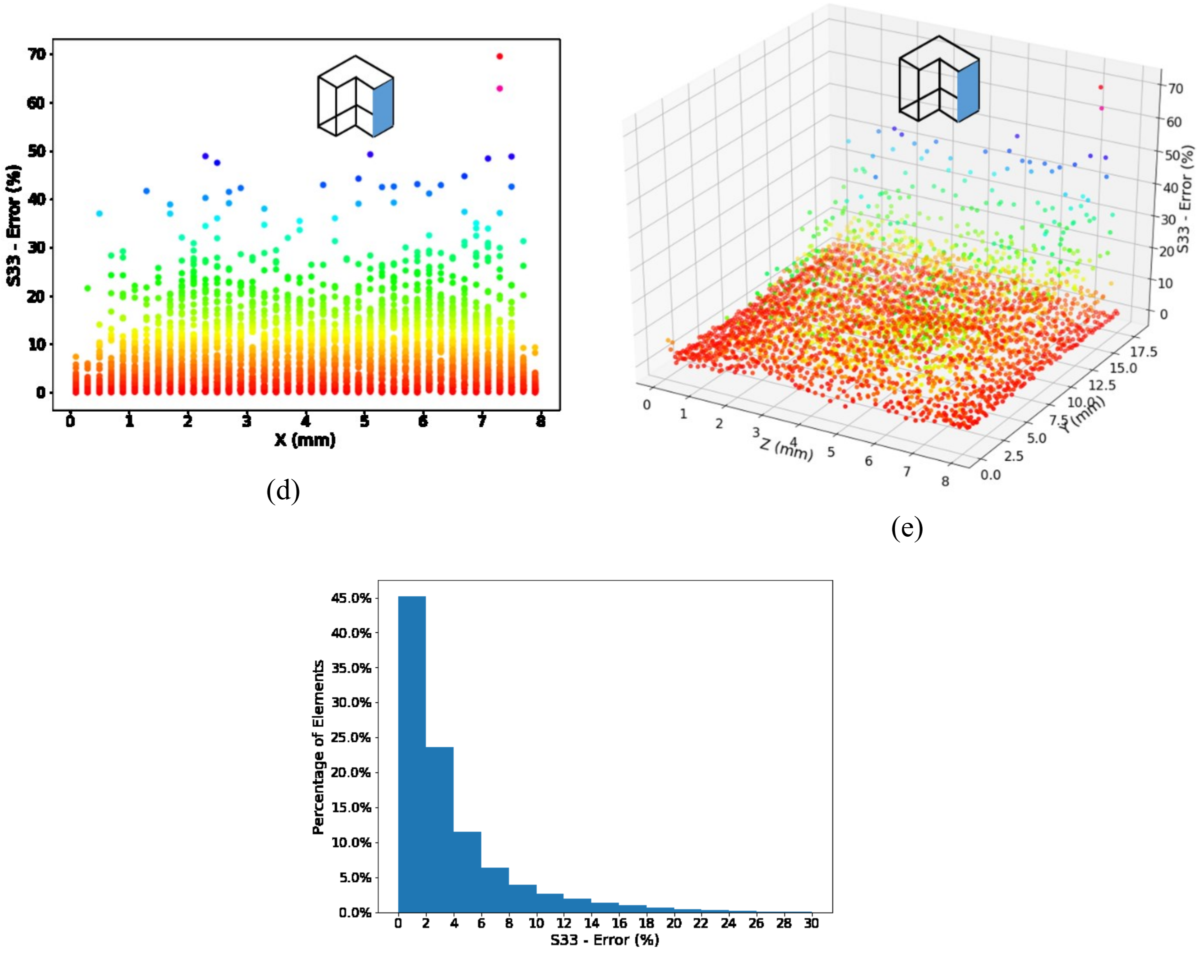

(d)

(e)

(f)

Figure 62 S33 distribution of 18-layers SemiBox wall (in MPa) (a) FINITE ELEMENT analysis (b) ANN prediction (c) error value (%) (d) 2D error scatter (Y-Z plane - right) (e) 3D error scatter (Y-Z plane - right) (f) histogram of the error

S22 – (Y-Z) plane – right

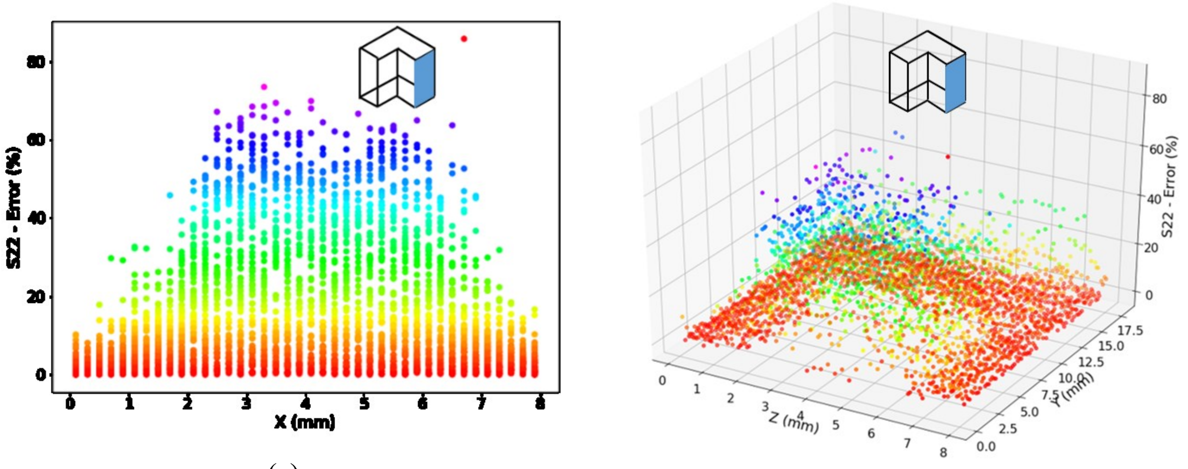

(a)

(b)

Figure 63 S22 distribution of 18-layers SemiBox (a) 2D error scatter (X-Y plane - front) (b) 3D error scatter (X-Y plane - front)

S11 – (X-Y) plane - front

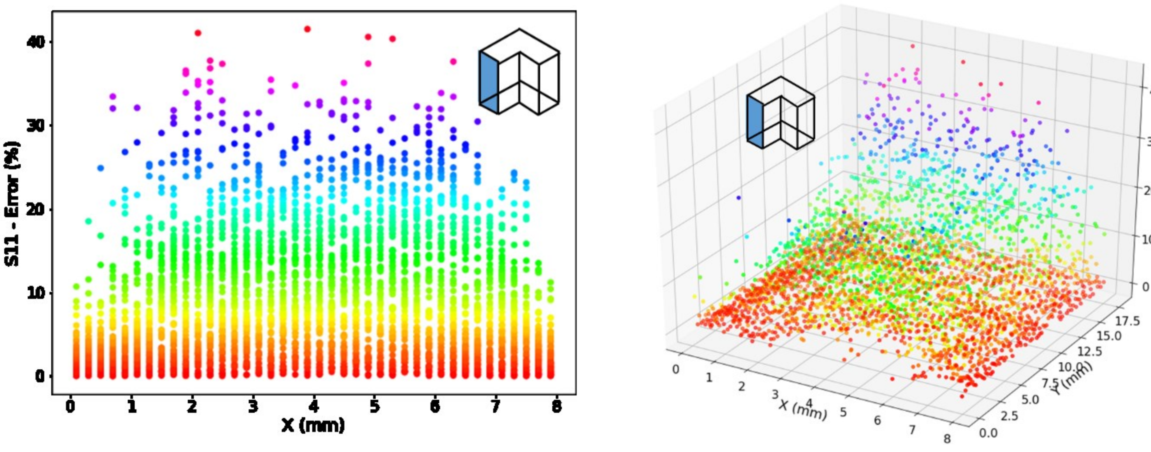

(a) (b)

Figure 64 S11 distribution of 18-layers SemiBox (a) 2D error scatter (X-Y plane - front) (b) 3D error scatter (X-Y plane - front)

S22 – (X-Y) plane - front

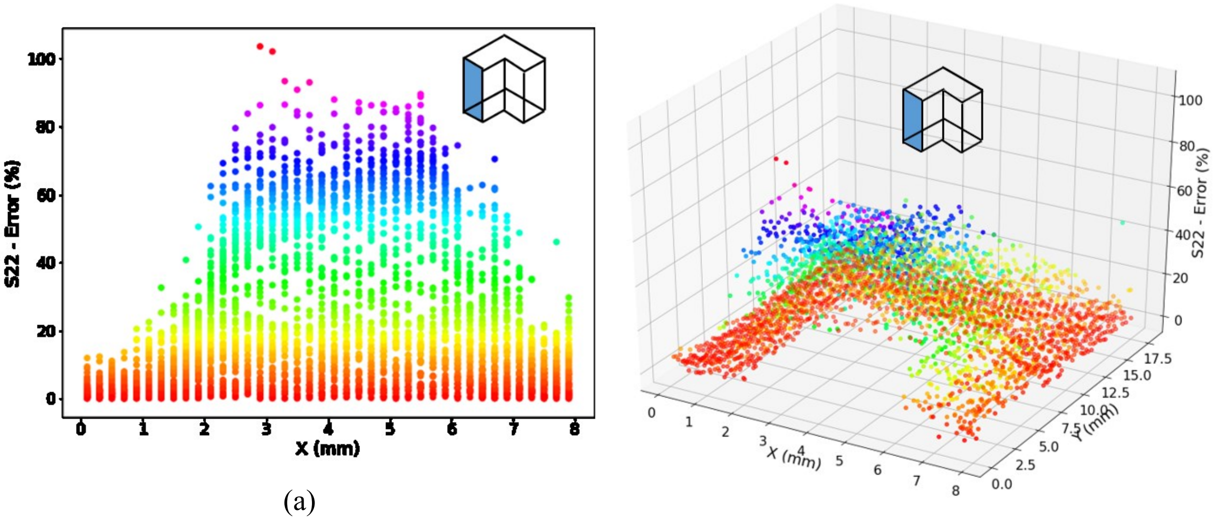

(a) (b)

Figure 65 S22 distribution of 18-layers SemiBox (a) 2D error scatter (X-Y plane - front) (b) 3D error scatter (X-Y plane - front)

S33 – (Y-Z) plane - left

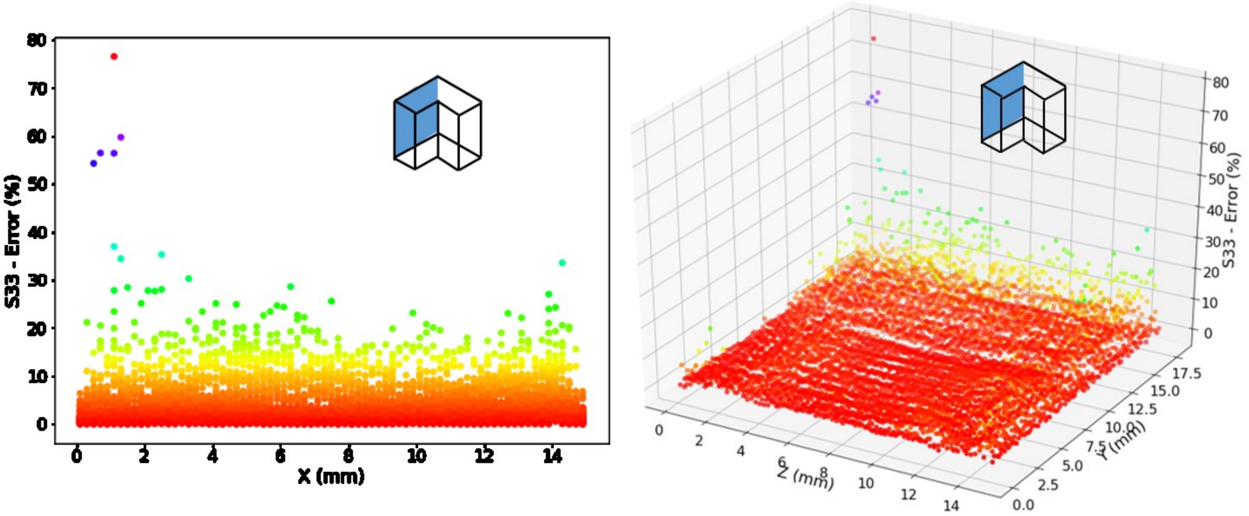

(a)

(b)

Figure 66 S33 distribution of 18-layers SemiBox (a) 2D error scatter (Y-Z plane - left) (b) 3D error scatter (Y-Z plane - left)

S22 – (Y-Z) plane - left

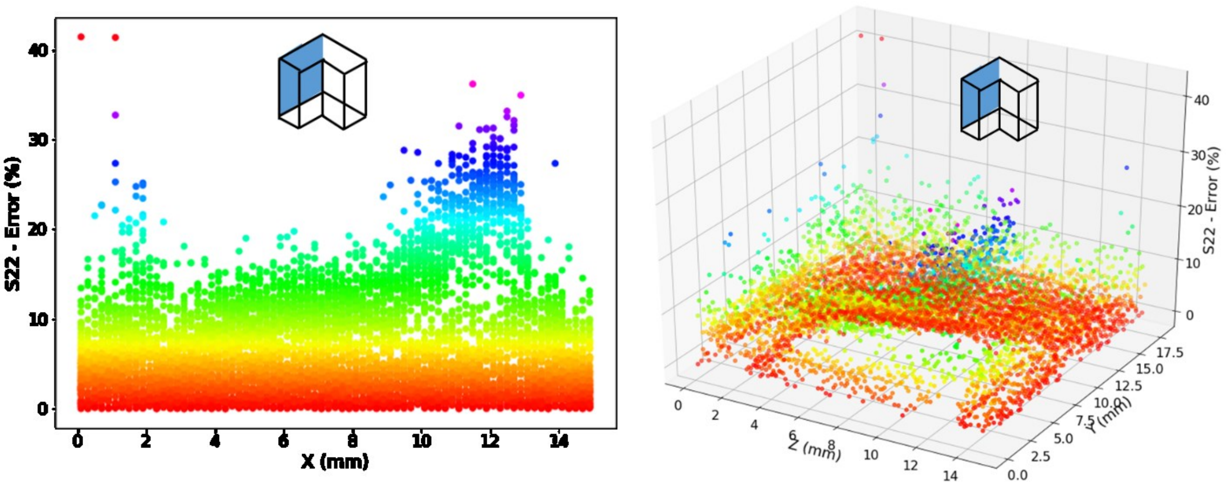

(a)

(b)

Figure 67 S22 distribution of 18-layers SemiBox (a) 2D error scatter (Y-Z plane - left) (b) 3D error scatter (Y-Z plane - left)

S11 – (X-Y) plane - middle

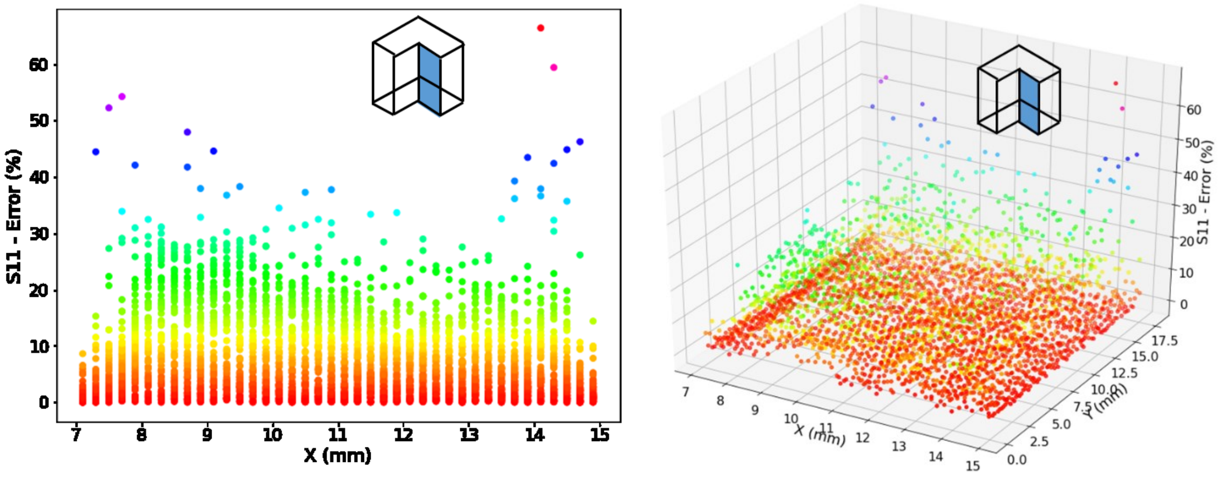

(a)

(b)

Figure 68 S11 distribution of 18-layers SemiBox (a) 2D error scatter (X-Y plane - middle) (b) 3D error scatter (X-Y plane - middle)

S22 – (X-Y) plane - middle

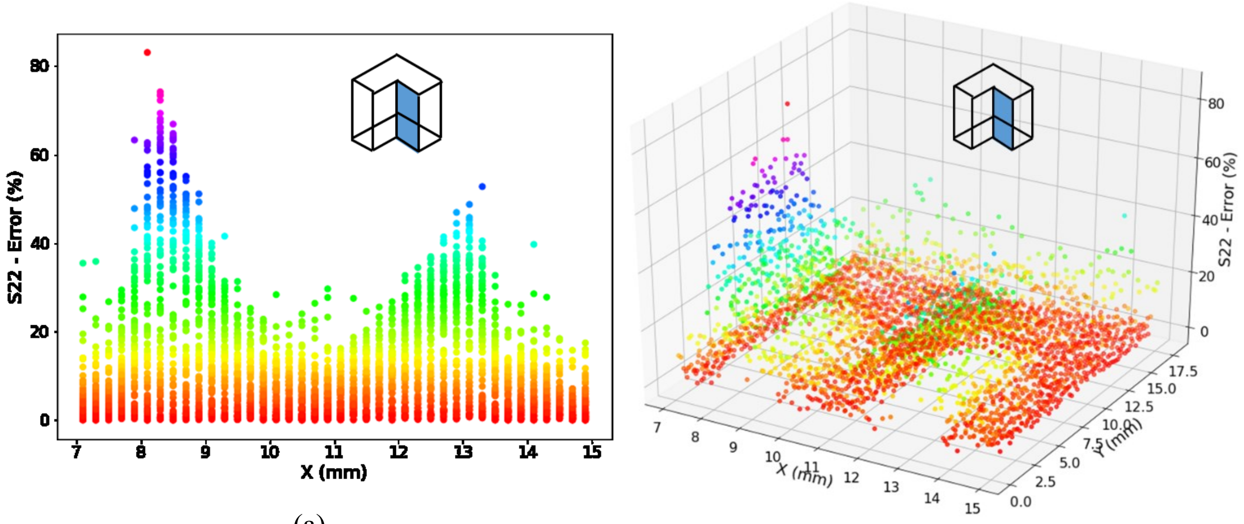

(a)

(b)

Figure 69 S22 distribution of 18-layers SemiBox (a) 2D error scatter (X-Y plane - middle) (b) 3D error scatter (X-Y plane - middle)

S33 – (Y-Z) plane - middle

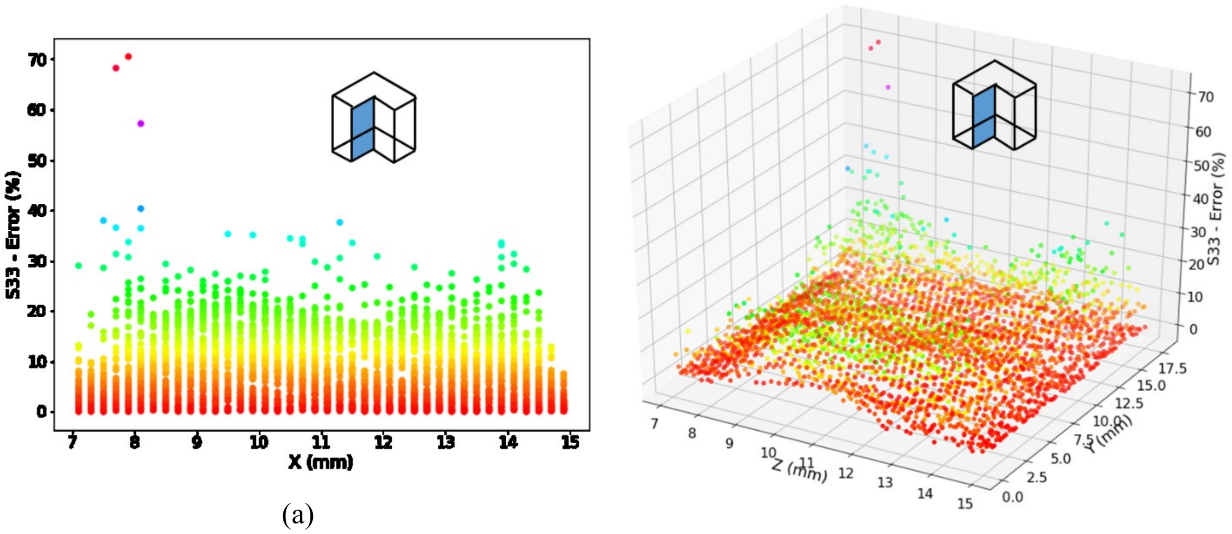

(a)

(b)

Figure 70 S33 distribution of 18-layers SemiBox (a) 2D error scatter (Y-Z plane - middle) (b) 3D error scatter (Y-Z plane - middle)

S22 – (Y-Z) plane - middle

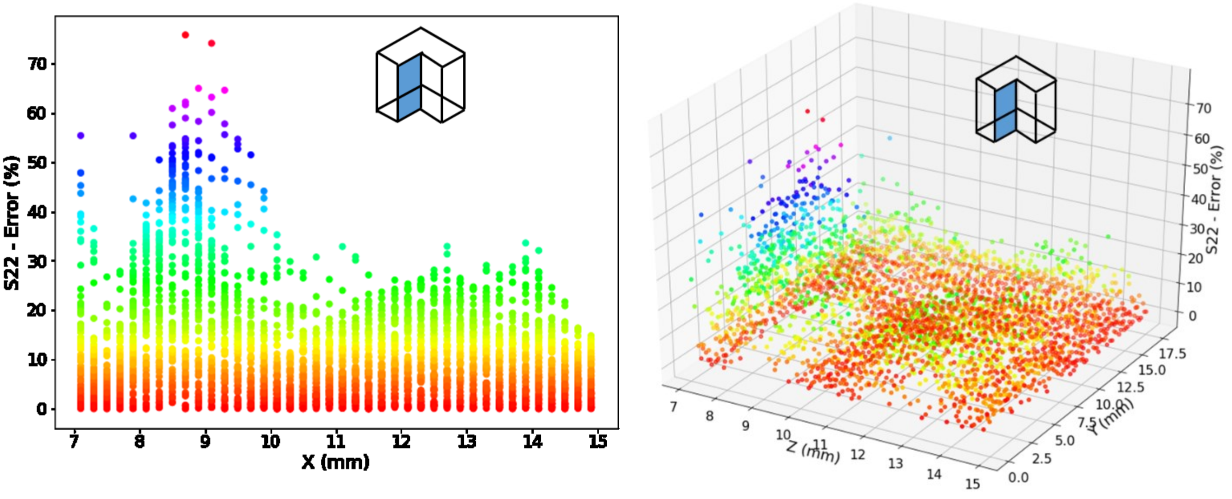

(a)

(b)

Figure 71 S22 distribution of 18-layers SemiBox (a) 2D error scatter (Y-Z plane - middle) (b) 3D error scatter (Y-Z plane - middle)

Hourglass-shape wall

S11 – (X-Y) plane – back

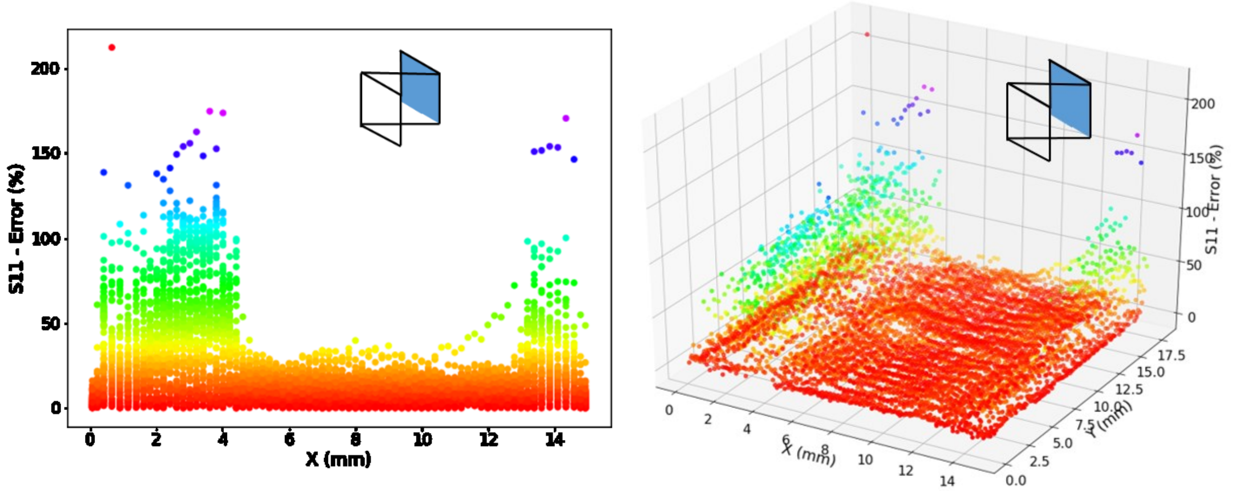

(a)

(b)

Figure 72 S11 distribution of 18-layers Hourglass-shape wall (a) 2D error scatter (X-Y plane - back) (b) 3D error scatter (X-Y plane - back)

S22 – (X-Y) plane – back

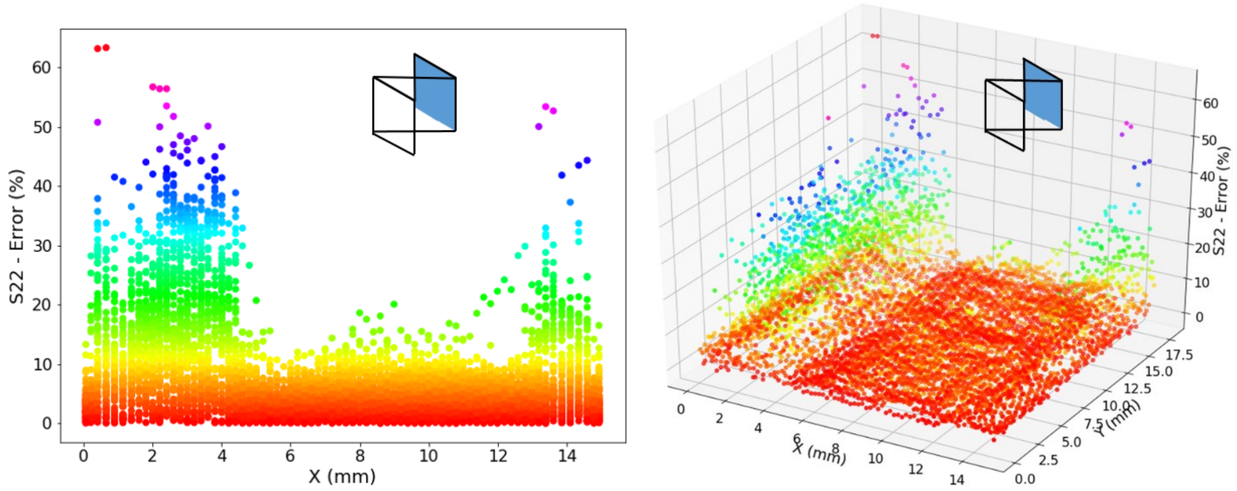

(a)

(b)

Figure 73 S22 distribution of 18-layers Hourglass-shape wall (a) 2D error scatter (X-Y plane - back) (b) 3D error scatter (X-Y plane - back)

S33 – 45 slope plane

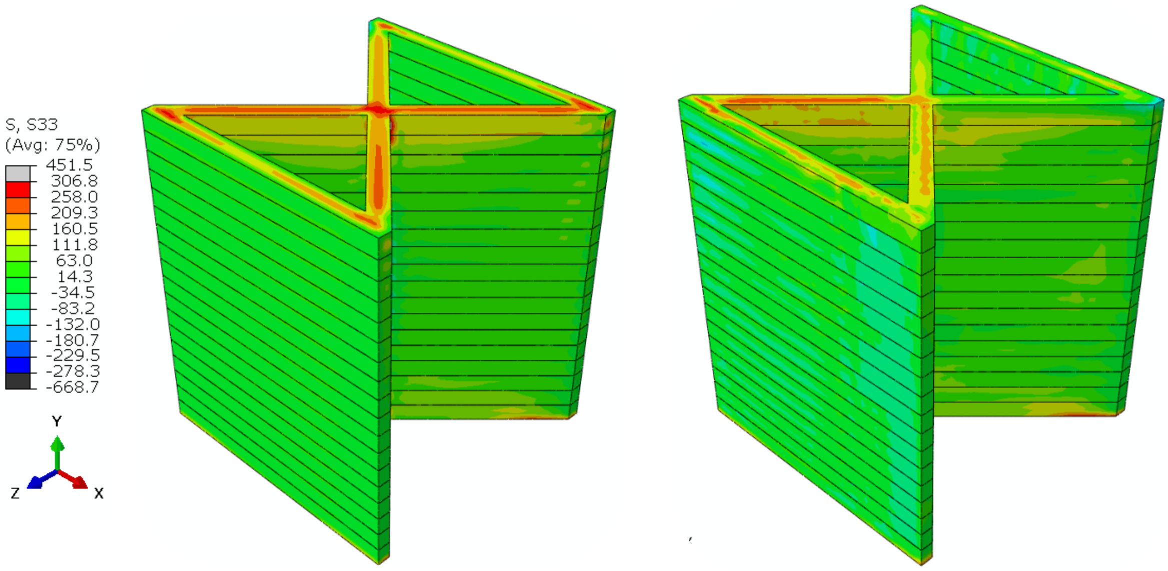

(a)

(b)

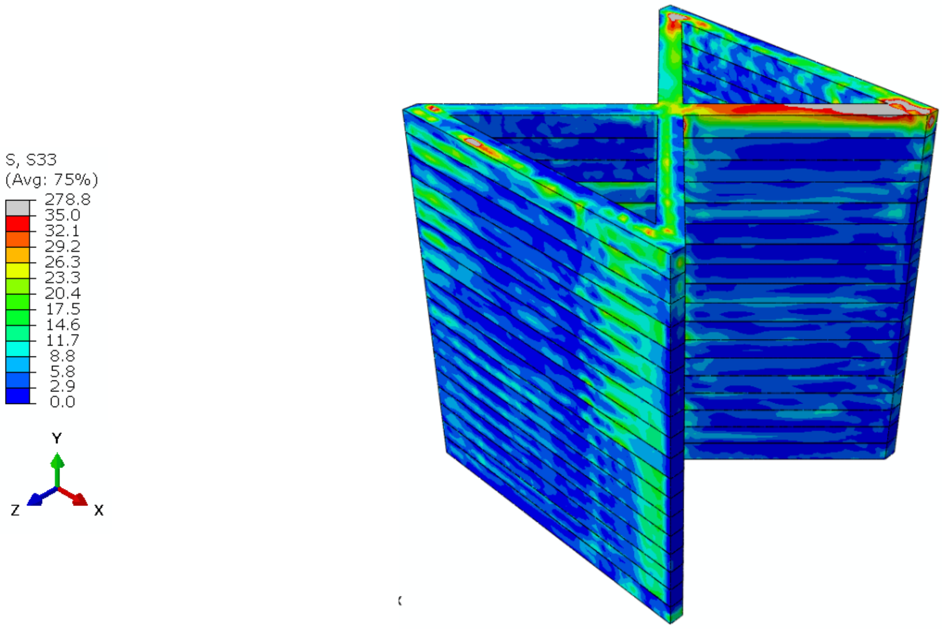

(c)

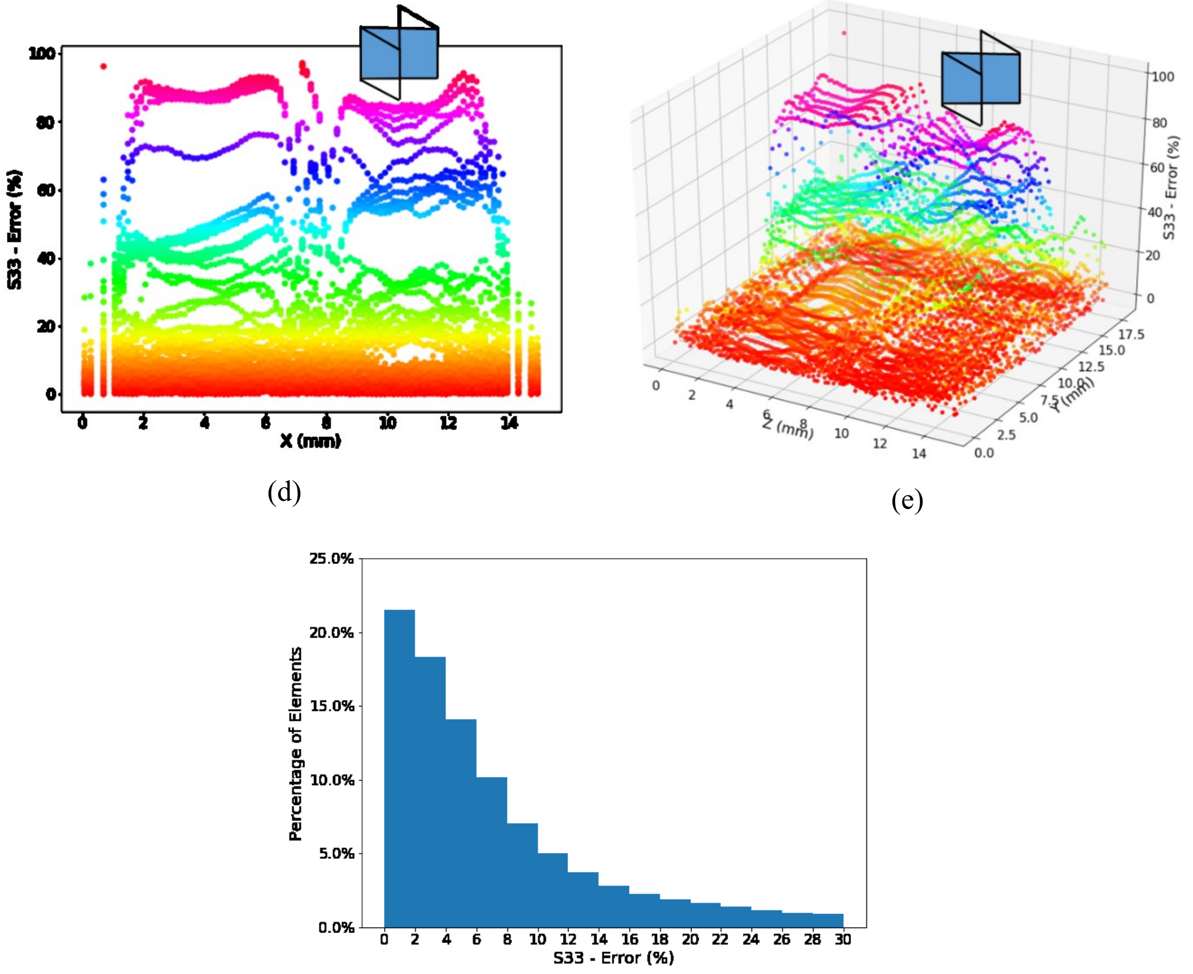

(d) (e)

(f)

Figure 74 S33 distribution of 18-layers Hourglass-shape (in MPa) (a) FINITE ELEMENT analysis (b) ANN prediction (c) error value (%) (d) 2D error scatter (45 slope) (e) 3D error scatter (45 slope) (f) histogram of the error

S22 – 45 slope plane

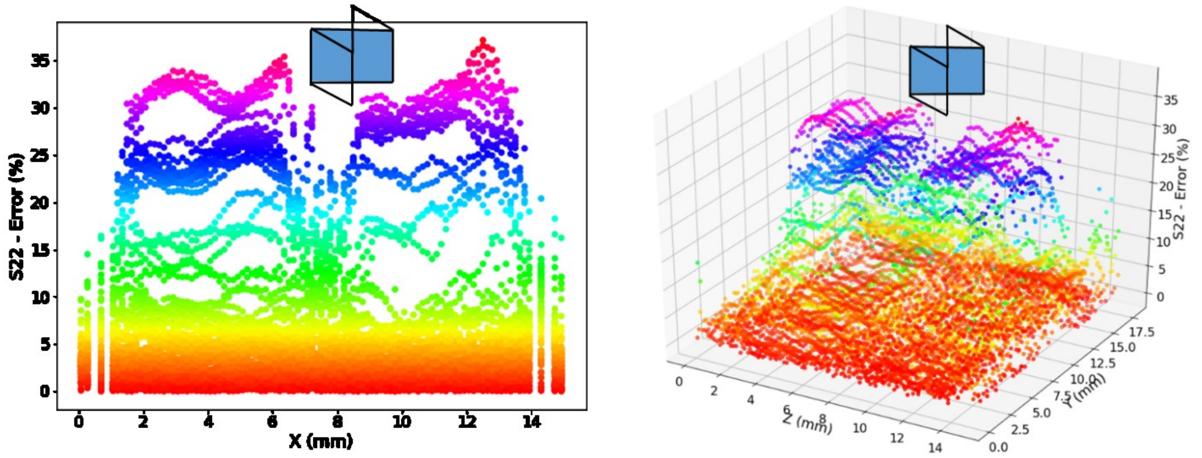

(a) (b)

Figure 75 S22 distribution of 18-layers Hourglass-shape wall (a) 2D error scatter (45 slope) (b) 3D error scatter (45 slope)

S33 – 135 slope plane

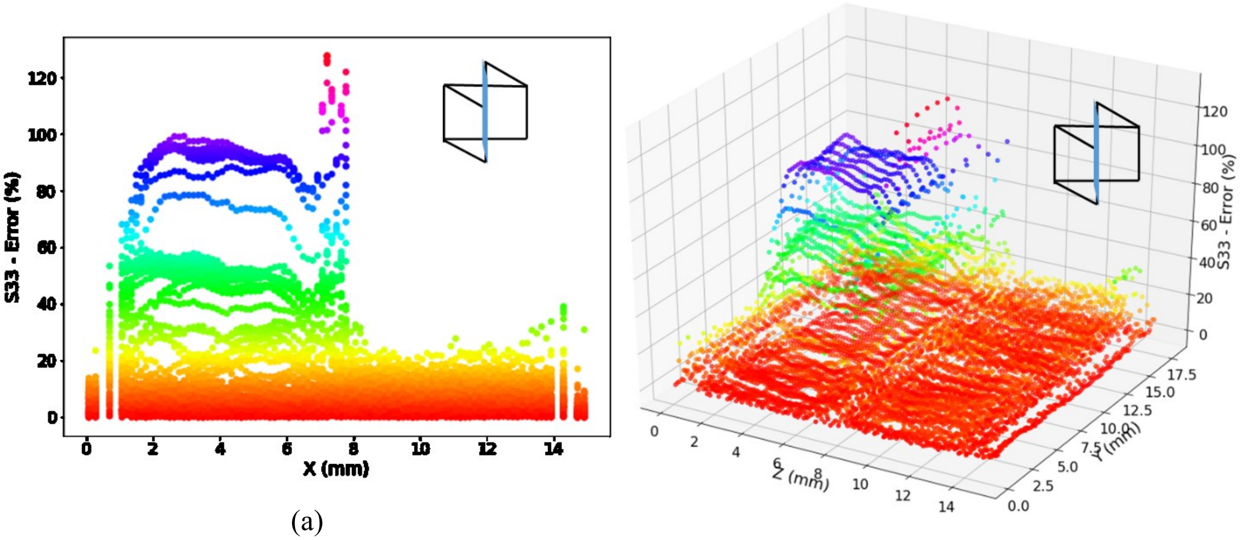

(a)

(b)

Figure 76 S33 distribution of 18-layers Hourglass-shape wall (a) 2D error scatter (135 slope) (b) 3D error scatter (135 slope)

S22 – 135 slope plane

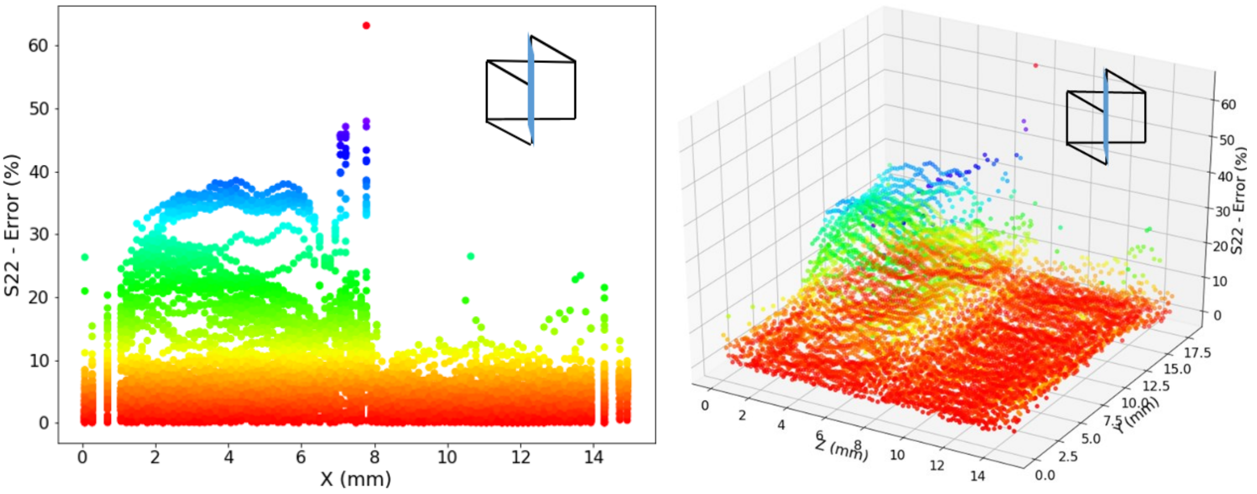

(a)

(b)

Figure 77 S22 distribution of 18-layers Hourglass-shape wall (a) 2D error scatter (135 slope) (b) 3D error scatter (135 slope)

Arrow-shape wall

S33 – (Y-Z) plane

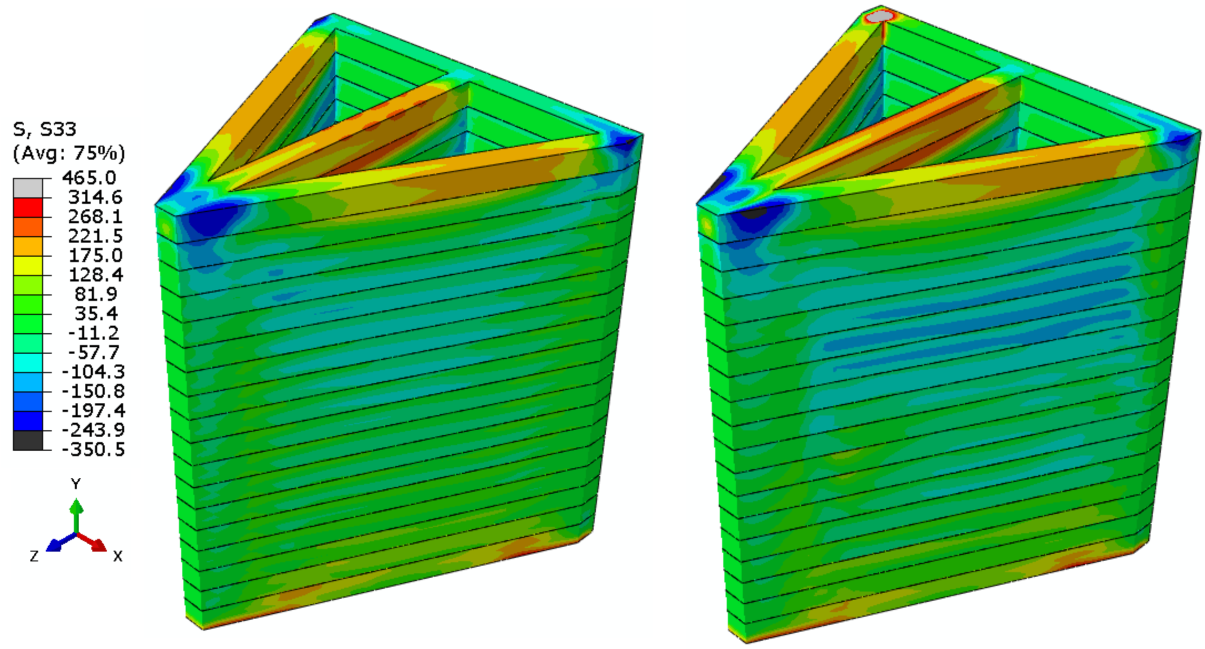

(a)

(b)

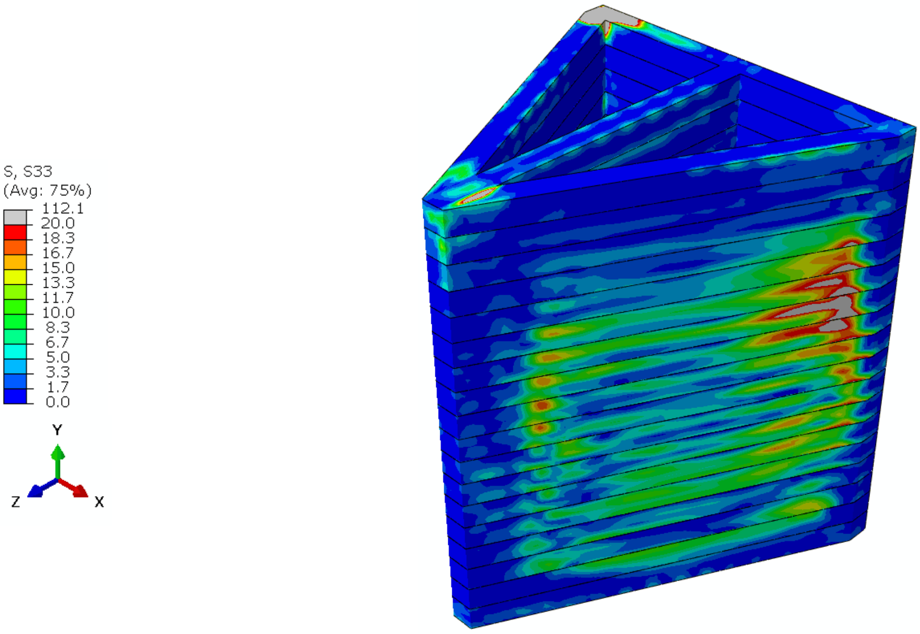

(c)

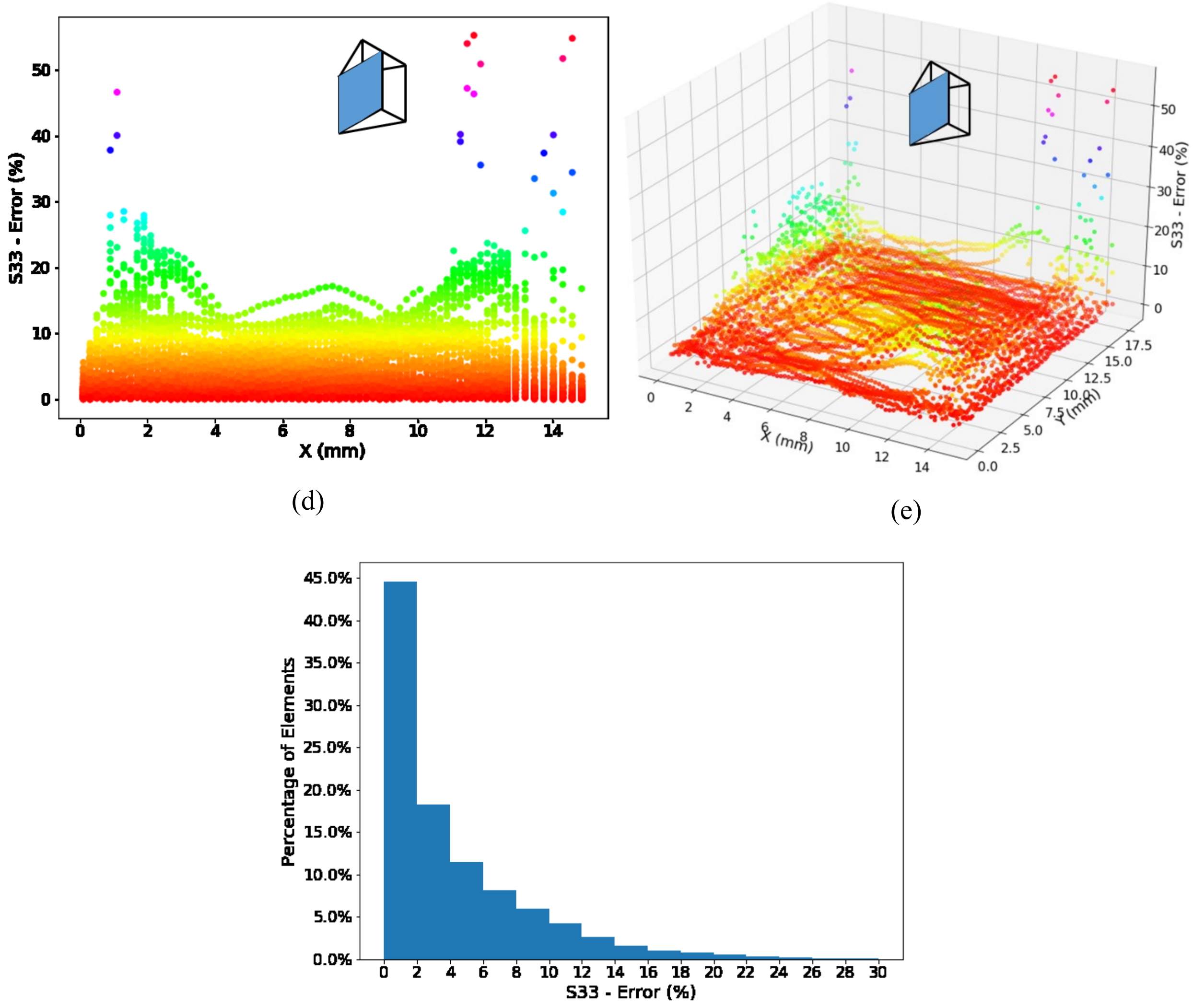

(d)

(e)

(f)

Figure 78 S33 distribution of 18-layers Arrow-shape wall (in MPa) (a) FINITE ELEMENT analysis (b) ANN prediction (c) error value (%) (d) 2D error scatter (Y-Z plane) (e) 3D error scatter (Y-Z plane) (f) histogram of the error

S33 – (Y-Z) plane

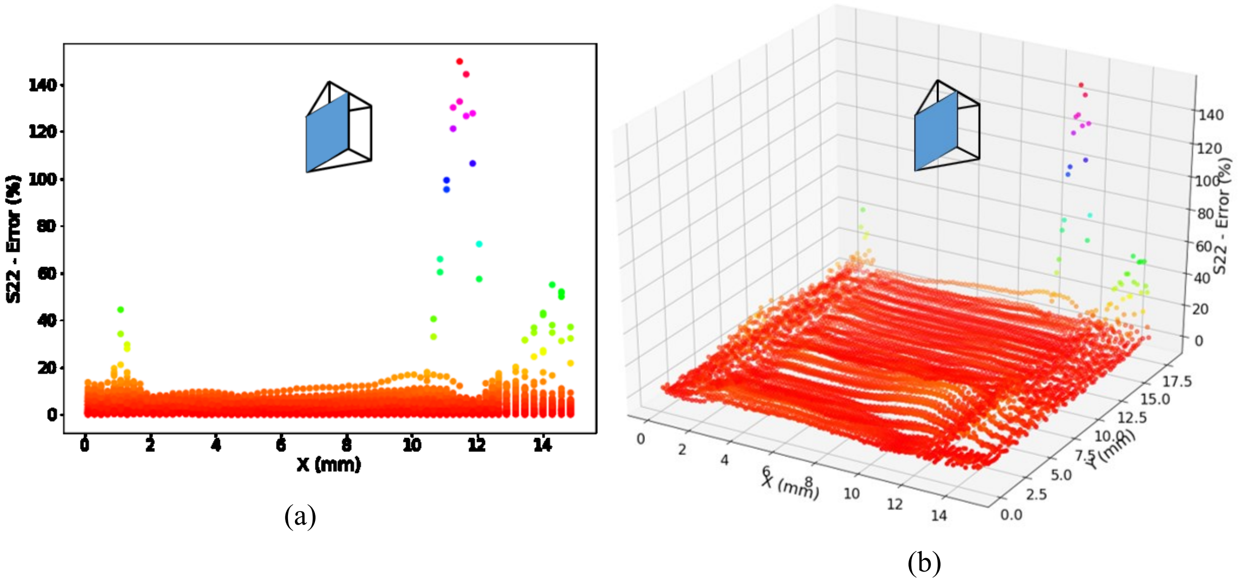

(a)

(b)

Figure 79 S22 distribution of 18-layers Arrow-shape wall (a) 2D error scatter (Y-Z plane) (b) 3D error scatter (Y-Z plane)

S22 – (X-Y) plane

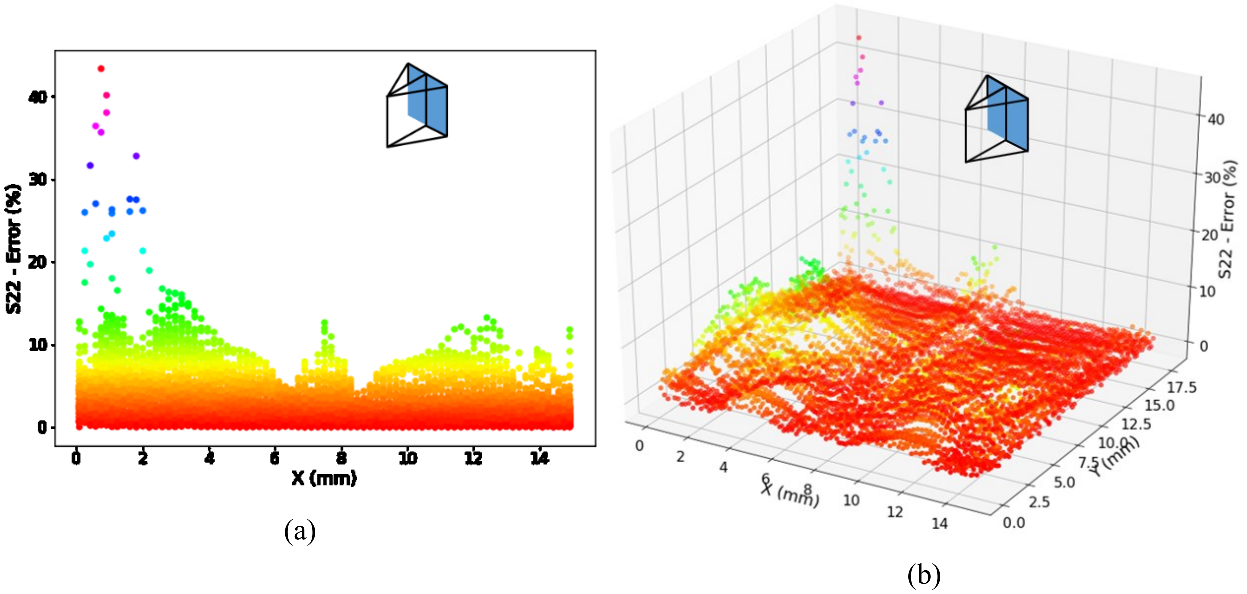

(a)

(b)

Figure 80 S22 distribution of 18-layers Arrow-shape wall (a) 2D error scatter (X-Y plane) (b) 3D error scatter (X-Y plane)

S33 – 45 slope plane

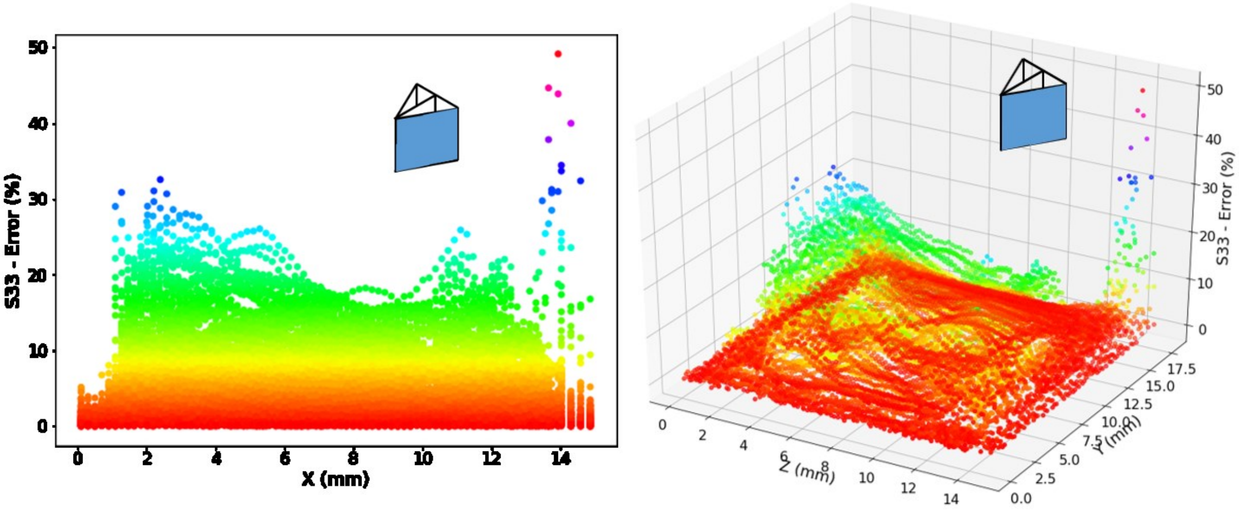

(a)

(b)

Figure 81 S33 distribution of 18-layers Arrow-shape wall (a) 2D error scatter (45 slope) (b) 3D error scatter (45 slope)

S33 – 135 slope plane

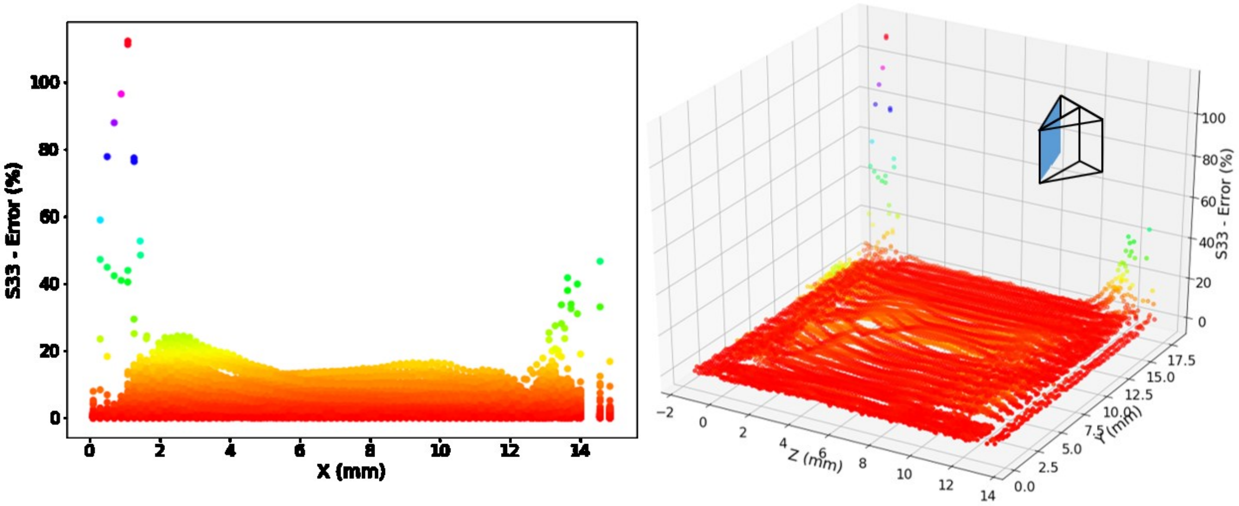

(a)

(b)

Figure 82 S33 distribution of 18-layers Arrow-shape wall (a) 2D error scatter (135 slope) (b) 3D error scatter (135 slope)

S22 – 135 slope plane

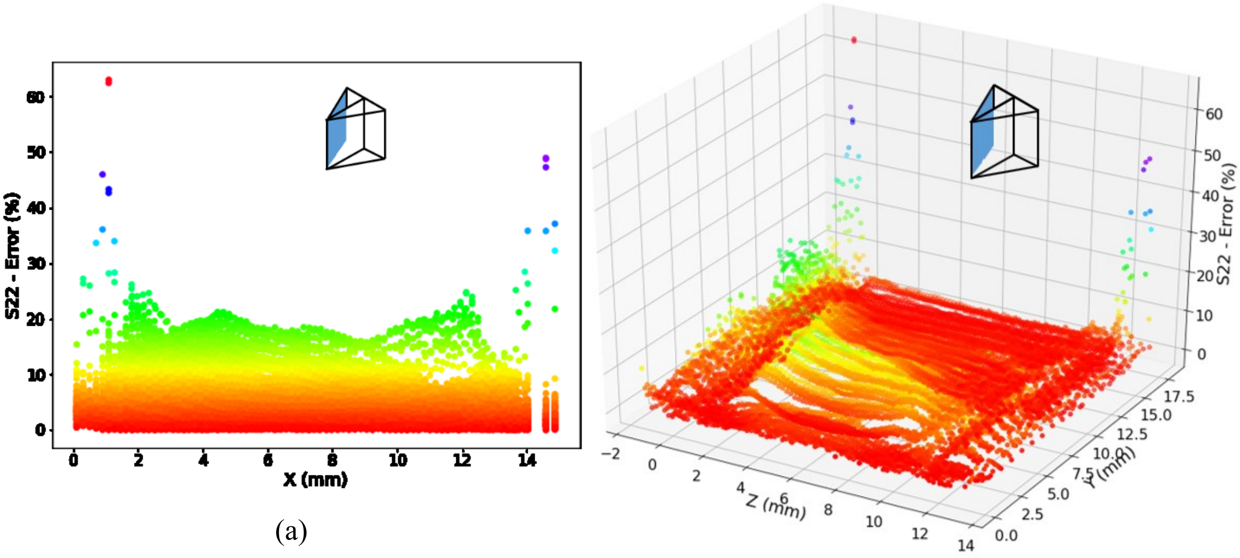

(a)

(b)

Figure 83 S22 distribution of 18-layers Arrow-shape wall (a) 2D error scatter (135 slope) (b) 3D error scatter (135 slope)

Appendix B: Developed subroutines

As discussed in the previous sections, the DMD and generally the DMD processes require certain techniques to account for the element addition or stacking through deposition by a laser beam. Commercial software packages such as ABAQUS do not offer the necessary modulus for the element activation and modeling/controlling of the heat source. Therefore, user-defined subroutines are developed to be coupled with the FE solution of a given geometry and discussed here. It should be noted that the user-defined subroutines are written in FORTRAN. Consequently, a FORTRAN compiler should be installed on the machine and coupled with ABAQUS in order to be able to run a user-defined-based developed model.

- UMATHT subroutine

This subroutine is used to develop a user-defined thermal constitutive behavior for a given material and assign arbitrary material properties for certain elements in an ABAQUS/STANDARD heat transfer problem [246]. By implementing this subroutine and defining specific rules or criteria for the activation of the elements, element activation can be achieved. Based on the laser beam trajectory and feed rate, the activation criteria are defined and the activated elements are assigned with real and actual thermal properties such as conductivity, specific heat, internal energy, … etc. However, the elements that are not deposited (inactive) yet, are assigned with scaled thermal properties to not have any role and impact in the heat transfer. The main reason to utilize such a technique is that almost all of the commercial FE packages such as ABAQUS, take the geometry of a part at the beginning of the analysis and form the stiffness matrices based on the elements' connectivity. Therefore, all elements should be defined at the beginning of the analysis and be assigned a material property that would define the material constitutive behavior. UMATHT subroutine main structure is shown in the following [246]:

```
SUBROUTINE UMATHT(U,DUDT,DUDG,FLUX,DFDT,DFDG,
     1 STATEV,TEMP,DTEMP,DTEMDX,TIME,DTIME,PREDEF,DPRED,
     2 CMNAME,NTGRD,NSTATV,PROPS,NPROPS,COORDS,PNEWDT,
     3 NOEL,NPT,LAYER,KSPT,KSTEP,KINC)
C
      INCLUDE 'ABA_PARAM.INC'
C
      CHARACTER*80 CMNAME
      DIMENSION DUDG(NTGRD),FLUX(NTGRD),DFDT(NTGRD),
     1 DFDG(NTGRD,NTGRD),STATEV(NSTATV),DTEMDX(NTGRD),
     2 TIME(2),PREDEF(1),DPRED(1),PROPS(NPROPS),COORDS(3)

      user coding to define U,DUDT,DUDG,FLUX,DFDT,DFDG,
      and possibly update STATEV, PNEWDT
      RETURN
```

```
      END
```

- DFLUX subroutine

This subroutine is used to define the user-defined heat source model that should be applied in the analysis [246]. ABAQUS modulus only provides the concentrated and uniform heat fluxes that cannot be applied to the DMD process. Goldak's double ellipsoid heat source model was utilized in the present study. Furthermore, the movement of the heat source model is defined based on the geometry of the part and the feed-rate magnitude in 3D space to account for the laser trajectories for different layers. The heat flux can be described as 3D body force and applied to the bulk or can be defined as 2D and applied on the specific surface of the part. A general format of DFLUX is represented in the following [246]:

```
SUBROUTINE DFLUX(FLUX,SOL,KSTEP,KINC,TIME,NOEL,NPT,COORDS,
     1 JLTYP,TEMP,PRESS,SNAME)
C
      INCLUDE 'ABA_PARAM.INC'
C
      DIMENSION FLUX(2), TIME(2), COORDS(3)
      CHARACTER*80 SNAME

      user coding to define FLUX(1) and FLUX(2)

      RETURN
      END
```

- UMAT subroutine

This subroutine can be used to impose user-defined mechanical constitutive behavior for a given material in ABAQUS/STANDARD [246]. Similar to UMATHT, the UMAT defines a certain criterion to account for the element activation in the structural FE model. the context of developing a UMAT subroutine requires vast knowledge of the elasticity and plasticity of deformable materials. Analogous to the thermal FE analysis, the whole part should be defined in the FE analysis prior to starting the solution and the deposited elements should be assigned with real and actual material properties such as Elasticity Modulus and Poisson ratio and the inactive elements should be assigned with scaled parameters not to encounter with the mechanical solution and evolution of stresses in the deposited regions. ABAQUS passes the coordinates of the nodes or integration points to the UMAT subroutine and it can be used to express the activation criteria as a function of time and coordinates. UMAT is one of the most advanced level subroutines that require considerable expertise in solid mechanics and shown in the following [246]:

```
SUBROUTINE UMAT(STRESS,STATEV,DDSDDE,SSE,SPD,SCD,
     1 RPL,DDSDDT,DRPLDE,DRPLDT,
     2 STRAN,DSTRAN,TIME,DTIME,TEMP,DTEMP,PREDEF,DPRED,CMNAME,
     3 NDI,NSHR,NTENS,NSTATV,PROPS,NPROPS,COORDS,DROT,PNEWDT,
     4 CELENT,DFGRD0,DFGRD1,NOEL,NPT,LAYER,KSPT,JSTEP,KINC)
C
      INCLUDE 'ABA_PARAM.INC'
C
      CHARACTER*80 CMNAME
      DIMENSION STRESS(NTENS),STATEV(NSTATV),
     1 DDSDDE(NTENS,NTENS),DDSDDT(NTENS),DRPLDE(NTENS),
     2 STRAN(NTENS),DSTRAN(NTENS),TIME(2),PREDEF(1),DPRED(1),
     3
PROPS(NPROPS),COORDS(3),DROT(3,3),DFGRD0(3,3),DFGRD1(3,3),
     4 JSTEP(4)

      user coding to define DDSDDE, STRESS, STATEV, SSE, SPD, SCD
      and, if necessary, RPL, DDSDDT, DRPLDE, DRPLDT, PNEWDT

      RETURN
      END
```

- UHARD subroutine

This subroutine is used to define the hardening of the material (the slope of the yield curve) in different stress/strain levels [246]. The values from this subroutine are passed to the UMAT subroutine to determine the plastic behavior in the von-Mises yield criteria in the adopted model. A general scheme of the UHARD subroutine is provided in the following [246]:

```
      SUBROUTINE
UHARD(SYIELD,HARD,EQPLAS,EQPLASRT,TIME,DTIME,TEMP,
     1     DTEMP,NOEL,NPT,LAYER,KSPT,KSTEP,KINC,CMNAME,NSTATV,
     2     STATEV,NUMFIELDV,PREDEF,DPRED,NUMPROPS,PROPS)
C
      INCLUDE 'ABA_PARAM.INC'
C
      CHARACTER*80 CMNAME
      DIMENSION HARD(3),STATEV(NSTATV),TIME(*),
     $          PREDEF(NUMFIELDV),DPRED(*),PROPS(*)

      user coding to define SYIELD,HARD(1),HARD(2),HARD(3)

      RETURN
      END
```

Appendix C: Developed Python-based scripts

ABAQUS offers a very user-friendly interface for generating 3D FE models. Every module in ABAQUS applies certain features to the model such as creating the geometry, material properties, interactions (contacts, convection, and radiation), boundary conditions, meshing, and performing the job [246]. However, for creating a robust and adjustable technique to generate the FE models for thermal and mechanical analyses of different structures and applying the contact interactions between the layers, it is recommended to use the parametric design procedure and develop all the steps in a well-written Python script. ABAQUS was developed based on the objective-oriented scheme and it is feasible to use the scripting tool as explained in detail in ABAQUS documentation [246].

Furthermore, Python-based algorithms were developed for the postprocessing and building of the dataset for training and testing the ANNs. A summary of the implemented Python-based scripts is presented in the following for generating the FE models as well as for the post-processing.

- Genrating FE models

```
from abaqus import *

from abaqusConstants import *

#### Thermal Model ####

# Creating material and assiging it to the parts

mdb.models['thermal'].Material(name='Material-1')

mdb.models['thermal'].materials['Material-1'].Density(table=((7800.0, ), ))

mdb.models['thermal'].materials['Material-1'].UserMaterial(type=THERMAL,
thermalConstants=(14.6, 462.0, 20.0, 35.0, 700.0, 1500.0))

mdb.models['thermal'].HomogeneousSolidSection(name='Section-1', material='Material-1',
thickness=None)

p = mdb.models['thermal'].parts['Substrate']

region = p.sets['Set-1']

p.SectionAssignment(region=region, sectionName='Section-1', offset=0.0,
offsetType=MIDDLE_SURFACE, offsetField=", thicknessAssignment=FROM_SECTION)

p = mdb.models['thermal'].parts['Layer']

region = p.sets['Set-1']
```

```
p.SectionAssignment(region=region, sectionName='Section-1', offset=0.0,
offsetType=MIDDLE_SURFACE, offsetField='', thicknessAssignment=FROM_SECTION)


# Moving instances to build the component
a = mdb.models['thermal'].rootAssembly
for i in range(2,19):
    a.translate(instanceList=('Layer-'+str(i), ), vector=(0.0, (i-1)/1000., 0.0))


# Generating stpes and adjusting field outputs
mdb.models['thermal'].HeatTransferStep(name='Step-1', previous='Initial', maxNumInc=100000,
initialInc=0.02, minInc=1e-08, maxInc=0.05, deltmx=10000.0)
for i in range(2,20):
    mdb.models['thermal'].HeatTransferStep(name='Step-'+str(i), previous='Step-'+str(i-1),
maxNumInc=100000, initialInc=0.02, minInc=1e-08, maxInc=0.05, deltmx=10000.0)
mdb.models['thermal'].fieldOutputRequests['F-Output-1'].setValues(variables=('NT', 'TEMP'),
timeInterval=0.005)


# Tie the instances
a = mdb.models['thermal'].rootAssembly
for i in range(2,19):
    region1=a.instances['Layer-'+str(i-1)].surfaces['top']
    region2=a.instances['Layer-'+str(i)].surfaces['bottom']
    mdb.models['thermal'].Tie(name='Constraint-'+str(i), master=region1, slave=region2,
adjust=ON, tieRotations=ON, thickness=ON)


# Apply the heat convection
region=a.surfaces['all-surfaces']
mdb.models['thermal'].FilmCondition(name='Convection', createStepName='Step-1',
```

```
surface=region, definition=EMBEDDED_COEFF, filmCoeff=5000.0, filmCoeffAmplitude=",
sinkTemperature=20.0, sinkAmplitude=", sinkDistributionType=UNIFORM, sinkFieldName=")

# Apply model change
for i in range(2,19):
   region =a.instances['Layer-'+str(i)].sets['Set-1']
   mdb.models['thermal'].ModelChange(name='Int-'+str(i), createStepName='Step-1',
region=region, activeInStep=False, includeStrain=False)
   mdb.models['thermal'].interactions['Int-'+str(i)].setValuesInStep(stepName='Step-'+str(i),
activeInStep=True)

# Apply initial temperature and body heat flux to the parts
region = a.sets['All-instances']
mdb.models['thermal'].Temperature(name='Predefined Field-1', createStepName='Initial',
region=region, distributionType=UNIFORM,
crossSectionDistribution=CONSTANT_THROUGH_THICKNESS, magnitudes=(20.0, ))
region = a.sets['All-layers']
mdb.models['thermal'].BodyHeatFlux(name='Load-1', createStepName='Step-1', region=region,
magnitude=1.0, distributionType=USER_DEFINED)
mdb.models['thermal'].loads['Load-1'].deactivate('Step-19')
# Generate the mesh on the parts
p = mdb.models['thermal'].parts['Layer']
p.seedPart(size=0.0002, deviationFactor=0.1, minSizeFactor=0.1)
p.generateMesh()
p = mdb.models['thermal'].parts['Substrate']
p.seedPart(size=0.0005, deviationFactor=0.1, minSizeFactor=0.1)
p.generateMesh()
####   Mechanical Model ####
```

```
# Creating the material
del mdb.models['mechanical'].materials['Material-1'].userMaterial
mdb.models['mechanical'].materials['Material-1'].Depvar(n=13)
mdb.models['mechanical'].materials['Material-1'].UserMaterial(mechanicalConstants=(200000000000.0, 0.3, 250000000.0, 0.0, 370000000.0, 0.03, 450000000.0, 0.07, 570000000.0, 0.11, 599000000.0, 0.17))
# Creating steps and modifying filed outputs
for i in range(1:20):
   del mdb.models['mechanical'].steps['Step-'+str(i)]
mdb.models['mechanical'].StaticStep(name='Step-1', previous='Initial', maxNumInc=100000, initialInc=0.001, minInc=1e-08, maxInc=0.02, nlgeom=ON)
for i in range(2,20):
   mdb.models['mechanical'].StaticStep(name='Step-'+str(i), previous='Step-'+str(i-1), maxNumInc=100000, initialInc=0.001, minInc=1e-08, maxInc=0.02, nlgeom=ON)
mdb.models['mechanical'].fieldOutputRequests['F-Output-1'].setValues(variables=('S', 'E', 'LE', 'U', 'NFORC', 'NT', 'TEMP'), frequency=LAST_INCREMENT)

# Apply model change
a = mdb.models['mechanical'].rootAssembly
for i in range(2,19):
   region =a.instances['Layer-'+str(i)].sets['Set-1']
   mdb.models['mechanical'].ModelChange(name='Int-'+str(i), createStepName='Step-1', region=region, activeInStep=False, includeStrain=False)
   mdb.models['mechanical'].interactions['Int-'+str(i)].setValuesInStep(stepName='Step-'+str(i), activeInStep=True)

#### Apply thermal load #####
mdb.models['mechanical'].predefinedFields['Predefined Field-
```

```
1'].setValues(distributionType=FROM_FILE, fileName='/nfs/speed-scratch/f_hajial/Plus-shape-18/thermal_18.odb', beginStep=1, beginIncrement=0, endStep=1, endIncrement=200)
for i in range(2,20):
    mdb.models['mechanical'].predefinedFields['Predefined Field-1'].setValuesInStep(stepName='Step-'+str(i), beginStep=i, endStep=i)
```

- Creating training dataset (Post-processing)

```
from abaqus import *
from abaqusConstants import *
import __main__
import odbAccess
from odbAccess import openOdb
import numpy as np
import os
totalInsNum = 18
maxInsNum = 12
resultDirPath = os.getcwd()
workDirPath = resultDirPath
jobName = 'thermal_18'
jobOdbPath = workDirPath + '/' + jobName + '.odb'
mainOdb = session.openOdb(name= jobName,path= jobOdbPath)
myInstances = mainOdb.rootAssembly.instances.items()
myInstancesLen = len(myInstances)
mySteps = mainOdb.steps
stepNum = len(mySteps)
nodes = myInstances[0][1].nodes
numNodes = len(nodes)
```

```
Elements = myInstances[0][1].elements
numElements = len(Elements)


# Generate temperature history as testing data
elementInputHistory_test = {}
outputStress_test = {}
for instanceNum in range(len(myInstances)-1):
    elementInputHistory_test[instanceNum+1] = {}
    outputStress_test[instanceNum+1] = {}
    for el in range(numElements):
        elementInputHistory_test[instanceNum+1][el+1] = []
        outputStress_test[instanceNum+1][el+1] = []
#
# for step in range(1,stepNum+1):
#     a = 0
#     stepName = 'Step-' + str(step)
#     myFrames = mySteps[stepName].frames
#     for frame in myFrames:
#         a = a + 1
#         instanceNum = 0
#         for instance in myInstances:
#             if instance[0]!='SUBSTRATE-1':
#                 instanceNum = instanceNum + 1
#                 if instanceNum<=2:
#                     if step<=13:
#                         for el in range(numElements):
#                             try:
```

```
#                   elTemp =
frame.fieldOutputs['TEMP'].getSubset(region=instance[1]).values[8*el].data
#                 elementInputHistory_test[instanceNum][el+1].append(int(elTemp))
#               except:
#                 elementInputHistory_test[instanceNum][el+1].append(20)
#         if instanceNum>=3 and instanceNum<=7:
#           if step>=myInstances.index(instance) and step<=myInstances.index(instance)+12:
#             for el in range(numElements):
#               try:
#                   elTemp =
frame.fieldOutputs['TEMP'].getSubset(region=instance[1]).values[8*el].data
#                 elementInputHistory_test[instanceNum][el+1].append(int(elTemp))
#               except:
#                 elementInputHistory_test[instanceNum][el+1].append(20)
#         if instanceNum>=8:
#           if step>=7:
#             for el in range(numElements):
#               try:
#                   elTemp =
frame.fieldOutputs['TEMP'].getSubset(region=instance[1]).values[8*el].data
#                 elementInputHistory_test[instanceNum][el+1].append(int(elTemp))
#               except:
#                 elementInputHistory_test[instanceNum][el+1].append(20)
#      print('**Element Input Data Preparation**  Step ' + str(step)+ ':  ' + str(a) + ' out of ' +
str(len(myFrames)) +' Frames Completed')
#
# #
```

```
# elCoords = {}
# for instanceNum in range(len(myInstances)-1):
#     elCoords[instanceNum+1] = {}
#
# instanceNum = 0
# for instance in myInstances:
#     if instance[0]!='SUBSTRATE-1':
#         instanceNum = instanceNum + 1
#         nodes = instance[1].nodes
#         numNodes = len(nodes)
#         Elements = instance[1].elements
#         numElements = len(Elements)
#         for el in range(numElements):
#             attachednodes = Elements[el].connectivity
#             xCent = 0.
#             yCent = 0.
#             zCent = 0.
#             for j in attachednodes:
#                 xCent = xCent + nodes[j-1].coordinates[0]
#                 yCent = yCent + nodes[j-1].coordinates[1]
#                 zCent = zCent + nodes[j-1].coordinates[2]
#             elCoords[instanceNum][el+1]=[xCent/8.,yCent/8.,zCent/8.]
#
#
elementInputHistory_test[instanceNum][el+1].append(round(elCoords[instanceNum][el+1][0],6)
)
#             elementInputHistory_test[instanceNum][el+1].append(0)
```

```
#
elementInputHistory_test[instanceNum][el+1].append(round(elCoords[instanceNum][el+1][2],6)
)
#           if elCoords[instanceNum][el+1][1] < 0.0002:
#               elementInputHistory_test[instanceNum][el+1].append(1)
#           else:
#               elementInputHistory_test[instanceNum][el+1].append(0)
#
elementInputHistory_test[instanceNum][el+1].append(round(elCoords[instanceNum][el+1][1]/(t
otalInsNum/1000.),6))
# np.save('elCoords_'+str(totalInsNum)+'.npy',elCoords)
# np.save('elementInputHistory_test_'+str(totalInsNum)+'.npy',elementInputHistory_test)
# #
# # #
#
# instanceNum = 0
#           elementInputData = open(resultDirPath + '/' +
'elementInputHistory_test_'+str(totalInsNum)+'.txt','w+')
# for instanceNum in range(len(myInstances)-1):
#     instanceNum = instanceNum+1
#     for el in range(numElements):
#         elementInputData.writelines(str(elementInputHistory_test[instanceNum][el+1])+ "\n")
#     print('Writing Data: Instance '+str(instanceNum)+' Completed')
mainOdb.close()
# elementInputData.close()

# Generate output data - stresses in integration points
jobName = 'mechanical_18'#+str(instanceNum)
```

```
jobOdbPath = workDirPath + '/' + jobName + '.odb'
mainOdb = session.openOdb(name= jobName,path= jobOdbPath)
myInstances = mainOdb.rootAssembly.instances.items()
mySteps = mainOdb.steps
lastStepNum = len(mySteps)
lastStep = 'Step-' + str(lastStepNum)
myStep = mainOdb.steps[lastStep]
lastFrame = myStep.frames[-1]

instanceNum = 0
for instance in myInstances:
  if instance[0]!='SUBSTRATE-1':
    instanceNum = instanceNum+1
    for i in range(numElements):
      S1 = lastFrame.fieldOutputs['S'].getSubset(region=instance[1]).values[8*i]
      S2 = lastFrame.fieldOutputs['S'].getSubset(region=instance[1]).values[8*i+1]
      S3 = lastFrame.fieldOutputs['S'].getSubset(region=instance[1]).values[8*i+2]
      S4 = lastFrame.fieldOutputs['S'].getSubset(region=instance[1]).values[8*i+3]
      S5 = lastFrame.fieldOutputs['S'].getSubset(region=instance[1]).values[8*i+4]
      S6 = lastFrame.fieldOutputs['S'].getSubset(region=instance[1]).values[8*i+5]
      S7 = lastFrame.fieldOutputs['S'].getSubset(region=instance[1]).values[8*i+6]
      S8 = lastFrame.fieldOutputs['S'].getSubset(region=instance[1]).values[8*i+7]

      S11_1 = S1.data[0]
      S11_2 = S2.data[0]
      S11_3 = S3.data[0]
      S11_4 = S4.data[0]
```

```
S11_5 = S5.data[0]
S11_6 = S6.data[0]
S11_7 = S7.data[0]
S11_8 = S8.data[0]
S11 = round((S11_1+S11_2+S11_3+S11_4+S11_5+S11_6+S11_7+S11_8)*1e-6/8.,3)

S22_1 = S1.data[1]
S22_2 = S2.data[1]
S22_3 = S3.data[1]
S22_4 = S4.data[1]
S22_5 = S5.data[1]
S22_6 = S6.data[1]
S22_7 = S7.data[1]
S22_8 = S8.data[1]
S22 = round((S22_1+S22_2+S22_3+S22_4+S22_5+S22_6+S22_7+S22_8)*1e-6/8.,3)

S33_1 = S1.data[2]
S33_2 = S2.data[2]
S33_3 = S3.data[2]
S33_4 = S4.data[2]
S33_5 = S5.data[2]
S33_6 = S6.data[2]
S33_7 = S7.data[2]
S33_8 = S8.data[2]
S33 = round((S33_1+S33_2+S33_3+S33_4+S33_5+S33_6+S33_7+S33_8)*1e-6/8.,3)

S12_1 = S1.data[3]
```

```
S12_2 = S2.data[3]
S12_3 = S3.data[3]
S12_4 = S4.data[3]
S12_5 = S5.data[3]
S12_6 = S6.data[3]
S12_7 = S7.data[3]
S12_8 = S8.data[3]
S12 = round((S12_1+S12_2+S12_3+S12_4+S12_5+S12_6+S12_7+S12_8)*1e-6/8.,3)

S13_1 = S1.data[4]
S13_2 = S2.data[4]
S13_3 = S3.data[4]
S13_4 = S4.data[4]
S13_5 = S5.data[4]
S13_6 = S6.data[4]
S13_7 = S7.data[4]
S13_8 = S8.data[4]
S13 = round((S13_1+S13_2+S13_3+S13_4+S13_5+S13_6+S13_7+S13_8)*1e-6/8.,3)

S23_1 = S1.data[5]
S23_2 = S2.data[5]
S23_3 = S3.data[5]
S23_4 = S4.data[5]
S23_5 = S5.data[5]
S23_6 = S6.data[5]
S23_7 = S7.data[5]
S23_8 = S8.data[5]
```

```
            S23 = round((S23_1+S23_2+S23_3+S23_4+S23_5+S23_6+S23_7+S23_8)*1e-6/8.,3)

            outputStress_test[instanceNum][i+1].append(S11)
            outputStress_test[instanceNum][i+1].append(S22)
            outputStress_test[instanceNum][i+1].append(S33)
            outputStress_test[instanceNum][i+1].append(S12)
            outputStress_test[instanceNum][i+1].append(S13)
            outputStress_test[instanceNum][i+1].append(S23)

        print('Element Output Data Preparation: Instance ',instanceNum,' Completed')

np.save('outputStress_test_'+str(totalInsNum)+'.npy',outputStress_test)

instanceNum = 0
elementOutputData = open(resultDirPath + '/' + 'outputStress_test_'+str(totalInsNum)+'.txt','w+')
for instanceNum in range(len(myInstances)-1):
    instanceNum = instanceNum+1
    for el in range(numElements):
        elementOutputData.writelines(str(outputStress_test[instanceNum][el+1])+ "\n")
    print('Writing Data: Instance '+str(instanceNum)+' Completed')

mainOdb.close()
elementOutputData.close()

# X_file = open('X_data_18.txt','w')
# X_data = str(elementInputHistory_test)
# X_file.write(X_data)
```

```
# X_file.close()
#
# y_file = open('y_data_18.txt','w')
# y_data = str(outputStress_test)
# y_file.write(y_data)
# y_file.close()
```